SOME ASPECTS OF FATIGUE AND FRACTURE IN A C-Mn STRUCTURAL STEEL

by

S.A.A. ABOUTORABI

Submitted to
The University of Glasgow
for the degree of
Doctor of Philosophy

Mechanical Enginering Department,
The University of Glasgow,
Glasgow G12 8QQ.
Scotland.

September 1985

To my wife Mehran

ACKNOWLEDGEMENTS

I am deeply grateful to Dr. M.J. Cowling for his admirable supervision during the period of research for this thesis. I am greatly indebted to him for his patience and encouragement throughout. Thanks are also due to Dr. D.K. Brown for his valuable advice and assistance with the numerical analysis.

This work was funded through Marine Technology Directorate of SERC under grant nos. GR/B/8872.3 and GR/C/7139.2, whose financial assistance is acknowledged. I would also like to thank Professor B.F. Scott, Head of the Mechanical Engineering Department, for providing adequate facilities for execution of this project.

Thanks are also due to Messrs. A. Torry, A. Birbeck and N. Flaherty of the technical staff for their assistance with the experiments.

I am indebted to Miss M. Dunlop who typed this thesis with excellent accuracy. Her skill is evident.

I wish to express my gratitude to my wife Mehran, whose love and care, while suffering herself, was a great inspiration throughout this work.

Finally tribute is due to my late father Mr. M.A. Aboutorabi who very much wanted to see this thesis.

Section 2 FAILURE MECHANISMS

Section 3 MATERIAL PROPERTIES

Section 4 POST YIELD FRACTURE TOUGHNESS PARAMETERS

Section 5 STRESS INTENSITY FACTORS FOR SEMI-ELLIPTICAL CRACKS

SUMMARY

The work described in this thesis comprised an investigation into a number of concepts associated with the failure of a C-Mn steel (BS4360 Grade 50D) which is frequently used as a prime structural material in offshore structures.

The initial investigation concerned the temperature dependence of the stress state sensitivity of the ductile failure strain of the material. For the limited range of the stress state studied, it was found that this sensitivity is independent of temperature.

Failure initiation characterizing parameters δ_i and J_i were also found to be sensitive to stress state in the crack tip region. This sensitivity however depends on the temperature and decreases with decreasing temperature in the ductile-brittle transition region. This behaviour was shown to be associated with the interruption of the ductile failure process by the lower temperature brittle fracture mechanism.

The investigation into the development of part through surface cracks under tensile fatigue loading indicated that the crack profile develops towards an equilibrium shape of $a/c = 0.8$.

The distribution of stress intensity factor K_I around the periphery of part through surface cracks under remote tensile loading was determined for a variety of crack geometries. This distribution was found to be a function of the crack profile. Various solutions were examined and it was shown that the numerical solution of Newman and Raju correlates relatively well with the experimental results for fractional depth in the range $0.22 \leqslant a/t \leqslant 0.6$.

It was observed that subsequent to the adoption of an equilibrium shape, further fatigue crack growth produced bul ging near the surface intersections. This behaviour was modelled by considering the variation of stress state and its effect on the plastic zone ahead of the crack tip.

The initiation and subsequent propagation due to post yield failure around the periphery of a part through surface crack of $^{a}/_{c}$ = 0.69 and $^{a}/_{t}$ = 0.7 subjected to montonic tensile loading was investigated. The distribution of initiation COD around the crack front was determined. It was found that this distribution is different from that for K_I. Initiation of ductile failure at ambient temperature occurs first in regions of high constraint at locations close to but under the plate surface. The subsequent crack propagation however is in a manner in which crack front progresses towards regions of lower constraint. It was shown that post yield failure from the part through crack geometry studied may be correlated with failure parameters measured in various types of standard laboratory through crack test pieces. Experimental limit loads were compared with empirical prediction procedures which were found to be in general conservative for the defect geometry studied.

INTRODUCTION

During the past three decades, the development of fracture mechanics has presented a useful tool to quantify the fracture behaviour of engineering materials. It has also provided a methodology to utilize laboratory test data derived from small samples to assure the structural integrity of large components in service, and to aid in the analysis of service failures.

The engineering application of fracture mechanics has been mostly concerned with Linear Elastic Fracture Mechanics (LEFM). While LEFM proves to be invaluable for the description of sub-critical crack growth due to fatigue loading and for final failure in brittle materials, it becomes less appropriate when applied to failure in lower strength ductile materials where extensive plasticity precedes and accompanies fracture. In recent years, much experimental and analytical work has been devoted towards development of elastic-plastic fracture mechanics (EPFM) where failure initiation and subsequent crack advance occurs under elastic-plastic conditions. EPFM has developed to the point where there are recommended procedures[1] incorporating the use of crack opening displacement (COD) for failure assessment of fusion welded structures, and test procedures[2] for the evaluation of fracture initiation toughness using the J integral approach. However, the useful application of EPFM for analysis of real structures is somewhat limited by the lack of adequate information concerning the conditions governing the behaviour of a crack in an elastic-plastic stress field.

In the majority of structures, service failures have been associated with failure from part-through surface breaking cracks which can be approximated by semi-elliptical shapes. Failure from such defects is little understood and a relationship between failure from such defects and standard laboratory test techniques has not been established.

In the work presented in this thesis, development of surface breaking cracks, both in fatigue and under monotonic loading has been studied. Considerable emphasis is placed on the effect of constraint on the fracture process in the post yield regime. The material used, was BS4360 grade 50D structural steel. This steel is a carbon manganese low strength (σ_y = 360 MPa) steel, extensively used in critical joints of offshore structures in the North Sea, which at ambient temperature exhibits a high degree of ductility.

The layout of this thesis is such that each section as well as being a sequential part of thesis, is in itself an integral essay, reporting and concluding on a phase of the overall investigation. A review of development of fracture mechanics to date is presented in a chronological order in section one, followed by a detailed review of micromechanisms of fracture in Section 2.

It has been shown[3] that for most structural steels, the requisite failure strain for the initiation of ductile fracture is a strong function of the state of stress (triaxiality). Consequently it should be expected that/

EPFM fracture characterising parameters are also affected by the degree of triaxiality. The initial investigation reported here was a study of the variation of failure strain with triaxiality in the ductile-brittle transition temperature regime. This part of work together with the basic properties of the material is reported in Section 3.

The effect of constraint on the EPFM parameters, COD and J, was investigated as a function of temperature across the transition temperature range, using two different specimen geometries which produce two markedly different degrees of constraint under plane strain conditions. This part of the investigation is presented in Section 4 which also contains the results of a finite element analysis which was performed to further understanding of the elastic plastic fracture behaviour of the SECT geometry.

In Section 5 the variation of stress intensity factor around the periphery of a semi-elliptical crack developing under fatigue loading is reported. An essential feature of this study was the accurate measurement of the crack profile by non-destructive test techniques. A measurement technique based on the A.C. potential drop technique was developed to satisfy this requirement.

Finally the results of a study of the post yield failure from a semi-elliptic surface breaking defect is reported in Section 6. This study included an analysis of failure initiation and subsequent monotonic crack growth when characterised by COD and the relationship between failure characterization for surface breaking and through-crack geometries.

References

1. British Standards Institution, ''Guidance on some methods for the derivation of acceptance levels for defects in fusion welded joints'', PD6493, 1980.

2. American Society for Testing and Materials ASTM, ''Standard Test for J_{IC}, a Measure of Fracture Toughness'', E813, 1981.

3. Cowling, M.J., Hancock, J.W. and Brown, D.K. ''The role of the state of stress in the failure prediction of offshore structures'', Proc. Int. Symp. Integrity of Offshore Structures, IESS, Paper 5, Glasgow 1978.

Section 1

FRACTURE MECHANICS CONCEPTS

1.1 Introduction

In this section the basic concepts of fracture mechanics are presented and the application of fracture mechanics in the prediction of failure of structures containing defects is discussed. This section provides a chronological review of the development of fracture mechanics to its present state. A state which in addition to providing improved safety standards, has an important economic role in reducing the cost of construction by encouraging less conservative and more adventurous designs.

A description of Linear Elastic Fracture Mechanics (LEFM) is given in the form of a discussion of the concepts of Elastic Strain Energy Release Rate and Stress Intensity Factors which form the foundation of modern fracture mechanics. The subject is then expanded, to include the concepts of Crack Opening Displacement (COD) and the Rate of Change of Potential Energy (J), for describing fracture behaviour associated with large scale plasticity, where LEFM is inadequate.

1.2 The elastic strain energy release rate

The engineering approach to fracture originates from the early work of Griffith[1], who observed a large discrepancy between the theoretical estimation of strength of elastic solids based on the atomic cohesive forces and experimental evidence of fracture stress. He derived a new theoretical/

criterion based on the energy theorem[2] that if the total potential energy of a cracked body was reduced by the incremental propagation of an existing crack then such propagation would indeed occur. The Griffith analytical model consisted of a thin unit thickness, biaxially loaded infinite plate having fixed boundary conditions and containing a through thickness crack (Fig. 1.1). By using the Inglis[3] solution for the elastic stresses in the vicinity of an elliptical hole in a uniaxially loaded thin lamina, Griffith calculated the elastic strain energy of the system as:

$$U_e = -\frac{1}{2}\frac{\sigma^2 \pi a^2}{E'}$$

where a is half crack length

σ is nominal applied stress

$E' = E$ Plane stress

$E' = \frac{E}{(1-\nu^2)}$ Plane strain

E is Young's modulus of elasticity

ν is Poisson's ratio

It was postulated that unstable fracture would occur if by incrementally increasing the crack length, the rate of change in elastic strain energy was equal to or greater than the rate of change in the energy required to create new surfaces. Defining the work done to create new surfaces as:

$$W = 2aT_e$$

where T_e is the specific surface tension, fracture will occur if:

$$dU_e/da \geqslant dW/da$$

i.e.

$$dU_e/da \geqslant 2T_e$$

The strain energy release rate dU_e/da was therefore considered as a criterion to assess the potential for fracture and given the symbol G:

$$G = dU_e/da = \frac{\sigma 2\pi a}{E'} \qquad (1.1)$$

The level at which unstable fracture takes place is designated G_c, the critical strain energy release rate. G_c is found to be a constant material property for a particular environment, strongly dependent on temperature and strain rate, in a similar manner to yield stress.

The critical stress level σ_c to initiate brittle fracture in a material containing a critical crack length $2a_c$ could therefore be calculated from above equation:

$$\sigma_c = (2E'T_e/\pi a_c)^{\frac{1}{2}}$$

It can also be postulated that at a given stress level, cracks with length smaller than $2a_c$ would not cause unstable fracture. The Griffith theory is the basis from which modern fracture mechanics has developed and it is important to remember its limitations i.e.

(i) the material is entirely brittle

(ii) the model considered is a large plate of unit thickness containing a very small through crack in form of a flat ellipse so that no boundary or size effects are imposed apart from the crack size.

(iii) the condition is for the onset of instability only and no information for conditions before or after that is given.

(iv) the only material properties involved are E and T_e which are assumed constant.

With this relatively simple procedure Griffith succeeded in explaining the discrepency between the theoretical and actual strength of brittle materials, and validated his work by performing experiments on glass specimens in which the length of defects was varied. After Griffith, there was not much development in the field for about 20 years, though energy release rate formulae were developed for some other simple geometries.[4-5]

From the limitations of the Griffith analysis outlined above, it is clear that in order to adapt the criterion to metals, it is necessary to modify it considerably to account for the plastic deformation before and during fracture. The work term dW/da cannot be taken simply as the theoretical surface energy 2T. It was essential to replace 2T by a term denoting the total work done against the resistance of material to fracture.

In 1947 Orowan[6] and in 1948 Irwin[7] independently provided the required modification to allow a more general application to metals which exhibit plastic deformation. This modification took the form of an additional term defined as the surface plastic energy absorption T_p:

$$G=\sigma^2\pi a/E=2(T_e+T_p)$$

It must be pointed out that the validity of the assumption depends on the fact that the plastic zone developed at a crack tip is significantly smaller than the crack dimension. In 1952 Irwin and Kies[8] approached the problem from another angle. They postulated that fracture would occur if the elastic strain energy is equal to the work done by a remotely applied load P to create an incremental displacement δ at the crack tip:

$$U_e = P\delta/2 = P^2C/2$$

where C is the linear elastic compliance of the specimen. The strain energy release rate G can then be found by differentiating the above equation:

$$dU_e/da = G = \frac{P^2}{2} \cdot \frac{dC}{da} \qquad (1.3)$$

It was suggested that by measuring the linear elastic compliance of similar specimens which contain different crack lengths, it would be possible to evaluate dC/da as a function of crack length. At fracture the initiation appropriate value of dC/da could then be substituted, along with the associated load to determine the level of G_c experimentally.

1.3 The Stress Intensity Factor (SIF)

In 1939, Westergaard[9] developed a relatively simple treatment, for the stress field in the vicinity of an elliptical internal void, based on the functions of a complex variable. Sneddon[10] used this treatment to calculate the rate of elastic strain energy, and developed a series of solutions for linear elastic stresses at the tip of a sharp crack. In 1957 Irwin[11] observed that the stress distribution local to the crack tip could be/

expressed in a singular characteristic form which decreased by the inverse square root of the radial distance measured from the crack tip, (Fig. 1.2).

$$\sigma_{ij} = \frac{K}{f(r)} \, F_{ij}(\theta)$$

where

σ_{ij} is the stress magnitude in the x, y and z coordinate direction at any point,

f(r) is a series function in terms of r,

$F_{ij}(\theta)$ is a function of θ and is dependent of the overall geometry of the problem

and finally K is a function of applied stress, crack length and crack geometry. K can be considered as a measure of the amplitude of the stress field singularity and subsequently it was called the Stress Intensity Factor (SIF).

In any loaded cracked body the crack tip stress intensity factor can be said to be unique for the particular mode of loading. There are three principal types of loading as illustrated in Fig. 1.3.

MODE I - Normal displacement of the crack surfaces relative to one another (opening mode).

MODE II - In-plane displacement of the crack surfaces relative to one another (shearing mode).

MODE III - Anti-plane displacement of the crack surfaces relative to one another (anti plane shearing mode).

The stress intensity factor was thus given a suffix appropriate to the corresponding mode of fracture K_I, K_{II} and K_{III}. The most common type of fracture/

is the opening mode. The stress and displacement distribution ahead of the crack in terms of stress intensity factor for this mode are:

$$\begin{bmatrix}\sigma_{xx}\\ \sigma_{yy}\\ \tau_{xy}\end{bmatrix} = \frac{K_I}{\sqrt{2\pi r}} \begin{bmatrix}\cos\frac{\theta}{2}\left(1-\sin\frac{\theta}{2}\sin\frac{3\theta}{2}\right)\\ \cos\frac{\theta}{2}\left(1+\sin\frac{\theta}{2}\sin\frac{3\theta}{2}\right)\\ \cos\frac{\theta}{2}\sin\frac{\theta}{2}\cos\frac{3\theta}{2}\end{bmatrix} + \ldots \qquad (1.4)$$

$$u = 2(1+\nu)\frac{K_I}{E}\sqrt{\frac{r}{2\pi}}\ \mathrm{Cos}\ \frac{\theta}{2}\left(2-2\nu-\mathrm{Cos}^2\frac{\theta}{2}\right)$$

$$v = 2(1+\nu)\frac{K_I}{E}\sqrt{\frac{r}{2\pi}}\ \mathrm{Sin}\ \frac{\theta}{2}\left(2-2\nu-\mathrm{Cos}^2\frac{\theta}{2}\right)$$

$$w = 0 \text{ for plane strain}$$

Since K characterises the crack tip field it has the potential to characterise failure of a cracked body i.e. failure occurs when $K_I = K_C$. Only for very specific conditions (plane strain, contained yielding) does the failure occur when $K = K_{IC}$ which is termed the fracture toughness.

In the case of a classical central crack of length 2a in an infinite remotely tensile loaded body SIF is given by:

$$K_I = \sigma\sqrt{\pi a} \qquad (1.5)$$

therefore for a material with fracture toughness K_{IC} the critical stress at the threshold of instability is:

$$\sigma_c = K_{IC}/\sqrt{\pi a_c}$$

This is a more reliable approach than the critical strain energy release rate, since it is based on a stress condition at the crack tip. However since both G and K are linear elastic characterizations, it is expected that/

they should be related to each other. Indeed by inspection of equation 1.1 and substituting for K from equation 1.5 it can be seen that:

$$G=\sigma^2\pi a/E'=K^2/E' \qquad (1.6)$$

This relationship permits the reverse determination of SIF for a finite geometry by experimental measurement of G from compliance methods.

The description of SIF given so far has been for the classical cracked thin infinite plate. A more general expression for K is given by:

$$K=F(g)\sigma\sqrt{\pi a} \qquad (1.7)$$

where F(g) is a function dependent on specimen geometry, crack shape, boundary conditions etc. The form of this function for specific geometries has been the subject of much research since the introduction of the stress intensity factor concept, e.g. Paris and Sih[12], Tada et al[13] and Sih[14]. Rooke and Cartwright[15] compiled a comprehensive handbook of solutions for SIF for different geometries, crack shapes and loading conditions. In 1981 Rooke et al[16] described the variety of methods available for determination of stress intensity factors.

1.3.1 Crack tip small scale yielding

The stress intensity factor has found great acceptance as a tool in assessing fracture since its introduction by Irwin. In order to be applicable to elastic-plastic problems, the effect of crack tip plasticity must be accommodated. The stress solutions of Irwin given in equation 1.4 predict that the stress at the crack tip (r=0) will be infinite. From a practical/

point of view this means that the crack tip material will yield producing a plastic zone within the surrounding elastic field. The effect of introducing a small plastic zone at the crack tip is to limit the maximum stress at the crack tip. If the plastic zone is very small its strain energy content will be negligible and its effect on the overall stress distribution will not be significant. As the plastic zone increases in size, its energy content will become larger, and its effect on the overall stress distribution will correspondingly increase. In this case the K and G values obtained from the linear elastic analysis, will not fully represent the problem.

Irwin in 1960[17] found that the range of applicability of the elastic solution could be extended by adjusting the position of the crack tip to take account of the local plasticity. From his earlier solution of the stress distribution around the crack tip he calculated the normal stresses ahead of the ctrack tip ($\theta = 0$) and by putting this stress equal to the material yield stress, estimated the radius of plastic zone.

$$r_y = \frac{1}{2\pi} (K/\sigma_y)^2 \qquad \text{Plane stress} \qquad (1.8a)$$

$$r_y = \frac{1}{6\pi} (K/\sigma_y)^2 \qquad \text{Plane strain} \qquad (1.8b)$$

where σ_y is nominal yield stress.

The allowance for a small amount of crack tip plasticity could be made if a distance r_y was added to the actual crack tip to create a fictitous elastic crack of length $a+r_y$. Thus the stress intensity factor would be modified as:

$$K=F(g,r_y)\sigma\sqrt{\pi(a+r_y)} \qquad (1.9)$$

This correction to the linear elastic stress intensity factor by artificially increasing the crack length is only valid if $r_y << a, W$. The regime in which the region of plasticity is small compared to crack length or net section has become known as contained yielding or Small Scale Yielding (SSY).

1.3.2 Fracture toughness testing

LEFM depends for success on the existence of a unique material fracture toughness value. Most materials exhibit a strong thickness effect on toughness. Fig. 1.4 shows typical behaviour where high toughness is associated with thin sections and shear fracture. Significantly lower toughness occurs when measured in thicker sections and is associated with ''flat'' fracture. The reason for this thickness effect is the changing size of the plastic zone size (Fig. 1.5) with constraint. As the material thickness increases the plane strain region becomes dominant leading to the minimum plane strain fracture toughness K_{IC} which is a material constant. Hence valid fracture toughness measurements require a minimum degree of plane strain. In 1974 the American Society for Testing and Materials ASTM, prepared a standard method for plane strain fracture toughness testing E399-74[18] this was followed by British Standard document BS5447-1977[19]. These standards require a validity check on the critical value of toughness K_C obtained in the test before assigning it the K_{IC} designation. This validity check requires that:

$$a,\ (w-a),\ B \geq 2.5(K_{IC}/\sigma_y)^2 \qquad (1.10)$$

where a, W, B are crack length, specimen width and specimen thickness respectively. $(\frac{K_{IC}}{\sigma y})^2$ is the measure of plastic zone size as given in section 1.3.1.

Having obtained a valid K_{IC} value for a material a critical defect size for a particular design stress level may be calculated by application of the particular equation, for the specific defect geometry, of the type (1.7).

1.4 Crack growth resistance curve

The ASTM E-399 and BS5447 procedures for determination of plane strain fracture toughness of materials, produce invalid results at the presence of plasticity and slow crack growth before the occurrence of fracture. On the other hand as Creager and Lui[20] stated, the fracture process of a cracked thin sheet is not usually comprised of a single sudden explosive-type change from initial crack length to total failure. As the load increases, considerable slow crack growth takes place prior to catastrophic failure. In 1961 Krafft et al[21] envisaged a unique relationship between the amount of slow crack growth prior to fracture and the applied stress intensity factor. They called it the crack growth resistance curve or R-curve.

The R-curve characterizes a material resistance to fracture during incremental slow crack growth and is an extension of LEFM theory in the SSY regime. A typical R-curve is shown in Fig. 1.6. The crack instability is represented as the tangency of the R-curve and the crack driving force at a given load. The application of the R-curve technique will be discussed in more detail when the Crack Opening Displacement and J-Integral are introduced as elastic-plastic fracture toughness parameters.

Summary of LEFM

The work of Irwin in developing the crack tip parameter K, was a major breakthrough in allowing practical assessment of cracked structures and for bringing modern fracture mechanics to its present state. However the limitation of the LEFM approach is that it is only applicable for situations where plasticity is limited to a region close to the crack tip. As the plastic zone becomes significant in comparison to the dimension of the crack, then the LEFM treatment becomes inadequate to provide accurate solutions for the problem. Valid K_{IC} test requirements outlined in section 1.3.2 demand very large testpieces to obtain valid K_{IC} values for tough materials. It is this dilemma which has provided the driving force for the development of elastic-plastic fracture mechanics.

1.5 Elastic-Plastic Fracture Mechanics (EPFM)

In the previous section it was indicated how LEFM procedures can successfully predict fracture in situations where the loading or geometry of a cracked body is such that none or only small scale plasticity is exhibited at the crack tip. This low energy type of fracture can be considered as one extreme form of failure, where the other extreme would be a plastic collapse mechanism in the uncracked ligament of the material. Between these two modes, fracture takes place with large scale plasticity which is sufficient to invalidate LEFM, but insufficient to initiate plastic collapse. This is then the territory of elastic-plastic fracture mechanics.

The elastic-plastic analysis of fracture characterization has evolved around many distinctive approaches. Among failure characterising parameters that have been presented are:

1. The value of the opening displacement at the tip of a crack (COD)
2. The value of the J-integral, which is effectively the change in strain energy of a cracked body for a given increment of crack length.
3. The two-criteria failure assessment approach, originally developed by Dowling and Townley[22] and adopted by Central Electricity Generation Board (CEGB) of The United Kingdom.

The third technique will not be described here since it is not used in this investigation. Reference 23 gives a description of this technique.

1.6 Crack Opening Displacement (COD)

When extensive plasticity occurs at the crack tip before the onset of failure the fracture process is controlled by the extent of the plastic strain field developed ahead of the crack. Wells[24] in 1961 proposed that the separation of the crack faces, which is a measure of the extent of normal deformation, could be considered as a characterization parameter of the strain and thus stress fields at the crack tip. Crack extension will then begin at some critical value of this separation referred to as critical Crack Opening Displacement.

Looking initially for a value of normal displacement in the elastic case, it can be seen from The Irwin analysis (equation 1.4) that this value is equal to zero since r=0. However with the Irwin plasticity correction[17] such that $a=a+r_y$, the displacement at the actual crack tip can be derived from equation 1.4 by substituting $r=r_y$ and $\theta = \pi$:

$$v = \frac{4K}{E} \sqrt{\frac{r_y}{2\pi}}$$

Since the crack opening is twice the value of the normal displacement and substituting for r_y from equation 1.8, the crack opening displacement is/

given by:

$$\delta = 2\gamma = 4K^2/\pi E\sigma_y \qquad (1.11)$$

From the linear elastic analysis presented in section 1.3, K in the above relationship can be expressed in terms of G (from equation 1.6) to relate the COD to the energy release at the crack tip:

$$\delta = 4G/\pi\sigma_y \qquad (1.12)$$

In 1963 Wells[25] by using Irwin-Westergaard stress function proposed that the energy balance required to produce an increment of crack extension is equal to the product of yield stress and the displacement at the crack tip (COD) prior to crack extension, since σ_y is the only acting stress across the plastic zone, therefore:

$$\delta = G/\sigma_y \qquad (1.13)$$

A comparison of equations 1.12 and 1.13 indicates a discrepancy between two approaches in the form of a factor $4/\pi$, which relates to the extent of the plastic zone. Wells[25] argued that this factor can be replaced by unity without disturbing the energy balance concept at the crack tip. Indeed a lower bound is given by

$$\delta \geq G/\sigma_y$$

and by substituting for G from equation 1.6:

$$\delta \geq K^2/E\sigma_y \qquad (1.14)$$

A different approach to evaluate the extent of the plastic zone and hence the plastic strain field was followed by Dugdale[26] through a strip yielding model. He introduced a new model, similar to that of Baranblatt[27] which like the Irwin crack model assumed a plastic zone geometry. The detailed behaviour at the crack tip was ignored, and attention was focused on the strain energy variation. Dugdale suggested that a crack of length 2a, in a linear elastic perfectly plastic media, could be represented by a hypothetical crack of length $2(a+r_p)$ as illustrated in Fig. 1.7, where r_p is the extent of plastic zone acted upon by a stress equal to the yield stress. This stress is thus assumed constant for all crack tip displacements i.e. the material is assumed to be non work hardening. Within the plastic zone the elastic strains are assumed negligible compared with the plastic strains i.e. within the plastic zone the material is rigid-plastic. Dugdale suggested that, by equating the work done in closing the crack by the restraining stress σ_y, with the change in internal energy due to shortening the crack, the displacement at the original crack tip could be estimated. Using Westergaard stress functions, Burdekin and Stone[28] evaluated the displacement at the tip of the real crack as:

$$\delta = (8\sigma_y a/\pi E) \ln \mathrm{Sec}(\pi\sigma/2\sigma_y) \qquad (1.15)$$

where σ is the applied remote tensile stress. It can be seen that when the applied stress approaches yield stress equation 1.15 indicates an infinite COD. This arises because the model was originally considered for a non hardening material as stated earlier.

In their work Burdekin and Stone expanded equation 1.15 to give

$$\delta = \frac{8\sigma_y a}{\pi E}\left(\frac{1}{2}\left(\frac{\pi\sigma}{2\sigma_y}\right)^2 + \frac{1}{2}\left(\frac{\pi\sigma}{2\sigma_y}\right)^4 + \ldots\right) \qquad (1.16)$$

Taking the first term of above equation and using the mode I relationship for stress intensity factor K:

$$\delta = \frac{\pi\sigma^2 a}{E\sigma_y} = \frac{K^2}{E\sigma_y} \qquad (1.17)$$

which agrees with the Irwin crack model given in equation 1.14. Taking the first and the second terms of the equation 1.16, the COD can be calculated as:

$$\delta = \frac{K^2}{E\sigma_y}\left[1+\frac{\pi^2}{24}(\sigma/\sigma_y)^2\right] \qquad (1.18)$$

which is similar to the LEFM treatment with a plane stress plastic zone correction (equation 1.8a) differing only in the term $\pi^2/24$ instead of $1/2$. It seems that for $\sigma/\sigma_y \leq 1$ the crack opening displacement is an extension of LEFM into the small scale yielding regime.

It is therefore postulated that even at very low applied load, plastic strains are present and that the material in the crack tip plastic zone will extend by an amount equal to δ. Hence the COD can be a useful parameter in assessing the fracture potential from the linear elastic region through to the limiting condition of plastic collapse.

1.6.1 Crack tip blunting

When a plane strain elastic plastic body containing a crack is loaded in tension, the crack tip blunts open forming a stretch zone until crack extension occurs. The shape of the blunted tip is not unique, it may have two or more vertices which is the indication that the opening is by shearing of the material at the corners, or it may be smoothly curved by imposing very high strains on the crack surface. McMeeking[29] has shown that the slip line field near a crack tip blunted by a vertex mechanism with sharp corners/

is similar to the slip line field around a smoothly blunted crack in the same specimen. Pelloux[30] has shown a simple model for the formation of the stretch zone at the crack tip deformed by a three vertices mechanism, Fig. 1.8. Shear initiates on a plane at 45 degrees to the crack tip, e.g. along AC in Fig. 1.8, until work hardening makes further shear on the AB more favourable. Thus deformation takes place by incremental shear that alternates between two planes at 45 degree to the crack direction, leading to an extension of the crack equal to half the crack flank opening displacement. Rice and Johnson[31] predicted the shape of the blunted crack tip using slip line theory for both small scale yielding and fully plastic cases and obtained values of crack extension equal to 0.55 and 0.65 δ respectively. Experimental observations have also shown that for both types of blunting the extent of the stretch zone is almost half the COD:

$$\delta = 2\Delta a \qquad (1.19)$$

1.6.2 Definition of COD

As discussed earlier, a unique definition of COD is required for its use as a fracture parameter. A clear understanding of physical significance of crack opening displacement helps in the establishment of such a definition. In general when an elastic-plastic material containing a sharp fatigue crack is loaded, the following physical events take place at the crack tip prior to total instability:

1. Blunting of the crack tip and formation of stretch zone.
2. Initiation of crack extension.
3. Stable crack growth
4. Onset of instability in the form of a fast fracture or plastic collapse of remaining ligament.

The schematic representation of these stages and the relation between the characteristic parameter (COD) and the crack growth increment Δa is shown in Fig. 1.9. Initially, as the crack blunts, material ahead of the tip is exposed to large strains and triaxial stresses. Under these conditions voids will nucleate and grow in suitable sites. The detailed mechanism of void nucleation and fibrous fracture will be discussed later. Nucleated voids will grow under plastic strains which develop ahead of the crack tip and eventually, at a critical value of COD, one or more of these voids will link up to the blunted crack, initiating crack extension. The advancing crack will concentrate stress and strain ahead of new tip, hence nucleating more voids and the process will continue until the crack ruptures the remaining ligament or a mechanical instability occurs.

Considering the progressive geometric changes at the blunting crack tip, a unique definition of COD is essential in order to establish the critical event leading to instability. Wells and Burdekin[32] suggested that the COD should be defined as the displacement at the elastic-plastic boundary. Although this definition is reasonable for the small scale yielding condition, it is not acceptable for situations where extensive plasticity exists at the crack tip in a hardening material. In these cases the elastic plastic boundary may move back a significant distance along the flanks of the crack[33], and COD becomes dependent on the crack length and is not therefore a one parameter description of the near tip environment. Dawes[34] in 1976 proposed that for mode I loading, COD can be defined as the displacement at the original crack tip position, i.e. the tip of the fatigue pre-crack in a COD test specimen or a natural crack in a structure. This definition recognises the formation of a stretch zone ahead of the original crack and avoids some of the ambiguity associated with earlier definitions based on the deformed crack tip profile and elastic/

plastic boundary. By defining the original crack tip as the reference position, consistency is maintained with experimental measurement of COD. However the use of COD in numerical analysis requires an alternative definition. Turner[35] in 1978 suggested that the COD should be defined at a reference point a distance J/σ_y from the actual crack tip where J is a path independent integral based on the potential energy variation around the crack tip and will be defined in a later section.

Analytical considerations by Rice[36] and Tracey[37] have led Shih[38] to suggest that COD could be identified with the points of intersection of the crack flanks and the symmetrical 90 degree included angle from the actual blunted crack tip as shown in Fig. 1.10. This definition is attractive since it is consistent with the experimental observation that the stretch zone is approximately equal to half the original crack tip COD. Good agreement is therefore expected between this theoretical definition of COD and the experimental original crack tip COD. In this work the definition of COD due to Dawes will be used.

1.6.3 Critical COD

The application of crack opening displacement in elastic plastic situations is based on the assumption that failure occurs at a critical value of COD (δ_{crit}) which may be a material constant independent of the degree of plastic deformation. In light of physical events leading to failure described in section 1.6.2, δ_{crit} may be defined as (i) COD at the onset of instability δ_c, if stable crack extension is followed by unstable fast fracture, (ii) COD at maximum load δ_m if failure occurs by plastic collapse of remaining ligament or (iii) COD at the initiation of crack extension.

A review of literature indicates that δ_c is affected by section thickness and crack acuity of the test piece, while δ_m is dependent on specimen dimensions and stiffness of the testing machine. Thus δ_c and δ_m should not be used as unique characteristic parameters for safe design. Alternatively studies on the value of COD at the initiation of crack extension δ_i show that under sufficient plane strain conditions δ_i is independent of dimension of test piece and thus has the potential to be a material constant for given temperature and loading condition. However it has been shown that the state of stress in the crack tip flow field does affect δ_i[39]. Work by Hancock and Cowling[40] on a high strength steel shows an order of magnitude difference between values of δ_i for high and low constraint geometries. Thus δ_i cannot be considered as a unique post yield fracture characterizing parameter. There is also experimental evidence to show that δ_i can be very conservative for use in design, though it is the best established toughness parameter in the elastic-plastic regime.

1.6.4 Determination of COD at initiation

The detection of the precise incident of crack initiation is rather difficult in practice and δ_i is usually determined from a crack growth resistance curve where a series of points on a plot of COD versus physical crack extension Δa, is experimentally determined. This relationship, the resistance curve, is then extrapolated back to zero crack extension. If the COD is measured as the displacement at the original crack tip, then the point of intersection of R-curve with blunting line, where there is zero crack extension, is considered as δ_i. A schematic COD-R curve is shown in Fig. 1.11. The blunting line in the R-curve procedure is given by $\delta = 2\Delta a$ as discussed in section 1.6.1.

The crack extension Δa is generally measured by visual measurement on a cross section through the specimen or on the fracture surface. Other techniques such as the compliance method or potential drop measurement have also been used. Values of COD can be determined by different methods such as clip gauge measurement of crack mouth opening displacement, replication technique using hardening silicon rubber, visual measurement on the specimen cross section, measurement of stretch zone size etc.

1.6.5 Significance of COD

The application of COD to elastic-plastic situations is based on the assumption that critical COD is a material constant independent of the degree of plastic deformation at the crack tip. The analytical evidence to support this point is as yet inadequate. However experimental evidence indicate that for small scale yielding condition critical COD is related to K_{IC} by:

$$\delta_{crit} = m(K_{Ic}^2/E\sigma_y) \qquad (1.20)$$

where m is a dimensionless constant dependent on the geometry, degree of stress triaxiality and possibly material work hardening capacity[41]. Irwin[11] assumed a value of $4/\pi$ for m by using his circular plastic zone (equation 1.11). Burdekin and Stone[28] found $m=1$ utilizing the Dugdale strain yielding model (equation 1.17). Rice[42] calculated $m=0.787$ using an approximate slip line solution whereas Levy et al[43] computed $m=0.469$ employing finite element calculations.

By calculating m for a particular material and geometry, it is possible to establish a unique relationship between COD and LEFM stress intensity factor in SSY condition and thus calculate the critical crack size./

This tends to validate the Crack Opening Displacement concept as a fracture characterizing parameter for the prediction of failure in large structures from small scale laboratory tests. For widespread plasticity equation 1.20 loses its validity. In this situation however, a COD design curve has been developed from which it is possible to determine the maximum tolerable defect size directly from a critical COD.

1.6.6 COD design curve

Burdekin and Stone[28] introduced a non-dimensional form for COD by rearranging equation 15 and replacing E by σ_y/e_y :

$$\phi = \frac{\delta}{2\pi a e_y} = \frac{4}{\pi^2} \ln \sec\left(\frac{\pi}{2} \cdot \frac{\sigma}{\sigma_y}\right) \qquad (1.21)$$

They also obtained an expression for the overall strain e, measured over a gauge length of 2y across the crack plane. By relating the non-dimensional COD to the overall strain they established a basis for flaw size estimation in the post yielding regime. Burdekin and Dawes[44] refined and modified this approach and introduced a design curve for determination of the maximum allowable crack size on the basis of attainment of a critical COD. After a series of further refinement by Dawes[45] supported by experimental data[46], the COD design curve was finally presented in British Standard Document PD 6493[47] and is illstrated in Fig. 1.12. The equations defining the COD design curve are:

$$\begin{aligned} \phi &= (e/e_y)^2 && \text{for } e/e_y \leq 0.5 \\ \phi &= (e/e_y - 0.25) && \text{for } e/e_y \geq 0.5 \end{aligned} \qquad (1.22)$$

which provide the method for determination of a tolerable defect size $\bar{a}_m$ as:/

$$\bar{a}_m = C(\delta c/e_y) \qquad (1.23)$$

The application of design curve in its present form has distinct advantages, (i) it is straight forward to use and (ii) it is based on the overall strain of the body, thus the secondary stresses such as residual and thermal can be taken into account. Against this there are also a number of objections, the major one is the manner in which critical COD is determined. Cowling and Aboutorabi[48] have discussed the effect of constraint on the COD and concluded that for high ductility low constraint configurations, the COD design curve is over-conservative.

1.7 J Integral

A further parameter for the analysis of non-linear elastic and elastic plastic crack problems was provided in 1968 by Rice[49], who introduced a path independent line integral which allows the charaterization of fracture phenomena.

This line integral was derived for a non linear elastic material as an expression for the rate of change of potential energy with respect to an incremental extension of the crack length[50]. Being therefore the rate of change of potential energy it would be expected that it would for LEFM be related to rate of change of elastic strain energy G. The J Integral is defined as:

$$J = \int_{\Gamma} (W dy - T_i \frac{\partial u_i}{\partial x} ds) \qquad (1.24)$$

Γ is any path surrounding the crack tip

W is the strain energy density (non-linear elastic) defined as:

$$W = \int \sigma_{ij} de_{ij}.$$

T_i is the traction vector defined according to the outward normal n along path Γ.

u_i is the displacement vector in the direction of T_i.

ds is increment of distance along the path Γ.

x and y are rectangular coordinates.

A schematic representation of J Integral definition is shown in Fig. 1.13. It should be noted that J is strictly valid for linear and non linear materials which unload along the same path as when loaded.

Rice used an analytical argument to prove that the value of J was independent of the path chosen. This means that the path can be selected in a way that it may be either wholly contained within the plastic region or be outwith in the surrounding elastic region.

For a linear elastic material a path could be chosen which follows the crack surfaces only. Thus the traction term T.du/dx must be zero since these surfaces cannot sustain any normal force action. Therefore for linear elasticity:

$$J = \int W dy = G \qquad (1.25)$$

The use of the J Integral as an elastic-plastic fracture criterion can be justified from a consideration of the Hutchinson[51] and Rice-Rosengren[52] (HRR)crack tip model. The HRR model predicts that for stationary cracks, the product of plastic stress and strain in the vicinity of the crack tip under/

yielding conditions, from small scale yielding to fully plastic condition, has a $1/r$ singularity where r is a near tip crack field length parameter. McClintock[53] has shown that the crack tip plastic stress and strain field for a sharp crack can be expressed from the HRR singularity as:

$$\sigma_{ij} \simeq (J/\sigma_{eq} r)^{N/N+1} \tag{1.26a}$$

$$^{e}p_{ij} \simeq (J/\sigma_{eq} r)^{1/N+1} \tag{1.26b}$$

N is the work hardening exponent which relates the equivalent stress to the equivalent plastic strain via the Ramberg-Osgood relation:

$$\sigma_{eq} = \sigma_{flow} (e^{P}_{eq})^{N} \tag{1.27}$$

Equations 1.26a and 1.26b state that for a given material the stresses and strains ahead of a crack are determined principally by the applied value of J. Hence if a critical crack tip stress field is required to initiate failure, a critical value of J specifies this field. Similarly if the failure mechanism is strain controlled then a critical J would characterize the critical strain condition ahead of the crack tip at failure. These equations are directly analogous to the linear elastic crack tip stress and strain equations where stress intensity factor K is the strength of the $r^{-1}/2$ singularity (equation 1.4). Thus it is envisaged that J characterizes the near tip stresses and strains in the plastic zone as K does in the elastic zone.

For the linear elastic condition J can be related to K and G by[54]:

$$J = G = K^2/E \tag{1.28}$$

It can be postulated that fracture occurs if J exceeds a critical value, J_{Ic}, (in plane strain) which is analogous to G_{Ic} and K_{Ic}.

$$J_{Ic}=G_{Ic}=(1-\nu^2)/E.K^2_{Ic} \qquad (1.29)$$

In the elastic plastic case a direct comparison between J_{Ic} and K_{Ic} as in equation 1.29 cannot be made. It has been suggested that J_{Ic} as a fracture criterion does not have to be related to K_{Ic} and can be considered as a fracture parameter defined independently[55]. Considerable work has been done to measure J in elastic plastic region. Amongst those are the work of Begley and Lands[56-60], Rice, Paris and Merkle[61], Turner[62-64] and others.

1.7.1 Determination of J

Although J was originally defined for nonlinear elastic materials as a path independent line integral, a number of finite element analyses have shown that path independence is still maintained for a large range of cracked geometries when deformed plastically. These numerical analyses, using equation 1.24, provide correlations between J and applied displacement which can be used to determine the fracture toughness characteristics of specific geometries.

A more practical method of estimating J is the interpretation provided by Rice[32]. Rice pointed out that in physical terms the J integral can be considered as the potential energy difference between two identically loaded bodies having crack lengths a and a+da. This interpretation is illustrated in Fig. 1.14 where a body with crack length a is loaded with opening force P. The corresponding displacement Δ is in the/

line of the applied force producing the load deflection curve shown. Assuming the nonlinear elastic interpretation of deformation theory, the work done in loading the body is different for crack length a and a+da where da can be regarded as an increment of crack extension. Rice[42] postulated that the difference in this condition is the energy made available for a crack extension of da which, from the definition of the J integral is equal to Jda, and is represented as the shaded area in Fig. 1.14b.

This interpretation was then extended to plastically deforming bodies since both J and the load displacement curves for a and a+da will be the same for nonlinear elastic or elastic plastic material response provided that unloading does not occur. Therefore an alternative representation for J for both nonlinear elastic and elastic-plastic conditions is given by:

$$J = -\int \frac{\partial P}{\partial a} \, d\Delta = \frac{-1}{B} \left(\frac{dU}{da}\right)$$

where U is the total absorbed energy at a particular load point deflection or the area under the load-load point deflection curve. B and a are the specimen thickness and crack length respectively. For specimens in which the uncracked ligament is subjected to bending, this takes the form:

$$J = \frac{2U}{B(W-a)} \qquad (1.30)$$

where W is the width of the specimen. Sumpter and Turner[65] presented a more general form of the above equation which is applicable to any geometry:

$$J = Je+J_p = \frac{K^2}{E1} + \frac{\eta_p U_p}{(W-a)B} \qquad (1.31)$$

U_p is the plastic component of total energy and can be calculated as the plastic area under the load-displacement curve. η_p is a geometry dependent constant and values for different geometries are given in Ref.66.

It must be emphasized that in the case of plastic behaviour where deformation is not reversible, J loses its significance as a crack driving force since it is no longer a measure of the energy available at the crack tip for crack extension. However it can still be regarded as the difference in energy imparted to a given geometry containing incrementally different crack lengths and may therefore be considered as a characterizing parameter for crack tip damage. The difference in unloading characteristics between a linear or non linear elastic material and that for a elastic plastic material essentially implies that J should be limited to situations with no unloading. Since crack extension leads to relaxation and thus unloading in the regions behind the growing crack tip, J should be restricted to monotonic loading situations and only be used to characterize events leading up to first crack extension. However work by Landes and Begley[57] and Logsdon[67] showed that with a limited amount of crack extension, the use of J may be justified.

1.7.2 Determination of J_{Ic}

The basic procedure for the determination of J_{Ic} is similar to that of δ_i, in which a number of identical specimens are loaded to different amounts of crack extention and load vs load point displacement is recorded. Values of applied J, measured by equation 1.31 are plotted against the amount of crack extension Δa. A linear regression line is fitted to the J-Δa data and the intersection of this line with the blunting line, where there is zero crack extension, is J_{Ic} (Fig. 1.15). The plot of J-Δa must fall/

between two limits. A lower limit of crack extension is chosen to ensure that actual crack extension is distinguishable from blunting. An upper limit is chosen to keep the total amount of crack extension small so that the data is confined to the initial linear part of the R-curve where J is valid.

The standard procedure recommended by the ASTM Committee E24.01.09 gives the following approximate equation for the blunting line:

$$J = 2\sigma_o \Delta a \qquad (1.32)$$

where σ_o is the material flow stress.

This equation is derived by assuming that the stretch zone is approximately equal to half the COD and thus:

$$J = m\sigma_o \delta \qquad \text{where } m = 1 \qquad (1.33)$$

This assumption may be inaccurate and in the next section it will be seen that the coefficient to equation 1.33 may be as high as 4.

1.7.3 Relationship between J and COD

In previous sections the detailed characteristics of both Crack Opening Displacement and J as single fracture parameters applicable under EPFM have been discussed. It has been demonstrated that for small scale yielding conditions, J and COD are simply related to the plane strain stress intensity factor K_I. In fact much of the experimental work on J has been concentrated on the evaluation of K_{IC} from small specimens which fail to meet plane strain validity criteria[56,57]. By considering the size requirements for/

valid K_{IC} tests[18,19] and valid J_{IC} tests[57] it is envisaged that it should be possible to predict K_{Ic} from J_{Ic} by using a specimen much smaller than that used for a direct determination of K_{Ic}.

A similar approach was used by Robinson and Tetelman[68] to estimate K_{Ic} from critical COD values by the use of equation 1.20. This approach is reasonable in the small scale yielding regime when the same micromodes of fracture initiation can be guaranteed in both the small specimen and the much larger valid K_{Ic} specimen.

Since both J and COD characterize the critical conditions at the crack tip, a relationship between these two parameters must exist. A relationship of the form:

$$\delta = MJ/\sigma_y \qquad (1.34)$$

based on the theoretical as well as experimental results is assumed, where M is a plastic constraint factor dependent on the work hardening capacity of the material as defined by equation 1.27 and independent of crack configuration under SSY conditions. For low work hardening materials M is thought to be configuration dependent in the fully yielded state[69]. By evaluating slip line fields for non-hardening materials Rice[49] estimated a value of 0.67 for M whereas Rice and Johnson[31] by considering the non-hardening limit of the HRR singularity field at crack tip obtained a value of 0.79. Shih[69] carried out a finite element analysis to determine the relationship between J and COD for the complete regime of elastic-plastic deformation by exploiting the HRR singularity dominance in the crack tip region. For the non-hardening case in small scale yielding conditions he found M=0.63.

For hardening materials Rice[70] presented the following relationship:

$$\delta = 0.55J/\sigma_o \qquad (1.35)$$

where σ_o is the flow stress in tension given by:

$$\sigma_o = \sigma_y/[\frac{2}{\sqrt{3}} \quad (1 + \nu)(1 + N)\sigma_y/NE]^N \qquad (1.36)$$

Parks[71] suggested that the coefficient of equation should be 0.65. Tracy[37] conducted finite element calculations for SSY conditions and proposed that:

$$\delta = 0.54(1+N)J/\sigma_o \qquad (1.37)$$

An experimental attempt to measure M was carried out by Robinson and Tetelman[68] using standard ASTM K_{Ic} specimens. Their results indicated a value of unity for M, substantially higher than values predicted from the analytical approaches given above. Brothers et al[72] measured stretched zone width in broken test pieces meeting ASTM specifications for K_{Ic} testing in different materials and their results showed a value of 0.7 for M for all the materials investigated.

1.8 The limitations on J_{Ic} and δ_i

For J_{Ic} or δ_i to be used as a single configuration-independent toughness parameter, the HRR fields (equation 1.24) must dominate over a region ahead of the crack tip which is large compared to the scale of the fracture events involved. For ductile fracture initiation in SSY, it has been shown that COD correlates well with the scale of the micromechanism of the failure process i.e. the spacing of voids, nucleating at second phase particles (see section 2.3). Thus COD, given by equation 1.34 sets the local size scale on which fracture process occurs and hence HRR field must be/

large compared to COD. This requirement, like the conditions for K_I-dominance and valid K_{Ic} measurement in LEFM, implies that certain specimen size limitations must be for a valid J_{Ic} (δ_i) measurement. In this context it can be envisaged that all specimen dimensions in a valid J_{Ic} (δ_i) test must exceed some multiple of $\delta_i = M J_{Ic}/\sigma_o$. Landes and Begley[56] proposed the following size requirement, where L is the dimension of remaining ligament:

$$a, B, L \geq 25\text{-}50 \frac{J_{Ic}}{\sigma_o}$$

Hancock and Cowling[40] by testing different crack geometries, representing different flow fields, found that the values of δ_i and J_{Ic} varied with changes in flow field configuration for a tempered and quenched steel similar to HY80, although all their specimens satisfied the above requirement. McMeeking and Parks[73] by using finite strain finite element analysis compared the fully plastic fields with that of small scale yielding and concluded that although for the limiting case of SSY, the specimen size limitation given in equation 1.38 essentially guarantees a unique geometry-independent J characterization of the fracture process, this uniqueness vanishes in the fully plastic fields. They suggested that the minimum specimen size requirement necessary to ensure a valid J_{Ic} (δ_i) value for low constraint fully plastic configuration should be:

$$L \geq 200 \frac{J}{\sigma_o} \qquad (1.39)$$

This means that for certain geometries, the size requirement for valid elastic-plastic fracture toughness parameters may be no less restrictive than that for K_{Ic} testing. The objectives of these size limitations are to set a condition in which a unique J_{Ic} or δ_i can be related to the K_{Ic} for determination of critical crack size or critical stress level. However in many structures the estimation of critical defect size from a

K_{Ic}/

procedure is invalid since LEFM conditions will not apply, and there are areas in a real structure where the constraint is low resembling a fully plastic flow field. In these situations the observation of size limitation as given in equation 1.39 may result in over conservative assessment of fracture behaviour. On the other hand, by elastic-plastic testing of a specimen with similar flow field and dimensions to that of the actual component of structure, a more realistic fracture toughness measure may be obtained irrespective of satisfying the size requirement.

In section 4 experimental analysis of dependence of the post yield fracture toughness parameter δ_i on the crack tip constraint in the transition temperature range is presented and the results of a finite element analysis of the flow field of a low constraint geometry are discussed.

1.9 Summary of EPFM

An important factor in application of fracture mechanics for assessing the significance of defects in structures, is the characterization of fracture toughness of materials. Many low to medium strength steels used in the section size of interest in different structures, develop a large plastic zone at the tip of an existing crack under static loading and therefore a toughness criterion in terms of K_{Ic} in the realm of LEFM is unable to characterize their behaviour.

Successful introduction of COD and J as toughness criteria in the elastic plastic regime have added a new dimension to practical application of fracture mechanics. In the preceding sections the theoretical foundation of EPFM as a natural extension of SSY to cases of large scale plasticity/

has been reviewed. Analysis based on the Dugdale strip yielding model confirms that COD is a characteristic parameter of local conditions at the crack tip whereas the main support for the J-Integral characterization of stress and strain fields local to crack tip comes from the HRR singularity fields. Based on these theoretical considerations, therefore, the critical values of COD and J at failure may be considered as toughness parameters. The critical values of J and COD are determined with laboratory fatigue pre-cracked specimens at the initiation of crack extension. An implicit assumption in the application of these values to predict the critical condition in service components is that initiation of crack growth constitutes the instability event. In reality many materials, in elastic plastic conditions, undergo a period of stable crack growth prior to instability, hence the critical initiation criteria (δ_i and J_{Ic}) may be conservative in these situations. However the conservatism contained within such an approach is obviously satisfactory from the viewpoint of safety and lack of a clear understanding of instability conditions, though it may lead sometimes to very costly overdesign of structures.

The objective of elastic plastic fracture mechanics is ultimately to develop a tool for assessing the presence of an allowable defect and/or an allowable stress level for safe design. This can be achieved by utilizing design curves based on either COD or J-Integral. To avoid errors in determination of critical values of COD or J, crack resistance curves may be generated and crack initiation toughness values be derived from these curves by extrapolating to zero crack extension.

The general philosophy in the use of critical values of fracture parameters, relies on an understanding of events leading to fracture. This can be achieved only by involving the micromechanisms of the fracture process which will be discussed in the following chapter.

1.10 REFERENCES

1. Griffith, A. A., 'The Phenomena of Rupture and flow in solids', Phil. Trans. Roy. Soc., London, Series A, 1920.

2. Griffith, A. A., Proc. 1st Int. Cong. Appl. Mechs., Delft 1924.

3. Inglis, C. E., 'Stress in a plate due to the presence of cracks and sharp corners', Trans. Inst. Naval Arch., Vol. 55, 1913.

4. Jack, R. A., 'Extension of Griffith theory of rupture to three dimensions', Proc. Phys. Soc., London, No. 58, 1946.

5. Stevenson, 'Tension of semi-infinite plate with notched boundary', Phil. Mag., Vol. II, No. 36, 1945.

6. Orowan, E., 'Fracture and strength of solids', The Physics Soc. Reports on Progress in physics, Vol. XII, 1949.

7. Irwin, G.R., 'Fracture Dynamics', ASM Seminar on the fracturing of metals, 29th Nat. Metal Cong., Chicago, 1947.

8. Irwin. G. R. and Kies, J. A., 'Fracturing and Fracture Dynamics', Weld. Res. Suppl. No. 17, 1952.

9. Westergaard, H. M., 'Bearing pressures and cracks', J. Appl. Mechs. Trans. ASME, 1939.

10. Sneddon, I. N., 'The distribution of stress in the neighbourhood of a crack in a elastic solid', Proc. Roy. Soc. London, 1946.

11. Irwin, G. R., 'Analysis of stresses and strains near the end of a crack traversing a plate', Trans. ASME, J. Appl. Mechs. Vol. 24, 1957.

12. Paris, P. C. and Sih, G. C., 'Stress analysis of cracks', ASTM Special Technical Publication STP381, 1965.

13. Tada, H., Paris, P. C. and Irwin G. R., 'The stress analysis of cracks handbook', DEL Research Corp., Pennsylvannis, 1973.

14. Sih, G. C., 'Handbook of Stress Intensity Factors for Researchers and Engineers', Inst. of Fracture and Solid Mechs., Pa., 1973.

15. Rooke, D. P. and Cartwright, D. J., 'Compendium of Stress Intensity Factors', HMSO, London, 1976.

16. Rooke, D. P., Bavatta, F. J. and Cartwright D. J., 'Simple methods of determining Stress Intensity Factors', Eng. Fracture Mechs., Vol. 14, PP 397-426, 1981.

17. Irwin, G. R., 'Plastic zone near a crack and fracture toughness', Proc. 7th Sagamore Ordnance Materials Conf., Syracuse University, 1961.

18. 'Standard Method of Test for Plane-Strain Fracture Toughness of Metallic Materials ASTM Designation E399-74, Part 10, ASTM Annual Standards.

19. 'Methods of Test for Plane Strain Fracture Toughness (K_{Ic}) of Metallic Materials', British Standard BS5447, 1977.

20. Creager, M. and Liu, A.F., 'The effect of reinforcements on the slow stable tear and catastrophic failure of thin metal sheet', American Inst. Aeronautics and Astronautics, Paper No. 71-113, Jan. 1971.

21. Krofft, J. M., Sullivan, A. M. and Boyle, R. W., Proc. Crack Propagation Symp. Cranfield, England, Vol. 1, pp 8-256, 1961.

22. Dowling, A. R. and Townley, C. H. A., 'The effect of defects on structural failure: A Two-Criterion approach', Int. J. Pressure Vessels and Piping, No. 3, 1977.

23. Harrison, R. P., Loosemore, K. and Milne, I., CEGB report R/H/R6, revised version, 1977.

24. Wells, A. A., 'Unstable crack propagation in metals-cleavage and fast fracture', Symp. on crack propagation, College of Aeronautics, Paper B4, Cranfield, 1961.

25. Wells, A. A., 'Application of fracture mechanics at and beyond general yielding', Brit. Weld. J., Vol. 10, P563, 1963.

26. Dugdale, D. S., 'Yielding of steel sheets containing slits', J. Mechs. Phys. Solids, Vol. 8, p. 100, 1960.

27. Baranblatt, G.I., 'The mathematical theory of equilibrium cracks in brittle fracture', Adv. Appl. Mech. Vol. 7, 1962 (previous papers by G.I. Baranblatt published in Soviet journals).

28. Burdekin, F. M. and Stone D.E.W., 'The crack opening displacement approach to fracture mechanics in yielding materials', J. Strain Analysis, Vol. 1 No. 2, P.144, 1966.

29. McMeeking, R. M., Trans. ASME, J. of Eng. Materials and Tech., p. 290, 1977.

30. Pelloux, R. M. N., Eng. Fracture Mech., Vol. 1, P.697, 1970.

31. Rice, J. R. and Johnson, M. A., in Inelastic Behaviour of Solids, ed. Kanninen et al, McGraw Hill, New York, P. 641, 1970.

32. Wells, A. A. and Burdekin, F. M., Int. J. of Fracture Mech., Vol. 7, P. 242, 1971.

33. Dawes, M. G., ASTM, Special Technical Publication, STP 668, P. 307. 1979.

34. Dawes, M. G., ASTM, Symposium on Elastic Plastic Fracture, Atlanta, U.S.A., Nov. 1977.

35. Turner, C. E., Conf. on Numerical Methods in Fracture Mechanics, University of Swansea, U.K., Jan. 1978.

36. Rice, J. R., Mechanics and Mechanism of Crack Growth, ed. M. J. May, British Steel Corporation, London, 1975.

37. Tracey, D. M., Trans. ASME, J. Eng. Materials and Technol., Vol. 98, P. 146, 1976.

38. Shih, C. F., Andrews, W. R., German, M. D., Van Stone, R. J., and Wilkinson, J. P. D., GEC, USA Report SRD-78-116, July, 1978.

39. MacKenzie, A. C., Hancock, J. W. and Brown D. K., Eng. Fracture Mech., Vol. 9, P. 167, 1977.

40. Hancock, J. W. and Cowling, M. J., 'Role of state of stress in crack tip failure processes', J. Metal Science, pp. 293-304, 1980.

41. Robinson, J. N., International Journal of Fracture, Vol. 12, 1976.

42. Rice, J. R., Mathematical Analysis in the Mechanics of Fracture, in Fracture, ed. H. Liebowitz, Vol. II, Academic Press, New York, pp. 191-311. 1968.

43. Levy, N., Marcel, P. V., Ostergren, W. J. and Rice, J. R., Small scale yielding near a crack in plane strain: A finite element analysis, Int. J. of Fracture Mechanics, Vol. 7, 1971.

44. Burdekin, F. M. and Dawes, M. G., Practical use of linear elastic and yielding fracture mechanics with particular reference to pressure vessels, Proc. Inst. Mech. Eng. Conf., London, 1971.

45. Dawes, M. G., 'Fracture control in high yield strength weldments', Weld. J. Res. Suppl., Vol. 53, p. 369. 1974.

46. Kamath, M. S., The COD design curve: an assessment of validity using wide plate tests, Welding Institute Members Report 71/1978/E, 1978.

47. British Standard Public Document., 'Guidance on some methods for the deviation of acceptance levels for defects in fusion welded joints', BSI PD 6493, 1980.

48. Cowling, M. J. and Aboutorabi, A. A., 'Defect tolerance in offshore structures', Proc. 2nd Int. Conf. Integrity of Offshore Structures, Ed. D. Faulkner et al, Applied Science Publishers, 1981.

49. Rice, J. R., A path independent Integral and the approximate analysis of strain concentration by notches and cracks, J. Appl. Mech. Trans. ASME, Vol. 35, pp. 379-386, 1968.

50. Rice, J. R., in Fracture, ed. H. Liebowitz, Vol. 2, Academic Press, New York, p. 191. 1968.

51. Hutchinson, J. W., J. Mech. Phy. of Solids, Vol. 16, pp. 13-31. 1968.

52. Rice J. R. and Rosengren, G. F., ibid pp. 1-12.

53. McClintock, F. A., in Fracture, ed. H. Liebowwitz, Vol. 3, Academic Press, New York, p. 47. 1968.

54. Bucci, R. J., Paris, P. C., Landes, J. D. and Rice, J. R., ASTM, Special Technical Publication STP 514, pp. 40-69, 1972.

55. Robinson, J. N., 'An experimental investigation of the effect of specimen type on the crack opening tip displacement and J integral fracture criteria', Int. J. Fracture, Vol. 12, No. 5, pp. 723-737, 1976.

56. Begley, J. A. and Landes, J. D., 'The J integral as a fracture criterion, ASTM Special Technical Publication, STP 514, Part II, pp. 1-23, 1972.

57. Landes, J. D. and Begley, J. A., 'Test results from J integral studies: an attempt to establish a J_{Ic} testing procedure', ASTM Special Technical Publication, STP 560, pp. 170-186, 1974.

58. Begley, J. A., and Landes, J. D., Int. J. Fracture, Vol. 12, No. 3, pp. 764-766, 1976.

59. Begley, J. A. and Landes, J. D, ASTM Special Technical Publication, STP 590, pp. 82-103, 1976.

60. Landes, J. D. and Begley, J. A., 'Recent development in fracture mechanics test method standardization', ASTM Special Technical Publication, STP 632, pp. 57-81, 1977.

61. Rice, J. R., Paris, P. C. and Merkle, J. G., 'Some further results on J integral analysis and estimates', ASTM Special Technical Publication STP 536, pp. 231-245, 1973.

62. Turner, C. E., in 'Advances in elastic-plastic fracture mechanics', ed. L. H. Larsson, Applied Science Publishers, London, pp. 301-317, 1979.

63. Turner, C. E., ibid, pp. 139-164, 1979.

64. Turner, C. E., 'Description of stable and unstable crack growth in the elastic-plastic regime in terms of J resistance curves', ASTM, Special Technical Publication STP 677, 1979.

65. Sumpter, J. D. g. and Turner C. E., 'Method for laboratory determination of J_c' ASTM Special Technical Publication STP 601, pp. 3-18, 1976.

66. Turner, C. E., in 'Post-yield fracture mechanics', ed. D.G.H. Latzko Applied Science Publishers, London, 1979.

67. Logsdon, W. A., in 'Mechanics of Crack Growth', ASTM Special Technical Publication STP 590, p. 43, 1976.

68. Robinson, J. N. and Tetelman, A. S., in 'Fracture toughness and slow stable cracking', ASTM Special Technical Publication STP 559, pp. 139-158, 1974.

69. Shih, C. F., General Electric Company, Technical Information Series Report, TIS No. 79CRD075, 1979.

70. Rice, J. R., Proc. 3rd Int. Conf. Fracture, Munich, Paper I441, 1973.

71. Parks, D. M. PhD. Thesis, Brown University, 1975.

72. Brothers, A. J., Hill, M., Parker, M. T., Spitzing, W. A., Wiebe, W. and Wolf, U. E., ASTM Special Technical Publication STP 493, p.3, 1971.

61. Rice, J. R., Paris, P. C. and Merkle, J. G., 'Some further results on J integral analysis and estimates', ASTM Special Technical Publication STP 536, pp. 231-245, 1973.

62. Turner, C. E., in 'Advances in elastic-plastic fracture mechanics', ed. L. H. Larsson, Applied Science Publishers, London, pp. 301-317, 1979.

63. Turner, C. E., ibid, pp. 139-164, 1979.

64. Turner, C. E., 'Description of stable and unstable crack growth in the elastic-plastic regime in terms of J resistance curves', ASTM, Special Technical Publication STP 677, 1979.

65. Sumpter, J. D. g. and Turner C. E., 'Method for laboratory determination of J_c ASTM Special Technical Publication STP 601, pp. 3-18, 1976.

66. Turner, C. E., in 'Post-yield fracture mechanics', ed. D.G.H. Latzko Applied Science Publishers, London, 1979.

67. Logsdon, W. A., in 'Mechanics of Crack Growth', ASTM Special Technical Publication STP 590, p. 43, 1976.

68. Robinson, J. N. and Tetelman, A. S., in 'Fracture toughness and slow stable cracking, ASTM Special Technical Publication STP 559, pp. 139-158, 1974.

69. Shih, C. F., General Electric Company, Technical Information Series Report, TIS No. 79CRD075, 1979.

70. Rice, J. R., Proc. 3rd Int. Conf. Fracture, Munich, Paper I441, 1973.

71. Parks, D. M. PhD. Thesis, Brown University, 1975.

72. Brothers, A. J., Hill, M., Parker, M. T., Spitzing, W. A., Wiebe, W. and Wolf, U. E., ASTM Special Technical Publication STP 493, p.3, 1971.

73. McMeeking, R. M. and Parks, D. M., 'On criteria for J-dominance of crack tip fields in large scale yielding', ASTM Symp. Elastic-Plastic Fracture, Atlanta, 1977.

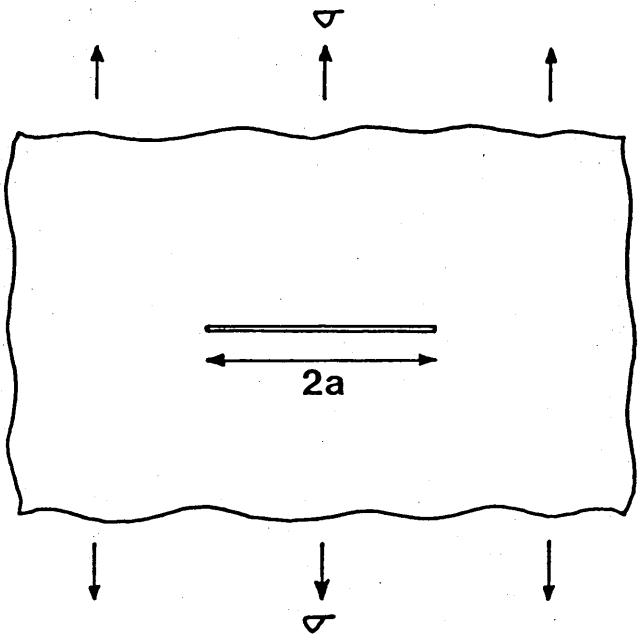

Fig. 1.1 Griffith's crack model

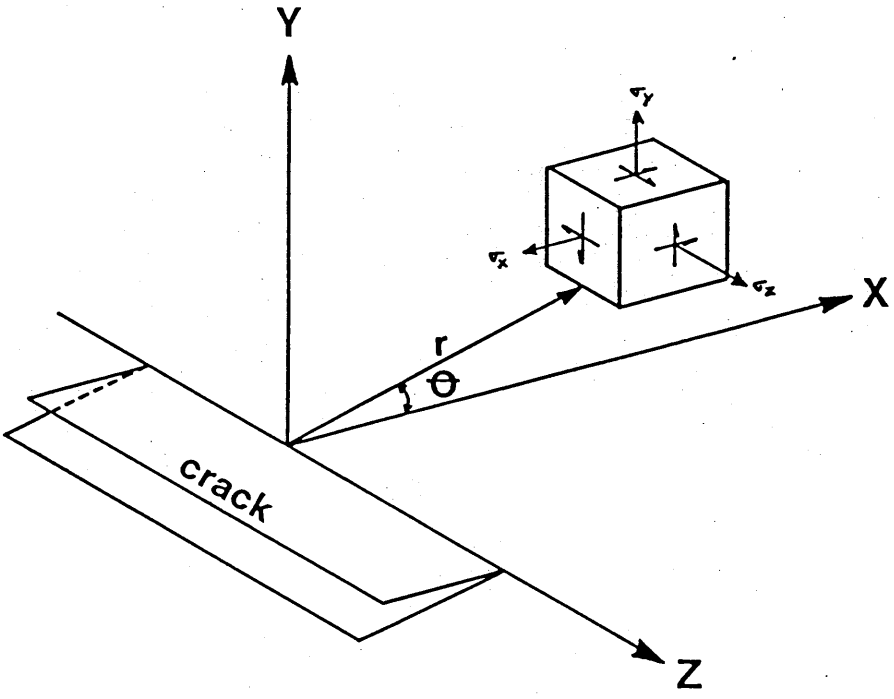

Fig. 1.2 Stress components ahead of a crack tip

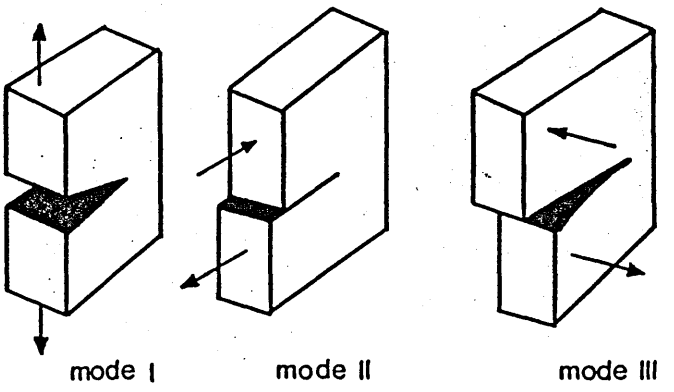

Fig. 1.3 Fracture modes

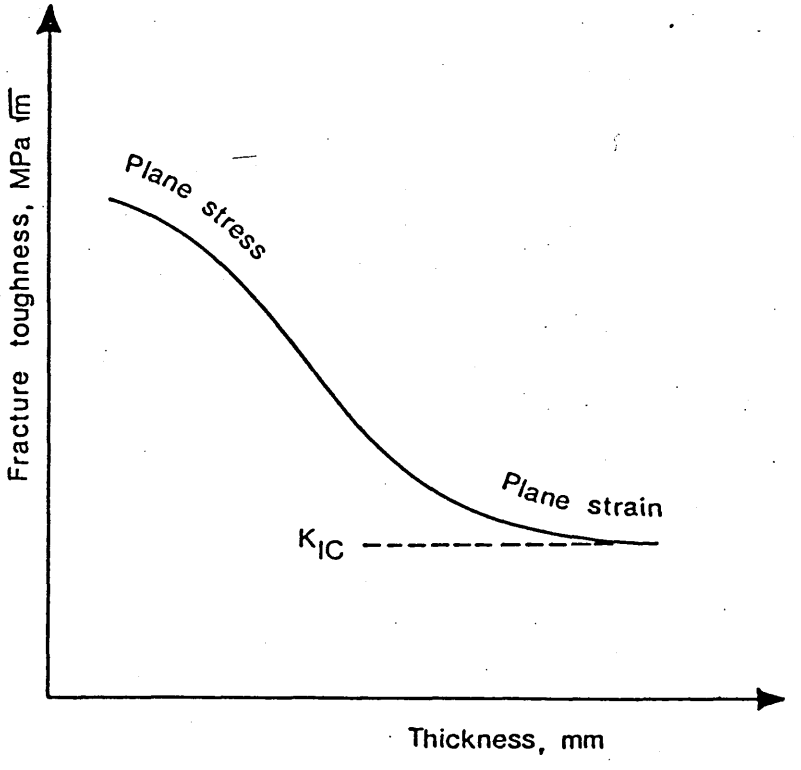

Fig. 1.4 Variation of fracture toughness with specimen thickness

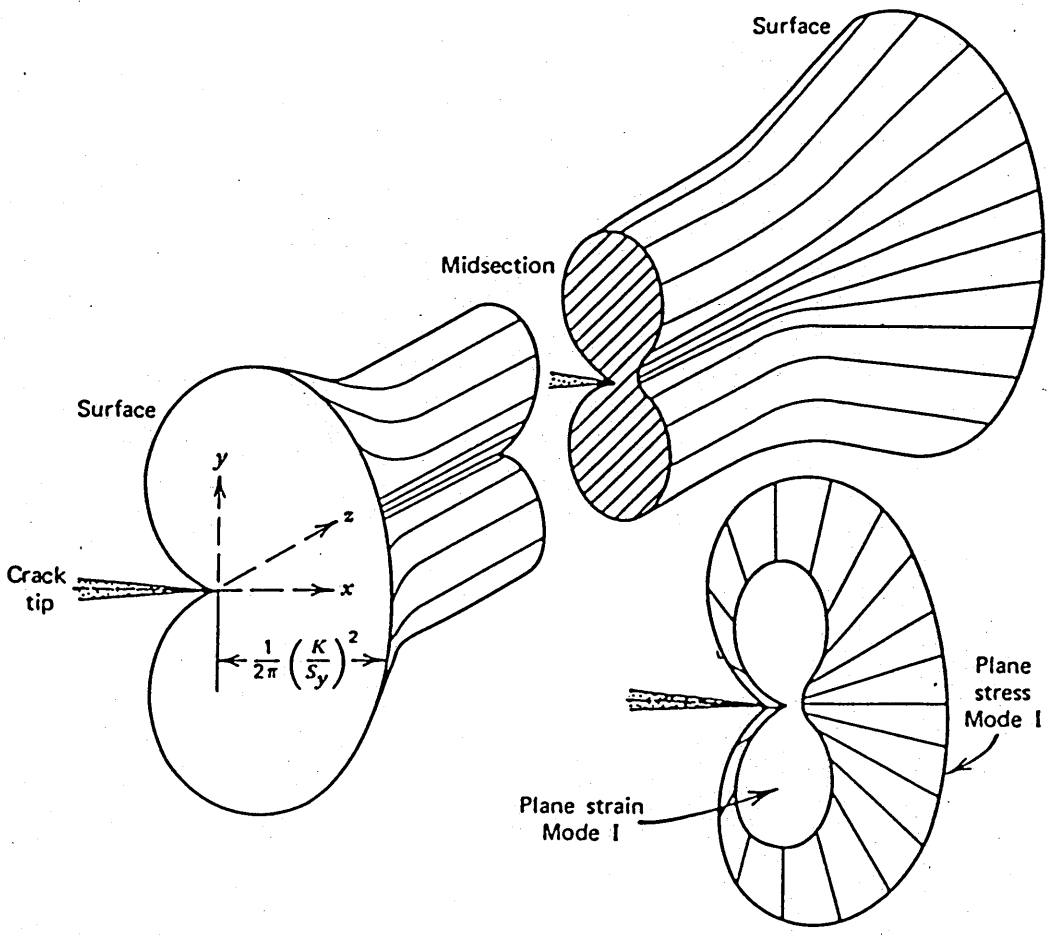

Fig. 1.5 Plastic zone ahead of a crack tip

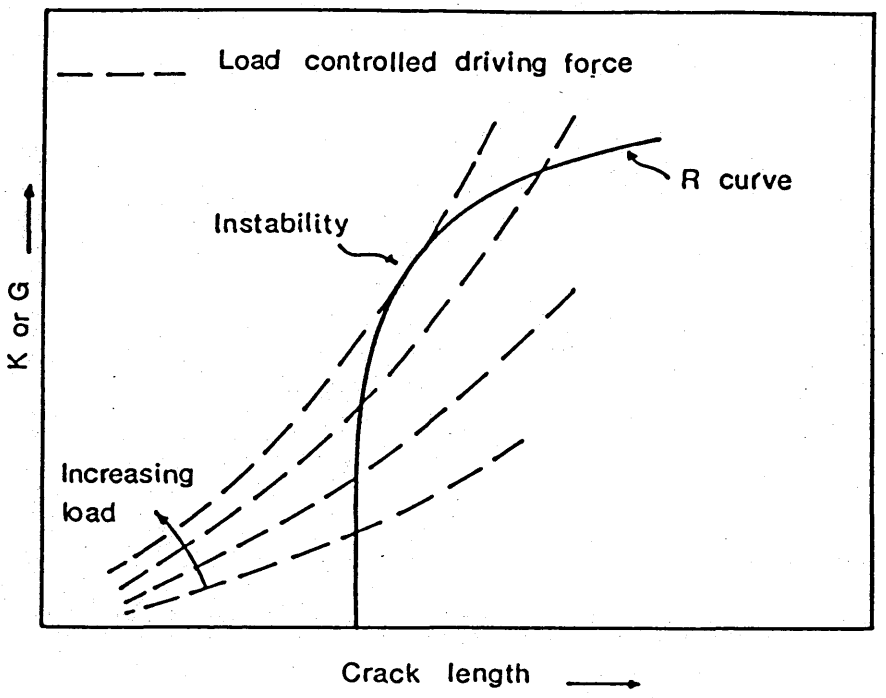

Fig. 1.6 Schematic LEFM resistance curve

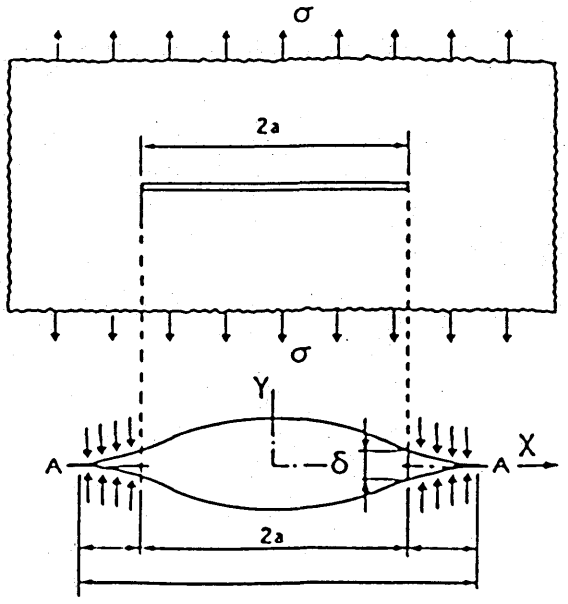

Fig. 1.7 Dugdale strip-yield model
of crack tip plasticity

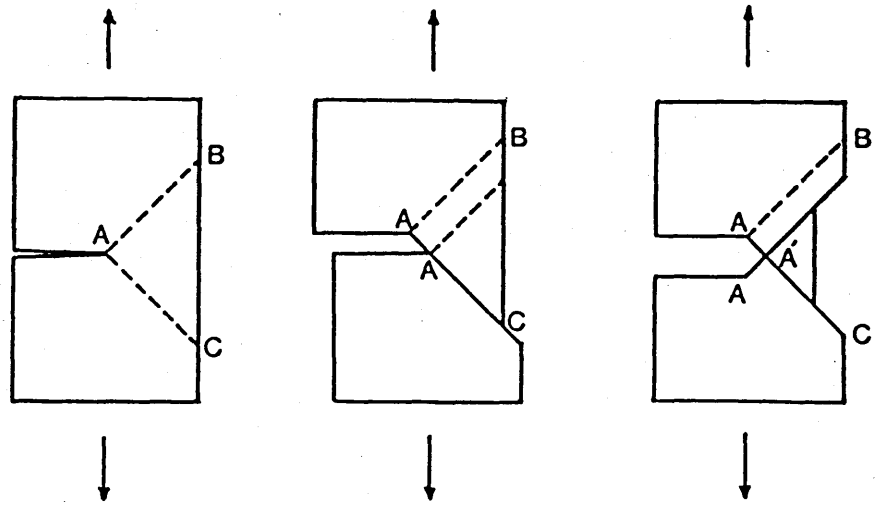

Fig. 1.8 Pelloux's model[30] for crack opening by an alternating shear mechanism

DUCTILE FRACTURE

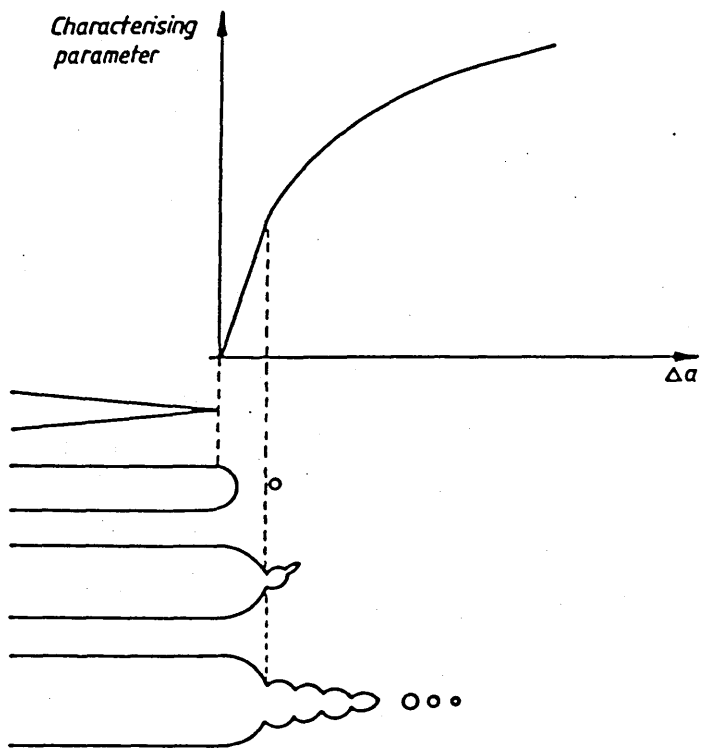

Fig. 1.9 Schematic illustration of ductile crack extension and the relation between the characteristic parameter (COD) and the crack growth increment (Δa)

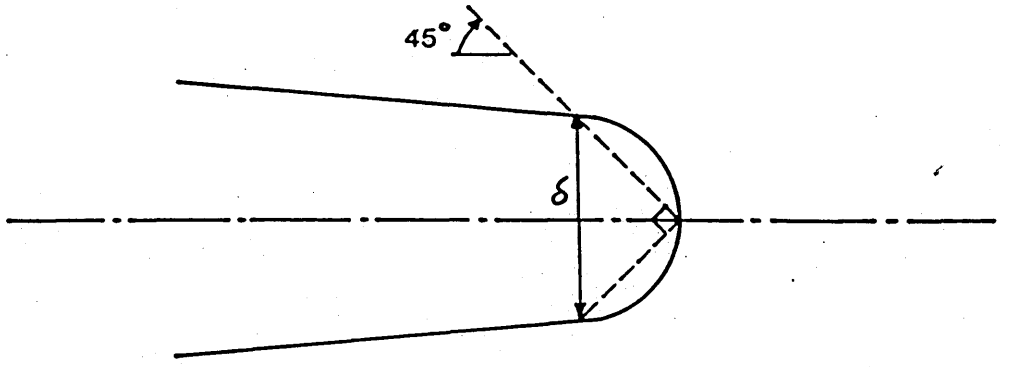

Fig. 1.10 Definition of crack opening displacement

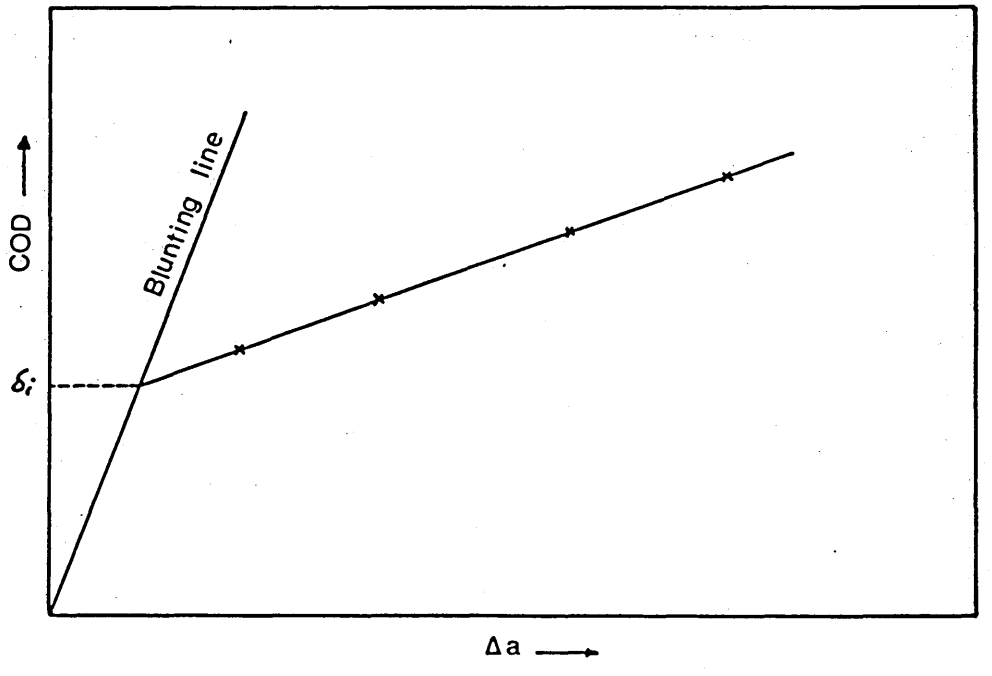

Fig. 1.11 Schematic COD R-curve

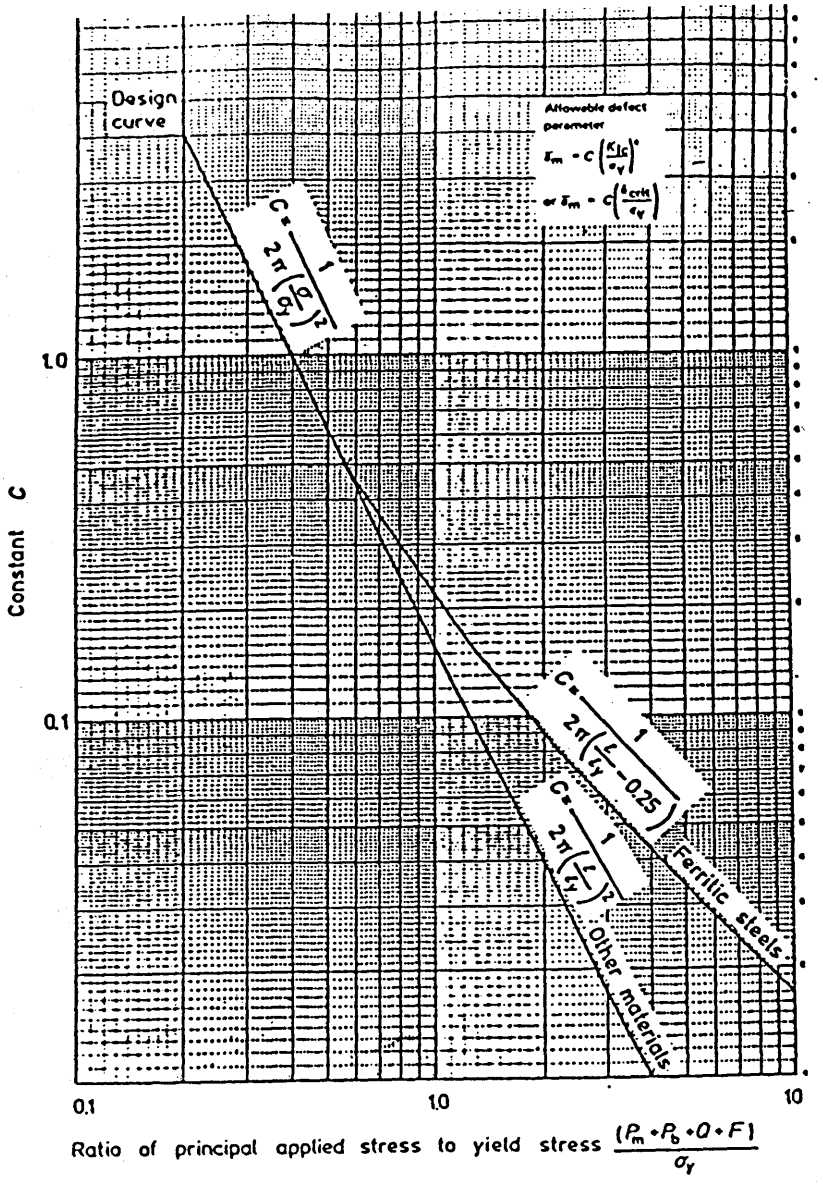

47

Fig. 1.12 COD design curve

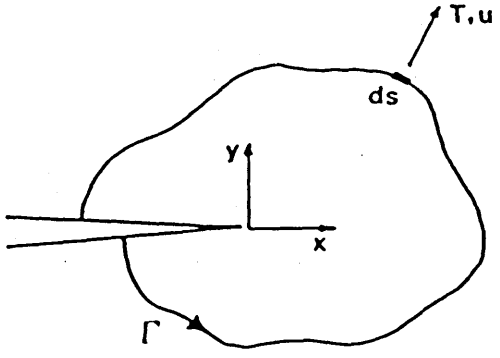

Fig. 1.13 Definition of the J-integral

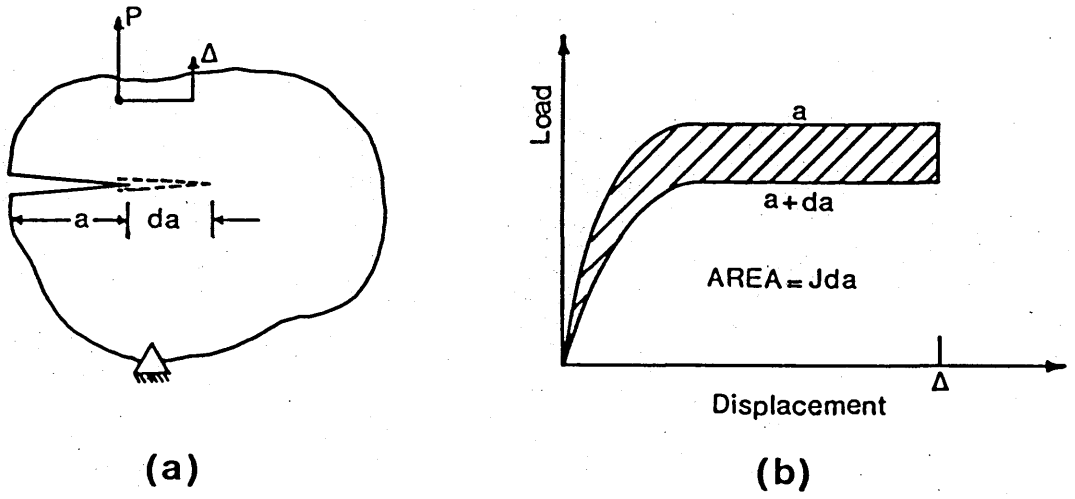

Fig. 1.14 Interpretation of the J-integral for a body with a crack subjected to a load

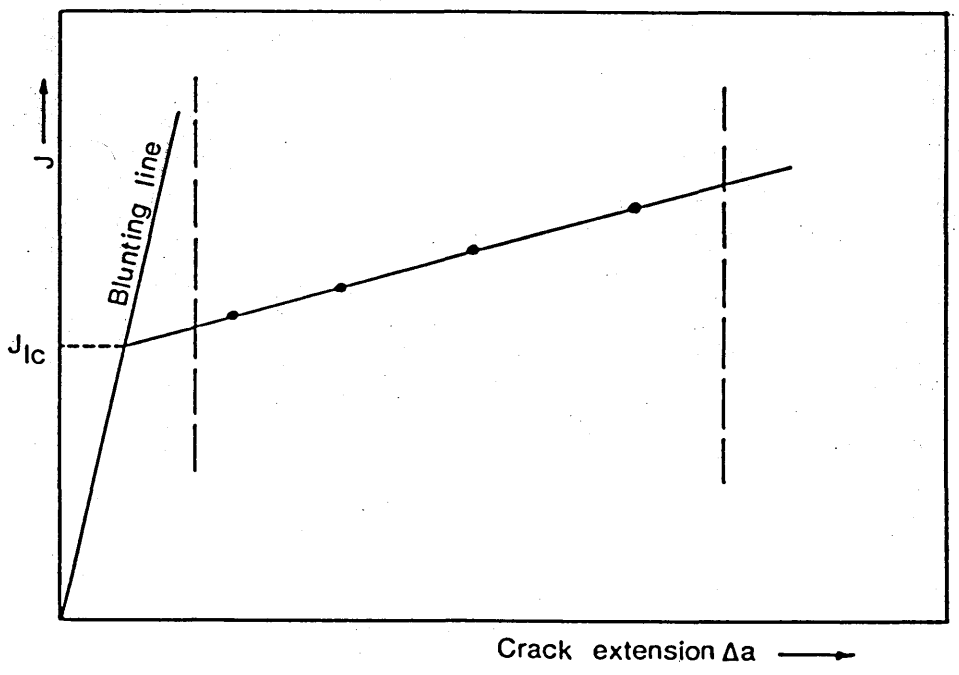

Fig. 1.15 Schematic J R-curve

Section 2

FAILURE MECHANISMS

2.1 Introduction

In this section the mechanisms of Brittle, Ductile and Fatigue failure processes are discussed.

2.2 Brittle fracture

Brittle fracture in metals is characterized by a rapid rate of crack propagation, with no gross plastic deformation, requiring very little energy. In steels it occurs by a process of transgranular cleavage producing bright, planar cleavage facets. Cleavage fracture is prompted by those factors that produce locally elevated tensile stress levels such as low service temperatures, high strain rates and the presence of stress concentrations especially in regions of high triaxial stresses.

Low[1] showed that for mild steel of a given grain size, tested at -196°C brittle fracture in tension occurs at the same or greater value of stress than is required to produce yielding in compression. It is envisaged therefore, that some plastic flow is a necessary step to promote cleavage and that yielding is involved in the nucleation of cleavage fracture.

It was suggested by Zener[2] that the stress levels at the head of a dislocation/

pile-up could be sufficient to produce the plastic flow required to cause cleavage fracture. Stroh[3] developed this idea by proposing that the dislocations could be squeezed together to produce a crack nucleus. He presented a theoretical analysis of this crack nucleation mechanism and calculated that the energy balance required for subsequent propagation of the crack is achieved by the squeezing together of dislocations, and hence the cleavage fracture is nucleation controlled. The Zener-Stroh model does not predict that cleavage fracture will be promoted by the local elevation of tensile stresses. Knott[4] examined the influence of tensile stress on cleavage of mild steel and concluded that the fracture obeyed a critical tensile stress criterion, and therefore it is propagation controlled.

Cottrell[5] proposed an alternative dislocation mechanism for the nucleation of cleavage cracks in essentially bcc (body centered cubic) metals such as ferritic iron. This mechanism involves the interaction of two dislocations slipping on intersecting [101] planes to form a tensile dislocation normal to the cleavage plane. This interaction is accompanied by a reduction in dislocation energy so that crack nucleation is easier than if it followed the Zener-Stroh model. The cleavage fracture by this mechanism will therefore be propagation controlled. This model not only predicts a tensile stress controlled cleavage fracture, but also explains the effects of grain size and yielding parameters on fracture. However the influence of other microstructural variables such as grain boundary carbide particles remain neglected.

Smith[6] proposed a theoretical model of cleavage fracture in mild steel similar to that of Zener and Stroh by assuming that a microcrack due to dislocation pile-up is formed in a grain boundary carbide particle and subsequently propagates into the ferritic matrix under the combined influence/

of the pile-up and the applied stress. Thus in addition to demonstrating the role of yielding parameters in determining the fracture stress, the influence of grain size and carbide particle size are also emphasized.

2.2.1 A model for cleavage fracture

It is evident from different models discussed above that an energy based interpretation of fracture toughness is not adequate to explain cleavage fracture in steels. The micromechanisms of fracture have to be incorporated with the stress field characterization by the stress intensity factor in order to predict the material fracture toughness. The stress distribution ahead of a loaded crack predicts that the maximum tensile stress elevated at the tip of a pre-existing crack declines rapidly with distance[7]. Dimensional considerations of aforementioned cleavage mechanisms, namely the grain size and carbide particle size imply that if fracture from a sharp crack is to occur at a critical stress intensity factor, then the attainment of a critical local tensile stress is not a sufficient criterion but a distance requirement must also be satisfied. Ritchie, Knott and Rice[8] proposed that the local tensile stress in steels had to exceed a critical fracture stress over some microstructurally determined distance ahead of the crack tip before fracture could occur. Thus with the knowledge of stress distribution which is characterised by the stress intensity factor at the crack tip and experimental determination of the critical fracture stress by a simple uniaxial test, it is possible to predict the fracture toughness if the characteristic distance is known. This model, referred to hereinafter as RKR, was used to predict the temperature dependence of the fracture toughness of mild steel. The prediction was in good agreement with experimental results when the characteristic distance was taken as being equal to two grain diameters. Although/

the RKR criterion was originally proposed for mild steel, it has been successfully applied to low strength low-alloy steels[9], higher carbon steels[10], titanium alloys[11] and high strength low alloy steels used in nuclear pressure vessels[12].

2.3 Ductile fracture

Conditions required for the initiation of a macroscopic brittle fracture and micromechanisms involved were discussed in the previous section. When there is local plasticity at the crack tip, instability is usually associated with some stable crack extension though final failure may still be of a brittle nature. Therefore ductile fracture is characterized by the local crack tip micromechanisms of crack extension, mainly the linkage of microvoids formed at second phase particles. In low strength steels voids form by the separation of the interface between the ferrite matrix and non metallic inclusions such as sulphide particles. Voids can also be nucleated at carbide particles either by interface separation or by the particle cracking. Nucleated voids grow under applied stress until they coalesce with the blunted crack tip producing a fracture surface consisting of dimples centred on the inclusions. This mode of failure known as fibrous fracture, requires the development of high strains in the matrix around and between the voids. When the matrix has a low work hardening capacity, plastic flow can become localised so that the voids link by shear decohesion along shear planes.

Rice and Johnson[13] analysed microvoid coalescence by considering a sharp crack subjected to a mode I plane strain stress state in Small Scale Yielding (SSY). They calculated the maximum tensile stress and tensile strain by constructing the slip line field at the crack tip. The slip line field/

solution for a sharp crack is shown in Fig. 2.1a. In regions A and B the fans are centered and the lines are straight, implying that there are no strain concentrations ahead of the crack tip. Intense shear concentrations form above and below the tip where the lines are curved in region C. In order to keep a continuity of displacement at the crack tip, when the body is loaded, the crack must blunt with the consequence that the fan region ahead of the crack tip is now non-centered and focuses intense strains into region D directly ahead of the blunted tip, Fig 2.1b.

Rice and Johnson[13] postulated that if the tip blunted into a semicircle of diameter δ, where δ is the crack opening displacement at the original crack tip, then region D would have exponential spiral slip lines and would extend a distance approximately 2δ ahead of the crack tip. They calculated the stresses and strains in this region for a nonhardening material as a function of distance from the blunted crack tip (x). Their results are presented graphically in Fig. 2.2. At the crack tip the strains become infinite whereas the stresses are limited by the yield stress but reach a maximum of $2.6\sigma_y$ (Tresca criterion) at the end of logarithmic spiral. Strain hardening raises all the stress levels and decreases the extent of spiral[14].

Macroscopic failure initiation may be defined as the point when the blunting crack tip first coalesces with the growing void nearest to the crack tip. As discussed in section 1.6.4 the value of COD at this fracture initiation point is a material fracture toughness parameter δ_i. Coalescence of the blunting crack with the nearest void causes a shift in the position of the crack tip to the far side of the void. Propagation would then progress by blunting of this new crack tip and the envelope of the next void into the new logarithmic spiral. Thus ductile fracture can be related to some physical measurement of inclusion spacing.

2.3.1 A model for ductile fracture

Mackenzie, Hancock and Brown[15] (MHB) proposed a model to predict fracture toughness of steels in the ductile regime. They suggested that macrocrack growth by coalescence of microvoids would occur if the local plastic strain exceeds a critical strain value over a microstructural characteristic distance. This characteristic distance was taken as some multiple of inclusion spacing. This model is analogous to that of RKR for brittle fracture by considering a critical strain criterion instead of critical stress. It has been established[16-17] that plastic strain at the crack tip is strongly dependent on the triaxial state of stress. Hancock and MacKenzie[18] showed that the ductility of some materials is decreased with increasing triaxiality. The MHB model recognizes the effect of triaxiality and proposes experimental determination of fracture strain as a function of triaxiality. This value is compared with the stress and strain distribution ahead of a crack and the value of COD (δ) at which the equivalent plastic strain just exceeds the fracture strain over the characteristic distance from the crack tip is then taken as δ_i.

Cowling and Hancock[19] used the MHB model to predict fracture toughness of a low alloy high strength steel and found a close agreement with experimentally determined fracture toughness. The characteristic distance was shown to be the size of an inclusion colony. Ritchie et al[12] applied this model to two nuclear pressure vessel steels and found that fracture toughness of both steels can be accurately predicted by taking the characteristic distance as some multiple of planar inter-inclusion spacing. They concluded that critical microstructural size scale must be regarded not only as a parameter indicating the spacing between particles, but also the critical number of voids which coalesce with the blunted crack tip at the initiation of crack growth.

2.4 Effect of temperature on fracture processes

So far two different approaches for the analysis of fracture processes have been discussed. These are the macroscopic approach which involves the fracture toughness parameters such as K_{Ic}, δ_i, J_{Ic} etc. (as reported in Section 1) and the microscopic or local approach which involves the micromechanisms of crack tip processes.

The fracture process of structural steels is greatly influenced by variation in temperature. The effect of temperature on the toughness is well known from the Charpy impact notch testing, in which the notch toughness of material is shown to be sharply reduced with decreasing temperature. A similar trend exists with other fracture parameters as shown in Fig. 2.3. This toughness transition may be explained in terms of the critical levels of stress and strain required to initiate brittle or ductile failure. For cleavage fracture, it is necessary to achieve a critical value of tensile stress below the crack tip to propagate microcracks. At low test temperatures, this is usually attained well below general yield loads. As the test temperature is increased, the yield stress decreases, thus the level of stress required for cleavage fracture increases beyond that required for general yield. As gross yielding is approached material at the vicinity of crack tip deforms plastically, making it impossible to develop a sufficient level of tensile stress to initiate and propagate microcracks at the crack tip. This therefore marks the transition in fracture mode from lower shelf cleavage fracture to the upper shelf ductile failure.

There has been considerable research in recent years into the temperature dependence of fracture toughness. Kalitassien[20] has reviewed the/

influence of temperature on yield stress and toughness. In very tough materials the fracture process may be initiated by a ductile mechanism even in the lower shelf region where the subsequent crack propagation is by means of the cleavage mechanism.

In lower toughness materials there is a gradual transition from upper shelf ductile to lower shelf cleavage initiation and propagation mechanisms. In the transition region the failure process involves a mixture of the two mechanisms with plasticity ahead of the opening crack tip producing void initiation and growth as in the upper shelf region. This void growth is interrupted before the coalescence stage by the triggering of the brittle cleavage mechanisms. A further study of these processes and the effect of constraint on them is reported in section 4.0 below.

2.5 Fatigue fracture

The life of most engineering structures is dominated by the growth of pre-existing defects which are introduced by the manufacturing process e.g. flaws in welded structures. Subcritical cracks which are inactive under static load, may propagate under repeated loading by a fatigue mechanism whereby the critical size is eventually achieved and failure will occur.

The application of the term fatigue to the failure of materials subjected to cyclic loading is indicative of the original observations of the eventual failure of components under loads which had been previously withstood many times. It was believed that, after a number of loadings, the component tired and suddenly failed when the material load carrying capacity was exhausted.

The most notable contribution to the early investigations of the fatigue phenomena was the experimental work of Wohler[21] between 1858 and 1870. From the results of his work on iron and steel, Wohler concluded that the cyclic life of his specimens was dependent on not only the maximum cyclic stress but also the range of stress in the cycle. He also noted that a minimum stress range exists below which fatigue would not occur. These observations led to the original presentation of the type of stress range/cyclic life fatigue curve, known as the S-N curve, still in normal use.

Early in the 20th century, attention was directed to the metallurgical aspects of fatigue leading to an understanding of the initiation of fatigue cracks by the development of slip bands in the crystallographic structure of the metallic materials. Further work in this area revealed the effects of the presence of non-metallic inclusions and material anistropy on fatigue strength and, later, considerable progress was made in defining the mechanism by which fatigue cracks propagate. More recently fracture mechanics has been used in the study of fatigue crack propagation in evaluating structural integrity. The use of fracture mechanics has been particularly successful in reducing the number of accidents in the pressure vessel industry over the last two decades. This success has been achieved through the evaluation of fatigue crack growth rate data and the application of LEFM to life prediction.

The fatigue growth of a macrocrack is a fracture process caused by the opening and closing of the crack. For ductile materials fatigue crack propagation has been shown to be crack extension producing a flat surface perpendicular to and controlled by the maximum tensile stress range.

The most successful mathematical presentation of fatigue crack growth data has been in terms of linear elastic fracture mechanics. This application of fracture mechanics was propsed by Paris and Erdogan[22], who argued that since the stress field around the crack tip was defined by the stress intensity factor, the rate of growth of the crack is dependent on the cyclic range of that parameter. By reviewing various empirical laws and examination of a large bank of experimental data, they concluded that the crack growth rate can be described by the following relationship:

$$da/dN=C\Delta K^m \qquad (2.1)$$

where C and m are empirically determined material constants, da/dN represents the rate of crack growth increment per load cycle and ΔK is the applied range of stress intensity factor at the crack tip i.e. the difference between the maximum and minimum values of SIF.

Crack growth behaviour under fatigue has been classified into three distinct stages as shown in Figure 2.4, where the crack growth rate versus ΔK curve is plotted in log-log form after Paris and Erdogan[22]. Region I indicates a threshold value of ΔK_{th} below which a crack does not propagate and remains inactive. In the intermediate stage II the crack grows steadily at an increasing rate which is primarily dependent on the level of applied ΔK as described by the Paris law. It is generally considered that the most of the life of a structure is spent in the stage I and II regions. In region II crack advance is associated with striation formation on the fracture surface, with striation spacing equivalent to da/dN.

The final stage III, is where the maximum crack tip stress intensity factor/

in the cyclic range approaches the level of K_{Ic} or K_c (or the applied load approaches the limit load). In this stage the crack growth mechanism can include the macroscopic static failure processes.

As indicated earlier, most structures contain pre-existing defects which can be considered to be readily available for propagation in the manner suggested by stage II. The Paris equation can therefore be used to calculate the number of cycles required to cause failure:

$$dn=da/C\Delta K^m \qquad (2.2)$$

$$N=\frac{1}{C}\int_{a_i}^{ac} \Delta K^{-m}\, da \qquad (2.3)$$

where a_i is the initial defect or crack length, or the size of the smallest defect detectable by a Non Destructive Testing (NDT) technique, a_c is the critical defect or crack length and N is the number of load cycles to cause failure. K is the range of applied stress intensity factor given by:

$$\Delta K=\Delta\sigma(\pi a)^{0.5}F(g) \qquad (2.4)$$

where F(g) is a geometric function dependent on the crack shape and boundary conditions. For defect geometries with complex geometry functions, integration of the Paris equation becomes extremely difficult. In such cases the integral can be calculated numerically using an interactive technique.

Fracture mechanics can therefore be used to predict the expected life of/

a structure, containing a pre-existing crack by a knowledge of fatigue crack growth resistance of material. Fatigue crack growth data is normally obtained by applying cyclic loads to a cracked specimen of material and monitoring the subsequent crack growth. The monitoring of the crack as it grows is usually achieved by using NDT methods. This procedure has been used during the present investigation to study the fatigue growth of part-through cracks and the results are reported in Section 5.

2.6 REFERENCES

1. Low, J. R., Trans. ASM, Vol. 40A, p. 163, 1954.

2. Zener, C., Trans. ASM, Vol. 40A, p. 3, 1948.

3. Stroh, A. N., Proc. Roy, Soc. A223, p. 404, 1954.

4. Knott, J., Iron steel Inst., No. 204, p. 104, 1966.

5. Cottrell, A. H., Trans. AIME, Vol. 212, p. 192, 1958.

6. Smith, E., Proc. Conf. 'Physical basis of yield and fracture', Inst. Phys. and Phys. Soc., Oxford, England, 1966.

7. Griffiths, J. R. and Owen, D. R. J., J. Mech. Phys. Solids, Vol. 19, p. 419, 1971.

8. Ritchie, R. O., Knott, J. F. and Rice, J. R., J. Mech. Phys Solids, Vol. 21, p. 395, 1973.

9. Parks, D. M., J. Eng. Materials Tech., Trans. ASME, Series H, Vol. 98, pp. 30-35, 1976.

10. Rawal, S. P. and Gurland, J., Met. Trans. A., Vol. 8A, p. 691, 1977.

11. Rack, H. J., Materials Sci. Eng., Vol. 24, p. 165, 1976.

12. Ritchie, R. O., Server W. L. and Wullaert, R. A., ICM 3, Vol. 3, p. 489, 1979.

13. Rice, J. R., Johnson, M. A., in 'Inelastic behaviour of solids', ed. Kanninen et al, McGraw Hill, New York, p. 641, 1970.

14. McMeeking, R. M., 'Large plastic deformation and initiation of fracture at the tip of a crack in plane strain', Brown University, Tech. Report 48, 1976.

15. MacKenzie, A. C., Hancock, J. W. and Brown, D. K., Eng. Fracture Mech., Vol. 9, pp. 167-188, 1977.

16. McClintock, F. A., Trans. ASME J. Appl. Mech., Vol. 35, pp. 363-371, 1968.

17. Rice, J. R. and Tracey, D. M., J. Mech. Phys. Solids, Vol. 17, pp. 201-217, 1969.

18. Cowling, M. J., Hancock, J. W. and Brown, D. K., 1st Int. Symp. Integrity of Offshore Structures, Glasgow, Paper 5, 1978.

19. Cowling, M. J. and Hancock, J. W., Proc. 4th Int. Conf. Fracture ICF 4, Vol. 2, p. 371, Waterloo, Canada, 1977.

20. Kotilainen, American society for Testing and Materials Special Technical Publication, ASTM STP 700, pp. 352-367, 1980.

21. Wohler, A., 'Wohler's experiments on the strength of metals' Engineering, Vol. 2, p. 160, 1967.

22. Paris, P. C. and Erdogan F., Trans. ASME, J. Basic Eng., Vol. 85, No. 4, 1963.

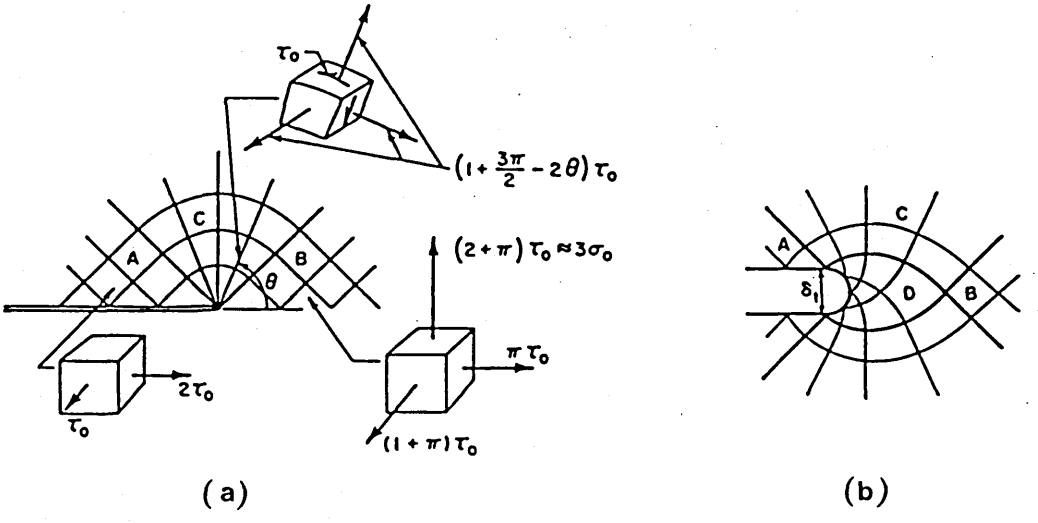

Fig. 2.1(a) Prandtl slip line field for contained plain strain yielding of a non-hardening material and (b) slip line solution for the blunting of an initially sharp crack in SSY

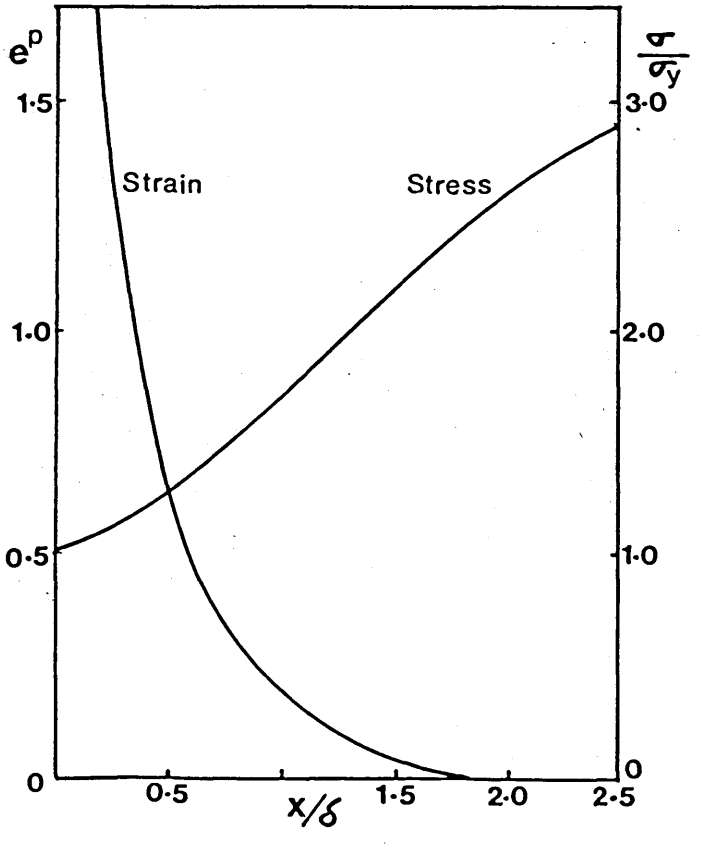

Fig. 2.2 stress and strain near the crack tip for small-scale contained yielding in a non-hardening material[13].

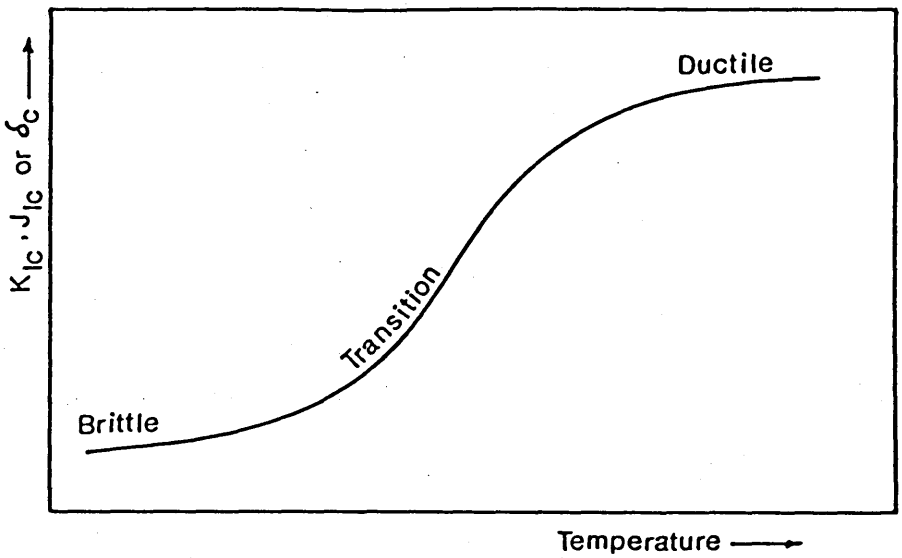

Fig. 2.3 Schematic illustration of ductile-brittle transition curve.

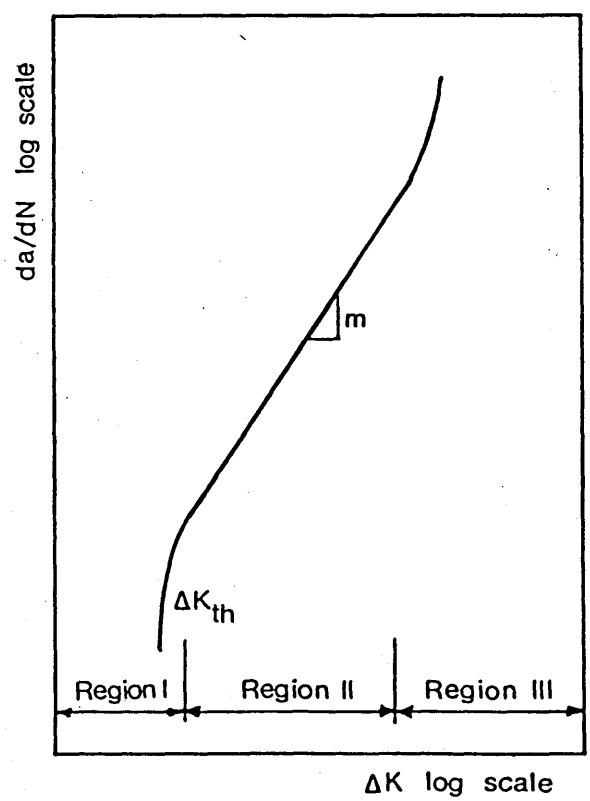

Fig. 2.4 Variation of crack growth rate with the range of stress intensity factor in a fatigue test, showing regions I, II and III.

Section 3

MATERIAL PROPERTIES

3.1 Introduction

In this section the basic material properties and the results of the experiments on the variation of yield stress with temperature, Charpy V-notch energy and the effect of degree of triaxiality on the effective plastic strain to failure in the transition temperature range are presented.

3.2 Material

The material used in this investigation was a carbon-manganese structural steel, to the specification of BS4360 grade 50D, typical of that used in critical joints of offshore structures. The steel was supplied by the British Steel Corporation in 25mm thick plates, normalized at 910°C. Chemical composition and mechanical properties of the as received plates are given in Table 3.1. Optical metallographic examination indicated a fine grained normalized structure, with an average grain size of d = 35μm measured by the linear intercept method. The inclusion particles were primarily manganese sulphide MnS. A quantitative examination of random metallographic sections gave the number of inclusions per unit area N_A as $6.3mm^{-2}$ and an average inclusion spacing of S = 200μm was calculated by[1]:

$$S = \frac{1}{2} \frac{1}{\sqrt{N_A}} \qquad 3.1$$

During the course of the present investigation the following test piece geometries were used: Uniaxial Tension, Notched Bar Tension, Single Edge Cracked (SECT) in Tension, Double Edge Cracked (DEC) in Tension, and Part Through surface Cracked (PTC) in tension. The specification of each geometry and the experimental procedures will be given in appropriate sections. All the test pieces, with the exception of PTC, were tested under montonic tensile loading at various temperatures. Therefore a versatile cryostat was designed to accommodate the low temperature testing of various geometries and is described in next section.

3.3 Low temperature testing method

Test temperatures below ambient were obtained by testing the specimens in a cryostat cooled with liquid nitrogen. The cryostat consisted of four sections, containing coiled copper tubes around the inside chamber in which the specimens were loaded. Two of the sections could be removed to form a smaller chamber for testing small size specimens. Liquid nitrogen was pumped continuously through the copper tubes or into the individual sections until the required temperature was achieved. For very low temperatures (-140 to -196°C), the chamber itself contained various levels of liquid nitrogen. By controlling the rate of liquid nitrogen flow, it was possible to achieve the requisite temperature and maintain it for the duration of test within $\pm$ 2°C. Specimen temperature was measured by a Cu-Con thermocouple glued to the specimen surface at the point of interest i.e. in the vicinity of the crack tip for SECT and DEC geometries and just above the notch for the notched round tensile specimens.

3.4 Variation in yield stress with temperature

Tensile tests were carried out on machined cylindrical tensile test pieces of 8mm diameter, conforming with BS18-Part 2- 1971 specification, cut in Transverse (T) direction from the parent plate. Tests were performed on a 250kN Instron TT-K servo-hydraulic testing machine at various temperatures in the range - 140 to + 20°C. Specimens were loaded under displacement control at a strain rate of 1.6×10^{-3} S^{-1}, and load-displacement curves were recorded. Extension was obtained via a strain gauge extensometer attached to the specimen on a gauge length of 25mm.

The results of tensile tests are shown in Fig. 3.1 where the lower and upper yield stress are plotted as a function of temperature. All flow curves exhibited an upper and lower yield point which is characteristic of low-carbon steels. Both the upper and lower yield stress increase with decreasing temperature although this trend is steeper for the upper yield point. The yield strength σ_y used in this investigation, refers to the upper yield stress. Yield data obtained here were introduced into a relationship due to Bennett and Sinclair[2], to obtain a single equation for σ_y as a function of temperature and strain rate:

$$\sigma_y = 745.6 - 0.056T \ln\left(\frac{A}{\sqrt{2\varepsilon^o}}\right) \qquad (3.2)$$

where:

σ_y is yield stress in MPa

T is temperature in °K

ε^o is strain rate in S^{-1} and

A is a constant equal to 10^8 S^{-1}

All subsequent values of yield stress for a given temperature and strain rate were derived from equation 3.2.

3.5 CVN impact testing

Charpy V notch impact tests were conducted in the temperature range of -80 to +20°C. The specimen dimensions and test procedure were in accordance with BS131 : Part 2 : 1972.

The results in the form of a plot of impact energy absorption versus temperature are given in Fig. 3.2, where each data point is the average of three tests. Fractography examination of fracture surface by optical and scanning Electron Microscopy revealed that at -80°C fracture occurs entirely by cleavage with no shear lips apparent on the surface. At temperatures of -60°C and above, cleavage is preceded by regions of ductile fracture indicating that fracture was initiated by a ductile mechanism. By increasing testing temperature, the amount of ductile fracture and the extent of the shear lips also increase which explains the increase in the absorbed energy. On the basis of fractography observations and the results presented in Fig. 3.2, the dynamic Nill Ductility Temperature (NDT) of the material is considered to be -60°C.

3.6 Variation of failure strain with triaxiality

As discussed in section two ductile fracture can be modelled as a strain induced process, in which failure, in form of void initiation, growth and coalescense, occurs when a critical strain is locally exceeded over some microstructurally characteristic distance[3]. It has been shown[3-4] that this critical strain is a strong function of multi-axial state of stress. Therefore/

a study of ductile failure necessarily involves the determination of the failure strain as a function of triaxiality. In this section the relationship between failure strain and triaxiality, for the material under investigation, is experimentally established and the effect of temperature is also studied.

Definition

The triaxial state of stress can be represented by the non-dimensional quantity $\frac{\sigma_m}{\bar{\sigma}}$, in which σ_m is the mean stress and $\bar{\sigma}$ the effective flow stress.

The mean stress is the hydrostatic component of an arbitrary state of stress which causes volume changes without plastic flow and is the average of the principal stresses,

$$\sigma_m = \frac{1}{3}(\sigma_1 + \sigma_2 + \sigma_3) \qquad (3.3)$$

The effective stress is defined by Von Mises equation in terms of principal stresses.

$$\bar{\sigma} = \frac{1}{2}[(\sigma_1 - \sigma_2)^2 + (\sigma_2 - \sigma_3)^2 + (\sigma_3 - \sigma_1)^2]^{\frac{1}{2}} \qquad (3.4)$$

The effective stress is associated with plastic flow in metals, which is accomplished by the movement of dislocations under the effect of shear stresses.

The degree of triaxiality $\frac{\sigma_m}{\bar{\sigma}}$ is infinite for a stress system of $\sigma_1 = \sigma_2 = \sigma_3$ (full triaxiality) and zero for stress system of $\sigma_1 = -\sigma_2$ and $\sigma_3 = 0$ (pure shear). In a uniaxial tensile test before plastic instability $\sigma_2 = \sigma_3 = 0$, hence $\bar{\sigma} = \sigma_1$ and $\sigma_m = \frac{1}{3}\sigma_1$ which results in a triaxiality of $\frac{\sigma_m}{\bar{\sigma}} = \frac{1}{3}$.

The effective plastic strain $\bar{e}^P$ is defined in terms of the increments of principal plastic strains:

$$de^P = \frac{2}{9}\left[(de^P_1 - de^P_2)^2 + (de^P_2 - de^P_3)^2 + (de^P_3 - de^P_1)^2\right]^{\frac{1}{2}} \quad (3.5)$$

$\bar{e}^P$ is a scalar quantity and is always taken to be positive. The dilation component of the strain, analogous to the mean stress, is not considered as volume changes during plastic deformation are negligible $(de^P_1 + de^P_2 + de^P_3 = 0)$. Thus in a uniaxial tensile test on a cylindrical test piece where $de^P_2 = de^P_3 = -1/2\ de^P_1$, for uniform deformation effective plastic strain can be written in terms of de^P_2 as:

$$\bar{e}^P = \int de^P = 2 \ln \frac{do}{d} \quad (3.6)$$

where d and do are the instantaneous and initial diameters.

3.6.1 Experimental Procedure

3.6.1.1 Specimens

Different triaxial stress states can be obtained by testing axisymmetric circumferentially notched specimens with varying notch severity[4] as shown in Fig. 3.3. In such a test piece failure initiates in the centre region of the notch where the triaxial stress state is most severe. Failure initiation can be detected by a sharp drop in the plot of the average stress versus effective plastic strain[4] which indicates a loss in load-bearing cross-section due to formation of a crack in the centre of the testpiece on the minimum cross section. The effective plastic strain associated with this discontinuity in specimen behaviour is defined as the effective plastic strain for failure initiation $\bar{e}_f$. Hancock and Mackenzie[4] used the Bridgman[5] analysis for the minimum section of a necked tensile specimen,/

to calculate stress and strain states for a notched test piece. In Fig. 3.4 the results of Bridgman analysis in the form of the distribution of stresses and effective plastic strain are shown. From these results $\bar{e}^P$ and $\frac{\sigma_m}{\bar{\sigma}}$ at the centre of a notched bar are estimated as:

$$\bar{e}^P = 2 \ln \frac{do}{d} \tag{3.7}$$

$$\frac{\sigma_m}{\bar{\sigma}} = \frac{1}{3} + \ln(1 + \frac{d}{4R}) \tag{3.8}$$

where R is the notch root radius and do and d are the original and current diameter of the notch. Earl and Brown[6] have pointed out that the extrapolation of Bridgman analysis to approximate the plastic flow field of notched specimens may produce erroneous results.

The finite element analysis of Hancock and Brown[7] provides more accurate solutions for the distribution of $\frac{\sigma_m}{\bar{\sigma}}$ and $\bar{e}^P$ as a function of $\frac{do}{d}$. These solutions are for selected notch geometries and are presented in graphical form in Ref.7. In the work presented here both Bridgman and Hancock and Brown solutions are considered although in subsequent sections only those results which have been processed by the latter solution will be used.

3.6.1.2 Test procedure

Circumferentially notched tensile specimens were machined from the transverse direction of the plate. The dimensions of specimen are given in Fig. 3.3. In addition unnotched specimens (labelled P_1) of diameter d = 7.6mm were also tested.

Tests were carried out on an 250kN Instron TT-K servo hydraulic testing machine, under displacement control at a constant strain rate of 1.5×10^{-3} S^{-1} and over the temperature range of -60 to 100°C. The diameter change at the minimum section of the notch was measured continuously with a strain gauge extensometer. A second extensometer mounted across the notch, controlled the axial displacement rate. The applied load, axial displacement and the diameter changes were continuously recorded by using a multi-channel data logger. Low temperature tests were performed in a manner similar to that for low temperature uniaxial tensile testing, and high temperature tests were carried out in a furnace attached to the testing machine. Loading was stopped when a sharp drop in the applied load was detected. After unloading, the minimum cross section and the curvature of the notch were measured for each specimen using an optical comparator. Specimens were subsequently sectioned longitudinally at the centre of the notch and prepared for optical examination by normal metallurgical specimen preparation techniques.

3.6.2 Results and Discussion

Fig. 3.5 shows the results of A and D notch specimens tested at room temperature, in which the average axial stress is plotted against effective plastic strain $\bar{e}^p$. The unnotched tensile result is also shown. The average stress was obtained by dividing the load by the current cross-section area, $\pi d^2/4$, and $\bar{e}^p$ was calculated from the diameter change of the specimen (equation 3.7). As shown the average stress rises as the material strain hardens and then drops sharply. Also it can be seen that with increasing severity of the notch the average stress for a given strain increases and the ductility of material decreases. The stress-strain curves/

for each specimen geometry as a function of temperature are shown in Figs. 3.6 to 3.8. All curves exhibited a sharp fall off in average stress at the point of failure initiation with the exception of the D notch specimen tested at -60°C which fractured before the load could be reduced.

Metallographic observations performed on the longitudinal sections at the centre plane of the specimens indicate that the failure in all specimens was initiated at the centre of the notch by coalescence of holes, nucleated and grown at inclusions. A typical failure initiation event is seen in Fig. 3.9, which shows the damaged area of the A notch specimen tested at -20°C and unloaded after the sharp fall off in the average stress curve. Although there are discrete holes, the failure is associated with linking up of large holes at the centre of the specimen which results in a loss in load bearing cross-section area of specimen and thus a sudden drop in average stress. Cowling and Hancock[8] observed the same behaviour in a low alloy high strength steel. In the more severe D notch specimen tested at -40°C failure occurred by localized micro cracking between the large holes as shown in Fig. 3.10. These micro cracks may be cleavage since on the fracture surface of same geometry tested at -60°C areas of cleavage were observed, though fracture initiation was still in a ductile manner. Similar behaviour was observed by Cowling and Hancock[9] where the effect of pre-straining prior to the introduction of a notch into the specimen at room temperature was studied. They found that for commercially pure iron a pre-strain of $\bar{e}_p = 0.2$ promoted a mixed mode fracture in the more severe D notch geometry whereas the A notch specimen failed by a complete ductile mechanism.

In Table 3.2 the results of the effective strain at failure initiation $\bar{e}_f$ and triaxiality parameter $\frac{\sigma_m}{\bar{\sigma}}$ are given for different notch geometries at various temperatures, using two different analyses. For the Bridgman[5] analysis original values of notch diameter, d, and notch minimum curvature, R, were used in equations 3.7 and 3.8 to calculate $\bar{e}_f$ and $\frac{\sigma_m}{\bar{\sigma}}$. This simplification underestimates the values of $\frac{\sigma_m}{\bar{\sigma}}$ by up to 20% for D and A notch geometries and assumes a uniaxial tension stress state of $\frac{\sigma_m}{\bar{\sigma}} = 1/3$ for unnotched geometry. Finite element analysis of Hancock and Brown[7] on the other hand gives the progressive distribution of $\frac{\sigma_m}{\bar{\sigma}}$ and $\bar{e}_p$ as a function of $\frac{do}{d}$ and therefore includes the stress state history. In this analysis $\frac{\sigma_m}{\bar{\sigma}}$ for the unnotched P specimen was obtained by using failure initiation values of d and R in equation 3.7. This was consistent with the Needleman[10] solution for a necking cylindrical bar as described by Hancock and Brown[7].

The results in Table 3.2 are presented graphically as failure loci in Figs. 3.11 and 3.12 for both analyses. The stress state history involved in the deformation is also included in Fig. 3.12. As it can be seen the failure strain $\bar{e}_f$ depends strongly on triaxiality and at a given $\frac{\sigma_m}{\bar{\sigma}}$ is independent of temperature. The influence of $\frac{\sigma_m}{\bar{\sigma}}$ on $\bar{e}_f$ has been observed by other workers[3,4]. Mackenzie et al[4] found that the dependence of ductility on triaxiality is a material property. For example Cowling et al[11] examined the ductile failure of BS4360 Grade 50D steel and showed that an increase in the sulphur content not only decreases the ductility of material but also decreases the stress state sensitivity of the failure strain. It has been shown[3] that the failure locus of steels is sensitive to the orientation of test piece with respect to the rolling direction.

The results of present study indicate that temperature, in the range studied has no apparent effect on the material failure loci. This can be attributed to the fact that in this temperature range failure is initiated by a ductile mechanism and that the requirement for such initiation i.e. attainment of a critical strain is essentially independent of temperature. The reduction in toughness of material in this range (transition) is however related to the incidence of alternative failure mechanisms which affect both failure initiation in crack tip stress fields (where the degree of triaxiality is higher than that achieved in the notched tensile tests) and the propagation of failure.

The results on the effects of triaxiality on ductility will be discussed fully in Section 4. The relevance of the results presented here is that they may be applied to crack tip stress and strain fields where the triaxiality is such that material behaviour in uniaxial tension is inadequate to understand the failure process in such flow fields.

3.7 References

1. Knott, J.F., Proc. conf. ''Micromechanisms of crack extension'', Cambridge, Inst. Phys. Met. Soc., 1980.

2. Bennett, P.E. and Sinclair, G.M., J. Basic Eng., Trans. ASME Series D, Vol. 88, pp. 518-524, 1966.

3. Mackenzie, A.C., Hancock, J.W. and Brown D.K., Eng. Fracture Mech., Vol. 9, pp. 167-188, 1977.

4. Hancock, J.W. and Mackenzie, A.C., J. Mech. Phys. Solids, Vol. 14, p. 107, 1976.

5. Bridgeman, P.W., ''Studies in Large Flow and Fracture'', McGraw-Hill, New York, 1952.

6. Earl, J.C. and Brown D.K., Eng. Fracture Mech., Vol. 8, pp. 599-611, 1976.

7. Hancock, J.W., Brown, D.K., J. Mech. Phys. Solids, Vol. 31, No. 1, pp. 1-24, 1983.

8. Hancock, J.W. and Cowling M.J., Fracture 1977, ICF4, Vol. 2, pp. 371-375, Canada, 1977.

9. Hancock, J.W. and Cowling, M.J., Fracture 1977, ICF4, Vol. 2, pp. 365-369, Canada, 1977.

10. Needleman, A., J. Mech. Phys. Solids, Vol. 20, p. 111, 1972.

11. Cowling, M.J., Hancock, J.W. and Brown, D.K., Proc. Int. Symp. Integrity of Ofshore Structures, IESS, Paper 5, Glasgow, 1978.

Table 3.1 Chemical composition and mechanical properties of the BS4360 grade 50D steel.

CHEMICAL COMPOSITION (Wt%)

C	Si	Mn	P	S	Cr	Mo	Cu	Nb
0.17	0.29	1.30	0.010	0.008	0.09	0.01	0.11	0.045

MECHANICAL PROPERTIES

Yield stress	Ultimate stress	Elongation	Reduction of Area
MPa	MPa	%	% AV
360	558	26	56

Table 3.2 Values of $\frac{\sigma_m}{\bar{\sigma}}$ and $\bar{e}_f$ at various temperatures for two different analyses

Test Temperature (°C)	Specimen	Bridgeman Analysis $\frac{\sigma_m}{\bar{\sigma}}$	Bridgeman Analysis $\bar{e}_f$	Finite Element Analysis $\frac{\sigma_m}{\bar{\sigma}}$	Finite Element Analysis $\bar{e}_f$
100	D	1.26	0.33	1.82	0.22
	A	0.77	0.48	1.04	0.45
	P	0.33	1.10	0.62	1.09
20	D	1.29	0.34	1.81	0.23
	A	0.76	0.47	1.02	0.44
	P	0.33	1.13	0.64	1.13
-20	D	1.29	0.35	1.87	0.24
	A	0.77	0.48	1.04	0.45
	P	0.33	1.13	0.64	1.13
-40	D	1.29	0.31	1.75	0.20
	A	0.77	0.46	1.02	0.43
	P	0.33	1.24	0.67	1.24
-60	D	1.3	0.33	1.80	0.23
	A	0.77	0.47	1.02	0.44
	P	0.33	1.11	0.63	1.10

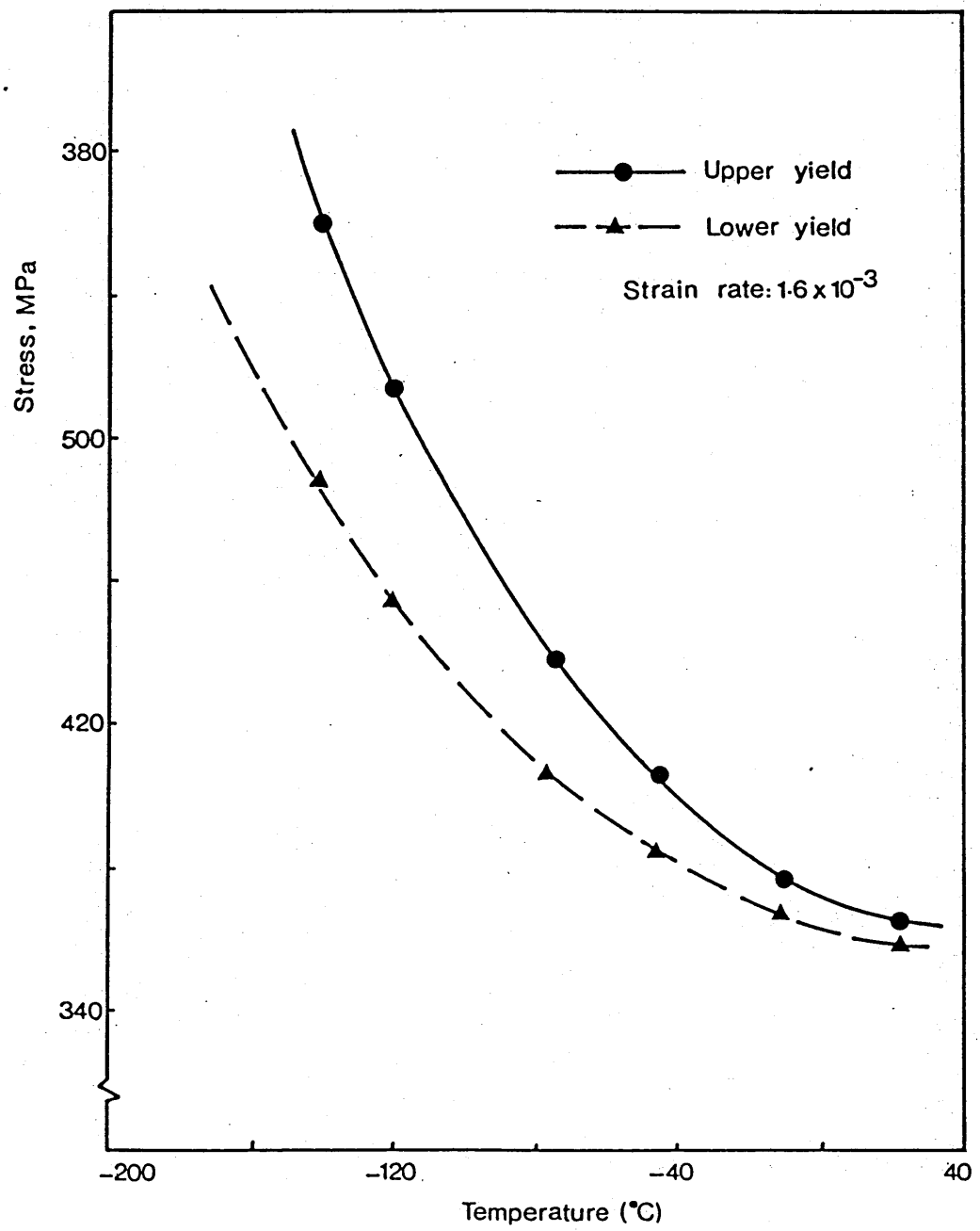

Fig. 3.1 Variation of upper and lower yield stress with temperature

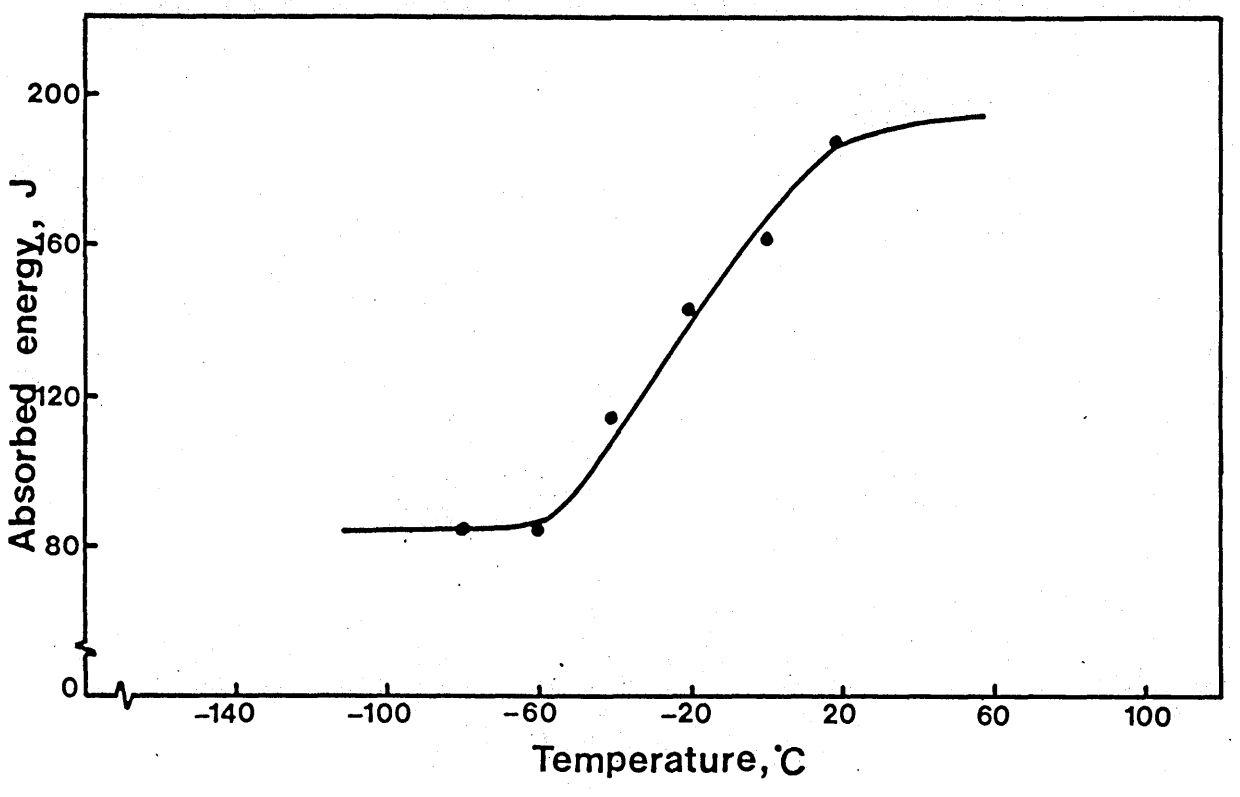

Fig. 3.2 Charpy transition curve

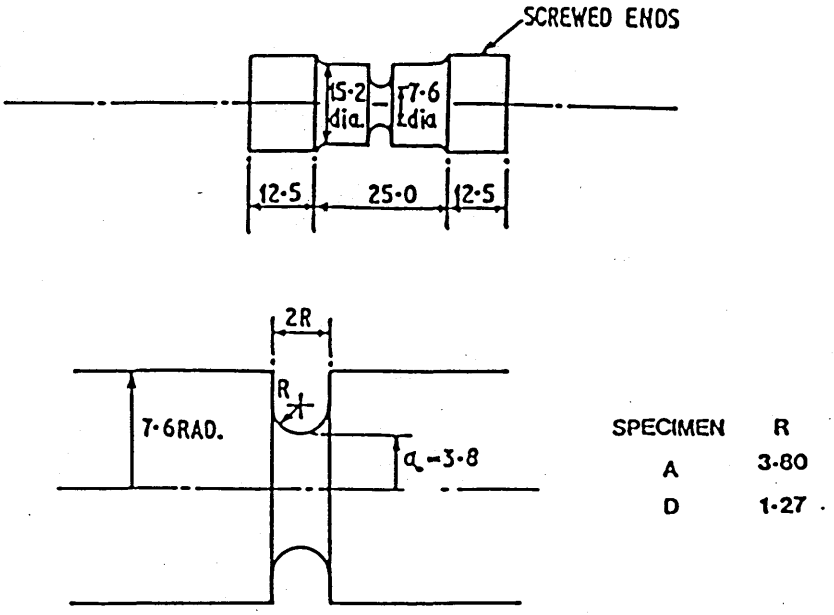

Fig. 3.3 Notch tension specimens
(all dimensions in mm)

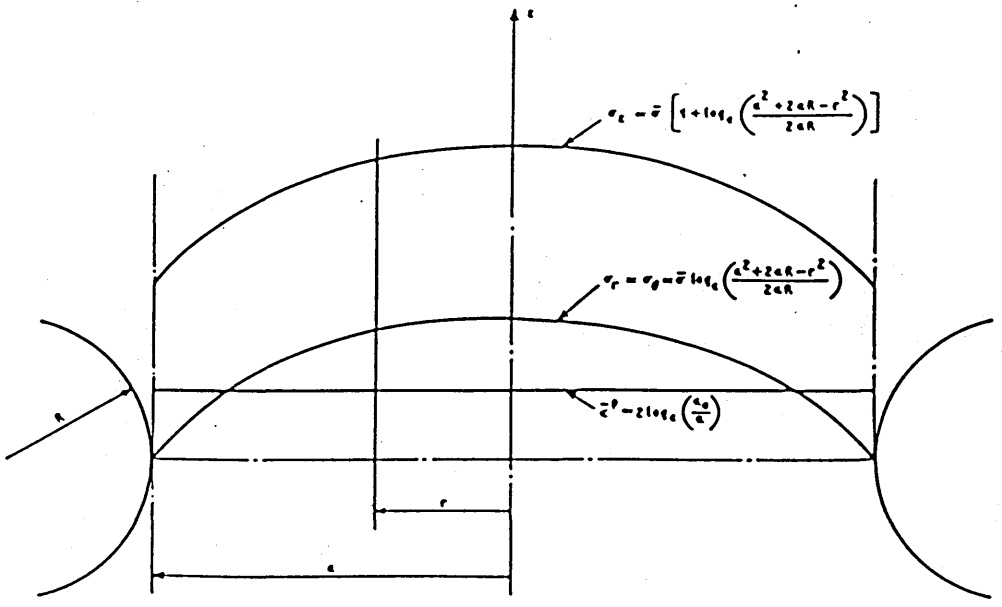

Fig. 3.4 Bridgeman[5] stress and strain distributions

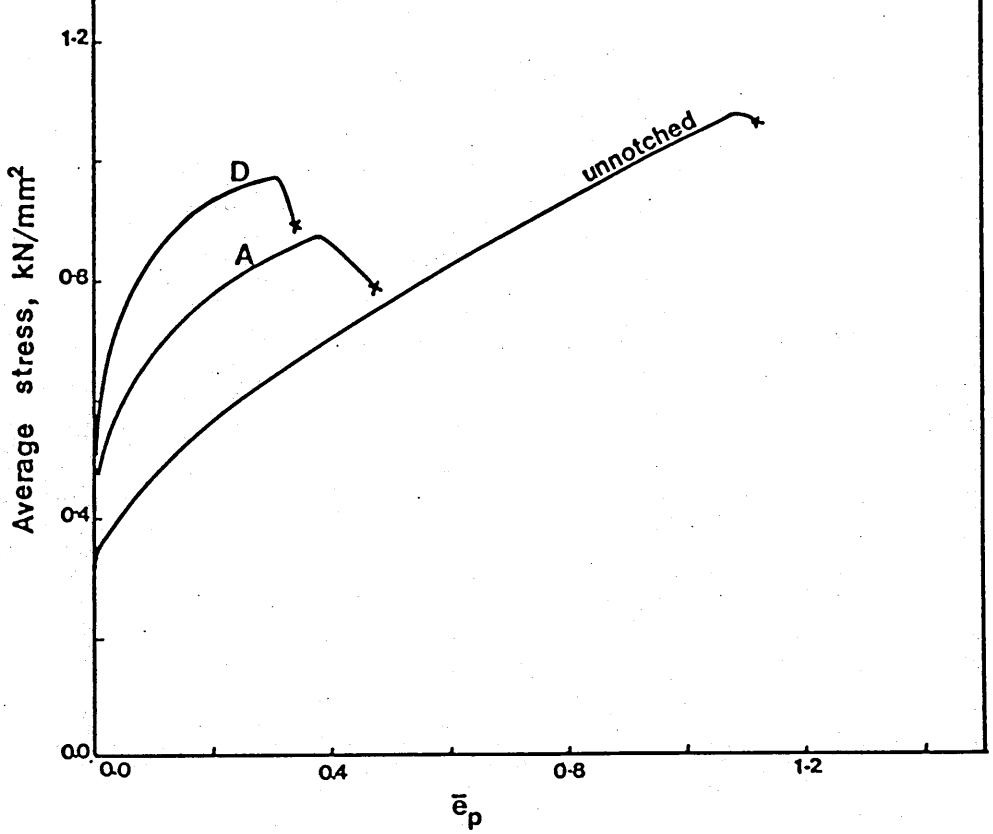

Fig. 3.5 Stress-Strain curves for the notched specimens tested at 20°C

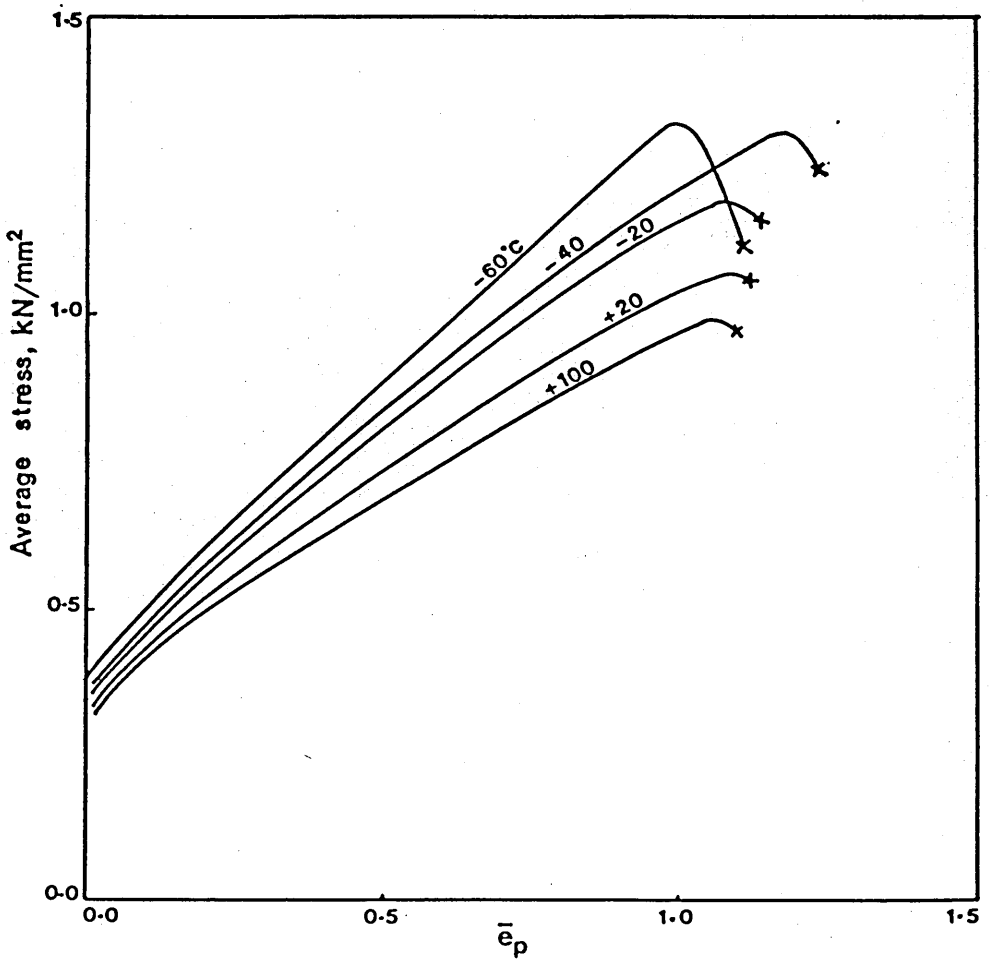

Fig. 3.6 Stress-strain curves for unnotched specimens tested at various temperatures

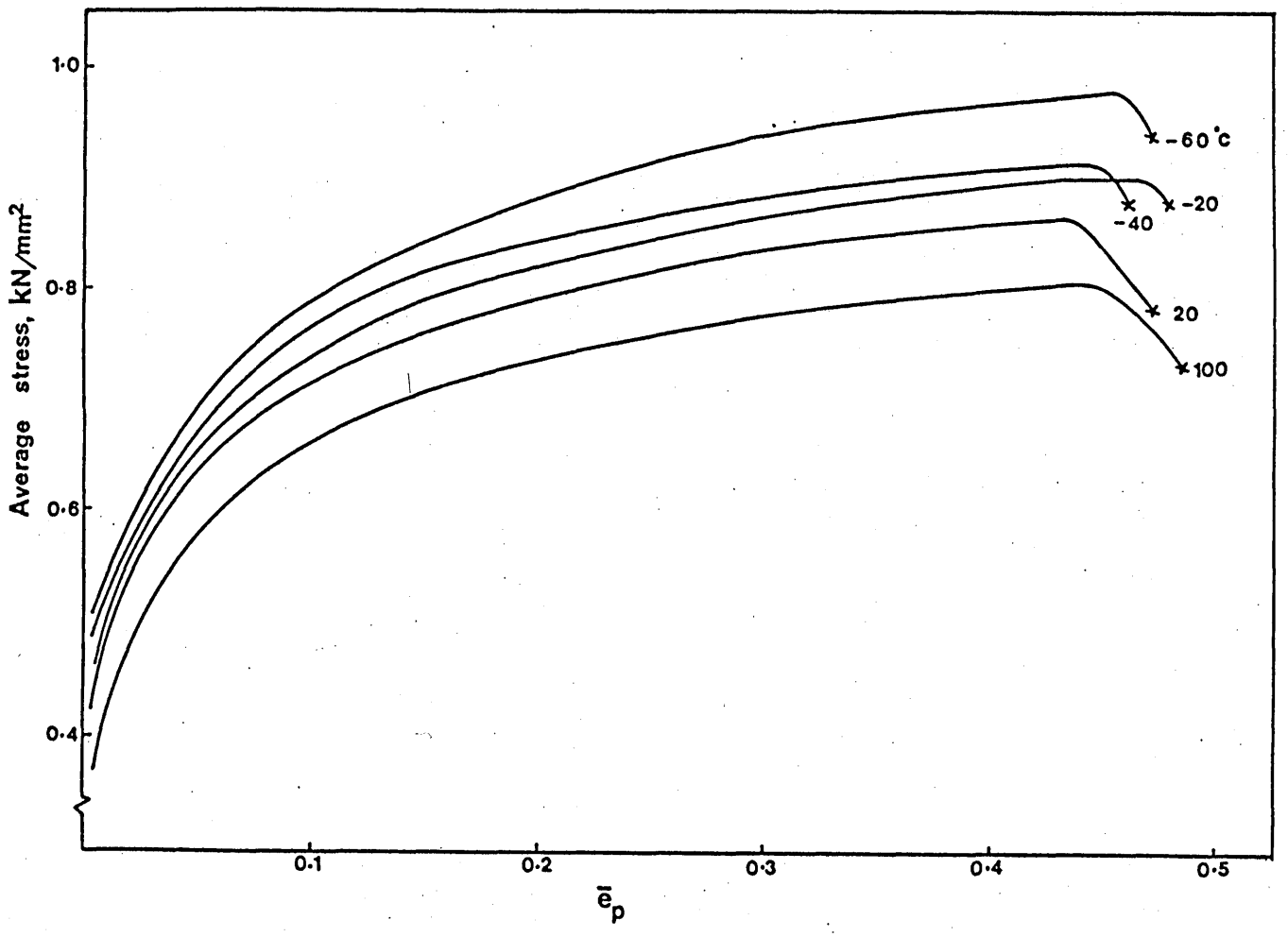

Fig. 3.7 Stress-strain curves for A notched specimens tested at various temperatures

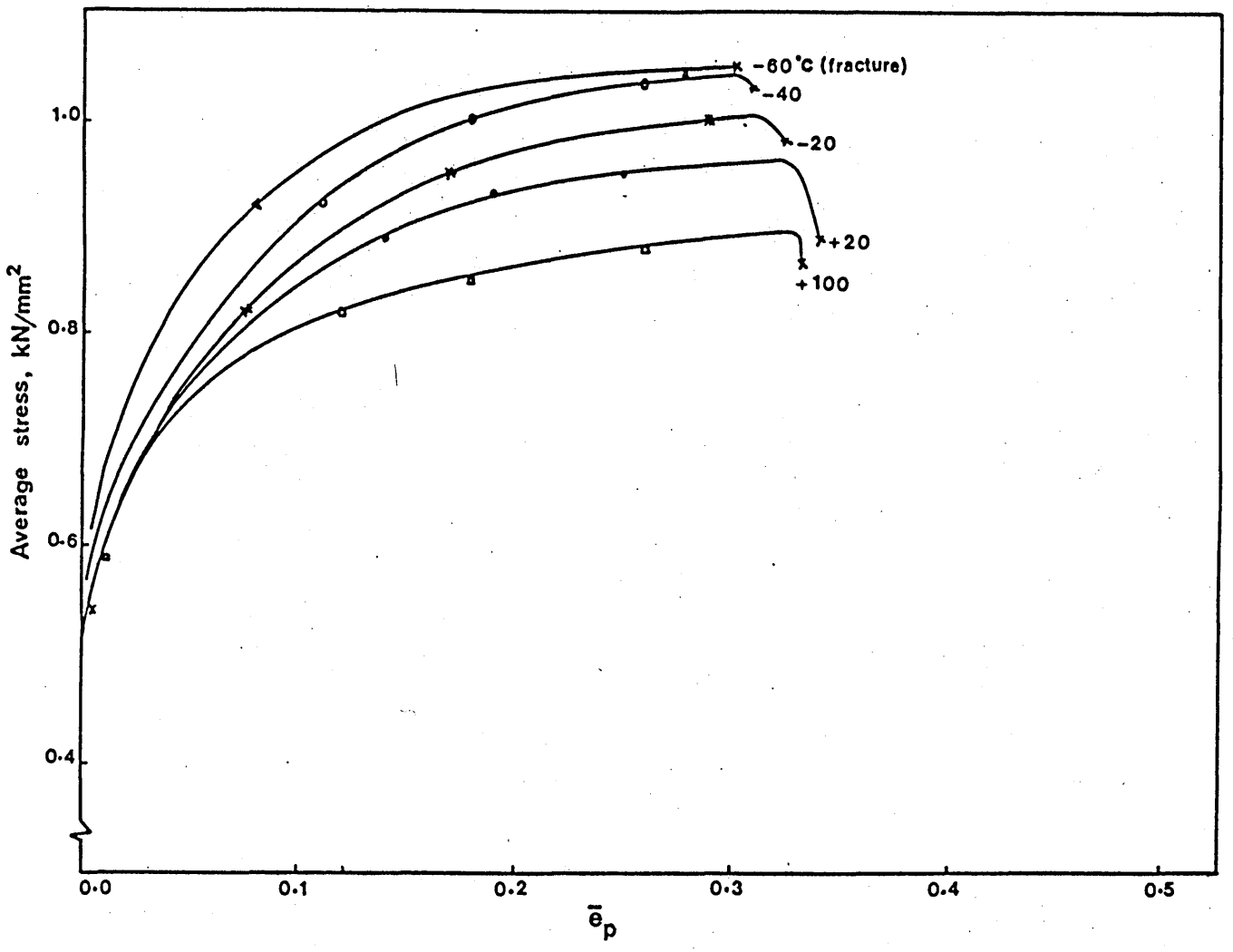

Fig. 3.8 Stress-strain curves for D notched specimens tested at various temperatures

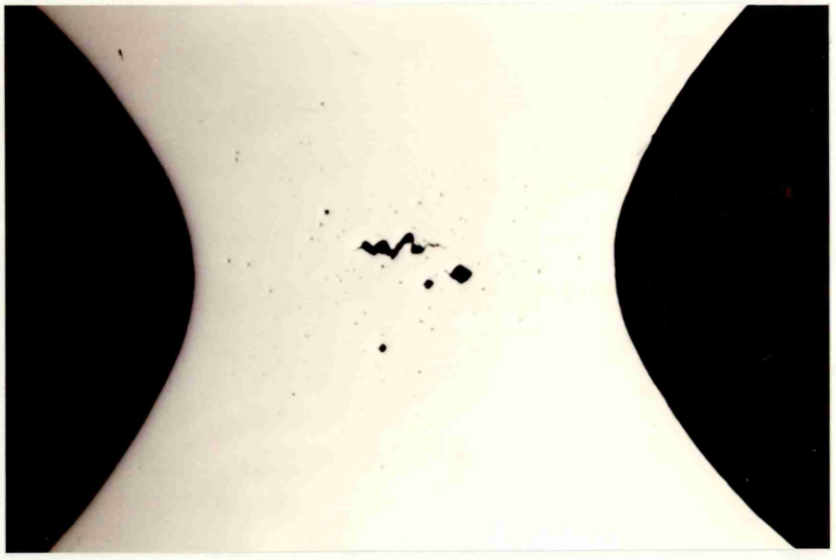

Fig. 3.9 Damaged area at the centre of an A notch specimen tested at -20°C showing the failure initiation event.

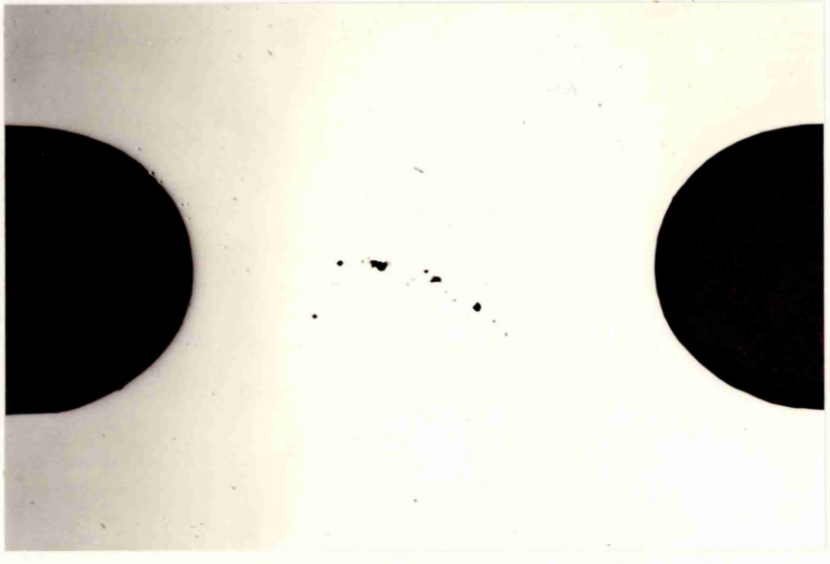

Fig. 3.10 Damaged area at the centre of a D notch specimen tested at -40°C showing that failure occurs by localized micro cracking between the large holes.

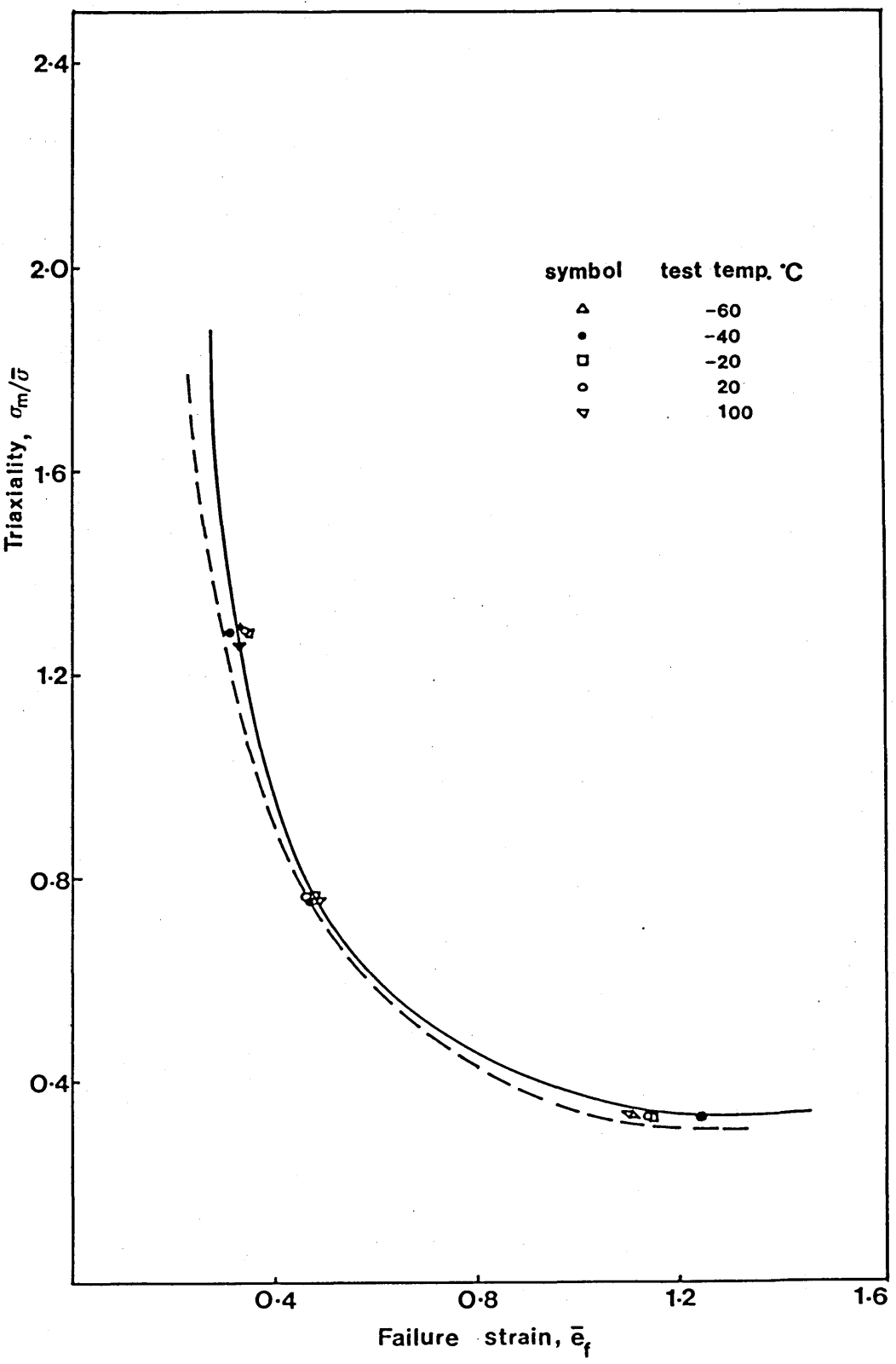

Fig. 3.11 Failure locus for notch tension specimens as a function of temperature, using Bridgeman analysis. Dotted line shows Cowling et al [11] result for the same material tested at 20°C.

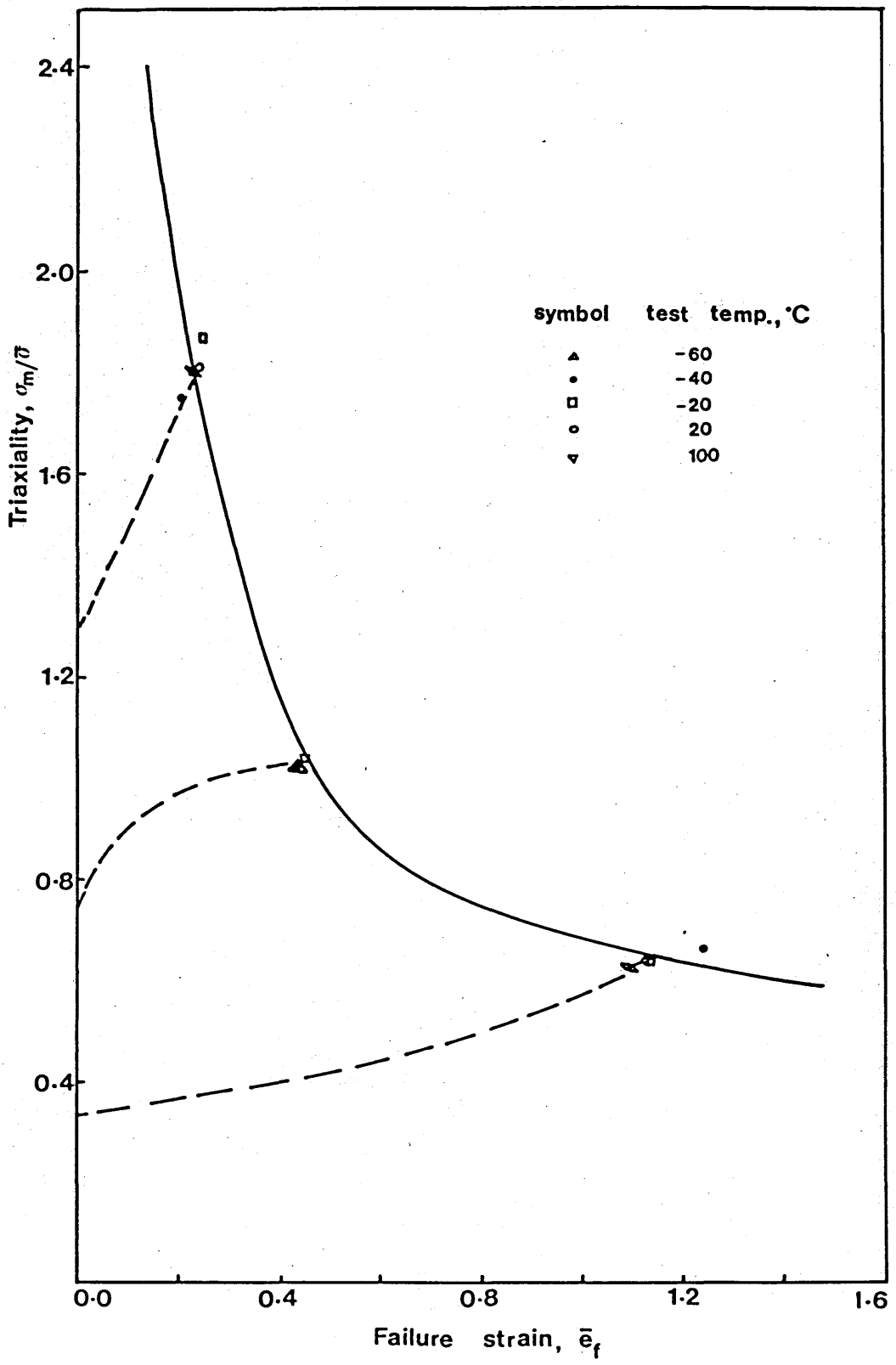

Fig. 3.12 Failure locus for notch tension specimens as a function of temperature, using Hancock and Brown[7] finite element analysis. (Dotted lines indicate the deformation history of specimens for all of the temperatures tested).

Section 4

POST YIELD FRACTURE TOUGHNESS PARAMETERS

4.1 Introduction

The fracture touchness of materials in the LEFM regime is characterized by a single parameter, K_{IC}, for which test pieces must obey certain dimensional restrictions[1]. For low strength tough steels, the minimum thickness of a valid test piece at a given temperature is excessively large, imposing a practical difficulty in determining K_{IC} for these materials. In addition, many sections in real structures do not have adequate sizes for a valid LEFM treatment. In these situations the use of other fracture toughness parameters su ch as COD and J which characterize the stress and strain conditions at the crack tip[2,3] becomes particularly attractive.

Some geometry restrictions are also necessary for J testing[4] as discussed in section 1.8. For COD measured at the initiation of crack extension (δ_i), which is claimed to be a material property provided that the plane strain condition is maintained[5], no restriction on specimen thickness has been agreed upon. The reason for this is that in the practical use of COD it is suggested[6] that tests should be carried out on specimens which have the same thickness as the material or structural section under consideration.

In the elastic-plastic regime failure is usually initiated by the ductile mechanism. It has been shown[7,8] that the microscopic events leading to ductile failure are influenced by the extent of the triaxial state of stress. Thus it is reasonable to expect that the macroscopic fracture/

toughness parameters are also dependent on the level of triaxiality. In this context Hancock and Cowling[9] tested different cracked configurations with varying degrees of constraint for a high strength low alloy steel. They found an order of magnitude change in upper shelf values of δ_i between the highest and lowest degrees of constraint studied i.e. the deep Double Edge Crack (DEC) geometry in tension with 10:1 width to ligament ratio and the Single Edge Crack Tension (SECT) geometry loaded at the centre of ligament. In contrast experimental work by Markstrom[10] on two different medium strength steels showed a unique value of J_c for the DEC (with 5:1 ratio) and Centre Cracked Panel (CCP) geometries. The CCP has a similar flow field to the SECT geometry. This discrepancy in experimental results is attributable to the specimens tested and the degree to which the size requirement for EPFM is satisfied. It should also be noted that the 5:1 DEC geometry does not incorporate a high level of triaxiality in the crack tip field and therefore differences between fracture characterizing parameters measured using this geometry and the CCP would not be expected to be large for most materials.

In the work presented in this section, the effect of constraint on the post-yield fracture toughness parameters over the entire temperature range, from the lower to the upper shelf regions, is investigated. Two different specimen geometries representative of two different flow fields have been tested and the results are discussed in terms of the failure mechanisms involved. A finite element analysis was also performed to obtain further information on the stress and strain fields associated with the SECT geometry.

4.2 Experimental procedure

4.2.1 Specimen geometry

The geometries selected for this study of the effect of constraints on the fracture toughness parameters were the deep Double Edge Crack in tension (DEC) and Single Edge Crack in tension (SECT) loaded at the centre of ligament. The DEC geometry with width-to-ligament ratio of 10:1 develops the full constraint of the Prandtl slip line field[11] as shown in Fig. 4.1a. The etching[12] study of Cowling and Hancock[13] on this geometry confirms that the plasticity is fully contained in the ligament between the crack tips. The triaxiality in the diamond ahead of the blunted crack tip can be obtained from the Hencky equation of slip-line field analysis:

$$\frac{\sigma_m}{\bar{\sigma}} = (1 + 2 \ln (1 + \frac{2X}{\delta})) / \sqrt{3} \qquad (4.1)$$

where σ_m is the mean stress, $\bar{\sigma}$ is the effective stress, δ is the crack opening displacement and X is the distance from the crack tip on the crack plane. At the end of the log-spiral where $X/\delta \simeq 2$ (see section 2.3) a triaxiality of 2.4 is achieved).

In the SECT configuration only modest triaxiality occurs ahead of the tip but intense shear strains develop on planes at 45 degrees to the crack plane. The slip-line field consists essentially of two straight lines at 45 degrees to the crack plane (Fig. 4.1b) provided that crack tip blunting is small compared with the ligament size, and there is no bending moment over the ligament. This geometry produces a fully plastic field with the lowest triaxiality associated with the plane strain condition:

$$\frac{\sigma m}{\bar{\sigma}} = \frac{1}{\sqrt{3}} = 0.57 \qquad (4.2)$$

The configuration and dimensions of the test pieces are shown in Fig. 4.2.

4.2.2 Test method

Both DEC and SECT specimens were subjected to increasing monotonic loads under displacement control, at various temperatures and the COD and J at failure initiation were determined. In the DEC test piece the onset of crack extension can be readily observed by a sudden drop in the load displacement curve under the displacement control condition[13]. For the SECT geometry, however, failure initiation is not easily detectable and thus a multi-specimen R-curve procedure, as discussed in Section 1.6.4 was adopted.

4.2.3 Test procedure

4.2.3.1 Fatigue precracking

All the test pieces were extracted in the transverse direction from the plate, with the fatigue cracks grown in the rolling direction. Fatigue precracking of all specimens was performed in a high frequency Amsler resonant fatigue testing machine under constant amplitude three point bending at a frequency of approximately 60 Hz and stress ratio of R = 0.2. For the DEC specimen two slits 1mm wide and 10mm deep were machined at opposite sides of specimen and saw cuts of 0.2mm width were introduced at the root of the slits. Fatigue cracks were initiated from the tip of saw cuts. The maximum applied load in the cyclic load range was 45 KN and 35KN for first and second crack respectively. This level of load produced a maximum stress intensity factor of less than 24 $MPa.m^{\frac{1}{2}}$ which developed plastic zones of less than 0.2mm at the tip of each crack. Care was taken to/

produce aligned fatigue cracks since it has been shown[14] that the slip-line field for non-aligned (non-coplanar) cracks is different from that shown in Fig. 4.1a, and results in a different level of constraint. Thus prior to monotonic loading each specimen was optically examined and non-aligned cracked specimens were rejected.

For the SECT specimen, the fatigue crack was initiated at the root of a 2mm deep V-notch, machined on the surface of the specimen. The maximum stress intensity factor in the cyclic range was less than 24 MPa.$m^{1/2}$. Subsequent to pre-cracking, SECT specimens were machined to produce screw threaded ends such that the tensile axis was applied to the centre of ligament.

4.2.3.2 Monotonic loading

Tensile loading of all specimens was carried out in a 250 KN Instron TT-K servo-hydraulic testing machine at a constant strain rate of 1.5×10^{-3} S^{-1} under displacement control. Crack opening displacement was measured by extensometers mounted across the mouth of the cracks. Values of load, cross-head displacement and crack mouth opening displacements were continually recorded. Low temperature testing was performed in a cryostat as described in section 3.3 and high temperature tests were carried out in a furnace attached to the testing machine. Tests on DEC specimens were stopped when a sudden fall off in the load-displacement curve were observed. At temperatures below -80°C DEC specimens fractured before the test piece could be unloaded. At least four SECT specimens were tested at any temperature to obtain sufficient data points for the construction of a resistance (R) curve. At -196°C SECT specimens fractured prior to any detectable crack extension. After testing,/

specimens tested at sub-zero temperatures including those fractured, were immediately transferred into an alcohol mixture to prevent water condensation and subsequent corrosion of the damaged crack tip on fracture surface. Unfractured specimens were then sectioned longitudinally at the centre line and prepared for optical examination by usual metallographic methods. COD at the original fatigue crack tip and the amount of crack extension were measured within $\pm$ 0.02mm using a micrometer attached to an optical microscope. The fracture surface of those specimens fractured were prepared for Scanning Electron Microscope (SEM) observation.

4.3 Results

The results of the experimental work are presented in terms of initiation values of COD (δ_i) and J-integral (J_i). In many practical situations the use of δ_i to derive critical defect sizes is considered too conservative and some relaxation is possible by the use of COD at maximum load (δ_m) where some stable crack extension in a structure may be allowed. However δ_i is an appropriate representative of material fracture behaviour in the elastic-plastic regime and characterizes the local events leading to failure.

4.3.1 δ_i for DEC geometry

Values of δ_i at various temperatures are given in Table 4.1. As noted earlier, with this geometry δ_i can be determined by a single specimen procedure. The geometry of the specimen and the loading configuration is such that the COD at the crack tip is approximately equal to the measured COD at the crack mouth. Indeed the crack mouth displacements measured by extensometers, correlated very well with the COD at/

the crack tip measured on the section profiles. The δ_i results given in Table 4.1 are presented in Fig. 4.3 as a function of temperature.

4.3.2 δ_i for SECT geometry

Values of COD and Δa measured for SECT specimens tested at various temperatures are given in Table 4.2. In Fig. 4.4 the variation of COD as a function of crack extension, Δa, at different temperatures is plotted in the form of a R-curve. It can be seen that, in general, the resistance to crack growth i.e. the slope of the R-curve, increases with increasing temperature. Similar results have been observed for a low alloy weld metal tested in three-point bending[15]. The COD at initiation of crack extension (δ_i) is obtained by the intersection of the R-curve with the blunting line (taken as $\delta = 2\Delta a$). Values of δ_i at different temperatures are given in Table 4.2 and plotted against temperature in Fig. 4.3 together with the DEC results.

4.3.3 Determination of J_i for DEC geometry

The use of the J-integral as an elastic-plastic fracture toughness parameter was outlined in Section 1.7. J values at the onset of crack extension, J_i, were obtained using two different analyses[16,17]. Rice, Paris and Merkle[16] proposed that for the DEC geometry, J can be estimated as:

$$J = J_{el} + \frac{2}{B(W-2a)} \int_0^{\delta_p} P d\delta_p - P\delta_p \qquad (4.3)$$

where B and W are the thickness and width of the specimen respectively, and 2a is the total crack length. J_{el} is the elastic component of the applied J/

and can be directly related to the strain energy release rate G and hence to the stress intensity factor K_I i.e. $J_{el} = K_I^2/E'$. The integral term in equation 4.3 can be interpreted as the area under the load-displacement curve as shown in Fig. 4.5. Using this analysis, J_i for the DEC specimen tested at room temperature is:

$$J_i = 0.241 \text{ KNmm}^{-1} \tag{4.4}$$

Sumpter and Turner[17] proposed another procedure for determination of J:

$$J = J_{el} + \frac{\eta_p U_p}{(W-a)B} \tag{4.5}$$

where U_p is the plastic area under load-displacement curve as shown in Fig. 4.6 and η_p is a geometry dependent function given by[18].

$$\eta_p = -\left(\frac{W-a}{W}\right) \frac{1}{P_L} \frac{\partial P_L}{\partial \left(\frac{a}{W}\right)} \tag{4.6}$$

where P_L is the limit load. For the tension case:

$$P_L = L\sigma_y B(W-a) \tag{4.7}$$

where L is a constraint factor which depends on geometry if the plane strain condition is maintained. From equations 4.6 and 4.7:

$$\eta_p = 1 - \left(\frac{W-a}{W}\right) \frac{1}{L} \frac{\partial L}{\partial \left(\frac{a}{W}\right)} \tag{4.8}$$

For the DEC geometry an approximate expression for L is given by[19]:

$$L = 1 + \ln\left(\frac{W-a}{W-2a}\right) \tag{4.9}$$

Differentiating equation 4.9 for the specimen dimensions and combining with equations 4.8 and 4.5, J_i for the DEC specimen tested at room temperature is:

$$J_i = 0.239 \text{ KNmm}^{-1} \tag{4.10}$$

which agrees very well with the estimation given by equation 4.4.

Values of J_i at various temperatures are given in Table 4.1 and are shown in Fig. 4.7 as a function of temperature. It can be seen that with decreasing temperature J_i decreases in a similar manner to the variation of δ_i with temperature. At -100°C, J_i satisfies the size requirement for a valid J_{IC} test, i.e. $(W-a)\ 25J/\sigma_y$, and can be considered as J_{IC}. From the results given in Table 4.1, it is deduced that there is a unique relationship between J_i and δ_i for all test temperatures:

$$\delta_i = M \frac{J_i}{\sigma y} \tag{4.11}$$

where M is approximately 0.5. This value agrees with the experimental results of DeCastro et al[6] who obtained values of M in a scatter band of 0.45 to 0.65 for the three point bend geometry with the same grade of material. This value of M also agrees with with the finite element analysis of Tracey[20] as described in section 1.7.3 (equation 1.36), when the flow stress in his analysis is taken as the mean value between yield stress and ultimate tensile stress.

4.3.4 Determination of Ji for SECT geometry

J_i for the SECT geometry at various temperatures was determined by using the R-curve technique. For calculation of J associated with each specimen the procedure due to Sumpter and Turner[17] was used as described in section 1.7.1:

$$J = J_{el} + \frac{\eta_p U_p}{B(W-a)}$$

where η_p is given by equation 4.8. For the SECT geometry with straight slip lines at 45 degrees to the crack plane and little constraint, $dL/d(a/W)$ in equation 4.8 is equal to zero and thus $\eta_p = 1$. Turner[21] also obtained $\eta_p = 1$ for a single edge crack specimen of a/W loaded in tension. U_p for each specimen was obtained by measuring the plastic area under load displacement curve as shown in Fig. 4.5. Values of J so obtained were plotted against the actual crack extension, $\Delta a'$ measured from the blunted crack tip (Fig. 4.8). In the recommended procedure for determination of J_i (Section 1.7.2.), values of J are plotted against Δa measured from the original crack tip and J_i is then taken as the intersection of the R-curve with the blunting line given by:

$$J = 2\Delta a \sigma_y \qquad (4.12)$$

Equation 4.12 is based on the assumption that a relationship of the form $\delta = MJ/\sigma_y$ with M=1 exists between δ and J. As outlined in section 1.7.3, the coefficient M is configuration dependent in the fully yielded state and therefore the use of equation 4.12 for the SECT geometry may produce erroneous results. By plotting the R-curve in the form of J versus/

actual crack extension, $\Delta a'$, the need for the blunting line is eliminated and hence an accurate J_i is determined. With this procedure, M can also be calculated accurately without imposing any pre-assumption. The values of J_i are given in Table 4.2 and are plotted as a function of temperature in Fig. 4.7. Values of M are also given in Table 4.2. It can be seen that M increases with decreasing temperature.

4.4 Application of the RKR model

As described in section 2.2.1, Ritchie, Knott and Rice[22] modelled the lower shelf fracture process by postulating that cleavage fracture occurs when the maximum local tensile stress exceeds a critical cleavage stress σ_f^*, over a microstructurally significant distance, X. The stress distribution ahead of a sharp crack is characterized by a unique singular field described by the stress intensity factor. Hence the fracture toughness of a material, K_{IC}, can be conveniently determined if the critical cleavage stress is known. The fact that at lower shelf temperatures, the DEC specimen geometry used in this investigation satisfies the valid J_{IC} size requirement implies that at these temperatures there is a unique mathematical relationship between J_i, δ_i and K_{IC} and therefore the RKR model can also be used to predict δ_i and J_i. To predict K_{IC} from the RKR model, the critical cleavage fracture stress of the material must be evaluated. Fractographic observation of DEC specimens indicated that at -100°C failure just initiated by a cleavage mechanism with negligible crack extension, thus the maximum tensile stress ahead of the crack at this temperature is equal to the critical stress for cleavage i.e. $\sigma_f^* = \sigma_{yy}\text{max}$. The maximum tensile stress ahead of the crack tip is obtained from the slip-line solution for this geometry.

$$\sigma_{yy}^{max} = 2k\left(1 + \frac{\pi}{2} - \frac{\theta}{2}\right) \qquad (4.13)$$

where k is yield stress in pure shear and θ is the notch flank angle. By assuming the Von Mises' yield criterion, the critical stress for cleavage fracture is obtained, σ_f^* = 1360 MPa which is assumed independent of temperature[23]. This value is based on the data from sharp-cracked specimens, whereas equation 4.13 is valid for notch angles greater than 6.4 degrees[24]. However it has been shown[22] that the error involved is small and is within the scatter band of experimental data.

The stress distribution ahead of a sharp crack as a function of distance ahead of the crack measured in terms of $(K_{IC}/\sigma_y)^2$ has been investigated by many workers[25-27]. Finite element analysis of Rice and Tracy[27] is shown in Fig. 4.9. By equating σ_f^*/σ_y to σ_{yy}/σ_y, K_{IC} at various lower shelf temperatures can be obtained from Fig. 4.8, if only the characteristic distance is known. Precise determination of the microstructural characteristic distance requires a complete understanding of the micromechanisms of cleavage failure. Ritchie et al[22] were able to produce good agreement with their experimental results on a mild steel, by choosing the characteristic distance equal to two ferrite grain diameters. There is of course no fundamental reason for the characteristic distance to equal precisely two grain diameters. However since for low strength steels cleavage is intergranular, it is reasonable to assume that the critical fracture event must occur over the first few grains from the crack tip. In the present work by taking the characteristic distance as 4 or 5 grain sizes, (0.12 or 0.15mm) the prediction of K_{IC} and therefore δ_i agrees well with experimental results as illustrated in Fig. 4.3. Above the cleavage-ductile transition temperature, however, the RKR prediction markedly underestimates the experimental data.

4.5 Application of the MHB Model

The upper shelf fracture toughness may be predicted by the Mackenzie, Hancock and Brown model[28] which postulates that ductile fracture occurs when a critical strain, which itself is a function of the state of stress, is exceeded over a minimum volume of material (see Section 2.3.2). This volume of material is characteristic of the scale of physical events involved. The application of this model involves experimental determination of the fracture strain $\bar{e}_f$, as a function of stress state. This is obtained by using circumferentially notched round tension specimens as described in section 3.6. The distribution of effective plastic strain $\bar{e}p$, and stress state $\sigma m/\bar{\sigma}$ ahead of a sharp crack for small scale yielding are then taken from the blunting solutions of McMeeking[25] or Rice and Johnson[26], as a function of distance ahead of the crack. δ_i can then be predicted by determining the value of COD where the equivalent plastic strain exceeds, over a characteristic distance, the strain to failure for the material. It is assumed that stress and strain field ahead of the crack in DEC geometry is described by the Rice and Johnson[26] small scale yielding analysis, since the flow field associated with this geometry is fully contained in the ligament between the crack tips. The upper shelf fracture toughness of the DEC geometry was, therefore, predicted using the MHB model. Values of critical strain at fracture $\bar{e}_f$ were obtained from the material failure locus analysed using the Hancock and Brown[29] finite element analysis (Fig. 3.12). By taking the characteristic distance as one inclusion spacing i.e. 200μm (section 3.2), it was found that the predicted upper shelf value of δ_i (shown in Fig. 4.3) correlated very well with experimental results. This is consistent with the fractographic studies of this geometry which indicate that on the upper shelf, failure is initiated by successive coalescence of holes to the blunted crack tip.

Values of characteristic distance of 1 to 10 times the inclusion spacing have been reported[23] for some high strength steels where failure is initiated by shear localization and shear decohesion between a number of voids.

It has to be noted that the application of both the RKR and MHB models to predict the macroscopic fracture behaviour of a wide range of materials is not feasible because of uncertainties in the magnitude of the characteristic distance. In most investigations, as here, the characteristic distances were chosen to fit the experimental data. However, the description of fracture toughness in terms of these models provides some insight into the micro-mechanics and mechanisms of failure.

4.6 Discussion of Experimental Results

The fracture toughness parameters, δ_i and J_i obtained for the DEC and SECT geometries show a transition from upper to lower shelf behaviour with decreasing test temperature (Figs. 4.3 and 4.7). In the DEC geometry tested on the upper shelf, fracture occured by a mechanism of void growth and coalescence to the crack tip. Fig. 4.10a shows a DEC specimen tested beyond the initiation point at room temperature, where failure is associated with the successive coalescence of holes to the blunted crack tip. The fracture surface of the same specimen shows the coalescence of large holes initiated from around the larger inclusions (Fig. 4.10b).

At lower temperatures however, hole growth in the high strain field ahead of the crack is limited by the interventiuon of cleavage cracking and failure. The damaged area ahead of the crack in a DEC specimen tested at -40°C is shown in Fig. 4.11a and illustrates cleavage microcracks in the ligaments/

between holes. The fracture surface of a similar specimen is shown in Fig. 4.11b and clearly shows the presence of cleavage facets cutting through holes. Also at this temperature the size of holes is smaller than those in specimens tested at room temperature indicating that the hole growth has been limited by the intervention of cleavage cracks. This behaviour may be explained in terms of the critical levels of strain and stress required to initiate failure. As the temperature is lowered, the increase in yield stress necessitates the attainment of a higher level of local tensile stress to develop the critical strain required for hole coalescence. This level of stress may exceed the critical cleavage stress on a local scale and thus initiate cleavage microcracks between holes. Thus the microscopic initiation of crack extension is by a mixed model mechanism resulting in a smaller δ_i than that achieved on the upper shelf. It has to be noted that the two dimensional idealization of ductile fracture in which the onset of failure is defined as the coalescence of the first fully grown hole to the blunted crack tip, is not appropriate in the transition region. Instead a mixture of ductile and cleavage damage is responsible for the extension of the crack. With further decrease in temperature the stress state ahead of the crack is such that cleavage cracks become involved in the initiation of crack extension at an earlier stage of the hole growth process which results in a further decrease of $'\delta_i$.

At temperatures less than -80°C fracture initiation and propagation occurs by the cleavage mechanism leading to immediate failure. The onset of catastropic crack propagation requires some yielding ahead of the crack to nucleate cleavage cracks from dislocation arrays and around stress concentrating second phase particles. Some voids may initiate in discrete locations in front of the crack, due to local variation in the inclusion content. Fig. 4.12 shows a narrow ductile band of less than 10 μm wide ahead/

of the fatigue pre-crack in a DEC specimen tested at -196°C. However these bands appear to have no effect on the macroscopic crack propagation by the cleavage mechanism.

The δ_i temperature transition for the SECT geometry can also be explained in the context of cleavage involvement in the failure initiation process. The precise mechanism of ductile crack extension in the SECT geometry on the upper shelf is not fully understood. Metallographic observations of crack profile indicate that crack blunting occurs with two vertices (Fig. 4.13) as opposed to the smoothly curved crack tip associated with DEC specimen as shown in Fig. 4.10a. It appears that in the SECT geometry, deformation takes place by alternate sliding along the shear bands at approximately 45° as modelled by Pelloux[30] (see Section 1.6.1). Fig. 4.14 shows the damaged crack profile of a SECT specimen tested at room temperature (on the upper shelf). It can be seen that crack propagation occurs directly ahead of the crack in the crack plane, and not in the direction of shear bands. The fracture surface of a similar specimen is shown in Fig. 4.15. This figure shows that regions of small voids are linked together by a shear mechanism. These voids are almost one order of magnitude smaller than those observed in DEC test pieces, suggesting that the void initiation, growth and coalescence mechanism observed in the DEC geometry is not the relevant mechanism associated with the ductile failure process in the SECT geometry. This feature has also been observed for a high strength steel[9] and a stainless steel[31]. To evaluate this behaviour, numerical analysis was carried out to determine the flow field and the states of stress and strain ahead of a crack in the SECT geometry. The results of this analysis are reported in Section 4.7.

A comparison between the δ_i versus temperature curves for the DEC and SECT geometries (Fig. 4.3) shows that δ_i is dependent on the level of constraint for the upper shelf region and the transition range. This dependence decreases as the temperature decreases and on the lower shelf the two curves are almost coincident. Similar behaviour is observed for J_i as shown in Fig. 4.7. As noted earlier the lowest level of triaxiality associated with plane strain condition is developed in SECT geometry. A study of the failure locus of the material (Section 3.6) indicates that at low triaxialities large effective plastic strains are required for initiation of ductile failure, and thus a large value of δ_i is expected. On the other hand in the deep DEC geometry plasticity is fully contained in the ligament and the full constraint of Prandtl slip-line field is developed. This high level of triaxiality requires little plastic strain for ductile failure initiation and is thus associated with a small δ_i. It was shown in Section 3.6 that the failure locus of the material is independent of temperature. Therefore the progressive reduction in the effect of triaxiality on δ_i may be attributed to the increasing involvement of cleavage in the fracture process which lessens the influence of factors controlling the operation of a ductile mechanism.

Results presented in Fig. 4.3 indicate that a change in triaxiality ($\sigma_m/\bar{\sigma}$) from 2.4 to 0.57 causes a maximum increase in δ_i, measured on the upper shelf, by a factor of 1.8. For the same constraint variation, factors of 4 and 10 have been found for A533B pressure vessel steel[15] and HY80 steel[9] respectively. These observations indicate that the effect of triaxiality on the fracture toughness parameters δ_i and J_i, is material dependent.

The effect of constraint on the elastic-plastic fracture toughness parameters has been investigated elsewhere on test pieces loaded in essentially bending configurations. It has been shown[32,33] that, in bending, constraint is relaxed by a reduction in both specimen thickness and crack length-to-width ratio ($^a/W$). Sumpter[34] obtained an increase in δ_i in a high strength welded steel when constraint was relaxed by decreasing the $^a/W$ ratio and Chipperfield et al[35] observed the same behaviour by changing the specimen size. You[36] investigated the effect of $^a/W$ on low alloy high strength steels with different strength levels and found that a change in $^a/W$ from 0.5 to 0.1 results in an increase in δ_i by a factor of 2.5 to 3 for all the materials investigated. The effect of constraint on fracture toughness has been observed by other workers[37-79] where fracture toughness was characterized using δ_m (maximum load COD), which has been recognised to be dependent on both geometry and testing configuration (see Section 1.6.3). The present experimental results however demonstrate that even δ_i (or J_i) cannot be considered as a unique material parameter in plane strain.

Results in Figs. 4.3 and 4.7 show that the ductile/cleavage transition temperature is altered by a considerable amount (about 60°C) as a result of the change in constraint. Sumpter[34] found a similar effect with a decrease in ($^a/W$) from 0.3 to 0.1 in a three-point band test of a high strength steel. Landes and Begley[40] observed an apparent increase in J_{IC} value with reducing specimen thickness for cast steel in the transition range. They attributed this effect to the scatter in the results for thin specimens. It was argued that a thick specimen samples more material than a thinner one, therefore local regions of low toughness control the behaviour of the large specimens whereas in the small specimen a high or a low toughness region may be sampled which results in a high degree of scatter.

Pisarski[41] by testing a homogeneous material and using a test procedure which ensured the uniform sampling of material, still found an increase in J_i with decreasing specimen thickness. Similar behaviour was obtained by Dawes[32] and Chell and Gates[37] by varying ($^a/W$) while thickness was kept constant.

It has to be noted that size restrictions for J_{IC} testing requires that the ligament should exceed 25 J/σ_y. At -100°C both the DEC and SECT geometries tested here meet this requirement (See Fig. 4.7) and yet J_i for SECT is higher than that for DEC. Ritchie[42] has proposed that the observed J_i variation with specimen configuration may be explained by the differing size requirements for J dominance for the various test piece geometries in which the levels of triaxiality (constraint) vary widely. Finite element calculations of McMeeking and Parks[43] estimated the size requirement for single-parameter J characterization in terms of the ligament dimension, L. It was found that, while for highly constrained geometries a 25 J/σ_y size limitation is appropriate, a more stringent limitation of $L>200\ J/\sigma_y$ should be applied to low constraint CCP and SECT specimens. Experimental results of Markstrom[10] on wide plate SECT and 5:1 DEC specimens show that $J_i = J_{IC}$ and is independent of configuration when these size requirements are satisfied. To obey the size restriction for the determination of J_{IC} in the present material on the upper shelf it is necessary to test DEC and SECT specimens with 165 and 400mm widths respectively, and a corresponding specimen thickness to maintain plane strain conditions. There are sections in engineering structures where constraint is low, with dimensions and flow fields similar to that of SECT geometry. In these situations, the size limitation imposes a practical limitation in characterizing the fracture behaviour. On the other hand δ_i or J_{IC} values derived from highly constrained geometries may introduce over-conservatism in assessing a tolerable defect size.

4.7 Numerical analysis

4.7.1 Procedure

To investigate the crack growth behaviour in SECT specimens, the distribution of stresses and strains around the crack tip was numerically evaluated using finite element analysis. The MARC finite element program, modified by Rice and Co-workers at Brown University (e.g. Ref. 44), was used. This program has a finite strain capability which enables an incremental determination of plane strain or axisymmetric elastic-plastic solutions, using the Prandtl-Reuss flow rule for an incompressible plastic solid. For power hardening cases the following power law stress-strain relationship was used:

$$\left(\frac{\bar{\sigma}}{\sigma_y}\right)^{\frac{1}{N}} - \left(\frac{\bar{\sigma}}{\sigma_y}\right) = \frac{3G\bar{e}_p}{\sigma_y} \qquad \bar{\sigma} \geq \sigma_y \tag{4.14}$$

where σ_y is the uniaxial yield stress, $\bar{\sigma}$ the effective stress, G the elastic shear modulus and N is hardening index. For the material under investigation an appropriate value of N is 0.2.

The finite element mesh contains 425 nodes and 384 plane strain isoparametric quadrilateral elements. The undeformed mesh representing one half of a SECT specimen and the detail of the near tip mesh is shown in Fig. 4.16. The mesh had an $a/W = 0.5$ and the ratio of undeformed notch width, b_o to ligament L, was $b_o/L = 2\times10^{-2}$. The analysis was performed for non-hardening (N=0) and 0.2 power hardening cases. A point force was applied at the centre of the ligament at an appropriate node on the top surface. An elastic step loading was carried out until a load just sufficient/

to initiate plastic flow in the first element was achieved. This load level was designated 100% of the elastic load regime. By means of further increments of load yielding was then allowed to spread gradually to other elements. Loading was stopped when a crack opening displacement δ equal to experimentally determined δ_i was achieved. This required a load level of 820% for the 0.2 power hardening material and 500% for the non-hardening material. The crack opening displacement δ was taken as the distance between the nodes that, in the undeformed configuration lay at the intersection of the straight flank and the semi-circular tip of the original notch. The nodes ahead of the tip on the crack plane were restrained to remain on that plane, as illustrated in Fig. 4.16.

4.7.2 Results and discussion

In Fig. 4.17 the distribution of maximum tensile stress σ_1, for the non-hardening case is plotted against the distance x from the crack tip for the material points ahead of the crack tip. The stress is normalised by the yield stress to give the non-dimensional σ_1/σ_y which is a measure of triaxiality if the Von Mises yield criterion is assumed. The position x is normalized by the current crack tip opening δ. It has been shown[43] that the original crack tip geometry does not influence the near tip stress and deformation fields after opening of the crack to about twice the original notch width. Fig. 4.17 has been plotted for an opening equal to the experimentally determined δ_i, which is large compared to the notch width. This gives a ligament to crack tip opening ratio of $L/\delta = 17$.

McMeeking and Parks[43] calculated the stress and strain fields for the Centre Cracked Panel (CCP) which according to slip-line analysis has a similar/

flow field to the SECT geometry. They used a finite element mesh with $b_o/L = 2\times10^{-4}$ so that much smaller openings in terms of ligament could be analysed. The solution used in the present work was considered desirable in order to extend their analysis to obtain crack openings compatible with experimental results. The McMeeking and Parks results for $L/\delta = 1182$, $L/\delta = 143$ and the McMeeking[25] finite element results for Small Scale Yielding (SSY) are also shown in Fig. 4.17.

It can be seen in Fig. 4.17 that where δ is small compared to ligament dimension, there is a reasonable agreement with SSY. Since δ and J are proportionally related to each other, it is then envisaged that in these situations J is independent of specimen geometry. However at larger deformations where conditions of general yielding are achieved, triaxiality deviates sharply from SSY, which implies that the crack tip field is considerably far from dominance by the HRR singular field. Thus δ_i (or J_i) can not be considered as a single geometry-independent fracture characterizing parameter.

It may be argued that the decrease of triaxiality ahead of the crack, shown in Fig. 4.17, could be the result of the non hardening idealization. However the same trend is shown in Fig. 4.18 for a material with the strain hardening exponent of N = 0.2. Again the triaxiality for large scale yielding (which is the case for $L/\delta = 17$) lies considerably below the SSY curve.

Fig. 4.19 shows the variation of effective plastic strain $\bar{e}_p$ (Section 3.6), for N = 0.2 on the crack plane ($\theta = 0^o$) and at $\theta = 45^o$ with distance ahead/

of the crack tip. It is apparent that for the fully yielded condition, crack tip plastic strain in both directions is greater than for contained yielding. Also it is evident that larger plastic strains occur on the macroscopic slip lines rather than on the crack plane. Rapid decrease of triaxiality and effective plastic strain ahead of the crack and amplification of plastic strain at 45 degrees suggest that the crack may extend in the 45 degree direction, in contrast to the more highly constrained DEC geometry. However experimental results from the present work and other investigations[9,31] indicate that, although large scale void growth has not been observed ahead of the extending crack, crack extension is always straight ahead of the crack tip. An analysis based on the numerical results was carried out to examine the failure condition ahead of the crack. The contours of distribution of plastic strain $\bar{\varepsilon}p$ and triaxiality $\sigma_m/\bar{\sigma}$ are shown in Fig. 4.20 and 4.21 for the non-hardening material and in Figs. 4.22 to 4.23 for the 0.2 power hardening material, at a crack opening displacement equal to the experimental δ_i. By superimposing these contours, it is possible to determine the values of triaxiality and effective plastic strain in each element around the crack tip and compare them to the ductile failure locus of the material (Section 3.6). The analysis indicates that for N = 0 only those elements which lie at 45° to the crack plane, and close to the crack tip, meet the failure criterion over and beyond the characteristic distance (Fig. 2.24) suggesting that crack extension may occur along the shear bands, consistent with the slip-line prediction. For N = 0.2, however, the analysis shows that the failure criterion is satisfied at a distance X = 0.3 mm on the crack plane, ahead of the crack, Fig. 4.25. Although this distance is only a fraction of the crack opening (X/δ = 0.6) compared to X/δ = 2 for contained yielding, it is in excess of the characteristic distance of the material, taken as 0.2 mm (Section 3). This suggests that failure may occur/

straight ahead of the crack as observed experimentally. Furthermore the confinement of the failure zone to the crack tip implies that the conditions required for void growth are not satisfied at greater distances from the crack tip. This is confirmed by the experimental observations of the crack profile e.g. Fig. 4.14 which shows that although the crack extends directly ahead no significant void growth is evident in the region ahead of the crack tip.

The crack tip behaviour may be explained to some extent by the ''unzipping model'' proposed by Liu[45], based on the alternating shear rupture mechanism. The characteristic crack tip deformation incorporated in the unzipping model is shown in Fig. 4.26. As the applied stress on a cracked solid is increased, the decohesion processes take place along slip lines a_1, b_2, b_1, c_2, c_1 and d_2 successively (Fig. 4.26) while the slabs between the neighbouring slip lines move like the teeth of a zipper during the unzipping process, causing crack tip blunting. The morphology of the crack tip and metallurgical observations mentioned above, suggest that the crack extension may also be modelled by the unzipping process. However this model is rather ambiguous in describing the initiation of crack growth and the critical events leading to initiation such as attainment of a critical COD as described by a resistance curve. Also the model does not indicate when a fracture process will intervene in the alternating sliding deformation model. Further work is required to study the exact mechanism of ductile crack extension for the SECT geometry.

4.8 Summary of section 4

The work presented in this section focussed primarily on the effect of constraint on the elastic-plastic fracture parameters. Two different geometries, representing two extreme cases of plane strain flow fields were studied. It was found that the upper shelf δ_i (or J_i) for the SECT geometry is 1.8 times that for the DEC geometry. On the upper shelf the crack tip in the DEC geometry blunts to a smoothly curved shape and crack extension is by a void growth and coalescence mechanism. In the SECT geometry crack tip blunting occurs with two vertices by a shear mechanism and the advancing crack tip maintains this morphology.

In the temperature transition region, the effect of constraint on δ_i(or J_i) is reduced. Metallurgical investigations indicate that the hole growth and coalescence mechanism in this region is interrupted by cleavage, resulting in a mixed mode crack growth initiation and extension process. On the lower shelf the cleavage mechanism is dominant.

The results of numerical analysis showed that for the work hardening material investigated, a failure zone (high triaxiality and/or plastic strain) is present at the tip of the crack in the SECT geometry. Although this failure zone is much smaller than that for SSY condition, it is large enough to initiate crack extension on the crack plane rather than in the direction of maximum shear strain.

4.9 REFERENCES

1. ''Standard Method of Test for Plane-Strain Fracture Toughness of Metallic Materials.'' ASTM Designation E399-74, Part 10, ASTM Annual Standards.

2. Wells, A.A., Symp. on Crack Propagation, College of Aeronautics, Paper B4, Cranfield, 1961.

3. Rice, J.R., J.Appl. Mech. Trans., ASME, Vol. 35, pp. 379-386, 1968.

4. Begley, J.A. and Landes, J.D., ASTM, Special Technical Publication, STP 514, Part II, pp. 1-23, 1972.

5. Green, G., Smith, R.F. and Knott, J.F. in Proceedings Conference on Mechanics and Mechanisms of Crack Growth, Churchill College, Cambridge, England, Paper 5, 1973.

6. de Castro, P.M.S.T., Spurrier, J. and Hancock, P., Fracture Mechanics, ASTM, STP 677, C.W. Smith, Ed., pp. 486-497, 1979.

7. McClintock, F.A., Trans. ASME, J. Appl. Mech., Vol. 35, pp. 363-371, 1968.

8. Rice, J.R. and Tracey, D.M., J. Mech. Phys. Solids, Vol. 17, pp. 201-217, 1969.

9. Hancock, J.W. and Cowling M.J., Metal Science, Vol. 14, pp. 293-304, August-September 1980.

10. Markstrom, K., Engineering Fracture Mechanics, Vol. 9, pp. 637-646, 1977.

11. Neimark, J.E., J. Appl. Mech., Vol. 35, pp. 111-116, 1968.

12. Hundy, B.B., Metallurgica, Vol. 49, p. 109, 1957.

13. Cowling M.J. and Hancock, J.W., Ch. 22, Fracture Mechanics in Engineering Practice, Ed. P. Stanley, Applied Science Publishers, 1977.

14. McClintock, F.A., Plasticity Aspects of Fracture, Fracture, Ed. H. Liebowitz, Vol. 3, Academic Press, New York, 1971.

15. Cowling, M.J. and Aboutorabi, A.A., Paper 18, Integrity of Offshore Structures, Ed. D. Faulkner et al, Applied Science Publishers, 1981.

16. Rice, J.R., Paris, P.C., and Merkle, J.G., ASTM, Special Technical Publication, STP 536, p. 231, 1973.

17. Sumpter, J.D.G. and Turner C.E., ASTM, Special Technical Publication, STP 601, pp. 3-19, 1976.

18. Turner, C.E., Fracture Mechanics, ASTM, STP 677, Ed. C.W. Smith, pp. 614-628, 1979.

19. Ewing, D.J.F. and Hill, R.J., J. Mech. Phys. Solíds, Vol. 15, p. 115, 1967.

20. Tracey, D.M., Trans. ASME, J. Eng. Materials and Tech., Vol. 98, p. 146, 1976.

21. Turner, C.E., Post-Yield Fracture Mechanics, Ed. D.G.H. Latzko, Applied Science Publishers, London, 1979.

22. Ritchie, R.O., Knott, J.F. and Rice, J.R. J. Mech. Phys. Solids, Vol. 21, p. 395, 1973.

23. Ritchie, R.O., Server, W.L.K. and Wullaert, R.A., ICM 3, Vol. 3, Cambridge, England, pp. 489-500, 1979.

24. Green, A.P. and Hundy, B.B., J. Mech. Phys. Solids, Vol. 4, 1956.

25. McMeeking, R.M., J. Mech. Phys. Solids, Vol. 25, p. 357, 1977.

26. Rice, J.R. and Johnson, M.A., In elastic behaviour of solids, Ed. M.F. Kanninen, McGraw Hill, New York, p. 641, 1970.

27. Rice, J.R. and Tracey D.M., J. Mech. Phys. Solids, Vol. 17, pp. 201-217, 1969.

28. MacKenzie A.C., Hancock, J.W. and Brown D.K., Eng. Fracture Mech., Vol. 9, pp. 167-188, 1977.

29. Hancock, J.W., Brown, D.K., J. Mech. Phys. Solids, Vol. 31, No. 1, pp. 1-24, 1983.

30. Pelloux, R.M.N., Eng. Fracture Mech., Vol. 1, p. 697, 1970.

31. Cowling, M.J., unpublished results.

32. Dawes, M.G., ASTM, Special Technical Publication, STP 668, pp. 307-333, 1979.

33. Milne, I. and Chell, G.G., pp. 358-377 ibid.

34. Sumpter, J.D.G., Int. J. Pressure Vessels and Piping, Vol. 10, p. 169, 1982.

35. Chipperfield, C.g., Knott, J.F. and Smith, R.F., Proc. ICF3, Vol. 2, I233, 1973.

36. You, C.P., Ph.D. Thesis, Churchill College, Cambridge, England, 1984.

37. Chell, G.G. and Gates R.S., Int. J. Fracture, Vol. 14, p. 233, 1978.

38. Milne, I. and Worthington, P.J., Mat. Sci. Eng., Vol. 26, p. 185, 1976.

39. Chell, G.G. and Davidson, A., Mat. Sci. Eng., Vol. 24, p. 45, 1976.

40. Landes, J.D. and Begley, J.A., ASTM Special Technical Publication, STP 632, pp. 57-81, 1977.

41. Pisarski, H.G., Int. J. Fracture, Vol. 17, No. 4, pp. 427-444, 1981.

42. Ritchie, R.O., Trans. ASME, J. Eng. Mats. Tech., Vol. 105, pp. 1-7, 1983.

43. McMeeking, R.M. and Parks, D., ASTM, Symp. on 'Elastic-plastic Fracture', Atlanta, U.S.A., 1977.

44. Rice, J.R. and Tracey, D.M., Numerical and Computer Methods in Structural Mechanics, Ed. S.J. Fenves, Academic Press, New York, 1973.

45. Liu, H.W., NASA Contract Report, NASA CR-2032, 1972.

Table 4.1 δ_i and J_i for DEC specimens tested at various temperatures

Test Temperature (^oC)	δ_i (mm)	J_i (KN/mm)	M ($\sigma_y \delta_i / J_i$)
140	0.370	0.265	0.50
20	0.325	0.241	0.48
-20	0.215	0.163	0.50
-40	0.159	0.126	0.51
-80	0.119	0.112	0.48
-100	0.073	0.07	0.49
-196	0.065	0.062	0.54

Table 4.2 Crack extension parameters for SECT specimens tested at various temperatures

Test Temperature (°C)	δ (mm)	Δa (mm)	δ_i (mm)	J (KN/mm)	Δa (mm)	J_i (KN/mm)	M $(\sigma_y \delta_i / J_i)$
140	1.030	0.81	0.520	0.480	0.525	0.352	0.530
	0.985	0.785		0.390	0.135		
	0.640	0.395		0.380	0.105		
	0.600	0.365					
20	1.200	1.140	0.580	0.53	0.850	0.355	0.588
	0.780	0.555		0.410	0.265		
	0.745	0.525		0.406	0.235		
	0.630	0.352					
-20	0.190	1.800					
	0.445	0.352		0.241	0.177	0.220	0.600
	0.358	0.210		0.228	0.035		
	0.636	0.758		0.322	0.583		

over/

Table 4.2 Cont.

Test Temperature (°C)	δ (mm)	Δa (mm)	δ_i (mm)	J (KN/mm)	Δa (mm)	J_i (KN/mm)	M $(\sigma_y \delta_i / J_i)$
-60	0.705	0.560	0.330	0.277	0.395	0.215	0.640
	0.584	0.430					
	0.450	0.300		0.238	0.135		
	0.432	0.255		0.226	0.090		
-110	0.307	0.434	0.150	0.146	0.359	0.095	0.750
	0.280	0.378		0.125	0.303		
	0.182	0.120		0.103	0.045		
-196	0.078	0.078		0.061		0.061	0.750

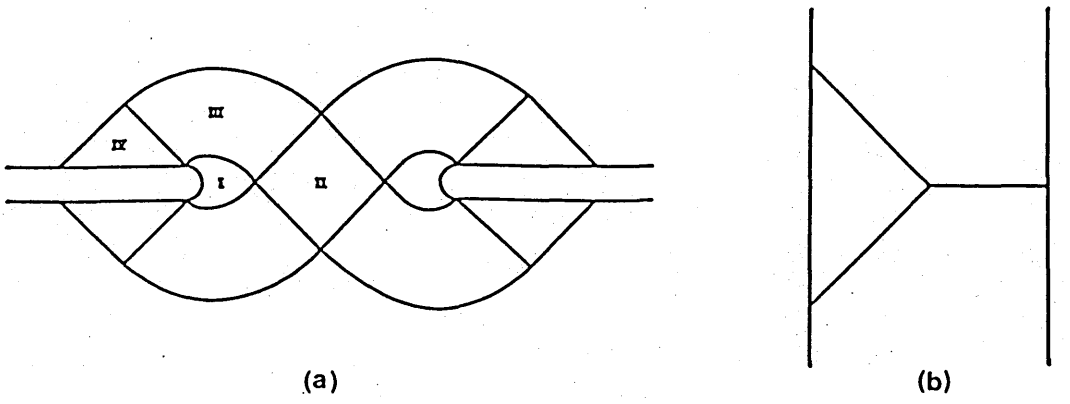

Fig. 4.1 Slip line fields for (a) deep DEC geometry and (b) SECT geometry.

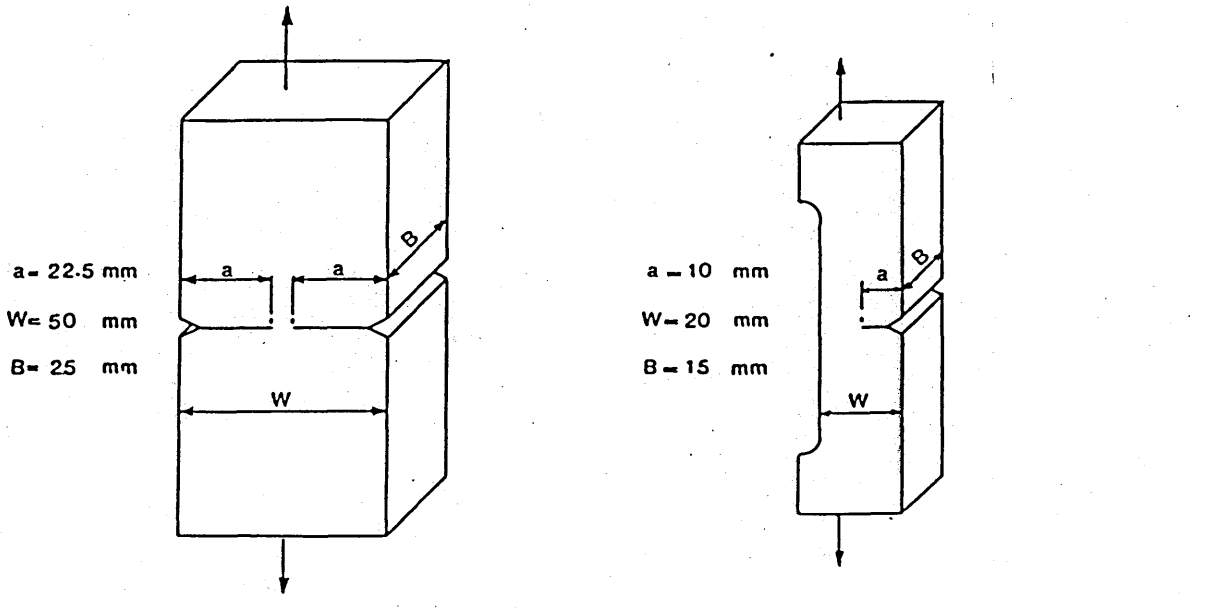

Fig. 4.2 DEC and SECT specimen geometries.

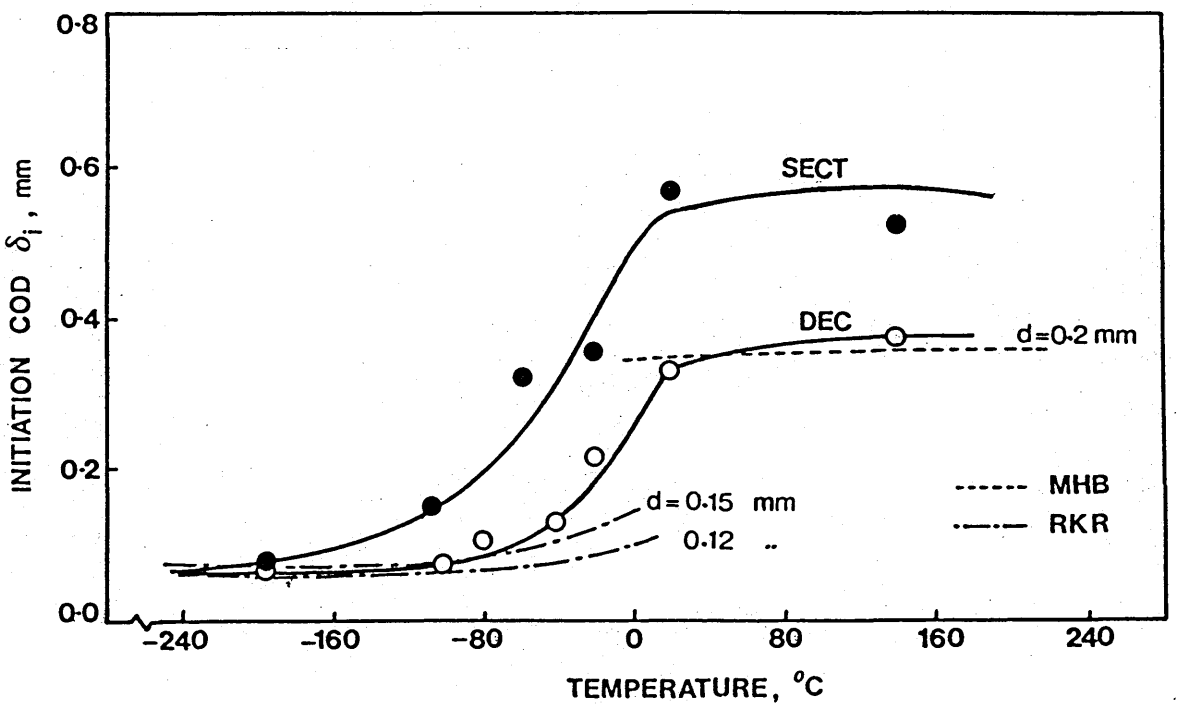

Fig. 4.3 COD at the onset of crack extension, δ_i, against temperature for DEC and SECT specimen geometries, showing the ductile-brittle transition. The prediction of upper and lower shelf fracture toughness values, using MHB[28] & RKR[22] models is shown.

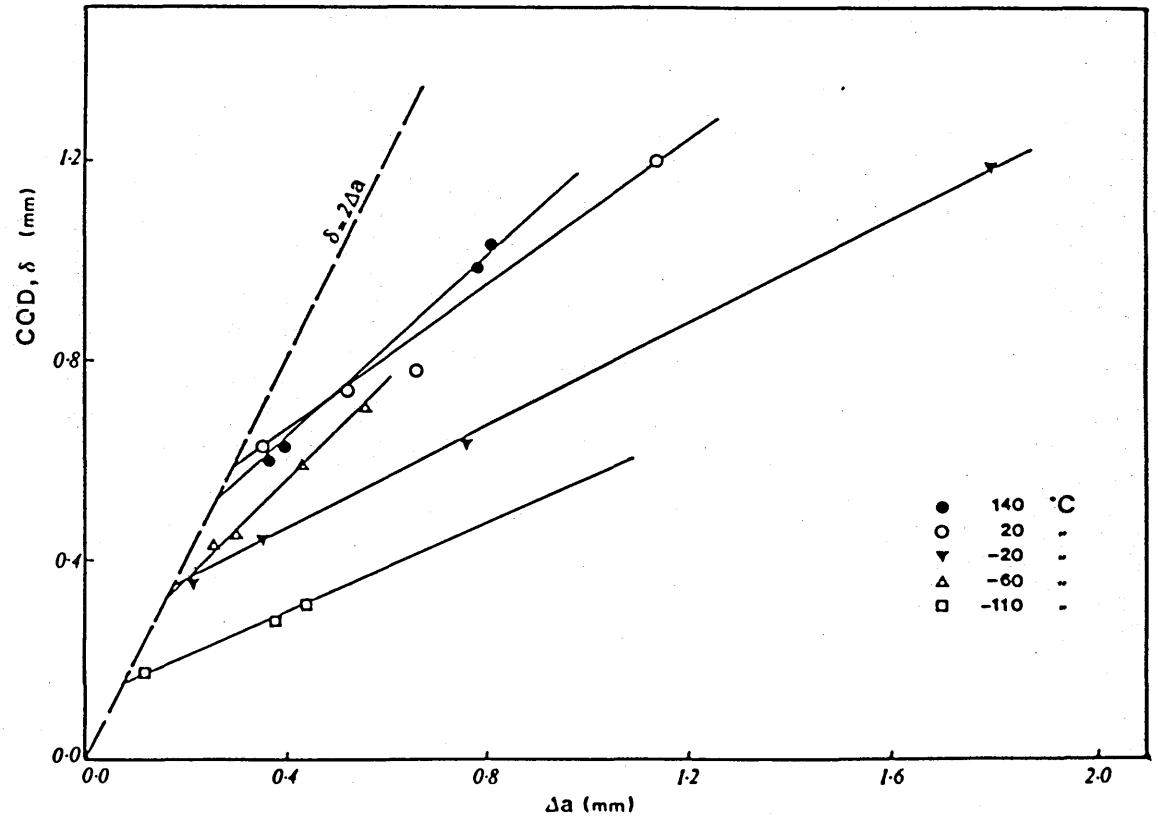

Fig. 4.4 COD R-curve for SECT test pieces at various temperatures

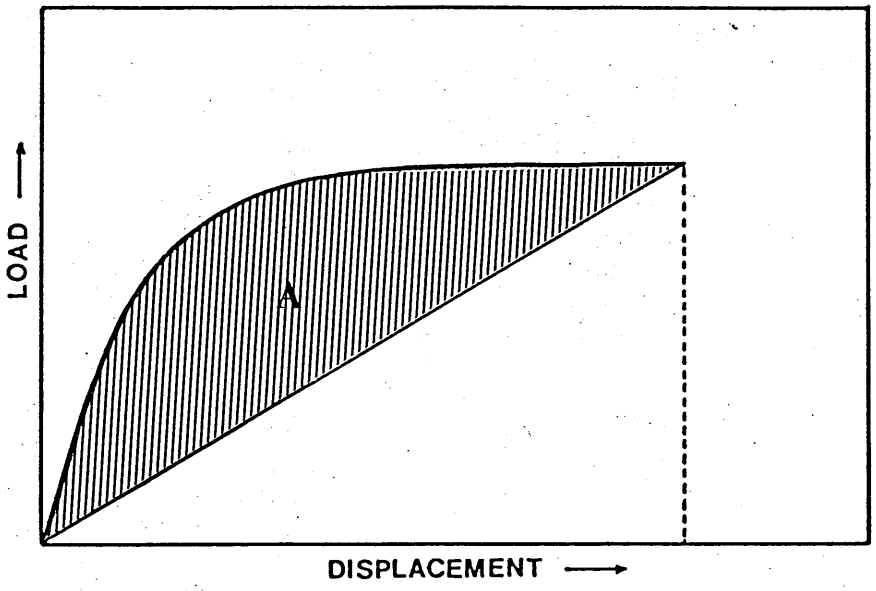

Fig. 4.5 Area under load-displacement curve used in Rice, Paris and Merkle[16] analysis for evaluation of J-integral associated with DEC geometry.

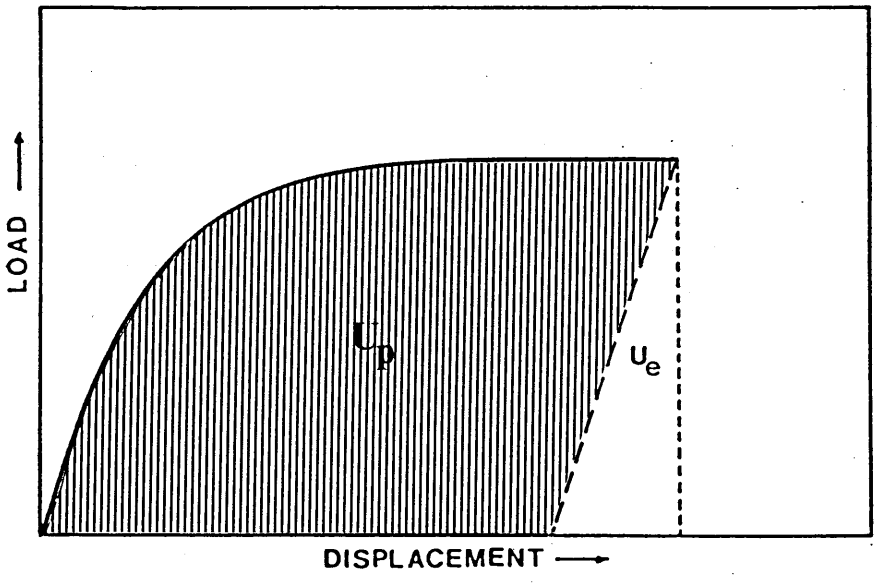

Fig. 4.6 Area under load-displacment curve used in Sumpter and Turner[17] analysis for evaluation of J-integral.

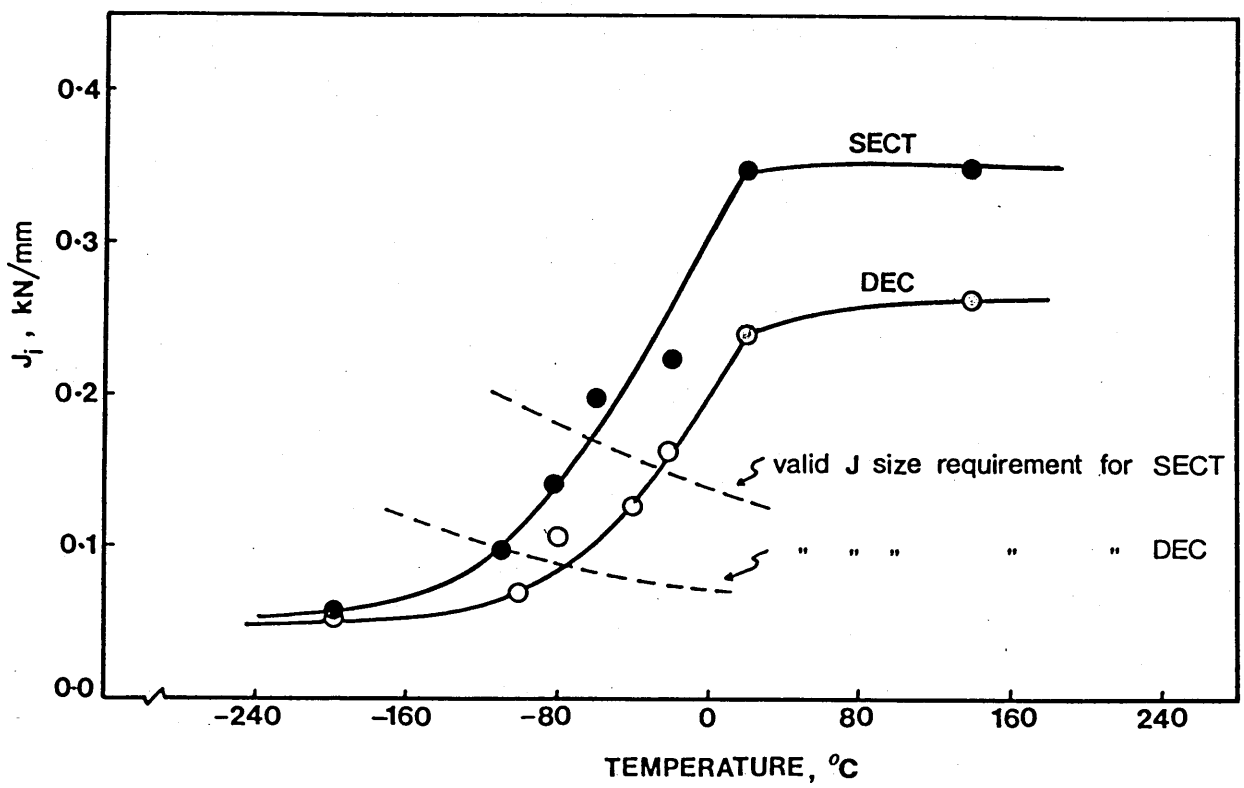

Fig. 4.7 Variation of initiation J as a function of temperature for DEC and SECT geometries, showing the ductile-brittle transition.

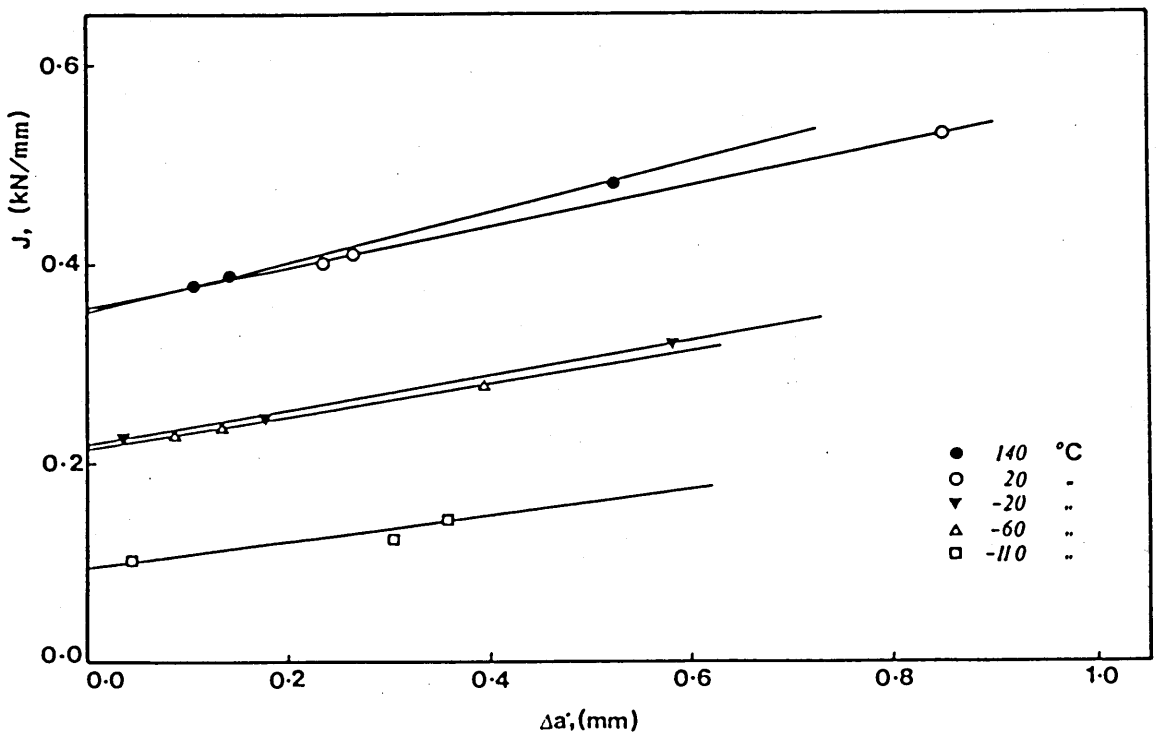

Fig. 4.8 J R-curve for SECT specimens at various temperatures

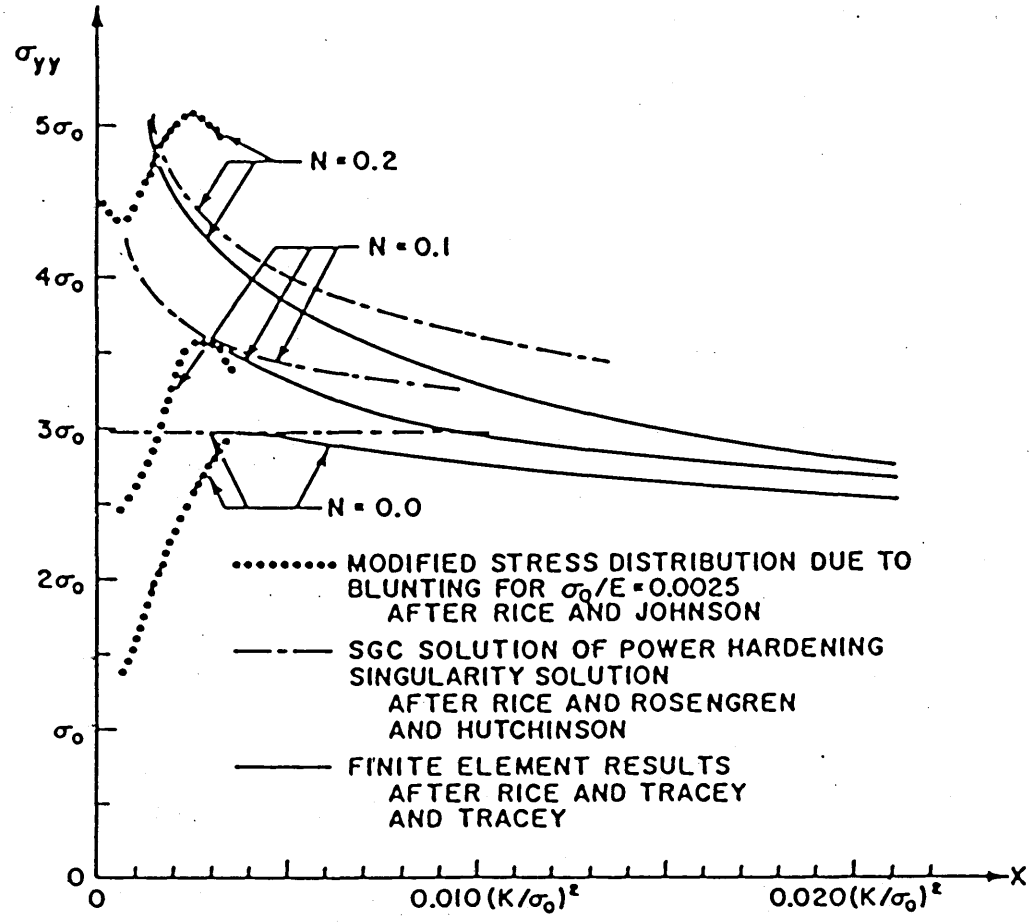

Fig. 4.9 Near tip distribution of normal stress ahead of an initially sharp crack in plane strain for small-scale yielding (Ref. 44).

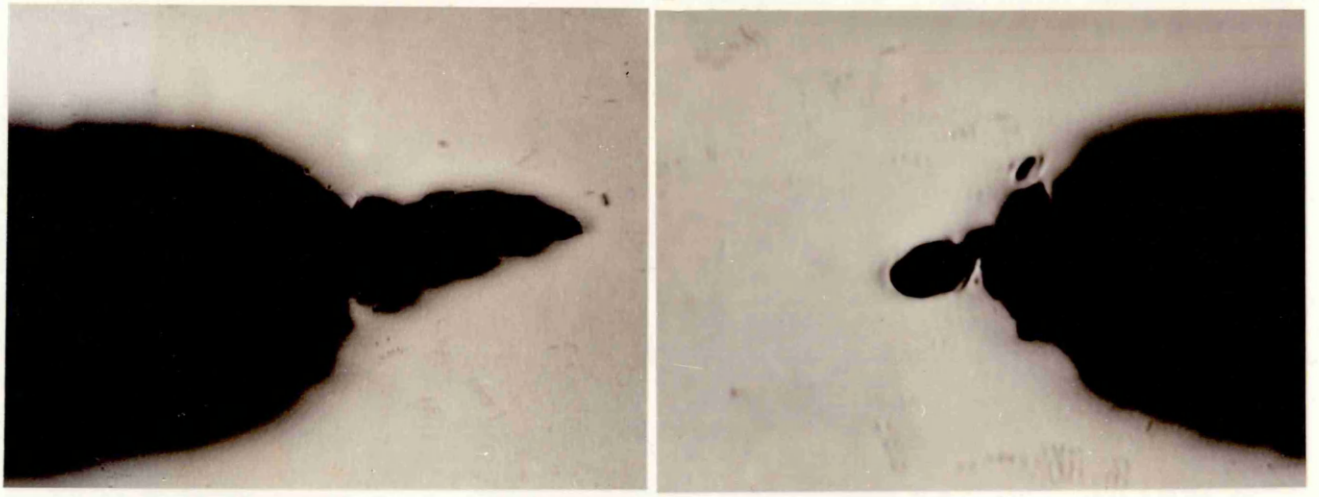

(a)

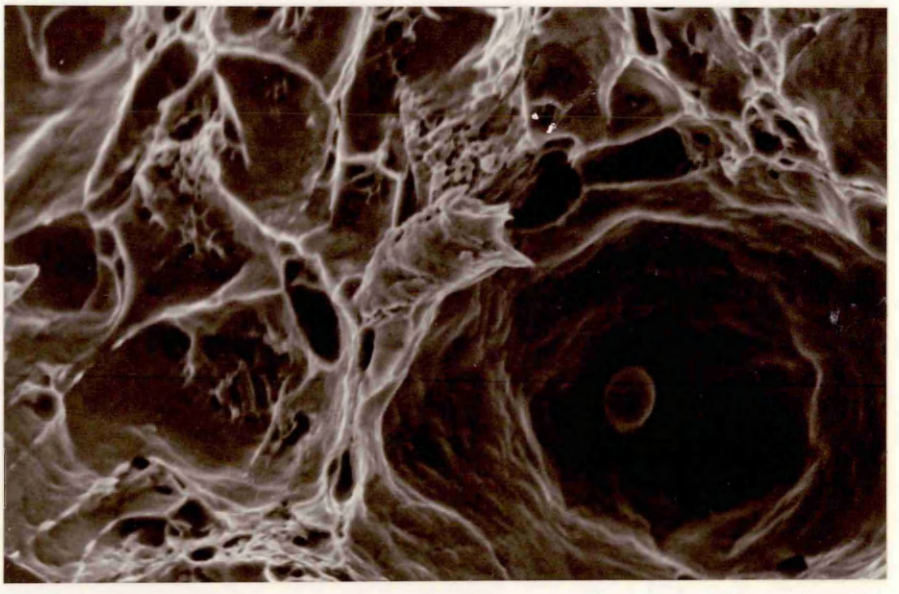

(b)

Fig. 4.10 (a) Crack profile for a DEC specimen tested at 20°C, showing that failure is associated with successive coalescence of holes to the blunted crack tip. (b) Fracture surface of the same specimen.

(a)

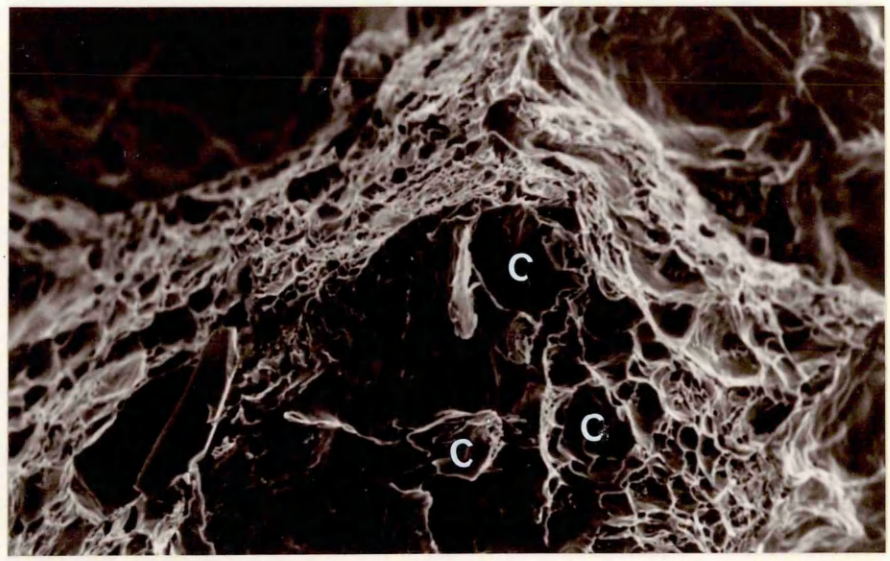

(b)

Fig. 4.11 (a) Damaged area ahead of the crack tip in a DEC specimen tested at -40°C, showing the cleavage microcracks between the holes. (b) Fracture surface of the same specimen showing that hole growth is interrupted by cleavage facets.

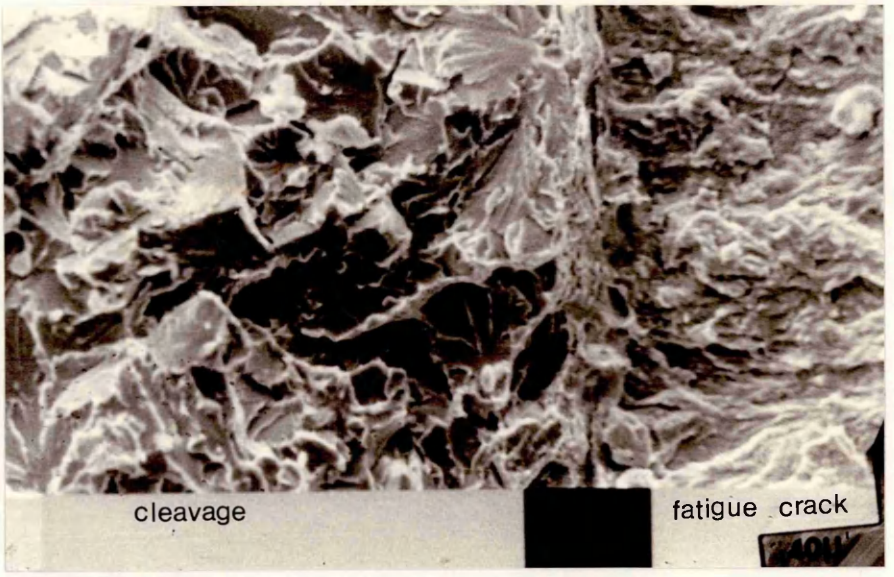

Fig. 4.12 Narrow ductile band ahead of the fatigue crack tip in a DEC specimen tested at -196°C.

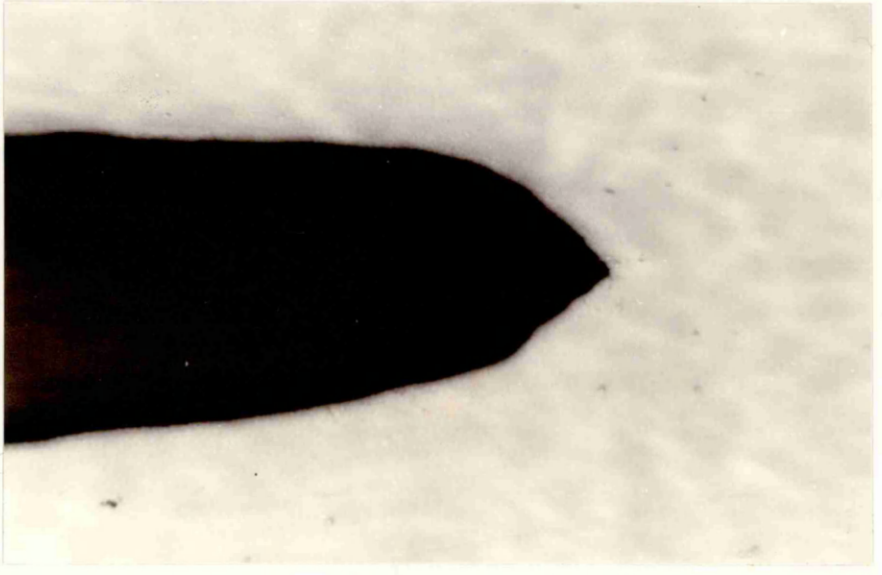

Fig. 4.13 Blunted crack tip in a SECT specimen tested at 20°C.

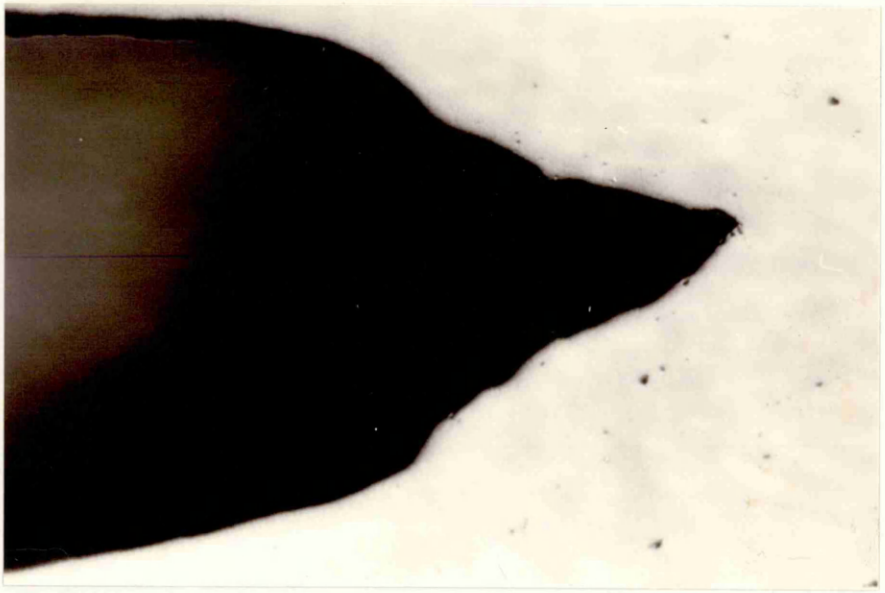

Fig. 4.14 Damaged area ahead of a SECT specimen tested at 20°C

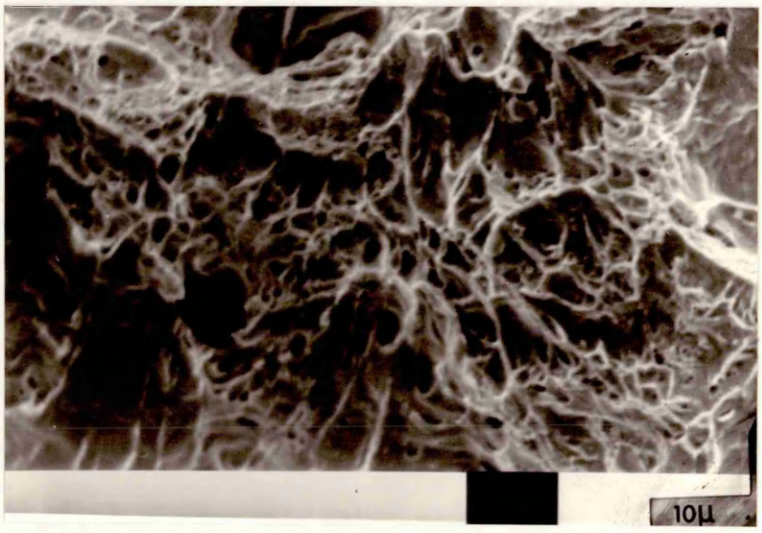

Fig. 4.15 Fracture surface of a SECT specimen tested at 20°C.

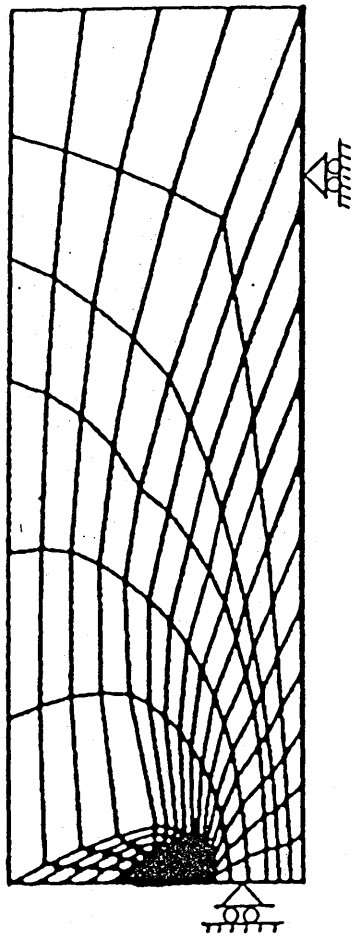

(a)

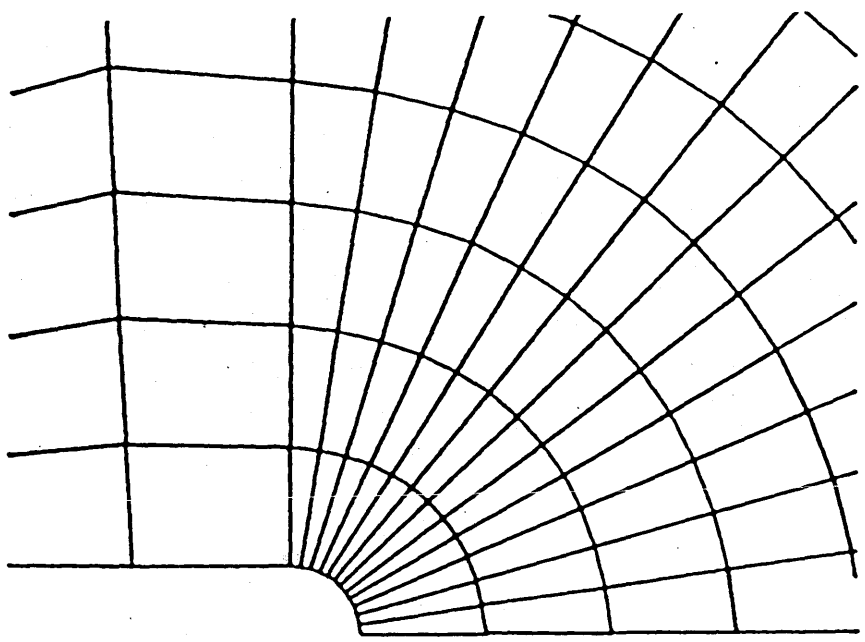

(b)

Fig. 4.16 (a) Two dimensional finite element mesh representing one half of a SECT specimen (b) Detail of near tip mesh.

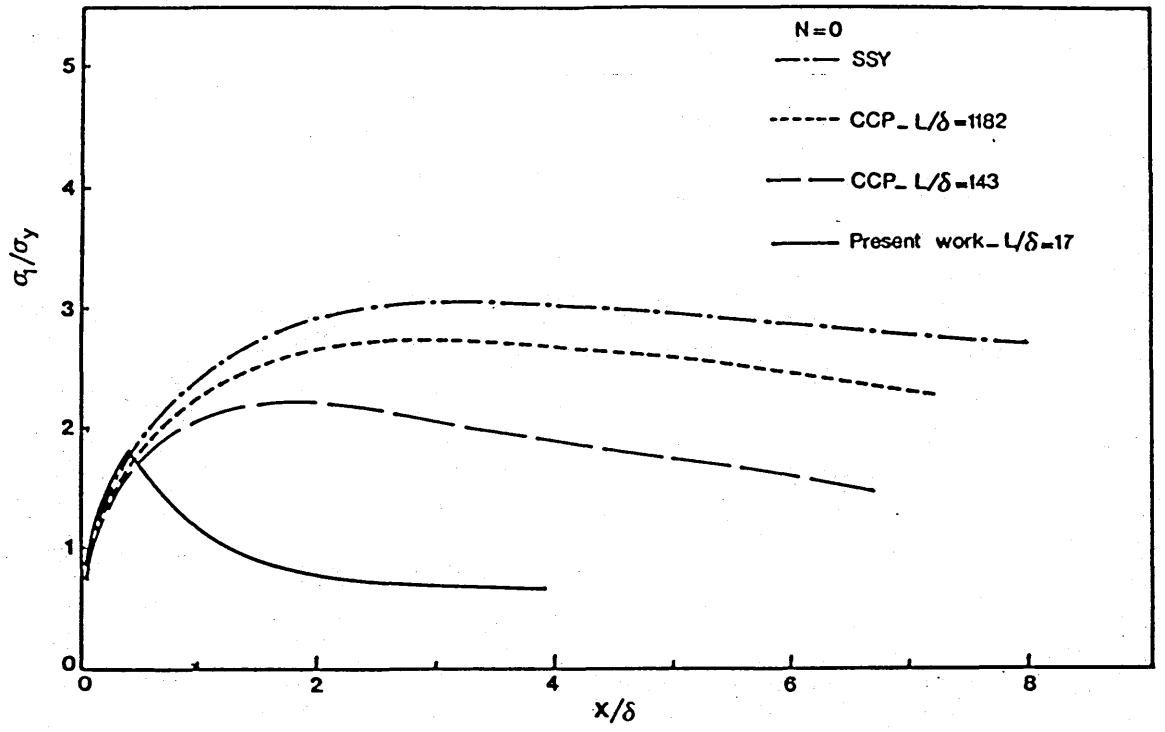

Fig. 4.17 Distribution of the maximum tensile stress ahead of the crack tip for the non-hardening material. The results of McMeeking[25] for SSY and McMeeking and Parks[43] for CCP geometry are also shown.

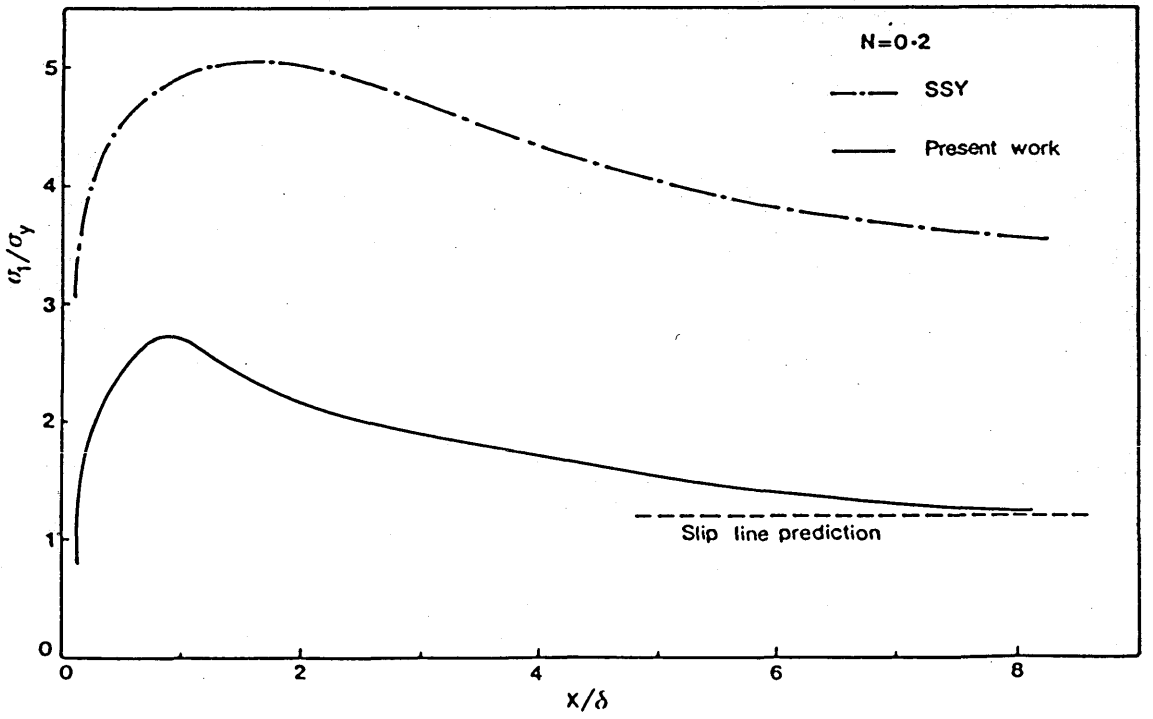

Fig. 4.18 Distribution of the maximum tensile stress ahead of the crack tip for the 0.2 power hardening material. The result of McMeeking[25] for SSY is also shown.

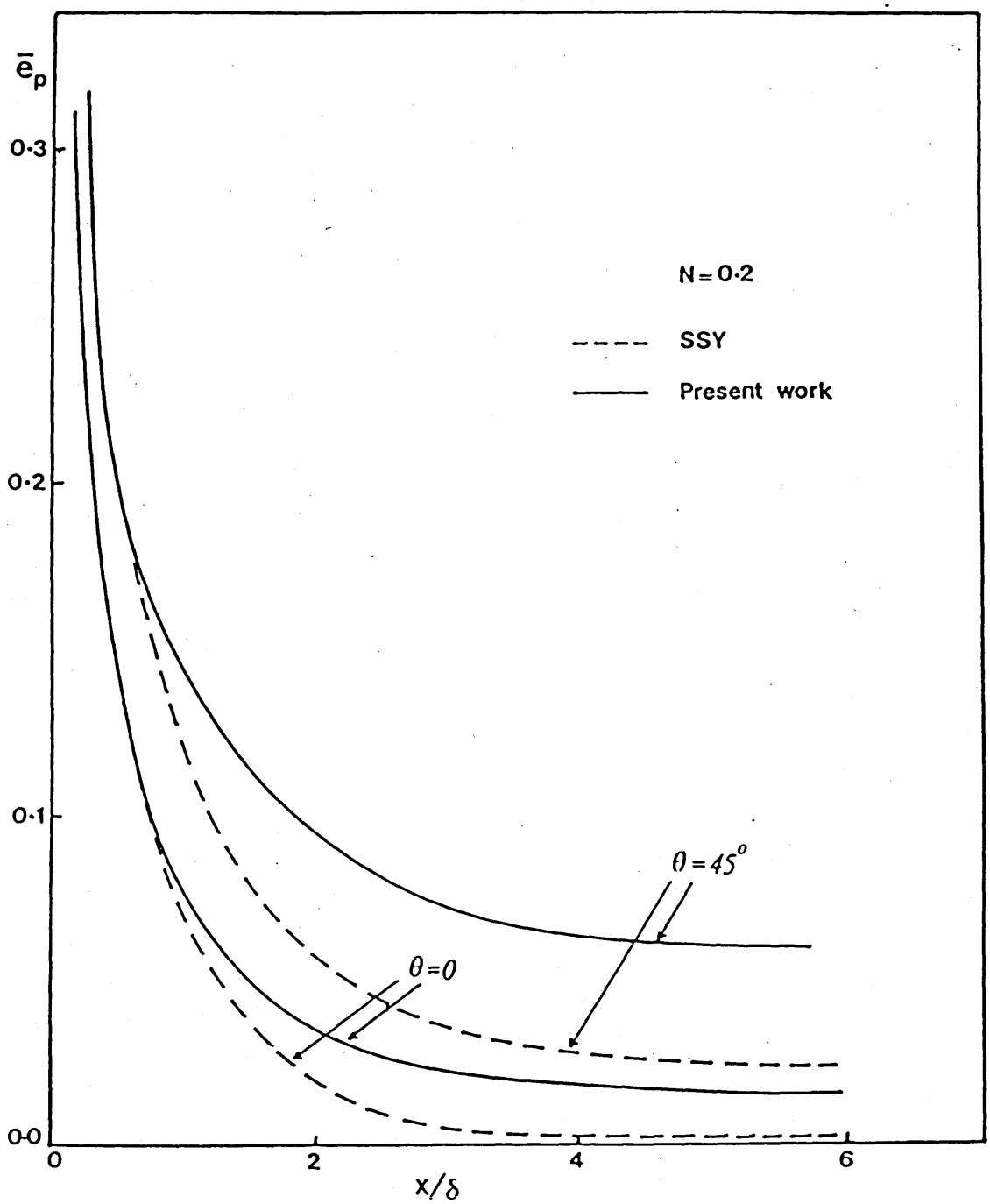

Fig. 4.19 Distribution of equivalent plastic strain ahead of the crack tip, on the crack plane and at 45° to the crack plane. The results of McMeeking[25] for SSY are also shown.

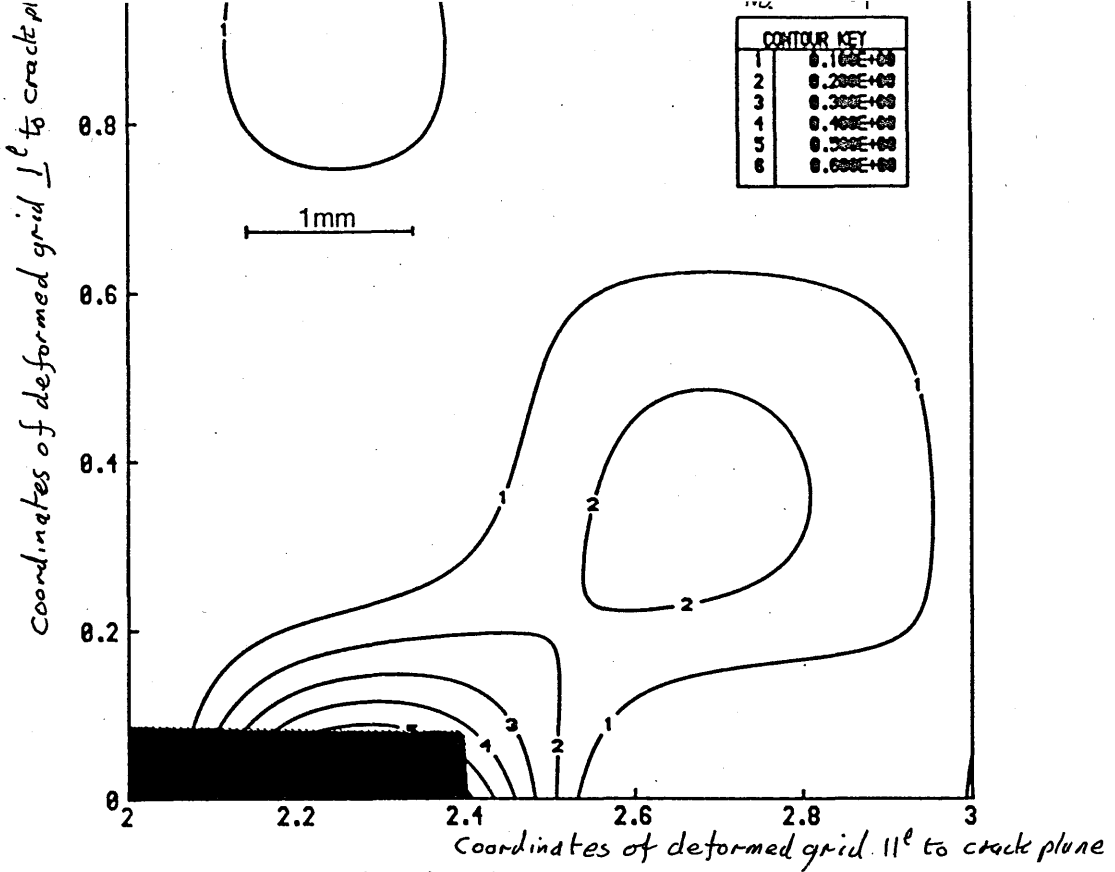

Fig. 4.20 Contours of distribution of effective plastic strain around the blunted crack tip in the non-hardening material.
(Crack tip shown in black)

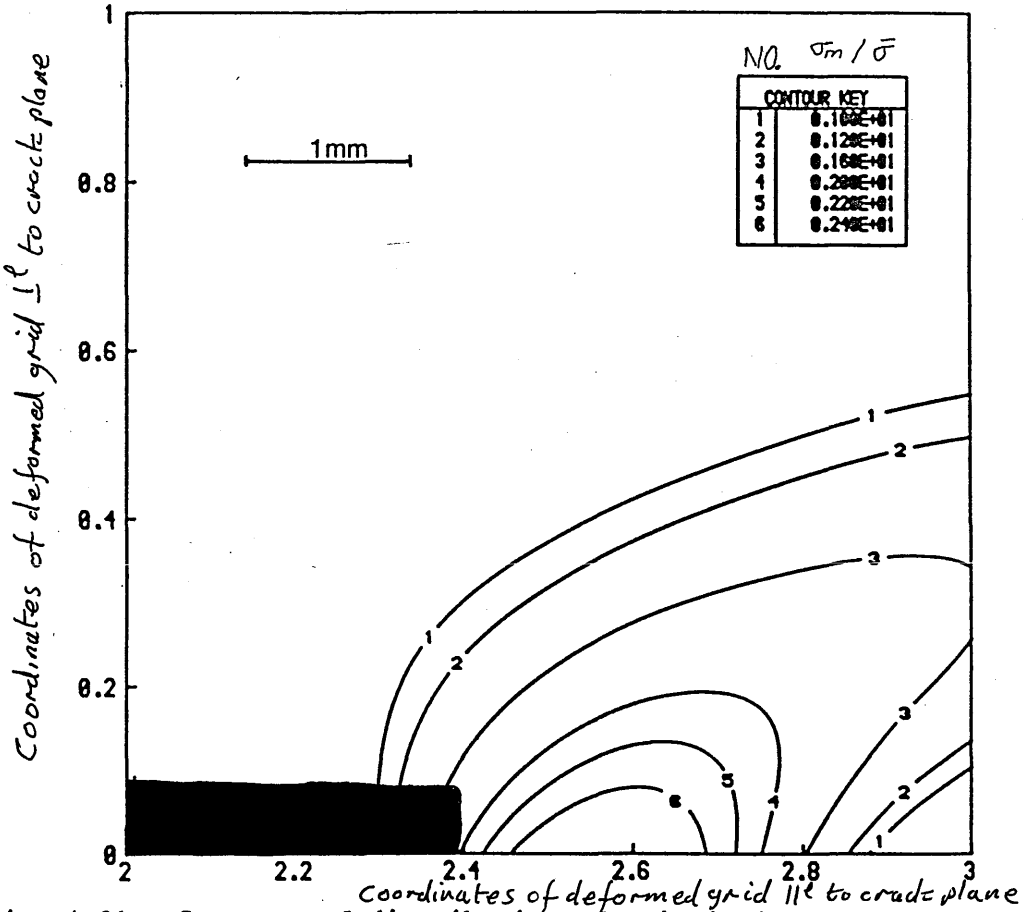

Fig. 4.21 Contours of distribution of triaxiality around the blunted crack tip in the non-hardening material.
(Crack tip shown in black)

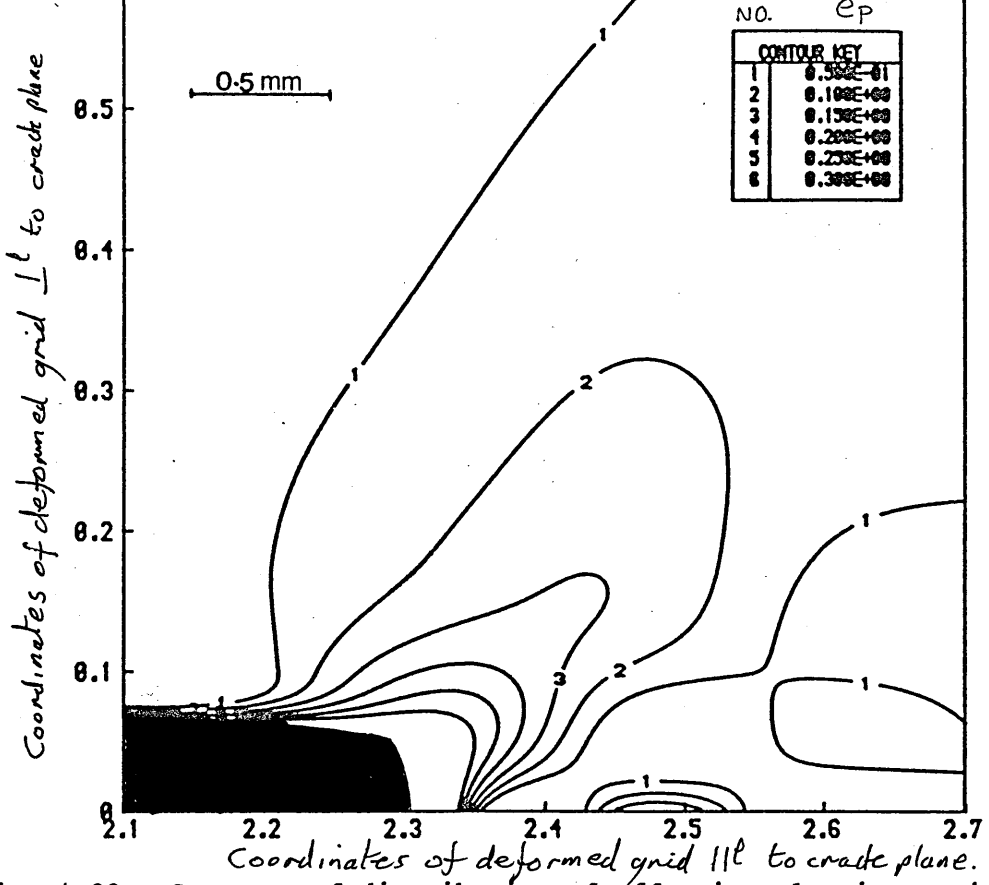

Fig. 4.22 Contours of distribution of effective plastic strain around the blunted crack tip in 0.2 power hardening material. (Crack tip shown in black)

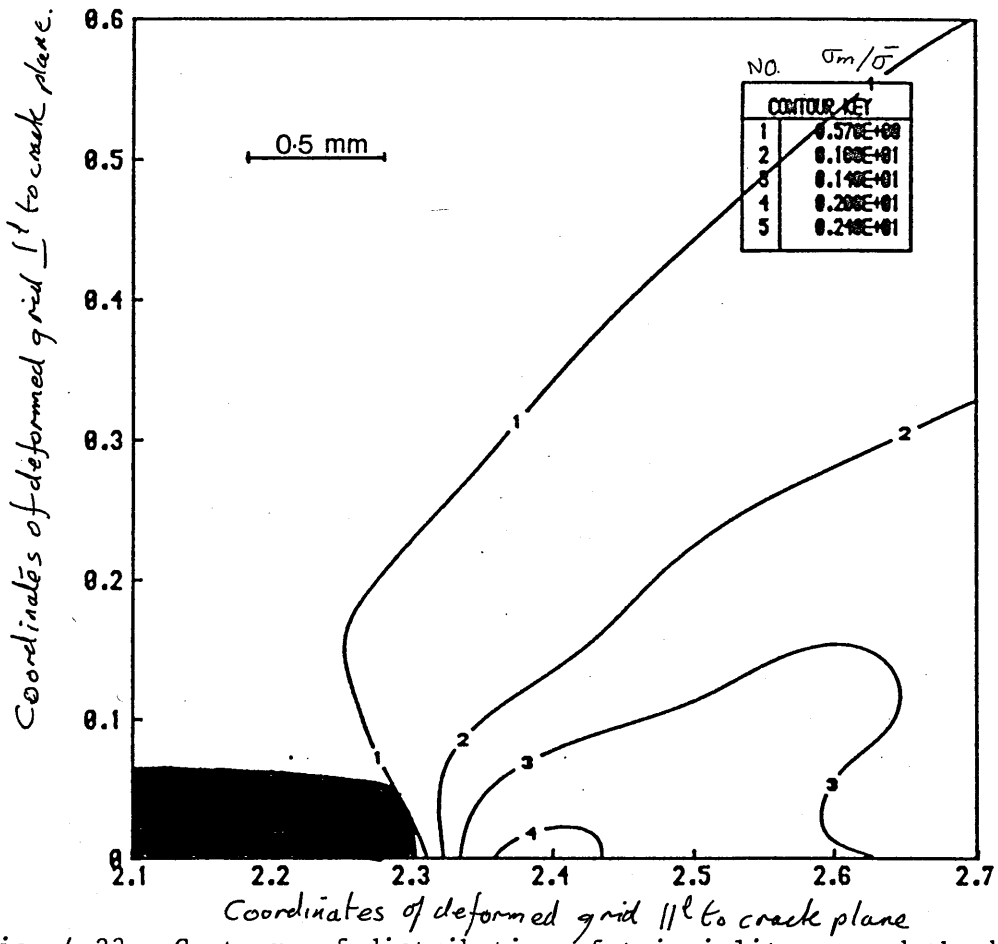

Fig. 4.23 Contours of distribution of triaxiality around the blunted crack tipin the 0.2 power hardening material. (Crack tip shown in black)

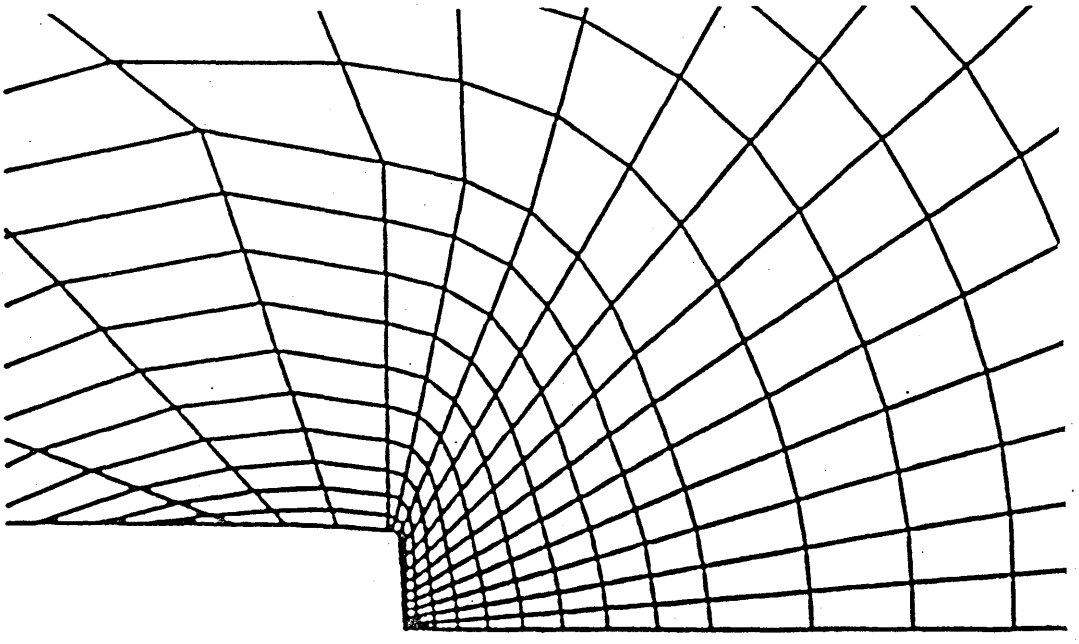

(a)

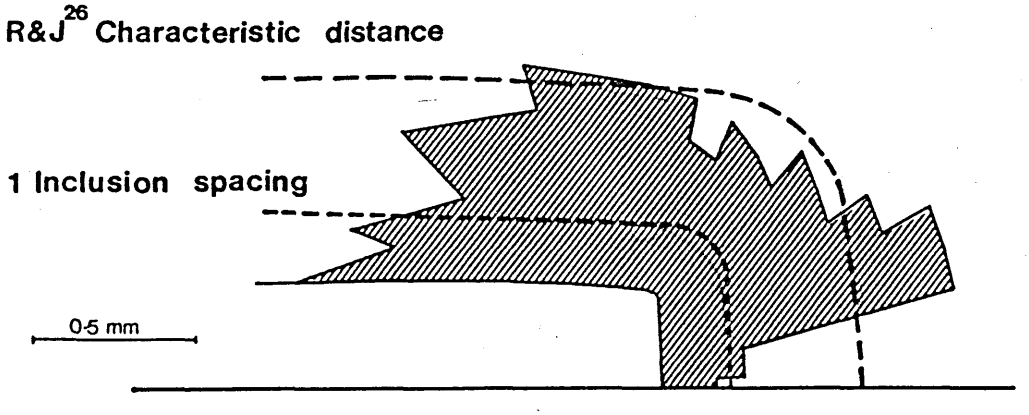

(b)

Fig. 4.24 (a) Deformed mesh for the non-hardening case.
(b) Failed elements around the blunted crack tip for which ductile failure criterion has been satisfied.

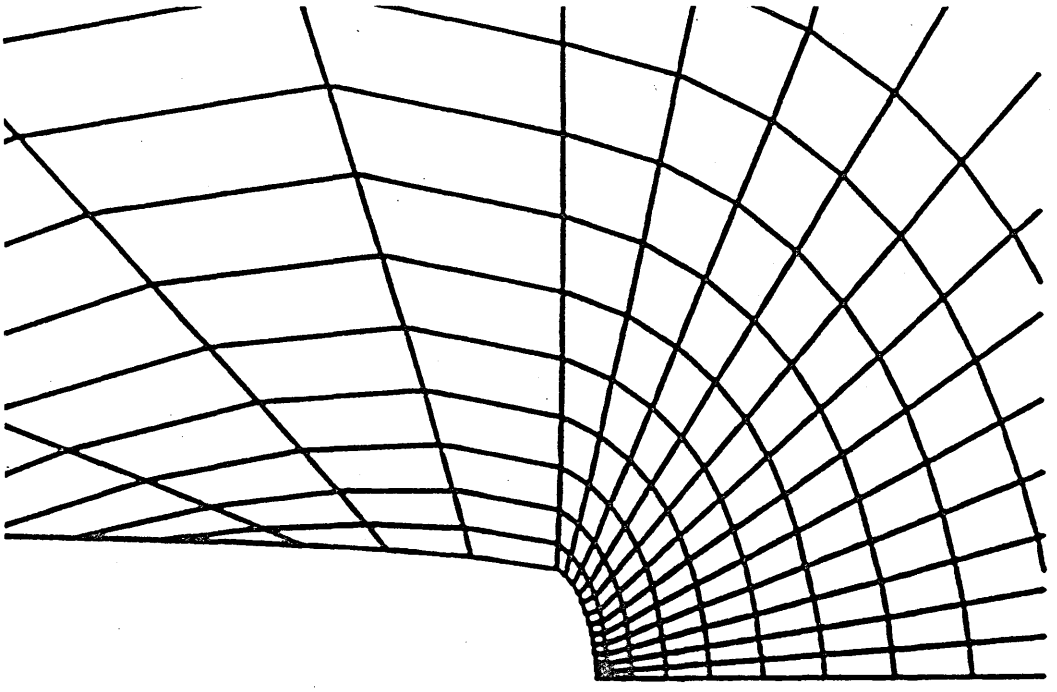

(a)

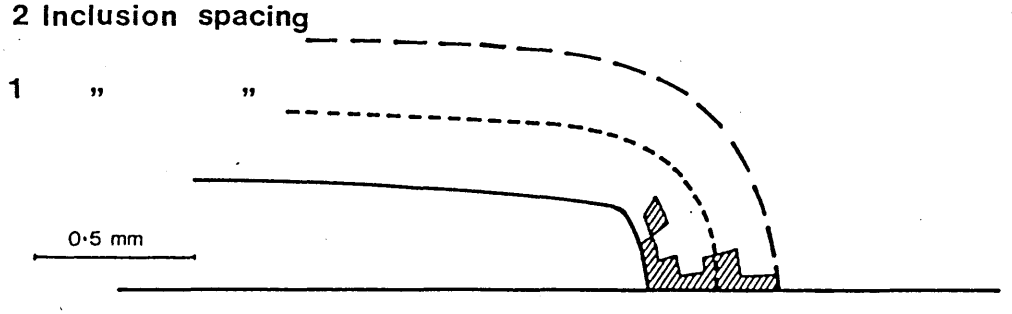

(b)

Fig. 4.25 (a) Deformed mesh for the 0.2 power hardening case.
(b) Failed elements around the blunted crack tip for which ductile failure criterion has been satisfied.

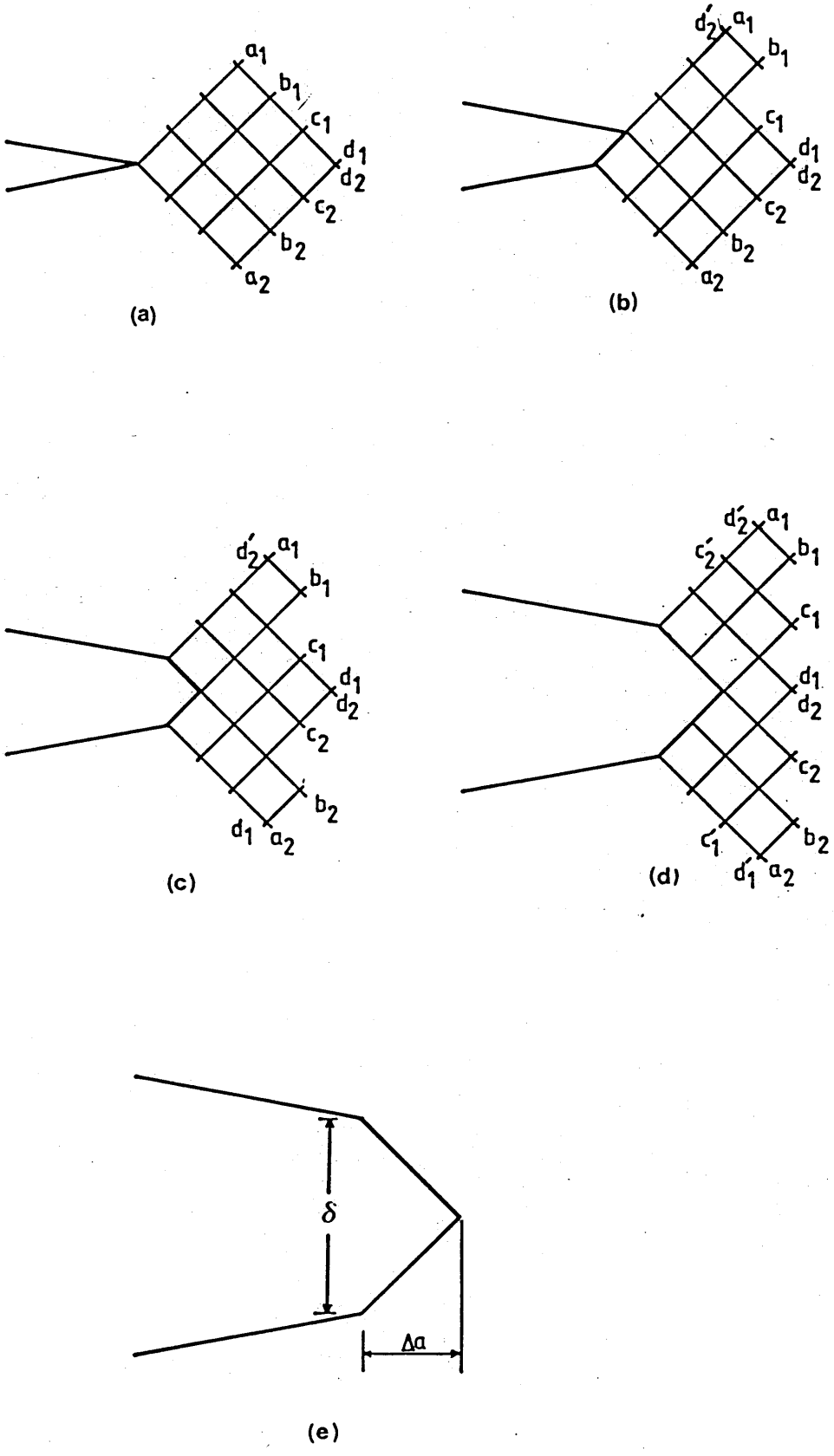

Fig. 4.26 Unzipping model for crack opening and advancing[45]

Section 5

STRESS INTENSITY FACTORS FOR SEMI-ELLIPTICAL CRACKS

5.1 Introduction

Part through semi-elliptical surface breaking cracks are among the most common types of defects in many engineering structures such as offshore structures, pressure vessels, aircraft structures etc. The increasing requirement for storing hazardous substances in pressurized containers and the construction of large welded tubular joints used in offshore oil production platforms, means that the evaluation of the behaviour of these cracks is very important in assessing structural integrity.

The stress intensity concept of linear elastic fracture mechanics and its unique characterization of crack tip stress fields, together with elastic-plastic fracture toughness parameters, have made it possible to assess in an approximate way the safety of structures in service. However no exact solution for the stress intensity factor around the periphery of a semi-elliptical crack is yet available. Several investigators have considered this problem and a number of approximate solutions based on analytical or numerical analyses have been proposed. A review of literature indicates that these solutions differ markedly and do not correlate well with experimental results.

In the work presented in this section an attempt has been made to obtain an accurate description of the stress intensity factor distribution along the entire front of a semi-elliptical crack subjected to remote tensile forces. Large plates of the material under investigation, containing part-through/

starter notches, have been carefully tested under fatigue loading and the crack profile development at various stages of crack growth has been monitored with the aid of a specially devised size measurement technique. The stress intensity factor was then calibrated by measuring the crack propagation rate, and the use of the Paris[1] law. Various solutions for stress intensity factors were examined and conclusions, as to the best fit to the experimental results, have been drawn.

Before presenting the details of experimental procedure, it is appropiate to review the practical difficulties in the analysis of surface cracks. In the next section an analytical investigation of semi-elliptical cracks is presented and various fracture mechanics solutions together with available experimental evidence are compiled.

5.2 Theoretical considerations

No exact solution exists for the stress intensity factor associated with a part-through surface crack. The elastic stress field introduced by such a crack configuration is singular, highly three dimensional and is complicated in practical situations by the influence of finite thickness and finite width of the body.

The surface cracked geometry is idealized as shown in Fig. 1. The plate is of thickness t and width W. The crack is ideally semi-elliptical with the dimensions a, the crack depth in thickness direction and 2c, the crack length along the surface. The crack can be characterized by the ratios of crack depth to crack half length a/c and crack depth to thickness a/t. The stress field remote from the crack is considered/

one of pure tension, perpendicular to the crack plane, which loads the crack in the Mode I configuration. The stress intensity factor varies with angular position θ around the crack front. The state of stress is plane strain at $\theta = 90^{o}$, where lateral constraint is afforded by the adjacent material. The stress state is plane stress on the surface where no such constraint exists.

The first fracture mechanics analysis was performed by Irwin[2], who calculated the stress intensity distribution around an elliptical crack embedded in a plate of infinite dimensions. The solution which is referred to hereinafter as K_{IR} is of the form:

$$K_I = K_{IR} = \frac{\sigma\sqrt{\pi a}}{E(k)} \left(\mathrm{Sin}^2\,\theta + \frac{a^2}{c^2}\,\mathrm{Cos}^2\theta\right)^{0.25} \qquad (5.1)$$

where σ is the applied tensile stress and E(k) is the complete elliptical integral of the second kind given by:

$$E(k) = \int_{o}^{90} \left(\mathrm{Sin}^2\theta + \frac{a^2}{c^2}\,\mathrm{Cos}^2\theta\right)^{0.5} d\theta \qquad (5.2)$$

The elliptical integral is expressed in terms of the elastic shape parameter Q and can be obtained from standard graphical representations. An approximate solution for E(k) was presented by Newman[3] as:

$$E(k) = \left[1 + 1.47\left(\frac{a}{c}\right)^{1.64}\right]^{0.5} \quad \text{for } \frac{a}{c} \leq 1.0 \qquad (5.3)$$

In the course of the present investigation, Equation 5.3 will be used.

The solution for a semi-elliptical crack in semi-infinite plate is obtained/

by hypothetically cutting the solid containing an embedded elliptical crack in half. This has the effect of raising the stress intensity factor due to the introduction of a free surface and thus a front face correction factor M_F, has to be applied to equation 5.1:

$$K_I = M_F K_{IR} \qquad (5.4)$$

M_F is dependent on the position along the crack front and is a function of crack aspect ratio a/c.

When the plate is of a finite thickness, it has been shown that semi-elliptical cracks subjected to fatigue loading tend to adopt a preferred profile. Figure 5.2 illustrates the experimental results of various investigations for the tension case in a variety of materials[20]. It is clear that in this case the crack shape development is towards that of a semi-circle while the fractional depth a/t is less than half. In general a small degree of ellipticity is then introduced as the crack grows towards the back face. This profile development suggests that the stress intensity factor on the plate surface may be higher than that at the deepest point. Equation 5.4 predicts that the maximum stress intensity is always maintained at the deepest point and therefore it does not describe the observed crack profile development. The shift in the maximum value of K_I from deepest point to surface intersection is due to the presence of the back surface and hence a back face correction factor M_B, has to be introduced to account for the effect of the thickness of the uncracked ligament:

$$K_I = M_F M_B K_{IR} \qquad (5.5)$$

M_B is a function of a/t and a/c and varies along the crack front.

In finite size specimens where the crack length to specimen width ratio, $c/_W$, is relatively large, the cracked area occupies an appreciable proportion of the cross section area. In this situation the stress intensity factor at the crack front is elevated by stress redistribution over the uncracked ligament and hence a finite width correction factor, M_W, has to be considered to account for the effect of fractional width $c/_W$.

Applying the front face, back face and finite width correction factors, the stress intensity factor around the periphery of a semi-elliptical crack in an elastic finite size plate subjected to Mode I uniform tension loading is given by:

$$K_I = M_F M_B M_W K_{IR} = MK_{IR} \qquad (5.6)$$

where

$$M = f(\frac{a}{c}, \frac{a}{t}, \frac{c}{W}, \theta)$$

Several solutions based on numerical, analytical and experimental techniques have been proposed to calculate the boundary correction factor M. In the following section a brief description of some of the proposed solutions and their limitations is presented.

5.3 Review of SIF solutions

In this section the proposed solutions for the correction factor M, for the calculation of the stress intensity factor for a semi-elliptical crack under tension loading are presented in a chronological order.

1962 - Irwin[4] approximated the correction factor at $\theta = \pi/2$, based on a analogy to the problem of an edge crack in a half plane

$$M = \sqrt{1.2} \simeq 1.1 \qquad (5.7)$$

This coefficient accounted for the combined effect of both the front face and back face in the range $0 \leq a/t \leq 0.5$ and $0 \leq a/c \leq 1$.

1965 - Paris and Sih[5] estimated the correction factor at $\theta = \pi/2$ which included a front face and back face correction for $a/t \leq 0.75$ and $a/c \leq 1$:

$$M = \{1 + 0.12(1 - \frac{a}{c})\}\sqrt{\frac{2t}{\pi a}} \tan \frac{\pi a}{2t} \qquad (5.8)$$

The tangent term was obtained from an analysis of an infinite plate containing an infinite periodic array of cracks.

1966 - Smith et al[6] by using the alternating method analysed the variation of stress intensity around the whole front of a semicircular surface crack. Later Smith[7] modified this solution to obtain an estimate of SIF for a semi-elliptical surface crack in a finite thickness plate. He proposed that the stress intensity correction along the entire front could be given by:

$$M = M_F \, M_B \, f(\alpha) \qquad (5.9)$$

where $f(\alpha)$ is an angular function of $\alpha = (90 - \theta)$. Values of M_F and M_B, calculated by alternating technique and graphical interpolation are given in graphical form in Ref. 7.

1969 - Kobayashi and Moss[8] estimated the boundary correction factor at $\theta=\pi/2$

$$M = M_F\, M_B \qquad (5.10)$$

where M_F, the front face correction factor was given by:

$$M_F = 1 + 0.12(1-\frac{a}{c})^2 \qquad (5.11)$$

The back face correction factor M_B, was obtained by solving the SIF for a pair of coplanar elliptical cracks under uniform tension, with a plane of symmetry which simulated the back face, located midway between the two cracks. The curves for the product of M_F and M_B are given in Ref. 8.

1969 - Masters, Haese and Finger[9] used an experimental method to derive the correction factor. They tested 2219-T87 Aluminium specimens containing surface cracks with various a/c and a/t ratios, under montonic tension at room and cryogenic temperatures. Calculated stress intensity factors were then equated to the plane strain fracture toughness K_{Ic}, at the same test temperature and the correction factors were obtained. The correction factor for $a/t \leq 0.85$ and $0.1 \leq a/c \leq 0.8$ was given as:

$$M = 1.1\, M_K \qquad (5.12)$$

The curves for M_K are given in Ref. 9.

1970 - Rice and Levy[10] determined the stress intensity factor at the deepest point using a line spring model, which reduces the three dimensional crack problem to a two dimensional one, similar to a single edge cracked plate. In this model the SIF was presented/

graphically in terms of the ratio of the SIF at the crack deepest point K_I to the SIF for a single edge Cracked Specimen K_∞ with a crack of the same depth. The correction factor for the range $0.1 \leq a/t \leq 0.7$ and $0 \leq a/c \; 1$ could then be presented as:

$$M = \left(\frac{K_I}{K_\infty}\right) F\sqrt{Q} \qquad (5.13)$$

where Q is the elastic shape factor, F is the correction factor for a single edge crack and $\frac{K_I}{K_\infty}$ is obtained from the curves in Ref. 10.

1970 - Anderson, Holms and Orange[11] modified the boundary correction for the equation of Paris and Sih (equation 8) by enhancing the effect of the back surface, and thus increasing its range of applicability for deeper cracks

$$M = \left[1 + 0.12\left(1 - \frac{a}{c}\right)\right]\left[\frac{2tQ}{\pi a}\tan\left(\frac{\pi}{2Q} \cdot \frac{a}{t}\right)\right]^{0.5} \qquad (5.14)$$

1972 - Newman[3] combined the analytical results of Smith and Alavi[12] for a near semi-circular crack ($a/c = 0.4 - 1.0$), Rice and Levy[10] for shallow cracks ($a/c = 0.1 - 0.2$) and Gross and Srawley[13] for a single edge crack ($a/c = 0$) to derive the following expression for M at the deepest point:

$$M = \left[M_F + \left(E(k)\sqrt{\frac{c}{a}} - M_F\right)\left(\frac{a}{t}\right)^p\right] M_W \qquad (5.15)$$

where:

$$M_F = 1.13 - 0.1\left(\frac{a}{c}\right) \qquad \text{for } 0.02 \leq \frac{a}{c} \leq 1 \qquad (5.16a)$$

$$M_F = \sqrt{\frac{c}{a}}\left(1+0.03\frac{c}{a}\right) \qquad \text{for } \frac{a}{c} \leq 1 \qquad (5.16b)$$

$$P = 2+8\left(\frac{a}{t}\right)^3 \qquad (5.17)$$

$$M_W = \sqrt{\text{Sec}\left(\pi \frac{c}{W} \cdot \frac{a}{t}\right)} \qquad (5.18)$$

1972 - Shah and Kobayashi[14] solved the stress intensity factor for an embedded elliptical crack approaching the free surface of a semi-elliptical solid[15] and derived an equation to calculate the front face correction factor M_F, for the deepest point of a semi-elliptical crack.

$$M_F = 1 + 0.12\left(1- \frac{a}{2c}\right)^2 \qquad (5.19)$$

1974 - Smith and Sorensen[16] used the alternating method to calculate M along the entire front of a semi-elliptical crack for $0.1 \leq a/c \leq 1$ and $a/t \leq 0.9$. The curves of combined effect of front and back face correction factors are presented in Ref. 16.

1976 - Kobayashi[17] calculated the boundary correction factor M, at the deepest point of a semi-elliptical crack by improving the boundary condition of his earlier alternating method. He used a two dimensional finite element model of a single edge crack in tension, to correlate the effect of bending restraints on the SIF.

The SIF was calculated for $a/c = 0.2$ and 0.98 and by interpolation between these two limits, the SIF for other aspect ratios were obtained. The results are presented in a graphical form in Ref. 17.

1979 - Raju and Newman[18] calculated the stress intensity factors along the whole crack front of a semi-elliptical surface crack in tension by using a three dimensional finite-element analysis with singularity elements around the crack front and linear strain elements elsewhere. The validity of the F.E. method was first tested by analysing embedded circular and elliptical crack configurations which produced accurate results within 1% of the exact solutions for these geometries[19]. The stress intensity boundary correction factor for a semi-elliptical crack in a finite thickness solid was then calculated by a convergence method, taking into account the effects of front and back surfaces. The results for $0.2 \leq a/c \leq 2$, $0.2 \leq a/t \leq 0.8$ and $c/W \leq 0.25$ are presented in graphical and tabular form in Ref. 18.

1981 - Scott and Thorpe[20] used the crack profile development during the fatigue crack growth process by integrating the Paris equation, to examine the accuracy of some of the analytical solutions outlined above. They concluded that the Raju and Newman finite element analysis correlated very well with experimental results. By fitting the Raju and Newman results into the Newman original equation (equation 16), they derived a new expression for boundary correction factor as:

$$M = [M_F + (E(k)\sqrt{\frac{c}{a}} - M_F)(\frac{a}{t})^P]M_W \qquad (5.20)$$

where

$$P = 1.6 + 3(\frac{a}{c})^3 + 8(\frac{a}{c})(\frac{a}{t})^5 + 0.008(\frac{c}{a}) \qquad \theta = \pi/2 \qquad (5.21a)$$

$$P = 0.3 + 1.15(\frac{c}{a})[1.3(\frac{a}{t})(\frac{a}{c})^{0.2}] + 0.8(\frac{a}{c})^3 \qquad \theta = 0 \qquad (5.21b)$$

and

$$M_F = 1.13 - 0.07(\frac{a}{c})^{0.5} \qquad \theta = \pi/2 \qquad (5.22a)$$

$$M_F = 1.21 - 0.1(\frac{a}{c}) + 0.1(\frac{a}{c})^4 \qquad \theta = 0 \qquad (5.22b)$$

To evaluate the influence of finite width on the SIF they used the Holdbrook and Dover[21] equation:

$$M_W = 1 + \frac{I(\frac{a}{c}) \cdot J(\frac{c}{W}) \cdot K(\frac{a}{t})}{(0.0599)^2} \qquad (5.23)$$

$$I(\frac{a}{c}) = 0.059 + 0.108(\frac{a}{c}) - 0.734(\frac{a}{c})^2 + 1.85(\frac{a}{c})^3 - 2.01(\frac{a}{c})^4 + 0.79(\frac{a}{c})^5$$

$$J(\frac{c}{W}) = -0.00252 + 0.274(\frac{c}{W}) - 0.354(\frac{c}{W})^2 + 1.008(\frac{c}{W})^3$$

$$K(\frac{a}{t}) = 0.0126 - 0.132(\frac{a}{t}) + 0.857(\frac{a}{t})^2 - 1.182(\frac{a}{t})^3 + 0.746(\frac{a}{t})^4$$

1981 - Newman and Raju[22] used their previous three dimensional finite element results[18] to develop an empirical equation for the stress intensity boundary correction factor around the periphery of a semi-elliptical crack in a finite size solid subjected to tension loading:

$$M = [M_1 + M_2(\frac{a}{t})^2 + M_3(\frac{a}{t})^4]g\, M_W \qquad (5.24)$$

where

$$M_1 = 1.13 - 0.09\left(\frac{a}{c}\right)$$

$$M_2 = -0.54 + \frac{0.89}{0.2 + \left(\frac{a}{c}\right)}$$

$$M_3 = 0.5 - \frac{1.0}{0.65 + \left(\frac{a}{c}\right)} + 14\left(1.0 - \frac{a}{c}\right)^{24}$$

$$g = 1 + \left(0.1 + 0.35\left(\frac{a}{t}\right)^2\right)(1 - \sin\theta)^2$$

and M_W is given by:

$$M_W = \left(\sec\left(\pi \frac{c}{W} \sqrt{\frac{a}{t}}\right)\right)^{0.5} \qquad (5.25)$$

The advantage of this solution is that it is easy to use and it gives the stress intensity factor along the entire crack front for a wide range of crack configurations, $0 \leq \frac{a}{t} < 1$, $0 < \frac{a}{c} \leq 1$ and $0 \leq \frac{c}{W} \leq 0.25$

Many of the solutions outlined above do not agree well with each other. Figs. 5.3 and 5.4 illustrate the variation of stress intensity correction factor, M, as estimated by the above solutions, as a function of fractional depth a/t, for two crack shapes. For a crack shape of $a/c = 0.2$, agreement between the results is reasonably good at a/t ratios less than 0.2. However for large ratios of a/t the differences among the various solutions are more marked and at $a/t = 0.6$ the difference between upper and lower bounds is as great as 80%. The same discrepancy is observed for $a/c = 0.6$ (Fig. 5.4), although the difference between extreme results is only about 20%.

5.4 Determination of stress intensity factors

5.4.1 Experimental procedure

The experimental method for calibration of stress intensity factor was based on a fracture mechanics analysis of the fatigue process. It is assumed that the range in alternating stress intensity factor ΔK, controls the fatigue crack growth rate $\frac{da}{dN}$ in the intermediate growth range (Section 2). For the material under investigation, the Paris[1] equation gives the relationship between ΔK and crack growth rate:

$$\frac{da}{dN} = C(\Delta K)^m \qquad (5.26)$$

where C and m are empirical constants and can be found from fatigue crack growth rate measurement made on specimens which have known stress intensity calibrations. By substituting the fatigue crack growth data for semi-elliptical cracks in the Paris equation, the range of stress intensity factor, ΔK, can be experimentally evaluated. This method has been successfully employed by various investigations to calibrate the SIF of particular geometries, or to check the K-calibrations calculated by other methods[23].

For materials with isotropic crack growth properties the Paris equation may be modified to give the growth rate at any point along the boundary of a surface crack

$$\frac{dR}{dN}_\theta = C(\Delta K_\theta)^m \qquad (5.27)$$

where R_θ is the distance of any point on the crack front from the centre point/

of the crack surface length and hereinafter is referred to as radial crack length. Clearly $R_0 = R_{180} = c$ the crack length and $R_{90} = a$ the crack depth. By measuring the radial crack length during fatigue test, the crack growth rate at any particular location on the crack front may be determined and through equation 27, the stress intensity factor may be calibrated for the entire crack boundary.

5.4.2 Crack size measurement technique

The A.C. Potential Drop technique was used to monitor the crack profile development. The Potential Drop (PD) technique is a widely accepted method of monitoring crack initiation and growth in controlled laboratory tests where an instantanious measure of crack size may be obtained while the test is in progress. The basic principle of crack sizing by this method relies on the fact that the resistance to flow of an electric current in a specimen or structure is changed by the presence of partial discontinuities such as a crack.

The main reason for the choice of A.C. is that at high frequencies the current is confined to the surface layer of the conductive test piece. The thickness of this layer is known as "skin depth". Calculations of skin depth for common metals indicate that it is relatively small compared with the thickness of most test specimens or structures, for instance at a frequency of 6KHz, the skin depths for Mild Steel and Aluminium alloys are 0.25 and 1.30 mm respectively[24]. Due to this feature, the apparent A.C. resistance is therefore much higher than that of D.C. for a given current which means that lower current can be used. Furthermore, since A.C. is concentrated at the surface, the proportional change in measured voltage due/

to a crack is much greater for A.C. than D.C. and thus cracks are sized more accurately. In the present work large specimens were to be tested and also the accuracy of crack profile measurement was crucial to ensure an accurate calibration of the stress intensity factor. These requirements led to the selection of the A.C. potential measurement technique.

In this technique, provided that the flow field is uniform, the crack depth is simply obtained by measuring the potential difference on the test piece surface between two measuring points a distance Δ apart:

$$d = \frac{\Delta}{2} \left(\frac{V_1}{V_2} - 1\right) \qquad (5.28)$$

where V_1 and V_2 are voltages measured across and adjacent to the crack respectively.

5.5 Fatigue crack growth test-series (i)

Specimens of dimension 850 x 150 x 25 mm were cut from the as-received plate with the major specimen axis at 90° to the rolling direction of the plate. Part-through surface notches were machined at the centre of the specimens using a slitting wheel 0.15mm thick introducing a surface flaw of aspect ratio a/c = 0.28 where a = 5 mm and 2c = 35 mm.

A fatigue crack was initiated and grown from the starter notch under constant amplitude, sinusoidal, tension to tension loading in a 1MN Dartec servo-hydraulic test machine at stress ratio R = 0.1 and a frequency of 1Hz.

To measure the crack size, a Unit Inspection ''Micro Gauge'' instrument was used. This instrument consists of a thermister-stabilised Wier bridge oscillator used to generate a 6KHz sine wave which supplies the necessary current to the specimen via a constant current power amplifier. The voltages detected on the specimen surface are relayed to a filter amplifier which in addition to amplification of pick-up signals, rejects other unwanted common mode signals. The signals are then passed through a rectifier which rejects pick-up signals from the power amplifier circuit and produces a linear and stable output.

To monitor the potential changes on the specimen, 24 voltage reading stations were attached to the specimen along the crack surface edge, 5 mm apart. Each station consisted of three contact terminals spot welded to the specimen on a line perpendicular to the crack surface edge as shown in Fig. 5.5. Terminals 1 and 2 measure the voltage across the crack V_1 and terminals 2 and 3 measure the voltage adjacent to the crack V_2. The distance between the terminals (Δ) was 20 mm. Current leads were connected to the specimen surface 200 mm either side of the crack.

The specimen was loaded to a maximum stress of 180 MPa half the uniaxial yield stress. By using the Scott and Thorpe[20] solution (equation 20), it was found that this stress introduced a maximum applied stress intensity of 22.3 $MPa.m^{0.5}$ which was enough to initiate the fatigue crack growth. The level of the applied stress intensity was maintained constant by reducing the applied load during the cyclic loading. At every 5000 cycle interval, loading was stopped and the specimen maintained under the mean load (to eliminate the effect of crack closure) while the voltages V_1 and V_2 were measured for all the contact stations. Equation 28 was used to obtain the crack/

size from V_1 and V_2 and graphs of crack profile development were produced. The fatigue test was terminated when the P.D. technique predicted that the crack had penetrated to 70% of specimen thickness. The specimen was then fractured under monotonic loading.

5.5.1 Results

Fig. 5.6 shows the predicted crack shape at the termination of the test compared to actual shape revealed on the fracture surface. As it can be seen, the A.C. measurements underestimated the crack depth by up to 50% and overestimated the crack surface length by a considerable amount. furthermore it predicted a zig-zag crack front whereas the actual crack front was relatively smooth.

These observations indicated that the A.C. technique, in the way it was employed, was inadequate to produce an accurate measurement of crack profile. The following points were considered to be the major sources of error:

5.5.1.1 Induced magnetic voltages

It is well known that if the magnetic flux enclosed in a coil of wire is changing, a voltage proportional to the rate of magnetic flux is induced in the coil (Faraday's law). Terminal wires connected to the specimen were found to form a complete loop enclosing some of the magnetic flux produced in the specimen by the current flow. The current and hence the flux was continually changing so that a voltage was induced in the loop. This voltage was in series with the measured surface voltage and thus caused a measurement/

error. In addition since the loop areas at various contact stations were unequal, induced voltages varied, resulting in the erroneous zig zag prediction of crack profile.

5.5.1.2 Non uniformity of the current flow field

Equation 5.28 is valid only if the current flow on the surface of the specimen is uniform. In finite bodies containing part-through cracks of finite size, the gradient of potential is not constant[27] as shown in Fig. 5.7. It was deduced therefore that a reading for reference voltage V_1, obtained off the crack on the specimen surface was not constant due to a divergence of the current flow in the vicinity of the crack. Neither did the reading for V_2 represent the potential drop due to actual crack depth, since the discontinuity in current flow across the crack surface edge was not constant. Thus equation 5.28 provided an inaccurate measurement of crack size.

5.6 Improved A.C. P.D. measurement

5.6.1 Induced voltage

To eliminate the loop induced voltages, the stationary spot welded terminals were abandoned. Instead a voltage sampling probe, with two contact points 10 mm apart was employed. The probe was designed such that the voltage pick up wires connected to contact points were pressed very close to the surface of specimen and thus the area of the conducting loop was reduced to a minimum.

Improvement was also made by minimizing the stray magnetic field induced/

in the specimen by current leads. The current leads were taken away from the connection poles in a plane perpendicular to the specimen plane, and they were eventually twisted together at a distance one metre from the specimen. This large loop of current ensured the minimum magnetic field because magnetic field strength is inversely proportional to distance from the wires. Thus eddy currents which might have affected the voltage probe circuit were minimised.

5.6.2 Uniform current flow field

Dover et al[25] have considered the non-uniform field problem mathematically for particular cracks by comparing the electrical flow field with the flow of a stream over a plane containing a circular arc indentation. By making use of relevant hydrodynamic solutions, they concluded that the conditions leading to equation 28 are not generally satisfied in the case of a finite part-through crack and that a modification factor in form of a multiplier, has to be applied to correlate the A.C. potential reading to true crack size. They proposed a modification factor, M, which is a function of crack aspect ratio and probe size:

$$d_2 = Md_1 \qquad (5.29)$$

where d_1 is the first estimation of crack depth by A.C. potential drop technique via equation 5.28 and d_2 is the measure of true crack depth. Michael and Collins[26] presented the values of M at the crack centre line only, for various crack shapes and probe sizes, in a graphical form. Dover and Collins[27] calculated the variation of M along the crack length for a specific probe size and crack aspect ratio. The disadvantage of their solution is that a prior knowledge of crack profile must exist before the modification factor is determined, a situation highly improbable in practice.

5.6.2.1 An empirical solution for A.C. modification factor

In the present work it was necessary to measure the crack profile development while the integrity of the test was preserved. Thus a calibration of the A.C. modification factor all along the crack front was required such that the A.C. potential drop output could be readily correlated to the actual crack shape. An experimental procedure was therefore carried out to achieve this.

The proposed modification factor is given by:

$$R_x = \frac{a_x}{d_x} = F(\frac{a}{2c} , \frac{\Delta}{2c} , x) \qquad (5.30)$$

where x is the distance along crack surface edge from the crack centre on the specimen surface, a_x is the actual crack depth and d_x is the first estimate of crack depth made by the use of equation 5.28.

5.6.2.2 Experimental Procedure

A series of specimens were tested under cyclic loading with testing procedure similar to that reported in section 5.5. To measure the crack size, the voltage sampling probe was manually traversed across the specimen on and off the crack, against a linear displacement transducer to give a continuous record of voltages V_1 and V_2, recorded on a x-y recorder. From these records the first estimate of crack depth d_x could be determined via equation 5.28.

The true crack depth a_x during the fatigue growth was obtained by delineating the crack front through a beach marking technique. Beach marks were produced by reducing the load amplitude to 50% of its previous value while/

the frequency increased to 2.5 Hz and the maximum load was kept constant. In this way, the value of K_{max} remained unchanged during both the marking and non-marking periods. It was found that the beach marks were visible only if there was a small but significant amount of crack propagation during the reduced-load period. A computer program was developed to determine the point of onset and duration of each reduced load period in order to produce a 0.1mm band of crack propagation at 1mm intervals. The method used consisted of a number of steps detailed below:

Step 1. ΔK was calculated at the surface and deepest point of the crack for initial values of a, c and fractional depth a/t, by using the Scott and Thorpe[20] solution (equation 20).

Step 2. An incremental growth of Δa=0.05mm together with the calculated ΔK was used in the Paris equation (equation 27) to determine N and Δc.

$$\frac{da}{dN} = C(\Delta K_a)^m, \quad \frac{dc}{dN} = C(\Delta K_c)^m$$

for the material in use, the constants C and m were taken as 2.51×10^{-12} metres per cycle (ΔK in $MPam^{0.5}$) and 3.25 respectively.

Step 3. The crack shape was updated to $a=a+\Delta a$ and $c=c+\Delta c$ and the procedure returned to step 1 until a growth of 1mm was achieved at the deepest point.

Step 4. The loading condition was changed to that required for beach marking (same K_{max}, R=0.5, F= 2.5 Hz) and steps 1 to 3 were repeated to obtain the number of cycles required/

to produce a crack growth band of 0.1mm. Conditions were then returned to normal loading and steps 1 to 4 repeated until the crack penetrated to 80% of specimen thickness.

After termination of the fatigue test, the specimen was fractured at room temperature under monotonic loading at a strain rate of $2.6 \times 10^{-3}\ s^{-1}$. The fracture surfaces containing beach marks were photographed and crack depths, a_x, were measured for each beach mark at 5mm intervals along the crack surface edge. These optical measurements on the fracture surface were then used to calibrate the potential drop measurements.

5.6.2.3 Results and discussion

The beach marks revealed on the fracture surface are illustrated in Fig. 5.8. Fig. 5.9 shows the variation of the A.C. potential field measured on the specimen surface across (V_1) and adjacent (V_2) to the crack. In Fig. 10 the actual crack profile at $a/c = 0.7$, revealed by the beach mark, and the first estimate of crack profile obtained by P.D. method are plotted together. As expected the P.D. underestimated the crack depth at the centre line by about 40% and predicted a larger crack length on the specimen surface. However these results illustrate a significant improvement over previous results, that is the prediction of a smoothly curved crack front consistent with the true crack. This indicates that the probe had properly sampled only the actual potential field and that the other induced voltages had been eliminated.

Modification factors were calculated for 11 different crack shapes using equation 5.30. Fig. 5.11 shows the values of the modification factor for/

the crack deepest point (denoted as R_θ=90 where θ is the angular position on the crack front) against P.D. first estimate, d'_{90}. Crack aspect ratio and probe size, normalized by the crack half length, are also plotted on the same graph. The initial increase in R_{90} is due to the increase of crack aspect ratio which enhances the non-uniformity of the flow field. The maximum however coincides with an apparent change in the rate of a/c increase which is due to the fact that the crack grows towards a preferred shape[20]. Adoption of a preferred shape means that the growth on the surface is higher than that through the thickness. Therefore the effect of Δ/c becomes more pronounced which results in a reduction of R_{90}. Eventually the effect of aspect ratio and probe size cancel each other out and the modification factor remains constant.

The variation of R_x along the entire crack front for a variety of crack shapes is shown in Fig. 5.12 in a manner readily usable for the sizing of defects within the range investigated, without a prior knowledge of crack shape. The results are presented for only half the crack front, since a semielliptical crack has a symmetric shape. To give a basic comparative criterion for different probe size, the value of R_x is normalized by Δ/c. Crack shape has been presented in aspect ratio term, a/c, as well as d_{90}/c. The advantage of latter representation is that without prior knowledge of crack shape, the crack profile can be predicted using only the potential drop technique.

5.6.2.4 Application of A.C. modification factor solution

The procedure outlined below demonstrates the use of the AC potential drop technique and modification factors presented in this section for exact sizing and profile determination of a part-through surface crack.

1. The crack length on the specimen surface (2c) can be measured by simple optical techniques.

2. The voltage sampling probe of the AC system is placed at the centre of the crack on the specimen surface and the voltages across and next to the crack (V_1 and V_2) are measured. These values are then used in Equation 5.28 to give the first estimate of crack depth at the deepest point (d_{90}).

3. From d_{90}, crack half-length c and probe size Δ, the curves in Figure 5.12 can be used to modify the predicted crack depth at any position x along the specimen surface. Thus, the true crack depth at any point may be determined and hence the accurate crack profile.

5.7 Fatigue crack growth-series (ii)

5.7.1 Experimental procedure

Specimens identical to those of series (i) (section 5.5) were tested under cyclic loading. Prior to fatigue cycling, each specimen was ground to provide a suitable surface for crack growth observation. The maximum applied stress, for a stress range ratio R=0.1, was 140 MN/m^2. This level of stress was kept constant during the test which implied that by increasing crack size the applied K would increase. Irwin[32] has suggested that following criterion must be satisfied in order to maintain a valid LEFM stress intensity factor:

$$(\frac{K}{\sigma_y})^2 \leq 0.3\pi c \qquad (5.31)$$

By using the Scott and Thorpe[20] solution, it was found that at the stress level used, a maximum SIF of 40 MPa.$m^{0.5}$ would be attained if the crack had penetrated to 80% of specimen thickness, which satisfies the above requirement.

To monitor the crack growth an A.C.P.D. Crack Micro Gauge instrument was used. The instrumentation and measuring method was similar to that outlined in sections 5.6.1 and 5.6.2.2. At certain predetermined cycle intervals, the specimen was held at mean load and A.C. voltage signals V_1 and V_2, corresponding to the crack shape, were measured. The crack surface length, 2c, was measured optically with the aid of a travelling microscope.

The actual crack depth at any point along the crack surface edge was determined by modelling the A.C. prediction of crack depth via the procedure outlined in section 5.6.2.4. Since the modification factors near the surface of specimen are not clearly defined, the crack profile close to the surface tip was determined by extrapolation between the surface tip and nearest point on the crack front which could be determined accurately. This technique proved to be successful especially in the later stages of the tests, where the crack bulging near the surface intersections was observed.

5.7.2 Results and Discussion

In Fig. 5.13 the crack growth rate at the deepest point and plate surface are shown. It can be seen that at initial stages of fatigue loading the growth at the deepest point is faster than that at plate surface. As the crack reaches half specimen thickness, the growth rate at the surface is increased whereas the crack depth increases at a constant growth/

rate. Holdbrook and Dover[21] observed the same trend for mild steel (BS 4360 Grade 50B) both under sinusoidal and random tensile fatigue loading.

Fig. 5.14 shows the variation of crack aspect ratio a/c against crack fractional depth a/t, which indicates the tendency for the crack to grow towards an equilibrium shape of $a/c = 0.8$. This tendency has been observed by other workers as shown in Fig. 5.15 which illustrates that the adoption of a preferred shape is independent of initial crack size and profile.

To determine the crack growth rates along the crack front, the R_θ vs N data at $\theta = 0$, 15, 30, 45, 60, 75 and 90 degrees, were smoothed by computing a weighted approximation to the data points. The degree of polynomial was computed such that the sum of the squares of the weighted residuals was minimized. The growth rates were then calculated as derivatives to the fitted curve. Fig. 5.13 shows the fitted curve to the data points at $\theta = 0$ and $\theta = 90$ where the maximum error deviation was less than 3% and shows the accuracy of measuring technique.

Crack growth rates calculated in this way, were used in modified Paris equation (equation 5.27) to determine ΔK and hence $K_{I\theta} = \Delta K_\theta/(1-R)$ around the crack boundary.

In Fig. 5.16 $K_{I\theta}$ is plotted against the radial crack length R_θ. Solid lines show the variation of $K_{I\theta}$ at fixed positions on the crack boundary (θ = constant) as the crack grows through the thickness. Dotted lines present the variation of $K_{I\theta}$ along the crack front, from $\theta = 0$ to $\theta = 90$, at any particular crack profile (constant a/c). The stress intensity factor all along the crack front is increased by increasing crack size as expected.

At/

aspect ratios less than 0.65 and before the crack penetrates to the mid-thickness of the plate, the rate of increase in SIF (slope of the solid lines, Fig. 5.16) is highest at the surface intersection. This is more pronounced at lower values of a/c where the fatigue growth is initiated on the specimen surface only when SIF reaches a threshold value. In this region, SIF decreases from a maximum at the crack deepest point to a minimum at the crack surface intersection (dotted lines, Fig. 5.16), which is consistent with the original formulation of Irwin in equation 5.1.

At aspect ratios greater than 0.65 the SIF is almost constant along the entire crack front. This may be attributed to the effect of the back surface and its interaction with the stress field ahead of the growing crack. If the plate was of infinite thickness K_I would have always been highest at deepest point and the crack would have grown towards a true semi-circular shape. However at $a/c = 0.65$, the crack has already penetrated to 55% of plate thickness whereupon the proximity of the back surface prevents the ideal profile developing.

Comparison between values of K_I on the specimen surface and at the 15° shows that the crack grows faster at locations near the surface intersection than at the crack surface tip. This observation indicates that once the crack has penetrated to mid-thickness of plate, the crack shape begins to deviate from that of a semi-ellipse and bulges at the ends of the major axis. This phenomena has been observed by other workers[28-29] and it may be attributed to the fact that the stress condition changes from plane stress on the specimen surface to the plane strain in the interior. This change in stress field triaxiality along the crack front results in a variation in the extent of crack tip plasticity. At relatively high applied loads, considerable plasticity may occur at the surface crack tip which/

retards the fatigue crack growth. The plastic zone size r, on the specimen surface and at the deepest point can be estimated. This is calculated for the crack profile of $^{a}/_{c} = 0.7$ where the crack has penetrated to a fractional depth of $^{a}/_{t} = 0.77$. At the crack deepest point, the state of stress is plane strain whereas on the specimen surface a plane stress condition exists, thus from Irwin[33] plastic zone correction (section 1.3.1):

$$r_{90} = \frac{1}{6\pi}\left(\frac{K_{90}}{\sigma_y}\right)^2 = 0.59\text{mm}$$

$$r_0 = \frac{1}{2\pi}\left(\frac{K_0}{\sigma_y}\right)^2 = 1.93\text{mm}$$

The state of stress at $\theta = 15^o$ is assumed to be somewhat between plane stress and plane strain:

$$r_{15} = \frac{1}{4\pi}\left(\frac{K_{15}}{\sigma_y}\right)^2 = 0.92\text{mm}$$

A notional elastic crack profile can now be assumed by adding the plastic zone sizes to the true crack profile such that $a_n = 20.03$mm, $c_n = 29.72$mm and $R_{15n} = 28.55$mm. An examination of this notional crack shape indicates that it satisfies the analytical equation for an ellipse i.e.

$$\frac{x^2}{c^2} + \frac{y^2}{a^2} = 1$$

Therefore it can be deduced that although the actual crack profile deviates from a semi-elliptical shape, the notional elastic crack profile maintains a semi-elliptical shape, which confirms the effect of state of stress on the crack profile development.

5.8 Correlation of analytical solutions

Data obtained in this work were also used to predict the stress intensity factor via analytical solutions outlined in section 5.3. Emphasis is placed on those solutions that have been shown to be consistent with changes of crack profile during fatigue growth and have produced the best correlation to experimental results reported in literature[20-22]. In addition only those solutions which have been presented in a numerical form are considered, Since they could be directly applied to solve the problem of a growing fatigue surface crack where both crack aspect ratio a/c and crack fractional depth a/t are continuously changing. Some published solutions are in tabular or graphical form (as presented in section 5.3) and show the variation of stress intensity factor against one variable parameter while the others are kept constant, and thus cannot readily be applied to a growing crack in which the aspect ratio is changing. With this in mind, four solutions due to Shah and Kobayashi[15] (Eq. 5.19), Newman[3] (Eq. 5.15), Scott and Thorpe[20] (Eq. 5.20) and Newman and Raju[22] (Eq. 5.24) were considered. In order to find the solution which gave the best correlation to experimental results, comparison was first made at the crack deepest point. Results are presented in Fig. 5.17, where stress intensity factor is plotted against crack fractional depth a/t. The Shah and Kobayashi solution which considers only the front face correction factor, predicts a very conservative value for K_I, even at low ratios of a/t where the effect of the back surface is thought to be minimal.

The Newman solution[3] agrees well with present results when the crack is small compared to the specimen dimensions ($a/t \leq 0.6$), but underestimates them by as much as 20% as the crack grows beyond $a/t = 0.6$.

The Scott and Thorpe[20] and the Newman and Raju[22] solutions were expected to produce similar results since both are mathematical interpretations of the same finite element analysis[18], but they differ slightly. The difference may be due to the effect of finite width correction factors. Indeed as the crack grows beyond the mid-thickness of the plate, the crack surface area becomes a considerable proportion of specimen cross section area (45% at $a/t = 0.77$) and hence the effect of finite width becomes significant. The Newman and Raju solution employed a finite width correction (equation 5.25) which is mildly dependent on the ratio of crack to specimen surface area. This solution underestimates the experimental results by up to 13% at $a/t = 0.77$. The Scott and Thorpe solution, on the other hand, uses a finite width correction (equation 5.23) which is more influenced by the finite size nature of the specimen and gives a better agreement with experiment.

Of the solutions discussed only Newman and Raju[18] calculated the stress intensity factor for all locations on the crack front. Figure 5.18 shows the variation of stress intensity correction factor on the crack front for some of the crack profiles developed. Similar results were observed for a maraging steel in reference[31]. Figure 5.19 shows a comparison between the predicted stress intensity factor by Newman and Raju solution and the experimental results, for all the data considered ($0.3 \leq a/c \leq 0.7$, $0.22 \leq a/t \leq 0.8$). The comparison at the crack surface tip ($\theta = 0^o$) shows that the prediction correlates well with experiment, within a 10% scatter band, for the whole range of a/t. The agreement between prediction and experimental results for all other locations on the crack front from $\theta = 15^o$ to 90^o is also good up to $a/t \leq 0.6$ but at higher ratios of a/t, the Newman and Raju solution tends to underestimate the experimental results.

If in this solution the finite width correction term is replaced by equation 5.23, then the prediction is improved by up to 3%. However the fact remains that as crack grows, the prediction differs from experimentally determined stress intensity factor. This is thought to be due to the fact that theoretical solutions assume that a semi-elliptical crack maintains its elliptical shape during cyclic loading and ignore the deviations such as bulging near the surface, as observed in present work, which may be material dependent. The variation of constraint along the crack front, from that of plane strain at the deepest point to that of plane stress at the point of crack intersection with the plate surface, is a major factor contributing to differences between predicted and observed fatigue crack growth behaviour.

5.9 References

1. Paris, P.C. and Erdogan, F., Trans. ASME. J. Basic Eng. Vol. 85, No. 4, p. 528, 1963.

2. Irwin, G.R., J. Basic Eng., Tran. ASME, Vol. 82, p. 417, 1960.

3. Newman, J.C., Eng. Fracture Mech., Vol. 5, p. 667, 1973.

4. Irwin, G.R., ''Crack-extension force for a Part-through Crack in a Plate'', J. Appl. Mech. Trans. ASME, Vol. 29, p. 651, 1962.

5. Paris, P.C. and Sih, G.C.M., Fracture Toughness Testing and Application ASTM, STP 381, p. 30, (1965).

6. Smith, F.W., Emery, A.F. and Kobayashi, A.S., J. Appl. Mech., Vol. 34, No. 4, Trans. ASME, Vol. 89, Series E, p. 953, (1967).

7. Smith, F.W., Stress Intensity Factors for a Semi-elliptical surface flaw, The Boeing Company, SDRM 17 (1966).

8. Kobayashi, A.S. and Moss, W.L., in Fracture, P.D. Platt, Ed. p. 31, Chapman and Hall, New York and London (1969).

9. Masters, J.N., Bixter, W. D. and Finger, R.W., ''Fracture Characteristics of Structural Aerospace Alloys containing Deep Surface Flaws'', NASA, CR-13487, (1973).

10. Rice, J.R. and Levy, N. Tech. Report, NASA NGL 40-002-080/3, Division of Engineering, Brown University, (1970),

11. Anderson, R.B., Holms, A.G. and Orange, T.W., NASA, TN D-6054 (1970)

12. Smith, F.W. and Alavi, M.J., Proceedings, 1st International Conference on Pressure Vessel Techcnology, Delft, The Netherlands, ASME, p. 783, (1969).

13. Gross, B., and Srawley, J.E., NASA TN D-2603, (1965).

14. Shah, R.C. and Kobayashi, A.S. in The Surface Crack: Physical Problems and Computational Solutions. Ed. Swedlow, J.L., p. 79 (1972).

15. Shah, R.C. and Kobayashi, A.S., Int. J. of Fracture, Vol. 9, No. 2, p. 133, (1973).

16. Smith, F.W. and Sorensen, D.R., NASA CR-134684, (1974).

17. Kobayashi, A.S., Proceedings, 2nd Int. Conf. on Mechanical Behaviour of Materials, Int. Conf., ASME, p. 1073, (1976).

18. Raju, I.S. and Newman, J.C., Eng. Fracture Mech. Vol. 11, No. 4, p. 817, (1979).

19. Green, A.E. and Sneddon, I.N. Proceedings, Cambridge Philosophical Society, Vol. 46, p. 159, (1950).

20. Scott, P.M. and Thorpe, T.W., AERE Report R10104 (1981).

21. Holdbrook, S.J. and Dover, W.D., Eng. Fracture Mech. Vol. 12, p. 347, (1979).

22. Newman, J.C. and Raju, I.S., Eng. Fracture Mech., Vol. 15, No. 2, p. 185, (1981).

23. Grandt, A.F. Jnr. and Sinclair, G.M., ASTM STP513, p. 37, 1972.

24. Taylor, K.A., Proceeding ''Crack Sizing Using AC Field Measurements'', University College, London, (1982).

25. Dover, W.D., Charlesworth, F.D.W., Taylor, K.A., Collins, R. and Michael, D.H., ASTM STP 722 (1981).

26. Michael, D.H. and Collins, R., Unit Inspection Int. Rep. UIC/Tech. 2005 (1981).

27. Dover, W.D. and Collins, R., ''Recent Advances in the Detection and Sizing of Cracks using A.C. Field Measurements'', Unit Inspection Technical Publication, 1980.

28. Sommer, E., Hodulak, L. and Kor disch, H., Tran. ASME, J. Press. Vessel. Tech. Vol. 90, p. 106, (1977).

29. Smith, C.W., Peter, W.H. and Kirby, G.C., Proceedings ''Analytical and Experimental Fracture Mechanics'', Rome, Italy, p. 699, (1981).

30. Hodulak, L., Kordisch, H., Kunzelmann, S. and Sommer, E., ASTM, STP 677, p. 399, (1979).

31. Leduff, A., Castagne, J.L., Miannay, D., LePoac, Ph. and Francoic, D., Proc. 5th Int. Conf. on Fracture ICF 5, France, Vol. 1, p. 59, (1981).

32. Irwin, G.R., The Surface Crack: Physical Problems and Computational Solutions, ASME, J.L. Swedlow Ed. p. 1, (1972).

33. Irwin, G.R., ''Plastic zone near a crack and fracture toughness'', Sagamore Ordnance Materials Conf., Syracuse University, (1961).

34. Portch, D.J., Central Electricity Generation Board Report, CEGB/RD/B/N4645, (1979).

35. Lloyd, G.J. and Walls, J.D., Eng. Fracture Mech., Vol. 13, p. 897, (1980).

36. Cruse, T.A., Meyers, G.J. and Wilson, R.B., ASTM, STP 631, p. 174, (1977).

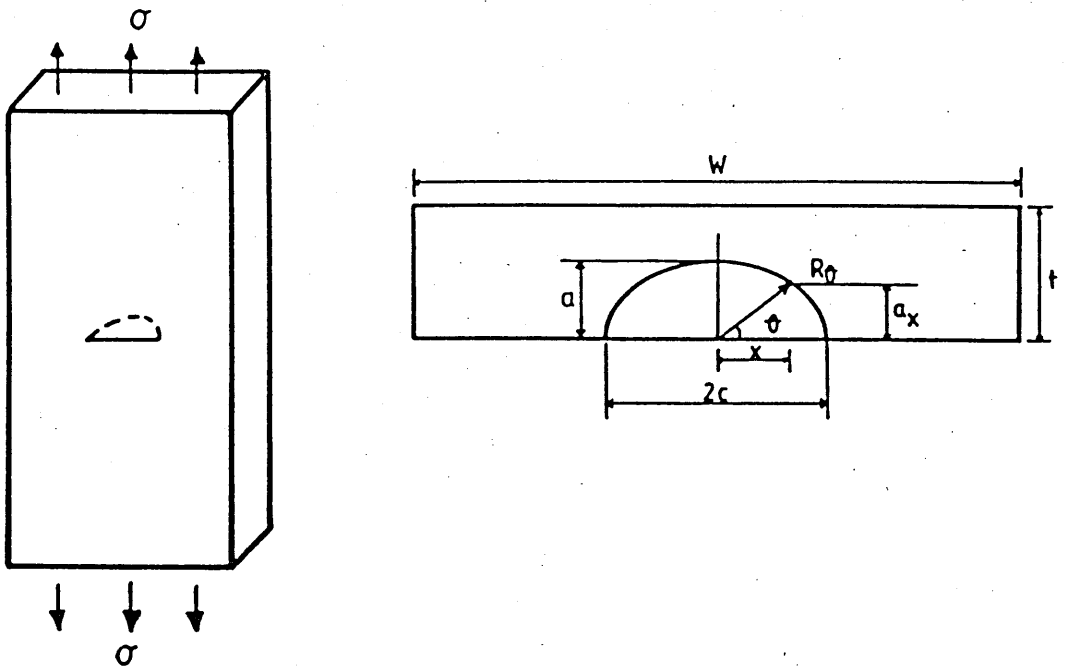

Fig. 5.1 Semi-elliptical surface cracked specimen.

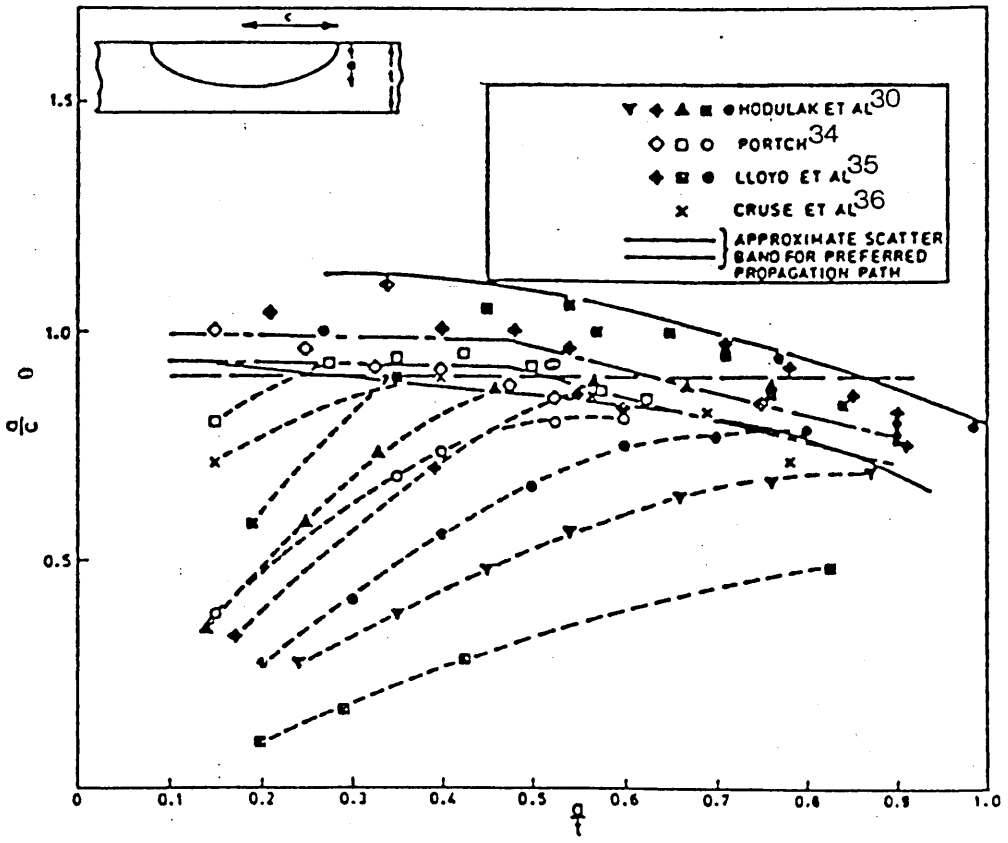

Fig. 5.2 Crack profile development under uniform tensile fatigue loading (Ref. 20).

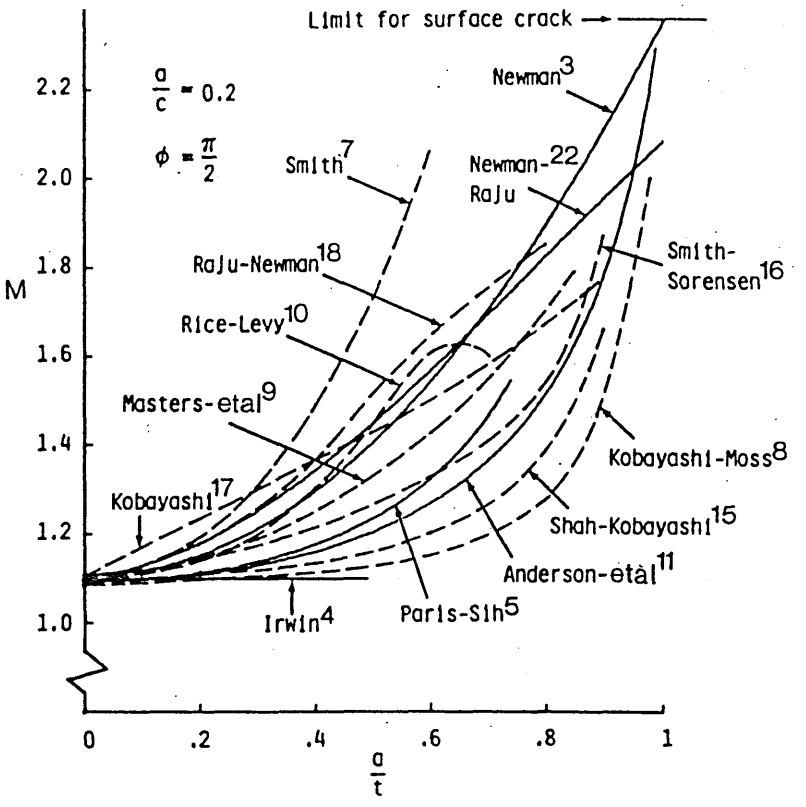

Fig. 5.3 Stress intensity correction factor at deepest point for a semi-elliptical surface crack of a/c = 0.2.

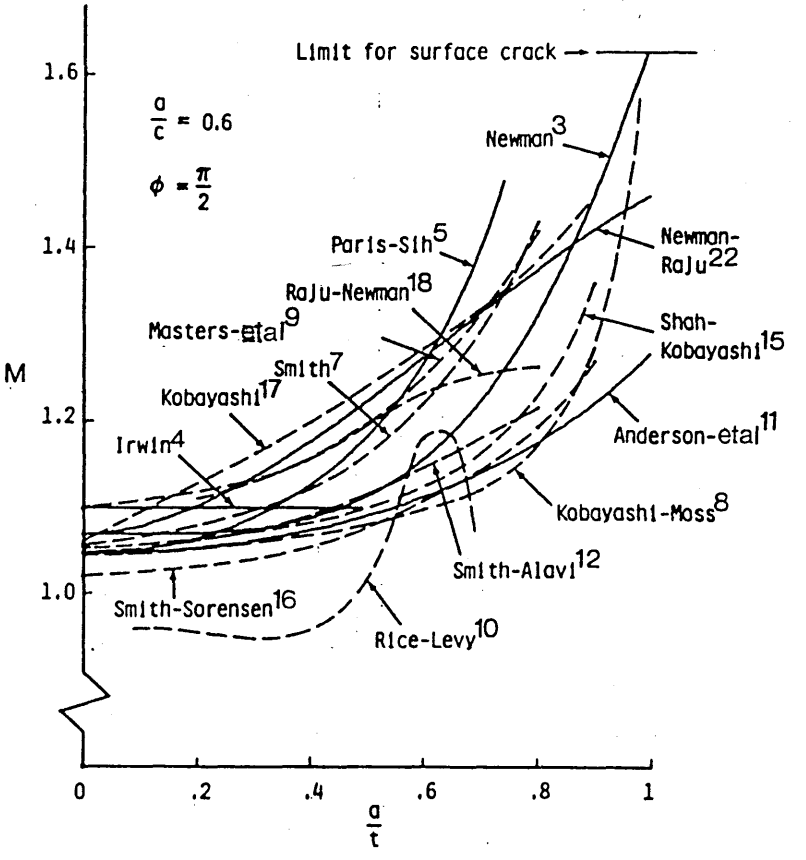

Fig. 5.4 Stress intensity correction factor at deepest point of a semi-elliptical surface crack of a/c = 0.6.

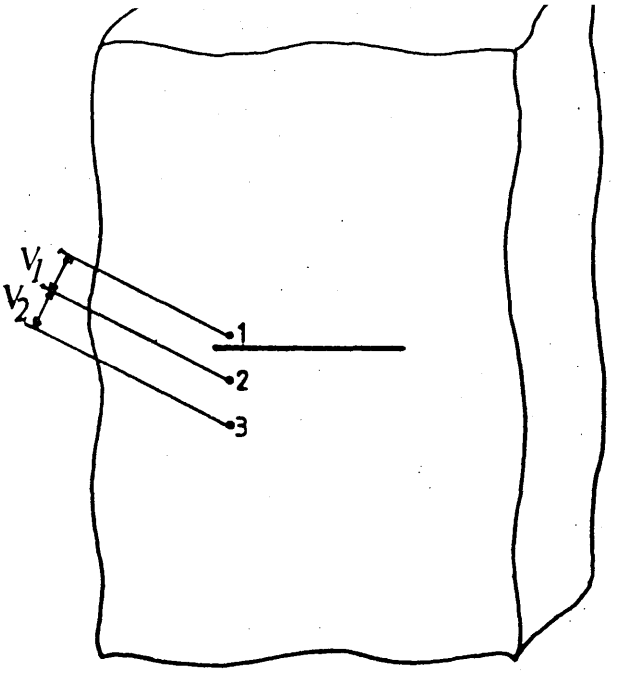

Fig. 5.5 ACPD crack size measurment for series (i) tests, showing the set up for one of the 24 voltage reading stations.

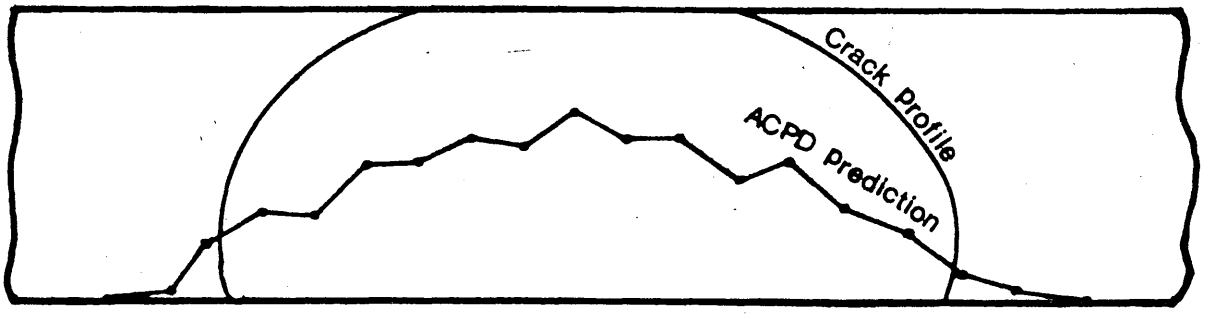

Fig. 5.6 Crack profile prediction by ACPD in series (i) tests.

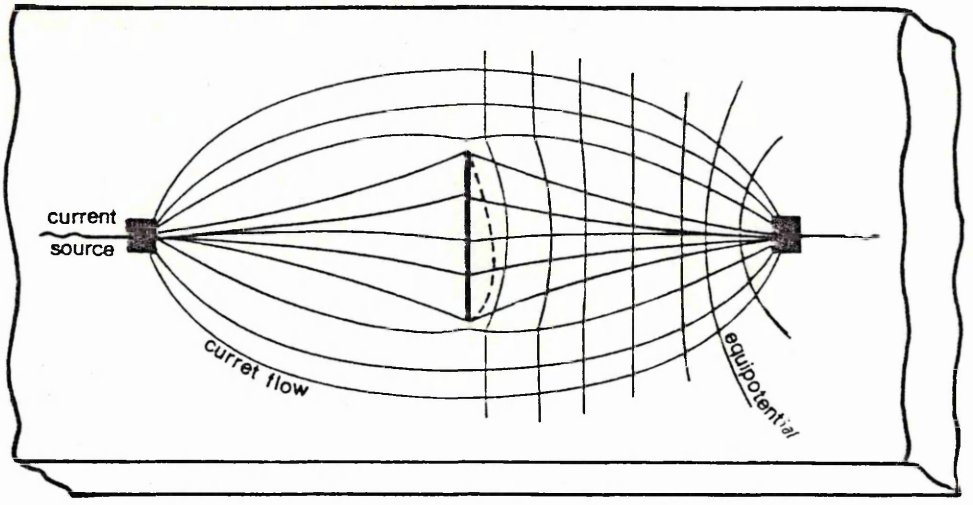

Fig. 5.7 Current flow on the surface of a conductive plate containing a part through surface crack.

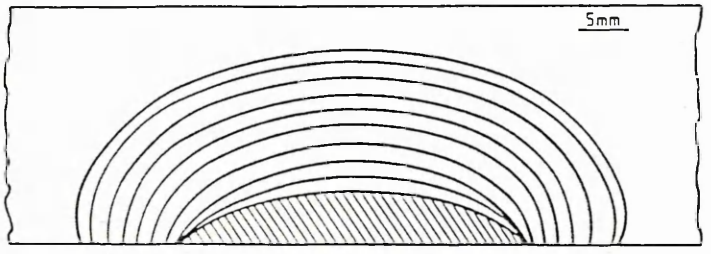

Fig. 5.8 Beach marks on the fracture surface.

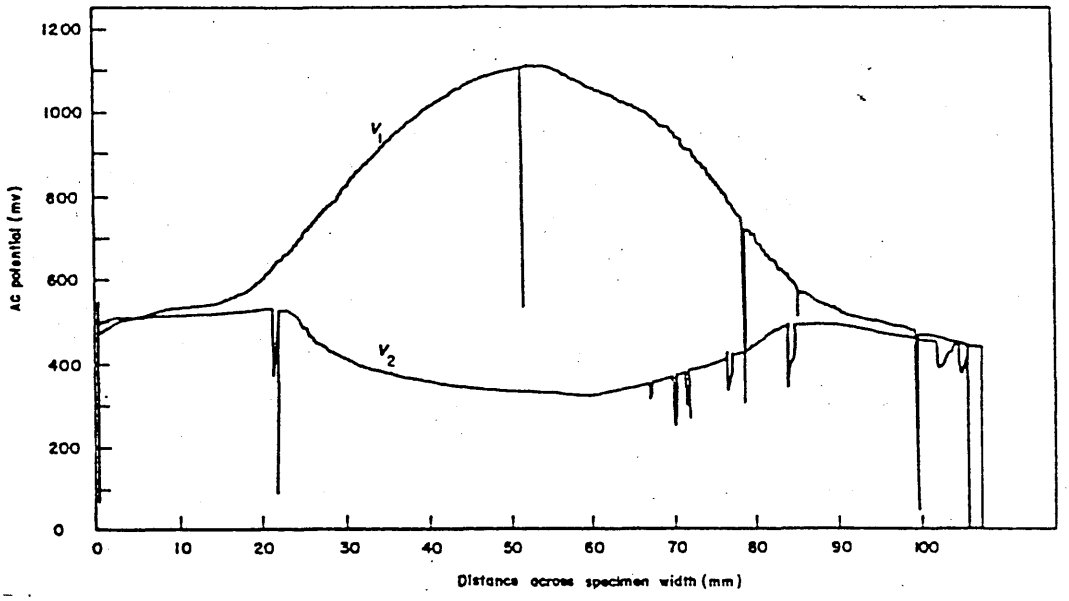

Fig. 5.9 Typical variation of the AC potential field, measured on the specimen surface across (V_1) and adjacent (V_2) to the crack.

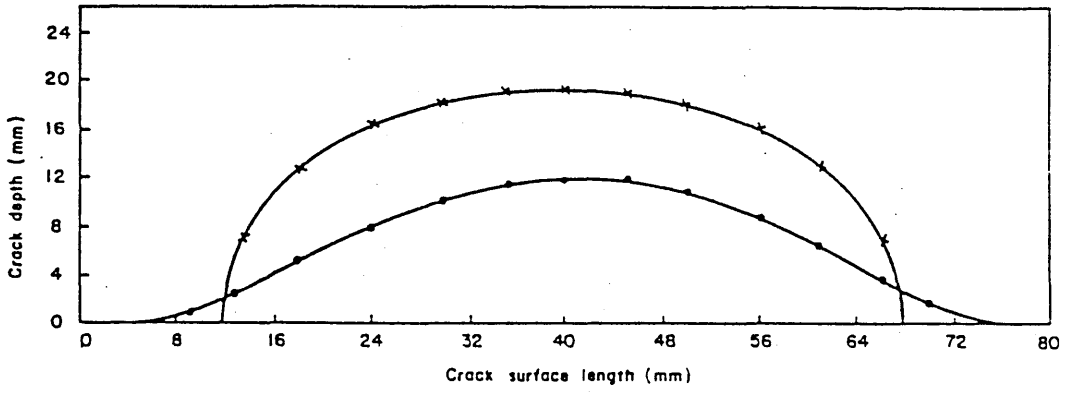

Fig. 5.10 Unmodified measurement of crack profile by improved ACPD technique.

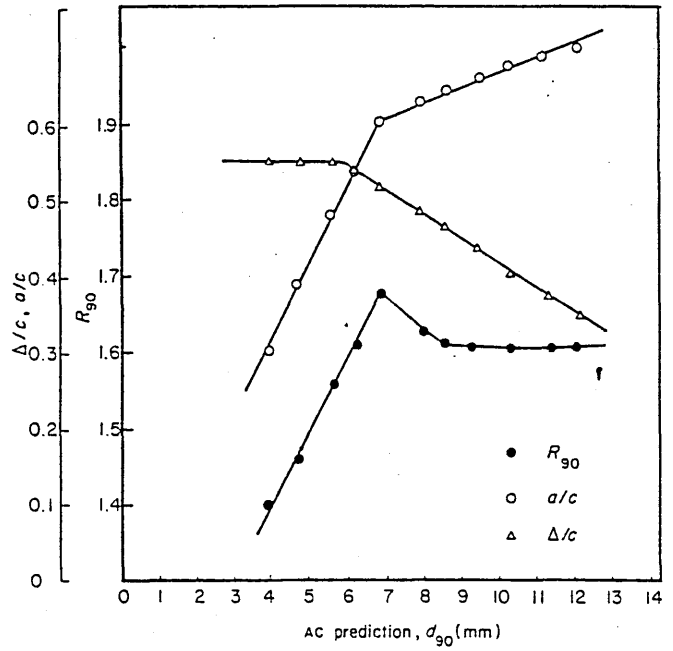

Fig. 5.11 Variation of modification factor, crack aspect ratio and probe size with the AC measurment of the crack depth at the crack deepest point.

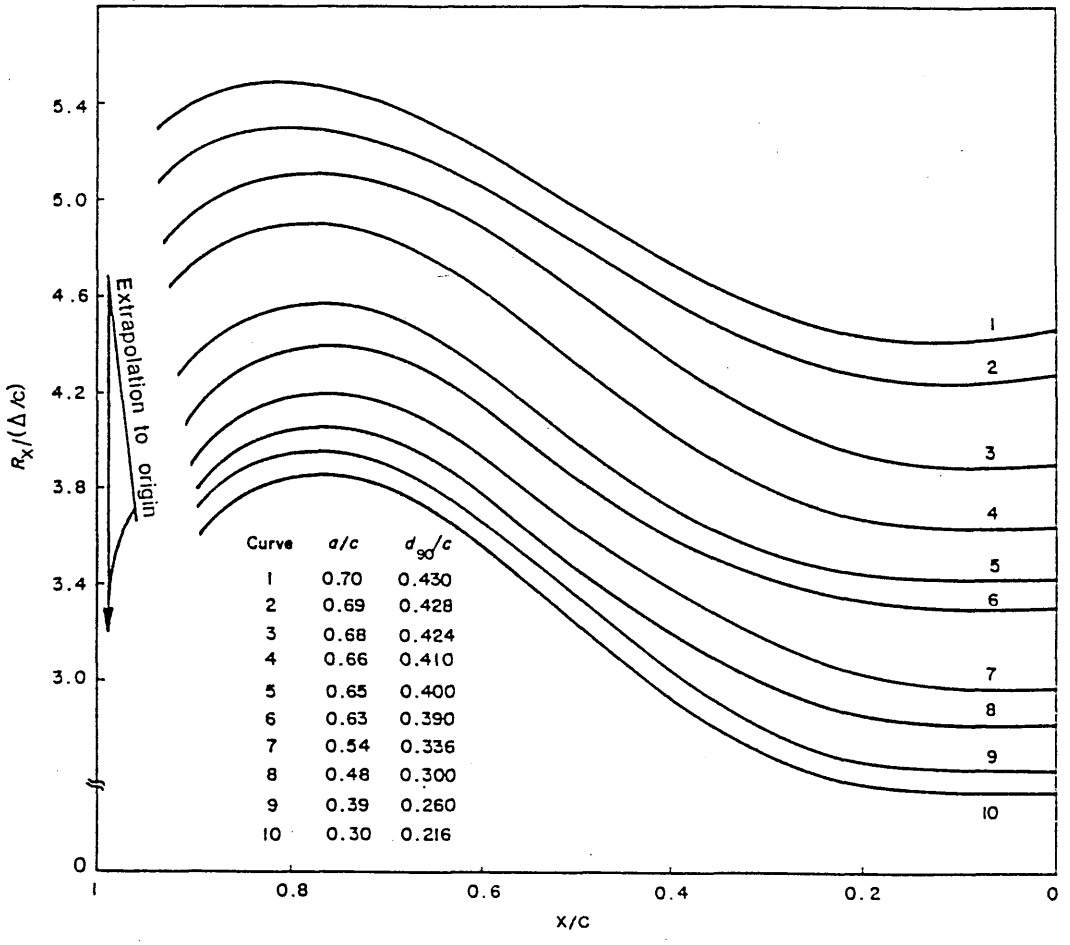

Fig. 5.12 AC modification factor along the crack front for different crack shapes.

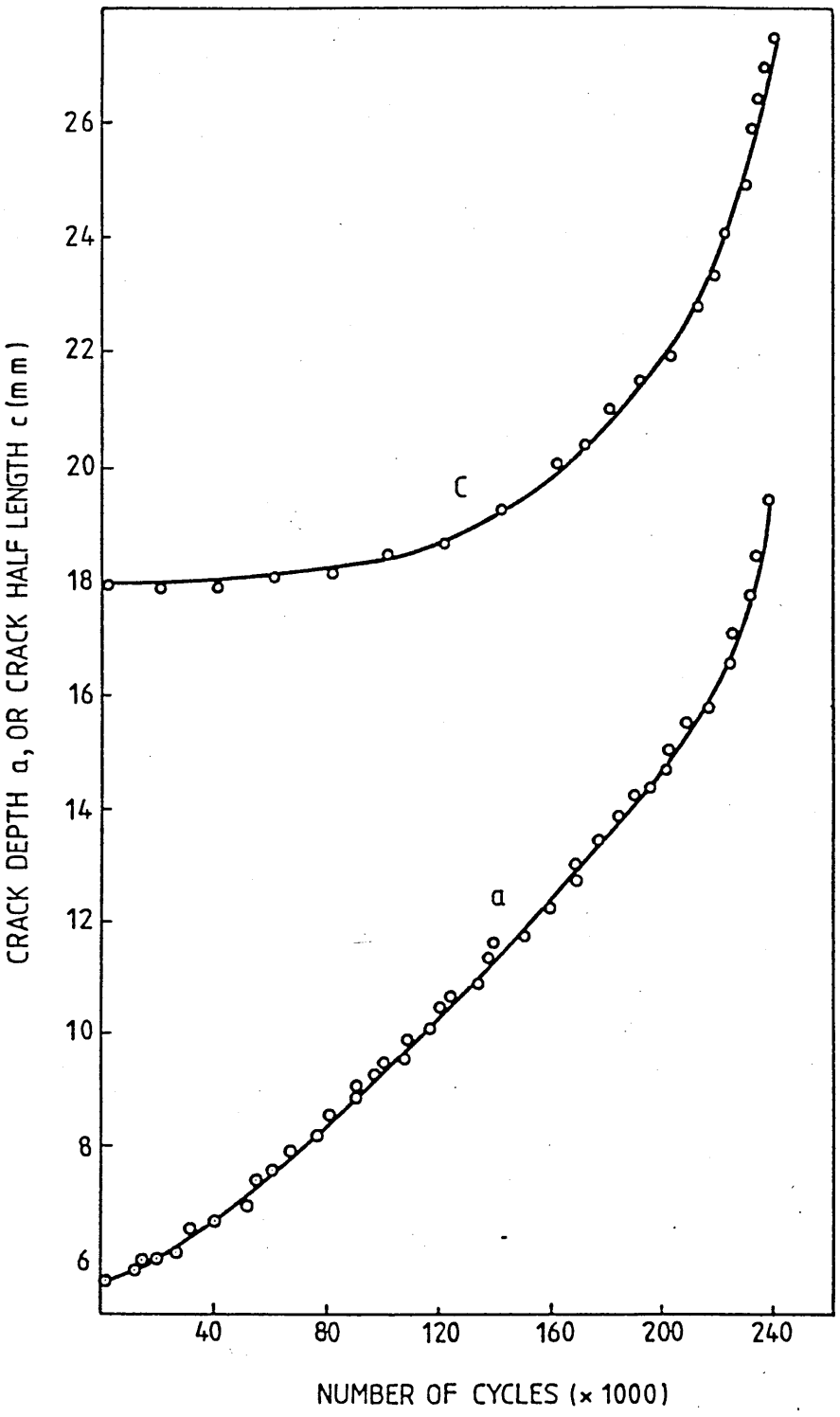

Fig. 5.13 Fatigue crack growth through the thickness and on the surface.

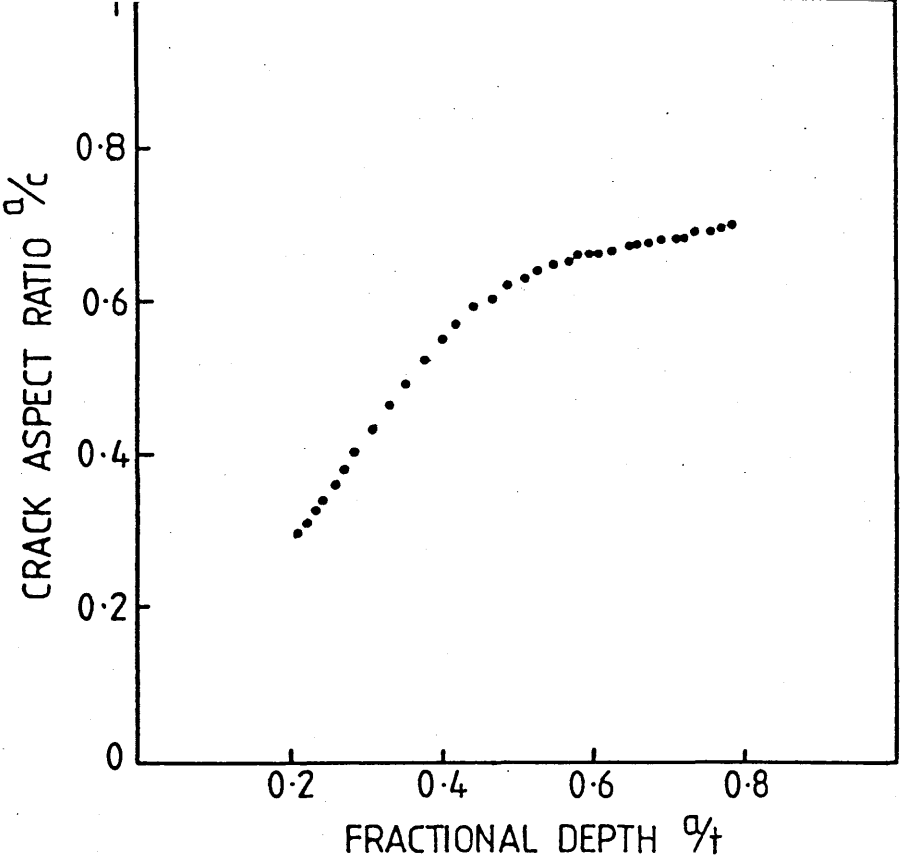

Fig. 5.14 Variation of crack aspect ratio, a/c, against crack fractional depth, a/t, showing the tendency for the crack to propagate towards a preferred shape.

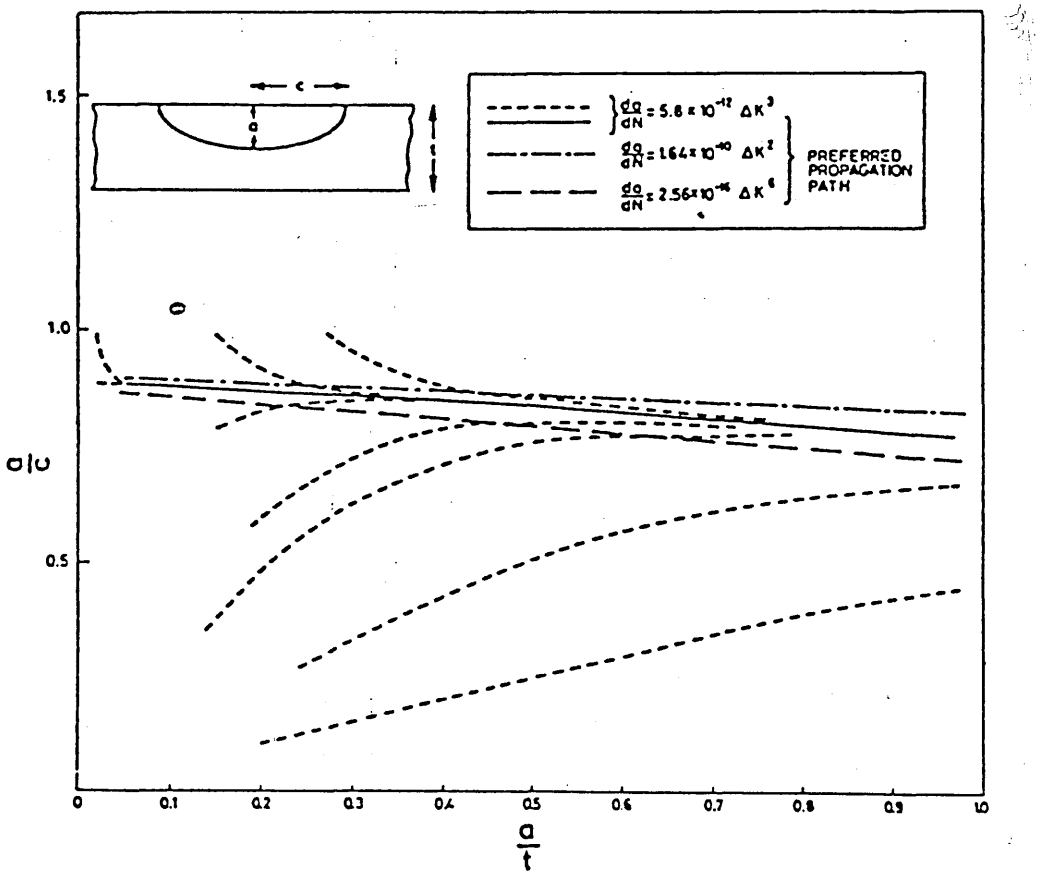

Fig. 5.15 Crack shape change during uniform tensile fatigue loading calculated by Scott and Thorpe [20].

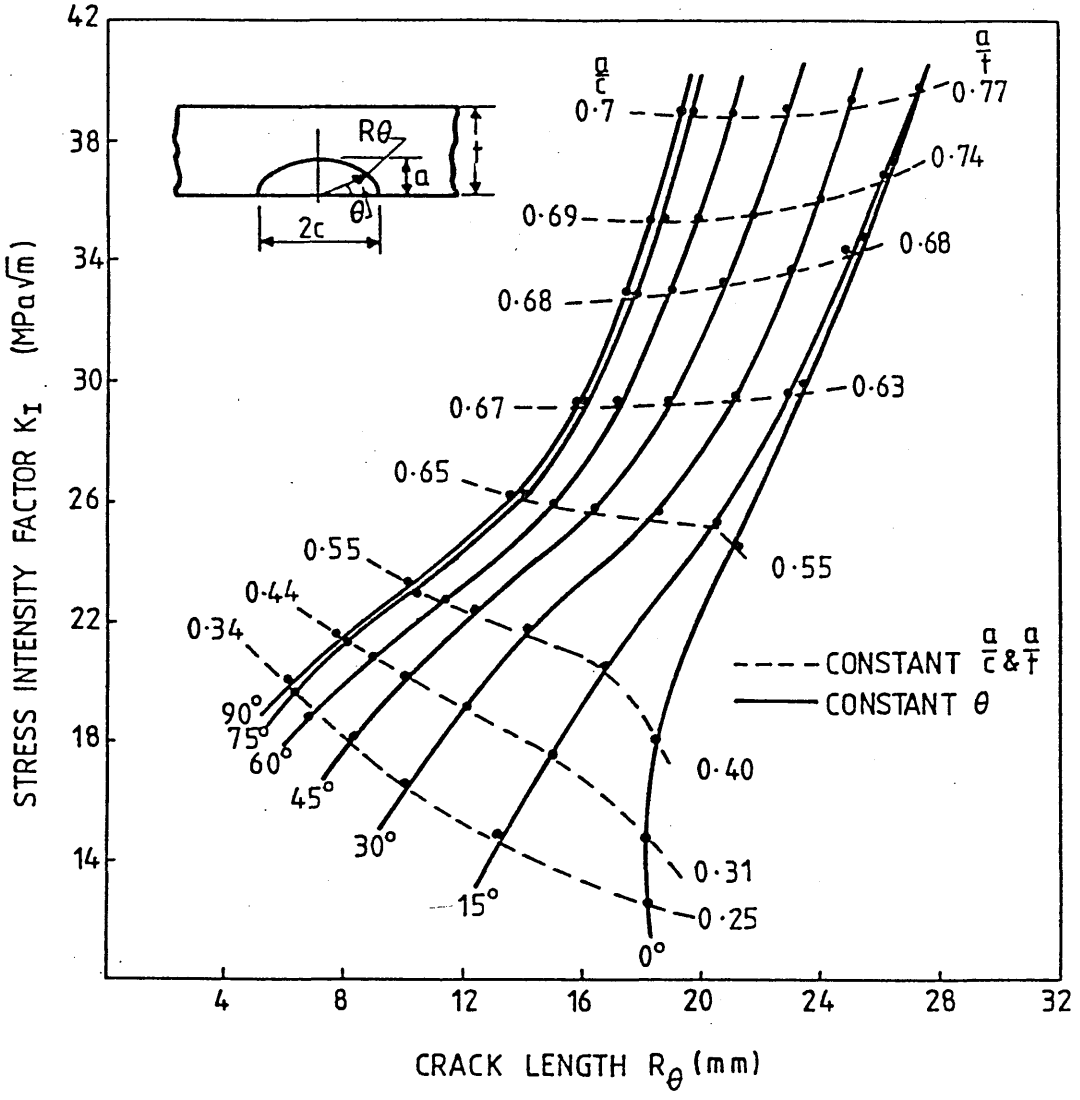

Fig. 5.16 Distribution of stress intensity factor along the entire crack front as afunction of crack shape.

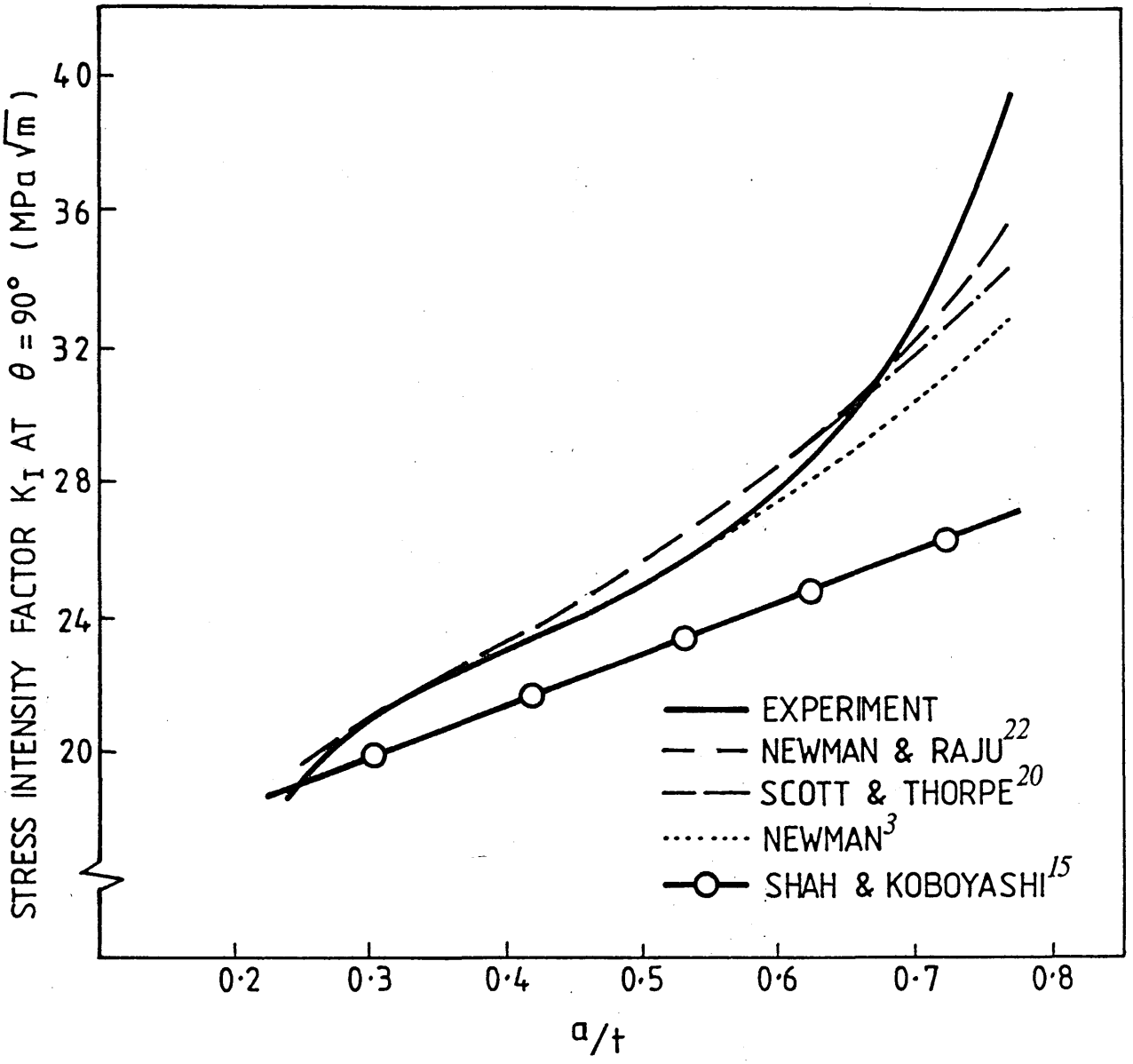

Fig. 5.17 Comparison of stress intensity factor at the deepest point with the prediction of the analytical solutions.

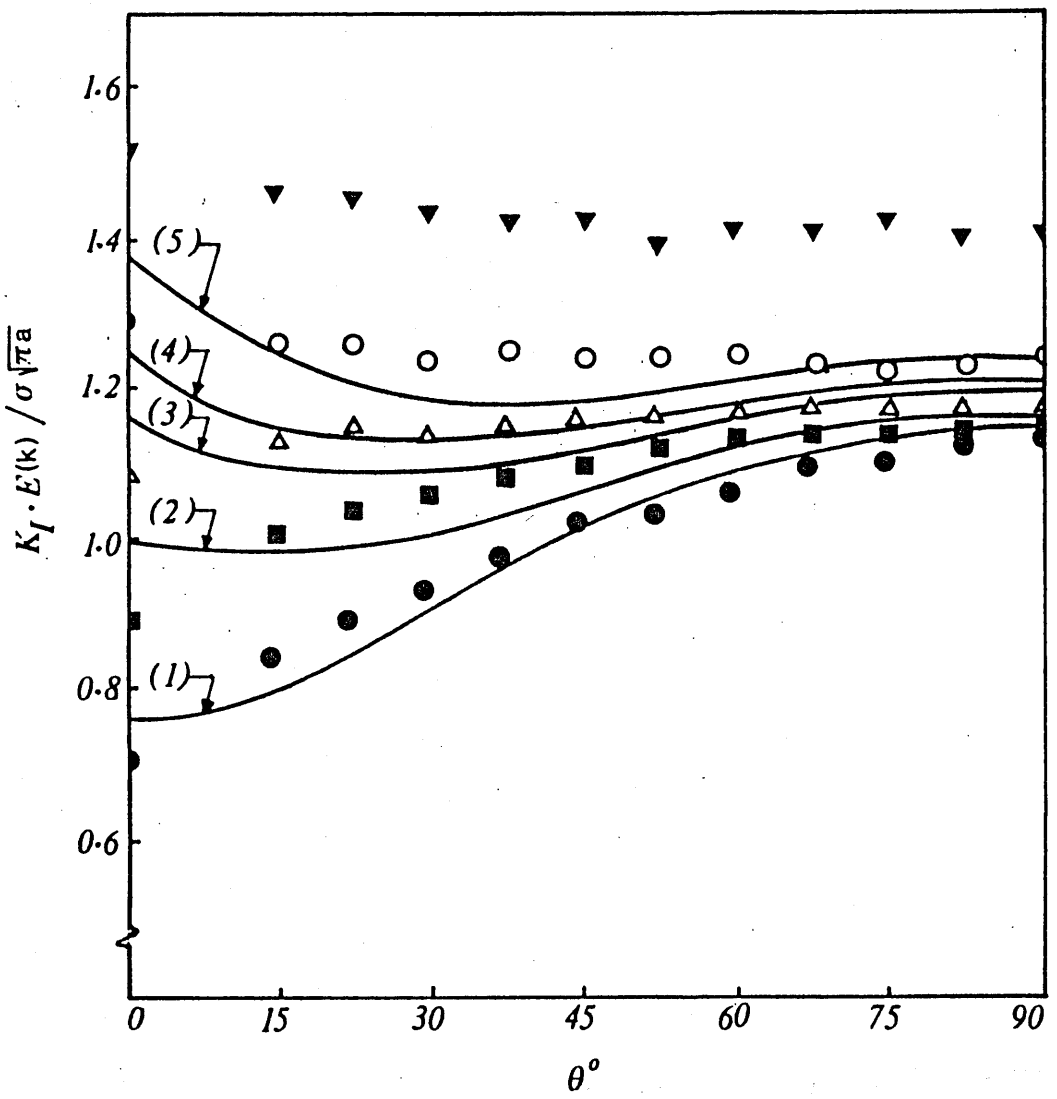

Experiment	Computed	a/t	a/c
●	1	0.25	0.34
■	2	0.40	0.55
△	3	0.55	0.65
○	4	0.63	0.67
▼	5	0.77	0.70

Fig. 5.18 Comparison of stress intensity correction factor around the entire crack front with the prediction of the Newman and Raju[22] solution.

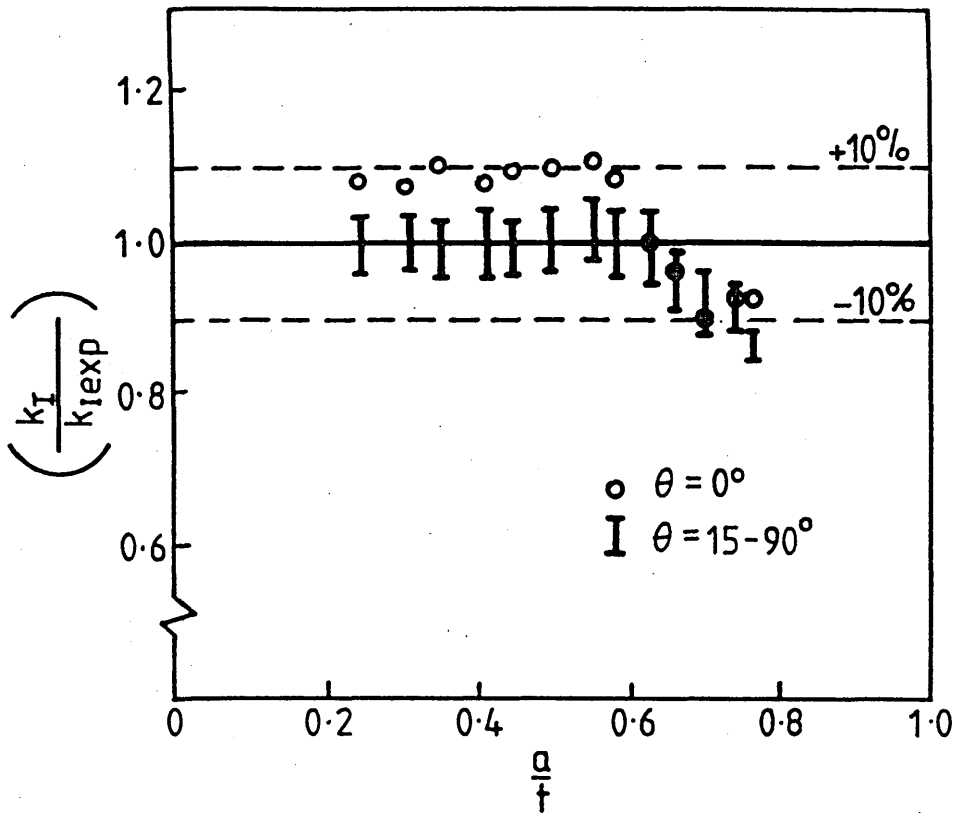

Fig. 5.19 Correlation of present results with the Newman and Raju[22] solution.

Section 6

ELASTIC-PLASTIC ANALYSIS OF PART-THROUGH SURFACE CRACKS

6.1 Introduction

Detailed examination of failure of engineering components reveals that in most cases crack propagation starts from a Part-Through Surface Crack (PTC). Increasing requirements for less conservative designs have increased the practical importance of elastic-plastic assessment of these defects. However due to the three dimensional nature of the problem, the analysis of fracture toughness parameters is more complex than that of the plane problem i.e. through thickness cracks.

In the work presented in this section, ductile fracture from a semi-elliptical surface crack subjected to tensile loading is considered. Crack Opening Displacement (COD) and crack extension all along the crack front has been experimentally measured and by using the COD R-curve technique, initiation COD, δ_i, is derived for the entire crack front. As an introduction to this section a review of previous investigations is presented. This is followed by a description of the experimental work carried out here and comparison of results with those obtained for through crack test pieces.

6.2 Review of experimental work on PTC

A review of literature indicates that while elastic analysis of PTC has received/

considerable attention, as discussed in section 5, there is relatively little work on the elastic-plastic fracture process from such defects.

The elastic-plastic fracture may be characterized by crack opening displacement. In small scale yielding (SSY), the relationship between COD and stress intensity factor K may be used to calculate critical defect size[1]:

$$K = \sqrt{\frac{1}{m}\ \delta E \sigma_y} \qquad (6.1)$$

In general yielding however final failure is associated with a large degree of plasticity and thus an approach which is capable of describing failure in the elastic-plastic and fully plastic regime is required. As discussed in section 1.6.6. a critical value of COD may be used directly as a post yield fracture parameter to assess the ductile failure of service components. Therefore a need exists to characterize COD at the tip of a surface crack and to relate this to COD measured in standard through thickness test pieces.

A typical semi-elliptical surface cracked plate is shown in Fig. 6.1. In a few of the experimental studies reported, because of difficulties involved in measuring crack tip displacement, COD was measured as crack mouth opening i.e. displacement of the crack faces on the specimen surface at the mid-point of the crack. Randall[2] was the first to measure crack mouth opening. His specimens were instrumented primarily to observe possible pop-in behaviour, but from the load-COD records he was able to correlate the COD values to the extent of plastic flow at the crack tip. Tiffany et al[3] used crack mouth opening measurements as a qualitative indication of sub-critical crack growth. Quantitative analysis of COD however, has been restricted by several factors. One is the lack of an exact/

solution for COD as a function of crack size and shape. Another factor is that no extrapolation formula exists to relate crack-mouth opening displacement to the actual crack tip displacement. Lack of such a relationship is due to a lack of understanding of the compliance of the cracked section.

Clearly measurement of COD on the specimen surface, though useful, does not measure directly the fracture characterizing parameter over the entire crack front. Prantl and Prodan[4] devised a technique to derive crack tip COD from the crack mouth displacements for a low strength structural steel. They measured the initial notch opening displacement in seven positions along the crack line on the surface by using a miniature COD-meter, in an attempt to record the spatial opening of the whole notch. The opening of the crack tip was then determined by extrapolating the notch opening displacements to the actual crack front. For a crack shape of $a/c = 0.4$ and $a/t = 0.5$ (a, c and t are defined in Fig. 6.1), they found that upon attainment of a certain load, crack extension occurs in the interior and only at loads very close to the maximum load does crack growth become noticeable on the surface of the specimen. This implies that for this particular crack profile initiation occurred at some point away from the specimen surface. It was also found that at low ratios of net stress to yield stress i.e. for conditions approximating to SSY, the crack front COD closely followed the linear elastic crack opening displacement $\delta = G/\sigma_y$. The onset of stable crack growth was also detected by acoustic emission techniques and results similar to those for measurement of COD when the SSY condition was exceeded were found. However caution should be excercised in using the Prantl and Prodan results because of poor accuracy in the COD measurements and the large scatter in the acoustic emission results.

6.3 Experimental procedure

The experimental procedure is based on the multi-specimen R-curve technique for determination of critical COD at the onset of crack extension. In this technique, testing of identical fatigue pre-cracked specimens is essential to obtain accurate results. The procedure adopted for determination of δ_i was as described in BS5762[20] (for deep through cracks). However, because of the difficulties involved in sizing of PTC, production of identical crack profiles can be very difficult. Some investigators[5] have used a single specimen method for surface cracks by periodically fatigue marking of the fracture surface. It is thought that extrapolation to zero crack extension with this single specimen method may not give an accurate evaluation of δ_i due to variation in crack profile development under the application of different load levels.

The successful use of the A.C. potential drop technique in the present study (section 5) made it possible to reproduce crack profiles and thus determine the COD R-Curve for part-through cracks. The procedure includes the following stages:

(i) Production of fatigue pre-cracked specimens with identical crack profiles.

(ii) Loading of the specimens to appropriate points on the load-displacement curve under displacement controlled conditions, at room temperature.

(iii) Recording load, displacement and the COD, at the crack tips on the specimen surface, as a function of time.

(iv) Sectioning of specimens (off load) into thin slices perpendicular to crack plane. Each side of each slice represents the crack tip profile at a certain position on the crack front, as schematically illustrated in Fig. 6.2.

(v) Determination of the exact position of each profile in the crack front, measurement of crack tip opening displacement δ and crack extension Δa.

(vi) Plotting of COD and Δa, for each position in the form of a R-curve and extrapolation to zero crack extension to obtain δ_i.

6.3.1 Test procedure

Three specimens with the dimensions h=850mm w=150mm and t=25mm were cut from the parent plate in the transverse direction. Each specimen was ground to provide a suitable surface for observing the crack growth. An initial notch of aspect ratio $a/2c$=0.14 where a=5mm and 2c=35mm was machined in all specimens with a 0.15mm thick slitting wheel.

Fatigue cracks were initiated and grown from the base of these notches by subjecting the specimens to constant amplitude, sinusoidal tension to tension cyclic loading in a 1MN Dartec servo-hydraulic testing machine at stress ratio of 0.1 and frequency of 1Hz. The maximum nominal net section stress in the fatigue loading range was 150 MNm^{-2} (40% of net section yield). This loading gave a maximum stress intensity factor of 40 $MPam^{0.5}$ as the crack grew to 70% of the specimen thickness.

To measure the development of the crack shape, the A.C. potential drop technique was used as reported in section 5.6. By precise monitoring of the crack profile development it was possible to grow identical semi-elliptical fatigue cracks with a = 17.4 $\pm$ 0.1mm and 2c = 50.2 $\pm$ 0.2mm. This shape was consistent with the preferred crack shape for the material, as described in section 5.7.2.

Since the load capacity of the testing machine was insufficient for static loading, the width of pre-cracked testpieces were reduced to 96mm, 94mm and 92mm for specimens 1, 2, and 3 respectively. To monitor the COD on the specimen surface, two clip gauge extensometers were positioned between knife-edges attached to the specimen surface above and below the crack plane, with an initial gap of 5mm. Specimens were loaded in tension under displacement control at a strain rate of 1.6×10^{-3} S^{-1}. Values of load, cross-head displacement and clip gauge displacements were continuously recorded at 30 second intervals by a multi-channel data logger, for subsequent processing.

The first specimen was deformed until a maximum load of 885KN corresponding to 6.80mm axial displacement was achieved. The second and third specimens were loaded to overall displacements of 4.54mm and 4.24mm respectively. On the attainment of prescribed load the specimens were unloaded and the deformed front and back surfaces photographed. The specimens were then sectioned normal to the crack plane into slices of approximately 3mm thick and 1.8mm apart Fig. 6.2. The sectioning sequence started at a position close to the centre line of the crack such that the deepest point of the crack would be contained on one side of the first section. By this procedure each section revealed two crack tip profiles of/

the damaged crack front, one on either side of each slice. The sections were then polished and the COD at the original fatigue crack tip δ and the crack extension Δa were measured to within $\pm$ 0.02mm. The measurement was made by using an optical micrometer attached to a stereo-microscope at an appropriate magnification. The exact position of each section profile on the crack front was determined by measuring the initial gaps between the sections and the thickness of each section prior and after polishing.

6.4 Results and discussion

The load-displacement curves for all three specimens are given in Fig. 6.3. It has to be noted that the width of specimens differed slightly resulting in different load-displacement curves. In Fig. 6.4 the clip gauge displacements for specimen 1, loaded to maximum load, are plotted against the applied load. The absence of a well-defined point on these curves to mark the initiation of crack extension, necessitated the observation of the damaged crack front for this specimen prior to the loading of the others. Fig. 6.5 shows the crack profile at $\theta = 45^{o}$ (for a definition of θ see Fig. 6.1) for specimen 1. In view of the large amount of crack extension associated with the application of maximum load, and on the basis of engineering judgment, specimens 2 and 3 were loaded to appropriate points on the load-displacement curve to give suitable data for the R-curves.

Observations during the test revealed that the yielding of all specimens occurred when the net section stress exceeded the uniaxial yielding stress of the material and just after that the first visual indication of plastic deformation, in the form of small surface depressions,/

observed at the crack tips on the specimen surface. Lack of lateral constraint on the specimen front surface reduces the hydrostatic stress component and material experiences extensive yielding characteristic of the state of plane stress. As a result surface contraction, or crack tip dimpling, develops at stress levels corresponding to those at which crack tip blunting occurs. These dimples are highly localized and are associated with plastic deformation introduced upon loading.

Fig. 6.6 shows the front surface of specimen 2 after unloading. Light reflection at the crack surface tips due to presence of dimples reveals the pattern of plastic zone development. This pattern is not a quantitative representation of plastic zone size. However it illustrates qualitatively that the shape of the plastic zone is characteristic of the plane stress condition in which the crack propagates by a shear mechanism along 45^{o} shear planes. The crack extension on the surface of specimen 1 is shown in Fig. 6.7. The form of failure is Mode II ductile shear along 45^{o} planes consistent with the plastic zone orientation. This behaviour has been observed by other workers for a variety of materials[6-9]. At high applied loads Mode III out of plane shear may also be involved in the failure process due to the action of a significant bending moment caused by the eccentric loading on the remaining ligament.

On the back surface of all specimens a large surface depression elongated in the width direction of specimen in the crack plane and with a length approximately equal to 2c was observed. This phenomena has been seen by other investigators[10,11]. Figs. 6.8 and 6.9 show the back surface morphology of specimens 1 and 2 respectively, and indicate that the extent of back surface depression is larger for specimen 1 which has undergone higher/

plastic deformations. It was intended to measure the size of back surface depressions by a replication method and correlate them with the values of crack tip COD and crack extension Δa along the crack front. However due to the difficulties involved in the procedure and the diversity from the main objective of the investigation, this intention was abandoned. Nevertheless the phenomena of back surface dimpling may provide a suitable technique for detection and evaluation of those surface cracks which are present on the inside surface of pressure vessels and which, therefore, may not be conveniently approached by direct detection methods.

The appearance of the crack tip damaged regions at $\theta = 90$, 60 and 15 degrees for all three specimens can be seen in Figs. 6.10 to 6.12. The mode of fracture in the specimen interior is Mode I ductile tearing as opposed to ductile shearing on the specimen surface (Fig. 6.7).

Results of COD and Δa measurements on the entire crack front, are given in Table 6.1, where x is the distance of each section profile from the crack centre line and θ is the angular position of each point on the crack front from the crack surface line. The symmetry of the problem allows the evaluation of only one half of the crack plane. For test 2 however, the complete crack front data is presented which validates the symmetry assumption. The COD at the crack tip on the specimen surface was determined from the clip gauge corrected for the elastic unloading component to allow comparison with the other COD results measured using the sectioning technique.

In Fig. 6.13 the variation of COD and Δa along the whole crack front are plotted against the angular position. Fig. 6.14 shows the same data plotted as a function of distance from the crack centre line.

As can be seen in Fig. 6.13 the crack extension Δa is almost constant for $\theta \geq 30^{o}$. As θ decreased below 30^{o} Δa increases to a maximum before approaching a lower value on the surface. The observation of crack front profile and the results presented in Fig. 6.13 indicate that for a given amount of loading, the crack extension at the positions some distance beneath the surface is greater than that at the deepest point. Assuming that the material is isotropic and homogeneous with respect to the crack extension through the thickness, this behaviour may be modelled as discussed below.

In part through surface cracks, the state of stress varies from that of plane stress on the specimen surface to plane strain in the interior. Thus the deepest point of the crack is in a region of relatively high plastic constraint. It has been shown[12] that the resistance to crack extension under this condition is low and hence a greater crack extension is expected at the deepest point than on the front surface. Comparison between Δa values at $\theta = 0$ and $\theta = 90$ degrees (Fig. 6.13) illustrates this tendency. Also experimental results of You[9] for a shallow surface crack ($^{a}/_{t} = 0.2$) show the same behaviour. With a deep semi-elliptical crack however (similar to that used in this work), the proximity of back surface produces a reduction of triaxiality in the crack tip flow field and results in higher crack growth resistance. Thus larger displacements (COD) are required at the deepest point both to initiate and continue crack extension. This requires further crack extension in the regions of higher triaxiality further from the back surface, to provide adequate displacements for crack extension at the deepest point. Furthermore there may be a small bending moment associated with a deep surface crack in a finite size plate loaded under uniform tension. This may affect the stress and strain fields along the crack front and thus the crack growth resistance.

Fig. 6.13 also shows the variation of COD along the crack front for all the tests. COD decreases from the deepest point towards the specimen surface with a mimimum value near the specimen surface (approx. $\theta = 15^{o}$). the intensity of this reduction increases as the amount of crack extension is increased i.e. from test 3 to test 1. In test 1 (maximum load), the development of considerable crack extension at the deepest point results in an elevation of crack growth resistance of the remaining ligament and thus a steeper variation of COD is expected.

From the data presented in Fig. 6.13, the crack opening displacement at the initiation of crack extension δ_i, is determined by constructing COD R-curves (described in section 1.6.4) for seven positions $\theta = 0$, 15, 30, 45, 60, 75 and 90 degrees on the crack front as shown in Fig. 6.15. The δ_i values are obtained from the intersection of the R-curves and the blunting lines ($\delta = 2\Delta a$) which assumes a semi-circular shape for an opening and blunting crack tip. In Fig. 6.16 the variation of δ_i along the entire crack front is shown.

From the work on the fatigue crack growth of semi-elliptical cracks presented in Section 5, the distribution of stress intensity factor around the periphery of this particular crack geometry has been evaluated and is presented in Fig. 6.17. It can be seen in Fig. 6.16 that on the surface ($\theta=0^{o}$) δ_i has the highest value. The same feature exists in the distribution of K_I (Fig. 6.17). This observation in both cases is expected since the tip of the crack on the specimen surface is in a region of plane stress. In the interior however, the distribution of δ_i and K_I vary markedly. Under SSY condition where plasticity is confined to the crack tip, K_I decreases from $\theta=15^{o}$ towards the deepest point ($\theta=90^{o}$) and

as/

discussed in Section 5, it is an indication that the crack maintains its preferred shape. In the post-yield regime the fracture toughness parameter δ_i, is a minimum at locations beneath the specimen surface ($\theta=15^o$) and increases towards the deepest point ($\theta=90^o$) suggesting that failure initiation occurs first at locations corresponding to θ in the range 10 to 20°. Hence the crack profile deviates markedly from the preferred LEFM shape. This behaviour is clearly shown in Fig. 6.18 where the sequential development of crack profile, from test 3 to test 1, is graphically illustrated. The fracture surface of an aluminium alloy specimen containing a semi-elliptical fatigue crack of $a/c = 0.68$ and $a/t = 0.35$ also shows this type of profile development under monotonic tensile loading[8] (Fig. 6.19).

A comparison between the metallographic studies of the present results and those for SECT and DEC geometries reported in Section 4, provides some insight into the fracture characteristics of semi-elliptic cracks. The crack tip morphology at the deepest point for all three tests, shown in Figs. 6,10a, 6.11a and 6.12a, is very similar to that of an extending crack in the SECT geometry (e.g. Fig. 4.13). In both cases the crack tip blunts during opening by a two vertix mechanism producing a wedge shaped tip. The crack extends directly ahead of the fatigue crack tip, in the crack plane, with little evidence of any macroscopic hole growth and coalescence process. Furthermore the measured δ_i of 0.550 mm at deepest point agrees well with the δ_i measured for the SECT geometry at the same temperature ($\delta_i = 0.580$ mm, Table 4.2). These similarities suggest that the stress and strain fields at the deepest point are very similar to and may be represented by that of SECT geometry. By recalling the results of numerical analysis reported in Section 4.7, it can be deduced that a low level/

of triaxiality associated with plane strain condition exists at the deepest point, with a confined region of high triaxiality and plastic strain very close to the crack tip ($x/\delta = 0.6$).

The morphology of the crack tip at $\theta=15^o$ is shown in Figs. 6.10c, 6.11c and 6.12c for all three tests. The crack tip shape and the mechanism of crack extension in this region is very similar to that for the DEC geometry shown in Fig. 4.10a in which the crack blunts during opening into a smoothly curved shape and extends directly ahead by a hole growth and coalescence mechanism. Also the measured value of δ_i at $\theta=15^o$ (0.340 mm) is very close to the δ_i obtained for the DEC geometry (δ_i = 0.325 mm, Table 4.1). Indeed these similarities indicate that the flow field at $\theta=15^0$ may be similar to that associated with DEC geometry, with a high triaxiality.

White et al[13] investigated the correlation between the tearing characteristics of semi-elliptical cracks in bending and the compact tension (CT) geometry. They used a multi specimen procedure to determine the J-resistance curve for the semi-elliptical cracked geometry with initial fatigue cracks of a/c ranging from 0.35 to 0.49 and a/t from 0.35 to 0.4. J was calculated using the line spring analysis of Parks and White[14]. For the CT geometry J was measured from the area under load-displacement curve. White et al[13] reported that in bending the crack extension, Δa, along the crack front from $\theta=20^o$ to $\theta=90^o$ is constant, (although the observation of a variation in Δa might have been hindered by a large scatter in their results), therefore only the result at $\theta=90^o$ was compared with CT geometry. It was concluded that J at initiation of crack extension was the same for the CT geometry and the semi-elliptical surface/

cracked geoemtry. This agreement can be attributed to the effect of crack geometry and loading configuration. The analogy between the deepest point of a semi-elliptical crack with $a/t = 0.35$ (as in White's study) loaded in bending and that of a through crack bend specimen of $a/W = 0.35$ implies that the crack tip at $\theta=90^o$ is in the position of high constraint. Also experimental work of You[9] has shown that under bending, the blunted crack tip at $\theta=90^o$ has a semi-circular shape and crack extension occurs, by the void growth and coalescence mechanism which is representative of highly constrained geometries. Therefore it is not unexpected that a J_i similar to the CT geometry is obtained. In the tension case and for the crack geometry investigated here ($a/c = 0.69$, $a/t = 0.7$) however, the flow field at the deepest point represents a region of low constraint and thus a higher δ_i (or J_i) than that expected for a CT geometry is achieved.

White et al[13] reported that despite a close agreement between J_i at $\theta=90^o$ and the CT geometry, the J tearing resistance, dJ/da, differed considerably, being higher for semi-elliptical cracked geometry.

In the present investigation the COD tearing resistances $d\delta/da$, all along the crack front measured from the slope of COD R-curves in Fig. 6.15 are given below:

θ^o	$d\delta/da$
15	0.625
30	0.7
45	0.775
60	0.82
75	0.85
90	0.85

A $d\delta/da$ = 0.75 for the SECT geometry at room temperature is obtained from the resistance curve shown in Fig. 4.4. For the DEC geometry it is not possible to calculate the tearing resistance from the results presented in Section 4, due to the fact that initiation of crack extension was readily detected without the need to construct the resistance curve. However a value of $d\delta/da$ = 0.61 for a structural steel similar to the one used here has been reported[15] using the three point bend geometry which has a slightly lower constraint flow field than that for the DEC geometry. These results indicate that the tearing resistance at $\theta = 15^o$ and $\theta = 90^o$ is only slightly higher than that of laboratory DEC and SECT specimens respectively, which from an engineering point of view it may be considered a fortunate circumstance.

From the above observations it may be concluded that the progressive increase of δ_i from $\theta = 15^o$ to $\theta = 90^o$ (Fig. 6.16) is an indication of the variation of the constraint along the crack-front. Thus in order to prevent excessive conservatism or unsafe designs during defect assessment for structures containing part-through surface breaking cracks, care must be taken to use an appropriate fracture toughness value which has been evaluated from small standard laboratory test pieces with constraint appropriate to the defected structure in question.

There are currently two commonly used methods in the U.K. for defect assessment in elastic-plastic situations, R6[16] and the COD Design Curve (PD6493[17]). The PD6493 determines a tolerable defect parameter, $\bar{a}_m$, from a knowledge of the fracture toughness of the material and the applied stress via the COD design curve described in section 1.6.6. In the elastic-plastic regime fracture toughness is taken as a critical COD measured by testing highly constrained three point bend specimens in accordance/

with BS5762[20]. A surface defect is regarded acceptable if the effective size, determined from its actual size[17], is smaller than the tolerable defect parameter. For elastic-plastic situations where slow stable crack extension occurs BS5762 recommends that the selection of the critical COD should be by agreement between the parties involved. The critical COD could for example be that at the initiation of crack extension (δ_i) or at the attainment of maximum load plateau, δ_m.

The results of the present work indicate that crack initiation occurs first at locations beneath the plate surface ($\theta=15^o$) where the crack tip is in a region of relatively high constraint. Therefore when no crack extension is allowed and δ_i is selected as the fracture toughness parameter, PD6493 defect assessment procedure may be used without excessive conservatism outwith the limits of safety accounted for[19].

By selecting δ_m (from standard laboratory tested pieces) as the fracture toughness parameter, some crack extension is thus allowed for. In this case the results presented here indicate that the crack profile is changed by considerable crack extension at $\theta=15^o$ relative to the deepest point, as shown in Fig. 6.18 (and Fig. 6.19 for an aluminium alloy). This implies that the instantaneous tip of the crack at $\theta=15^o$ moves towards lower constraint regions and it is expected that the tearing resistance $d\delta/da$ at this location increases, approaching the resistance associated with the deepest point. This suggests that the crack advances in a manner in which it develops an almost straight front. Provided that the structure containing such a crack sustains the level of crack advance from the fatigue profile to the preferred tearing profile, then the crack behaviour may be conveniently characterized by the tearing resistance of the SECT geometry. In this case the use of δ_m obtained from highly constrained/

three point bend geometry introduces unnecessary conservatism into the defect assessment process. It appears that the appropriate critical COD for defect tolerance with respect to a PTC in a tensile field is that associated with maximum load in the SECT geometry provided that the associated tearing can be shown to be stable. Although the results of the present work are insufficient to be regarded as definitive, they do however provide valuable experimental evidence to support this hypothesis.

In both methods (R6 and PD6493) recommendations are given for the evaluation of plastic collapse condition prior to the detailed fracture mechanics assessment. The analysis in PD6493 is based on the assumption that plastic collapse occurs when the net stress on the cross section ligament reaches the flow stress. For hardening materials the flow stress is taken as the average of the yield and ultimate tensile stress. If such a criterion is satisfied, a part-through surface crack should then be assessed as a through crack as a result of the ultimate fracture of the PTC ligament. For surface cracks in tension, PD6493 suggests that the limit load condition is achieved when:

$$P_m = \sigma_o(1-\frac{a}{t}) \qquad (6.2)$$

where P_m is the average membrane stress and σ_o is the flow stress. In this analysis the crack is assumed infinitely long and no allowance is made for the load carrying capacity of the uncracked ligaments either side of the crack, associated with short cracks. This is clearly a conservative approach.

For the specimen loaded to maximum load (test 1), the failure stress is evaluated as P_m = 368MPa. By using the collapse analysis in PD6493 (equation 6.2) a failure stress of 140 MPa is predicted i.e. an underestimation by a factor of 2.6. Willoughby[18] investigated the plastic collapse phenomena for a variety of steels containing surface cracks of different geometries and found that PD6493 under-predicts the failure stress by a factor ranging from 1.2 to 5. Furthermore he observed that the severity of this over-conservatism increases by increasing crack aspect ratio. As mentioned above this excessive conservatism is attributed to the fact that PD6493 ignores the load distribution on the side ligaments. For the specimen geometry used in this investigation, the ratio of the remaining cross section ligament to the ligament considered by PD6493 is about 2.3. If therefore the predicted failure stress is elevated by this factor, a close agreement with experimental results is obtained. It should be noted however that the collapse analysis, considers only the initial defect size and hence should be sufficiently conservative to allow some crack extension if in the subsequent fracture assessment the maximum load COD is used. It should also be noted that the PD6493 defect assessment analysis has a built in factor of safety of 2-2.5 for evaluation of a tolerable defect size[19]. Therefore it is expected that a similar degree of conservatism is assumed for collapse analysis, although the scatter in plastic collapse data is usually smaller than fracture toughness data.

In the CEGB R6 method allowance is made for the uncracked ligaments on either side of short part through cracks. This is done by assuming that the defect is semi-elliptical in shape and that the stresses on the defect are redistributed over a length equal to (2c+t). In tension the R6 prediction of the membrane stress at collapse is given by:

$$P_m = \frac{\sigma_o (1-C)^2}{C + ((C)^2 + (1-C^2))^{0.5}} \qquad (6.3)$$

where C is the ratio of the area of the semi elliptical crack to the area of the containing rectangle defined by R6. For slender cracks, the effect of side ligaments is ignored.

$$C = \frac{\pi ac}{2t(2c+t)} \qquad \text{for } \frac{a}{c} \geq 0.2 \qquad (6.4)$$

$$C = \frac{a}{t} \qquad \text{for } \frac{a}{c} < 0.2 \qquad (6.5)$$

In this analysis R6 assumes a freely rotating pin joint at the back wall and thus incorporates a bending moment applied to the net section which reduces the collapse stress. Using this analysis the failure stress for test 1 in the present study is predicted at P_m = 169MPa which is approximately half of the experimental result. Willoughby[18] obtained a safety factor between 1 and 4 for a variety of crack geometries contained in different steel plates. However for the crack geometry studied here R6 is less conservative than PD6493. By removing the pin-joint assumption and considering rigid restraint[18] i.e.:

$$Pm = \sigma_o (1-C) \qquad (6.6)$$

then a value of 292 MPa is predicted for the failure stress which underestimates the experimental result by a factor of only 1.2. Thus it appears that the assumption of a pin-joint in R6 is over conservative for surface breaking cracks in practical tensile loading situations, especially for short cracks where the side ligaments provide certain degree of restraint. The finite crack length correction however seems to be justified.

6.5 References

1. Clark G., El Soudani S.M., Ferguson W.G., Smith R.E., and Knott J.F., I. Mech. E. Conf. ''Tolerance of Flaws in Pressurized Components'', Paper C90/78, London, 1978.

2. Randall P.N., Report No. AFML-TR-66-204, Air Force Materials Laboratory, Wright-Patterson AFB, Ohio, U.S.A. 1966.

3. Tiffany C.F., Lovenz P.M., and Shah R.C., The Boeing Co., Seattle, NASA Cr-722521, 1966.

4. Prantl G. and Prodan M., in ''Fracture and Fatigue'' Edit. Radon J.C., Proc. ECF3, p. 185, Pergamon Press, London 1980.

5. Lewis J.C. and Sines G., ASTM STP743, pp. 360-374, 1981.

6. Wiltshire, ''Crack Growth in Marageing Steels'' PhD. Thesis, University of Cambridge, 1980.

7. Collipriest (Jr) J.E., ''The Surface Crack: Physical Problems and Computational Solutions'' Ed. J.L. Swedlow, pp. 43-61, 1972.

8. Hoduluk L., Kordisch H., Kunzelmann S. and Sommer E., Int. J. Fracture, Vol. 14, pp. R35-R38, 1978.

9. You C.P., ''Mechanisms of Fracture in High Strength Structural Steels'' PhD. Thesis, University of Cambridge, 1984.

10. Francis P.H., Davidson D.L., and Forman R.G., Eng. Fracture Mech. Vol. 4, p.617, 1972.

11. Francis P.H., Int. J. Fracture Mech., Vol. 7, No. 4, pp. 475-477, 1971.

12. Cowling M.J. and Aboutorabi A.A., Paper 18, Proc. 2nd Int. Conf. Integrity of Offshore Structures, Ed. D. Faulkner, et al, Applied Science Publishers, 1981.

13. White C.S., Ritchie R.O., and Parks D.M., ASTM, STP 803, Vol. 1, pp. 384-409, 1984.

14. Parks D.M. and White C.S., J. Pressure Vessel Tech., Vol. 104, pp. 287-292, 1982.

15. Garwood S.J., and Turner C.E., Int. J. Fracture Vol. 14, pp. R195-R198, 1978.

16. Harrison R.P., Loosmore K., Milne I. and Dowling A.R., ''Assessment of the integrity of structures containing defects'', CEGB Report R/H/R6, Rev. 2, April 1980.

17. British Standards Inst. ''Guidance on some methods for the derivation of acceptance levels for defects in fusion welded joints'', PD6493, 1980.

18. Willoughby A.A. Research Report No. 191/1982, The Welding Institute, Cambridge, 1982.

19. Kamath M.S., Int. J. Pres. Ves. and Piping, Vol. 9, pp. 79-105, 1981.

20. British Standrads Inst. BS5762, ''Methods for Crack Opening Displacement (COD) Testing'', 1979.

Table 6.1(a) Values of COD and Δa around one half of the crack front in test 1. Distance x and angle θ are defined in Fig. 6.1.

x mm	θ degree	δ mm	Δa mm
-1.58	96.2	2.77	2.84
0.65	87.8	2.81	2.95
2.48	81.8	2.80	2.92
4.94	74.0	2.79	2.94
6.68	68.2	2.69	2.90
9.13	60.3	2.68	2.94
10.9	54.5	2.66	2.92
13.35	46.5	2.58	2.94
15.06	39.7	2.50	2.96
17.53	31.4	2.51	3.00
19.33	25.0	2.40	3.07
21.14	16.3	2.35	3.24

Table 6.1(b) Values of COD and Δa around the entire crack front in test 2. Distance x and angle θ are defined in Fig. 6.1

x mm	θ degree	δ mm	Δa mm
-20.49		1.07	1.29
-18.89		1.08	1.25
-16.64		1.06	1.16
-14.35		1.15	1.12
-11.87		1.14	1.06
-9.59		1.11	1.04
-7.28		1.16	1.07
-5.06		1.18	1.02
-2.53		1.16	1.05
0.25	89.1	1.19	1.07
2.26	82.8	1.19	1.06
4.55	75.2	1.18	0.98
7.04	67.0	1.16	1.03
9.23	60.0	1.17	1.02
11.77	51.3	1.09	1.05
13.90	44.5	1.13	1.08
16.20	36.8	1.09	1.08
18.43	28.9	1.06	1.19
21.18	16.5	1.01	1.28

Table 6.1(c) Values of COD and a around one half of the crack front in test 3. Distance x and angle θ are defined in Fig. 6.1

x mm	θ degree	δ mm	Δa mm
0.08	89.7	0.94	0.73
2.08	83.1	0.91	0.73
4.58	75.0	0.92	0.70
7.03	67.1	0.88	0.68
9.53	58.9	0.88	0.71
11.75	51.74	0.87	0.70
14.26	43.6	0.86	0.68
16.47	32.3	0.82	0.72
18.98	26.5	0.81	0.76
21.2	16.5	0.78	0.85

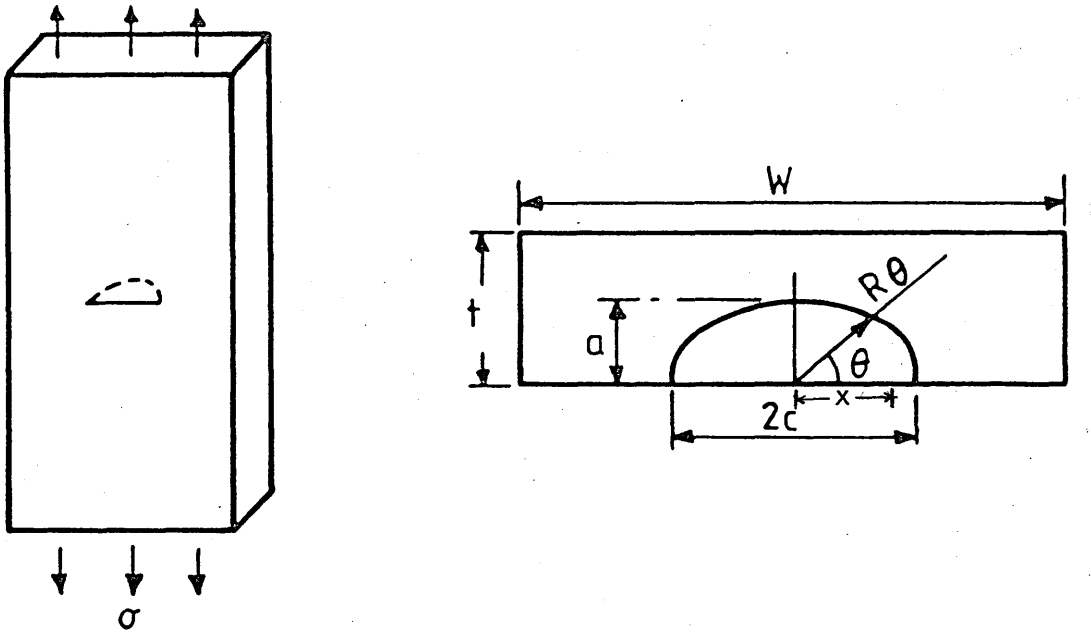

Fig. 6.1 Semi-elliptical surface cracked geometry.

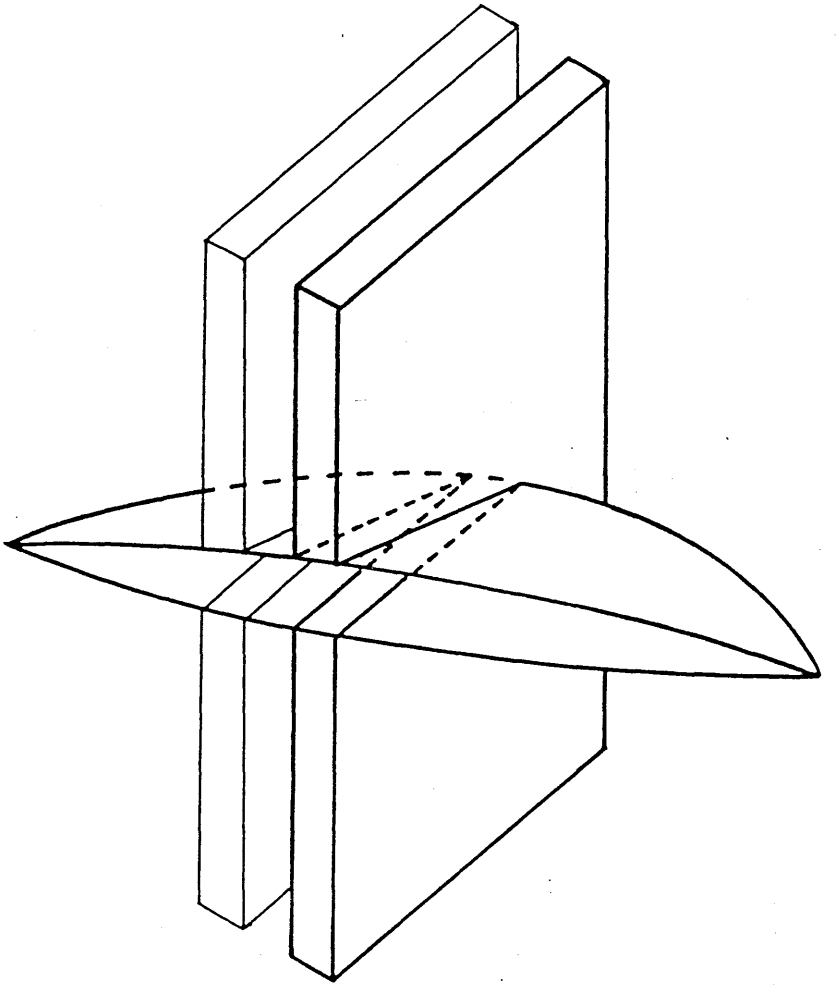

Fig. 6.2 Schematic illustration of the sectioning procedure.

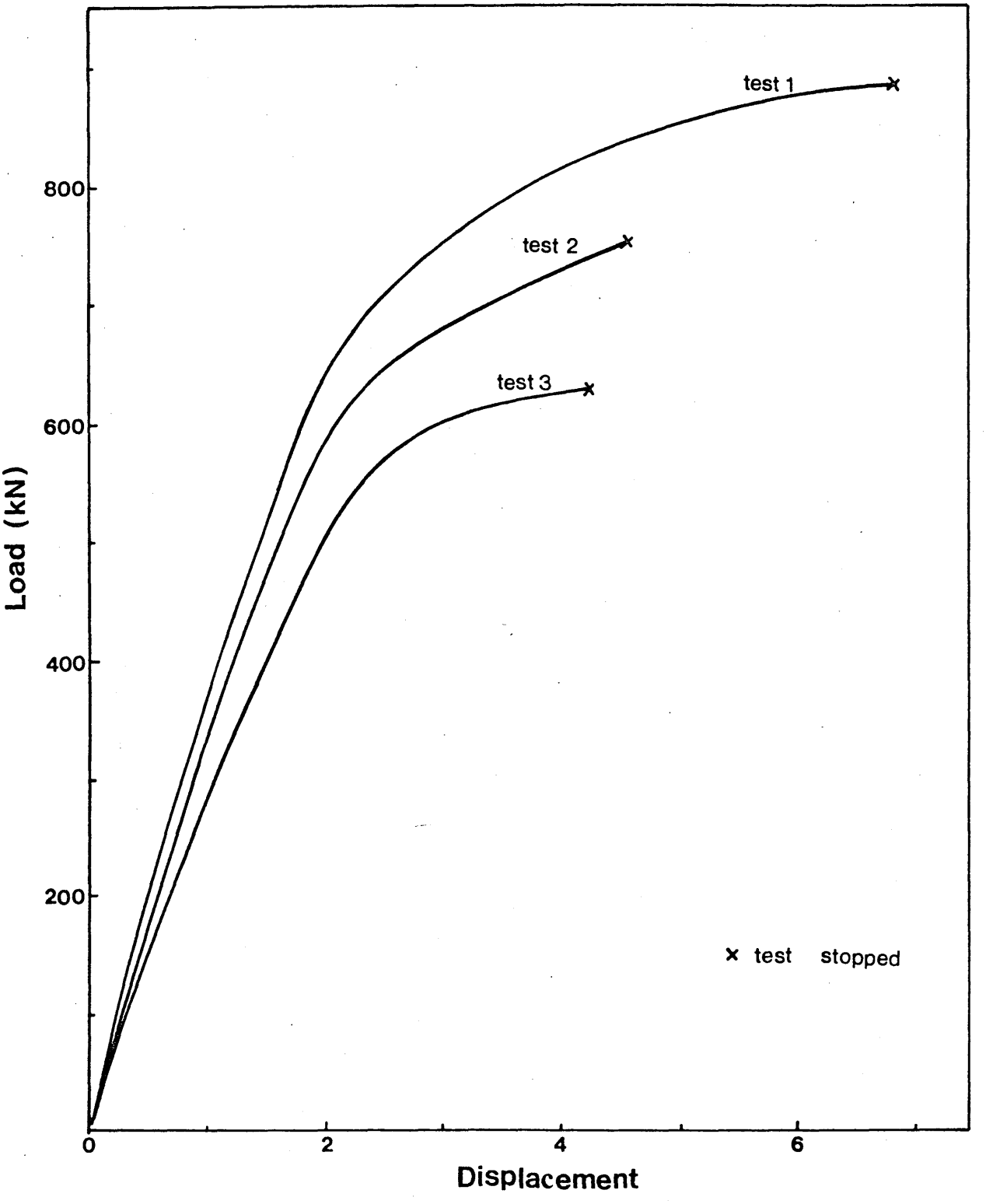

Fig. 6.3 Load-displacement record for tests 1,2 and 3.

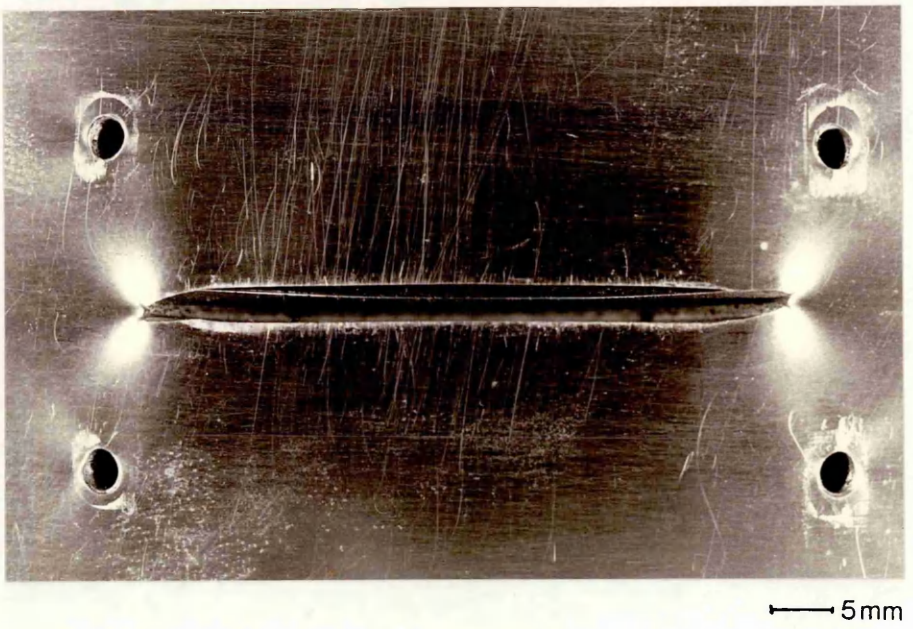

Fig. 6.6 Pattern of plastic zone development at the crack tip on the specimen surface in test 2.

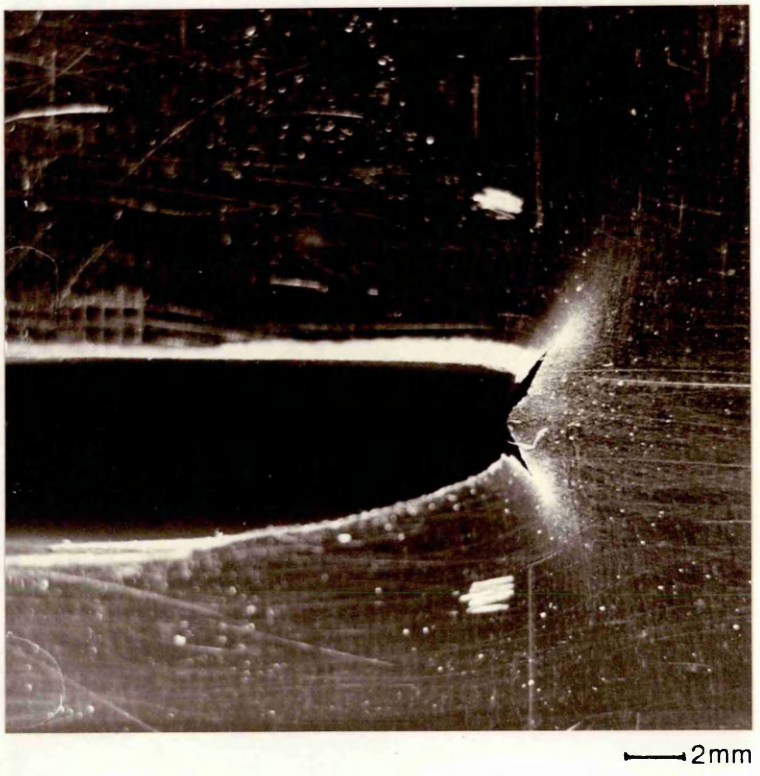

Fig. 6.7 Damaged area at the crack tip on the specimen surface in test 1 indicates that the failure is Mode II ductile shear.

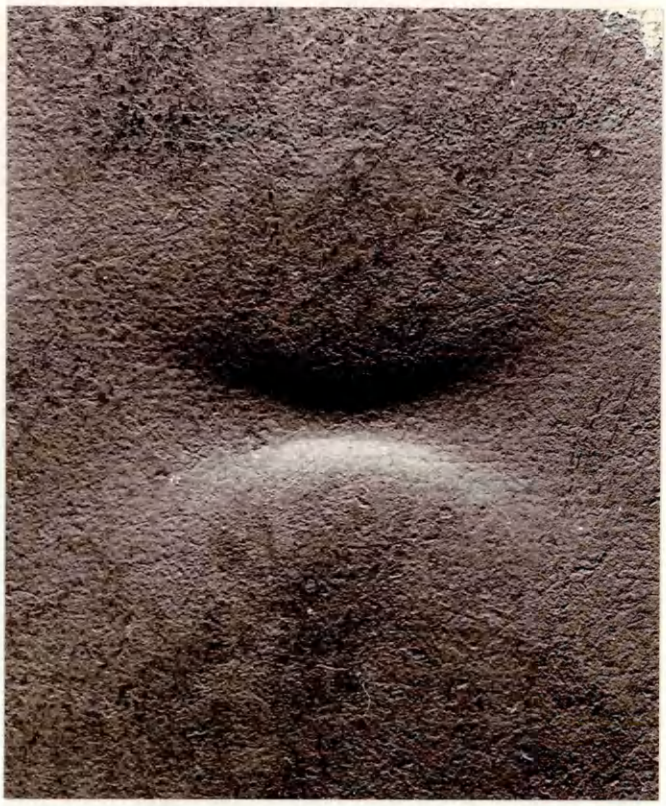

Fig. 6.8 Morphology of surface depression on the back of specimen in test 1.

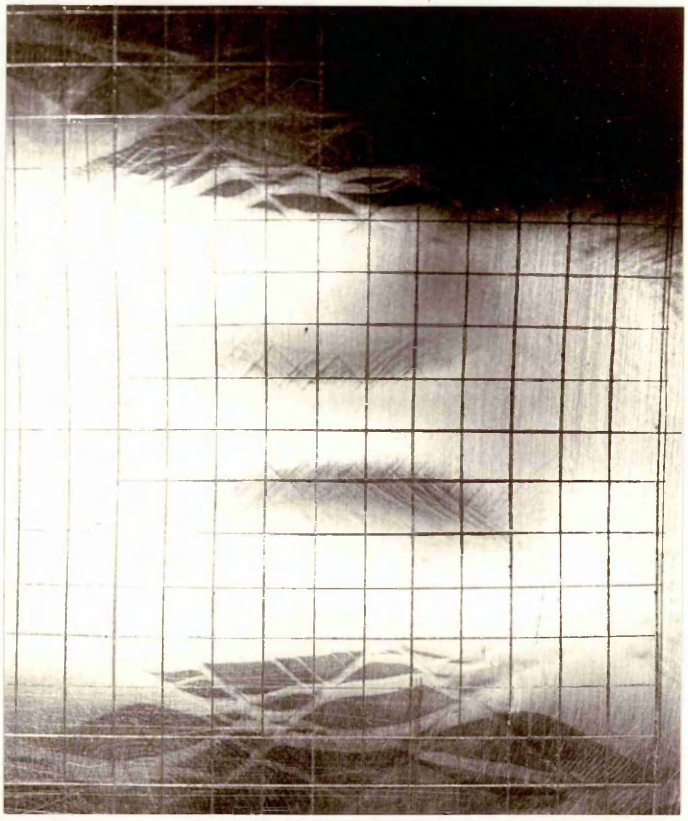

Fig. 6.9 Morphology of surface depression on the back of specimen in test 2.

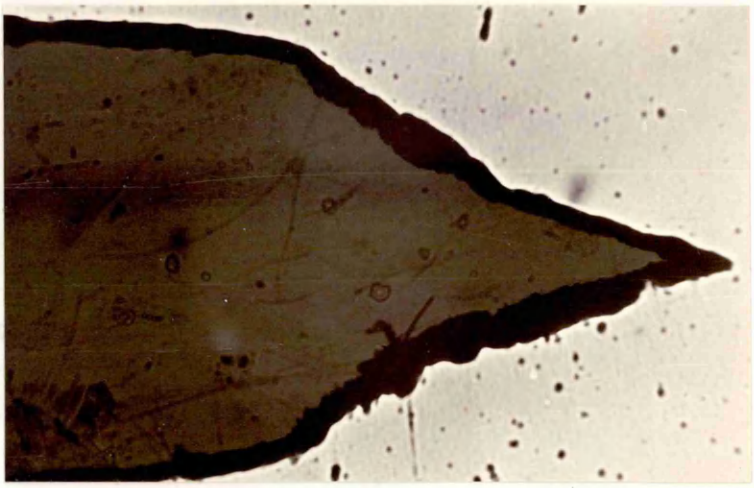

(a)

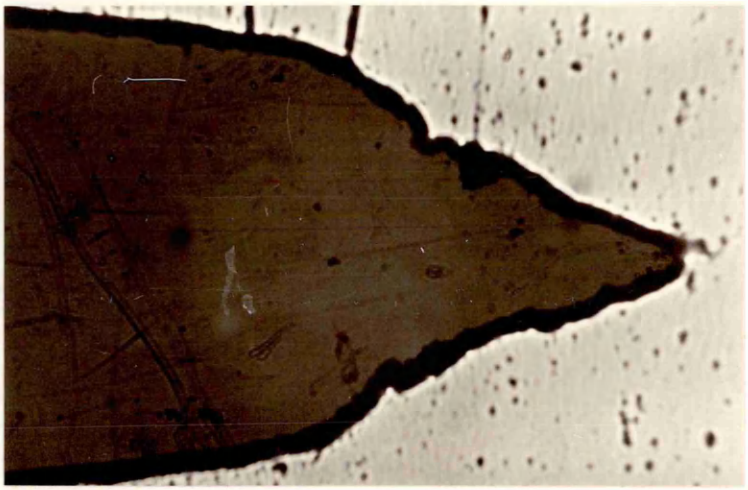

(b)

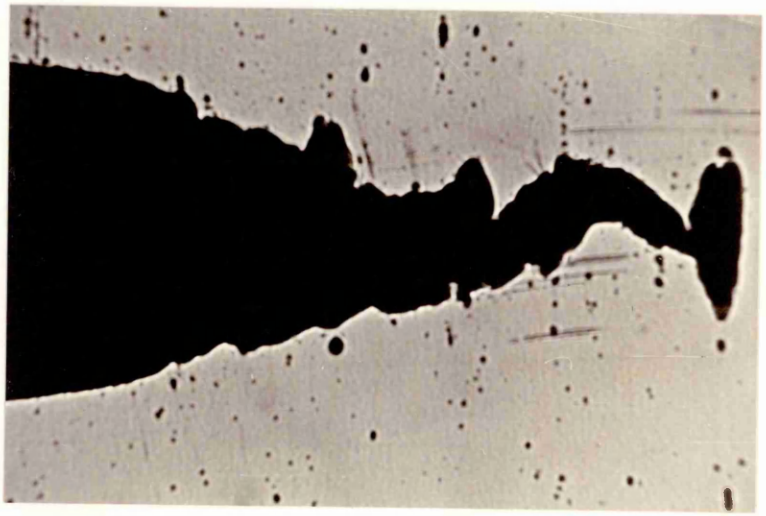

(c)

0.5 mm

Fig. 6.10 Crack tip damaged area at (a) θ=90 ,(b) θ=60 and (c) θ=15 in test 1.

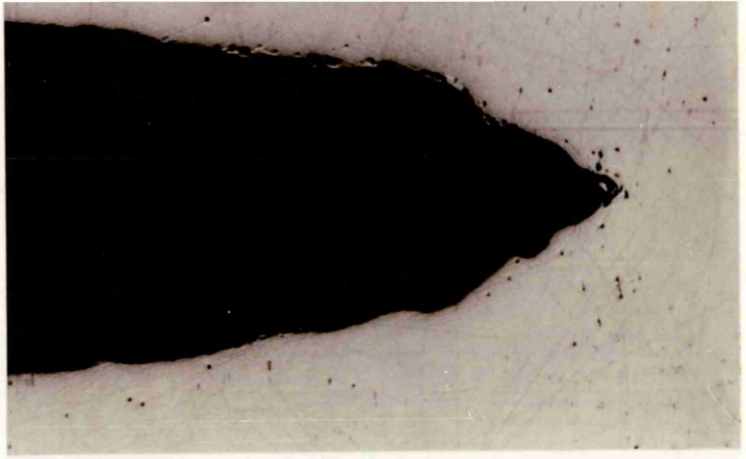

(a) 0.5 mm

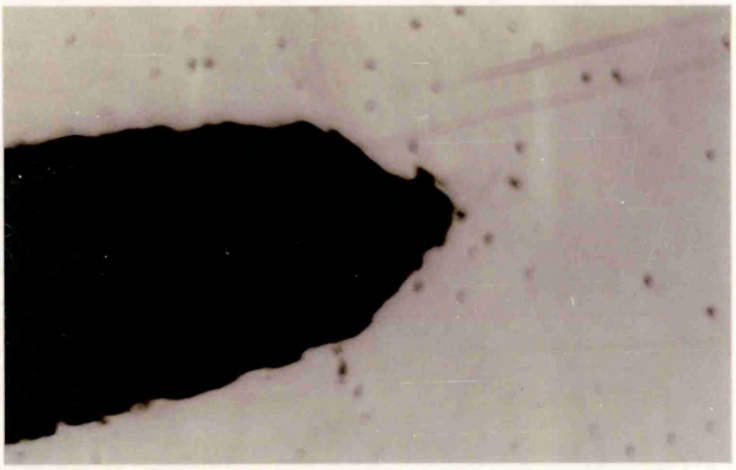

(b) 0.5 mm

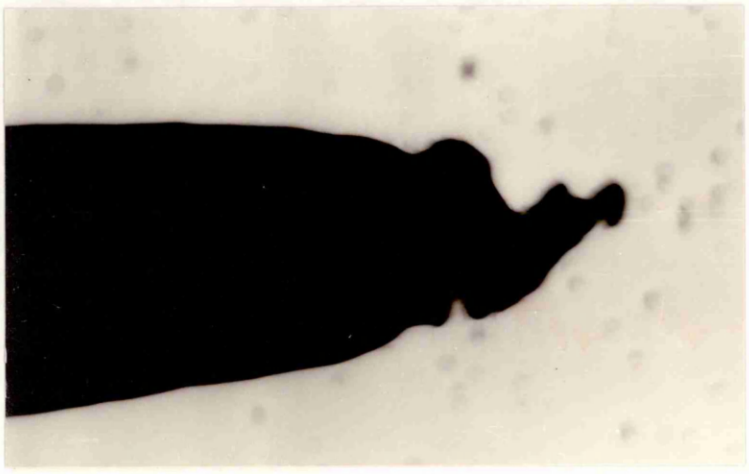

(c) 0.5 mm

Fig. 6.11 Crack tip damaged area at (a) θ=90 ,(b) θ=60 and (c) θ=15 in test 2.

(a) 0.5 mm

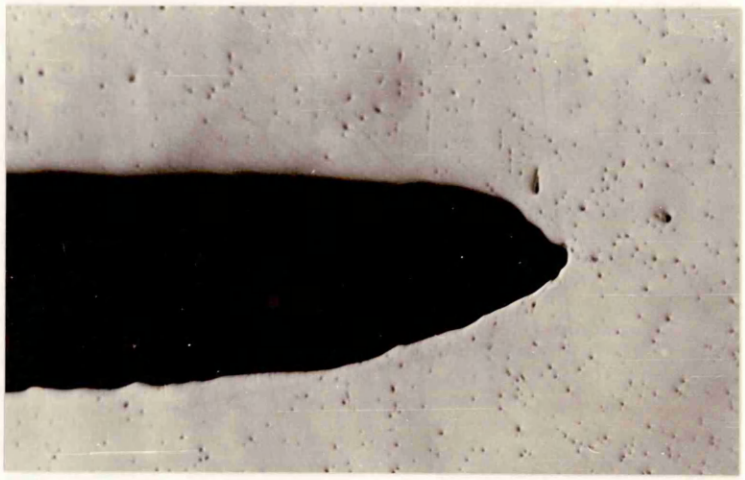

(b) 0.5 mm

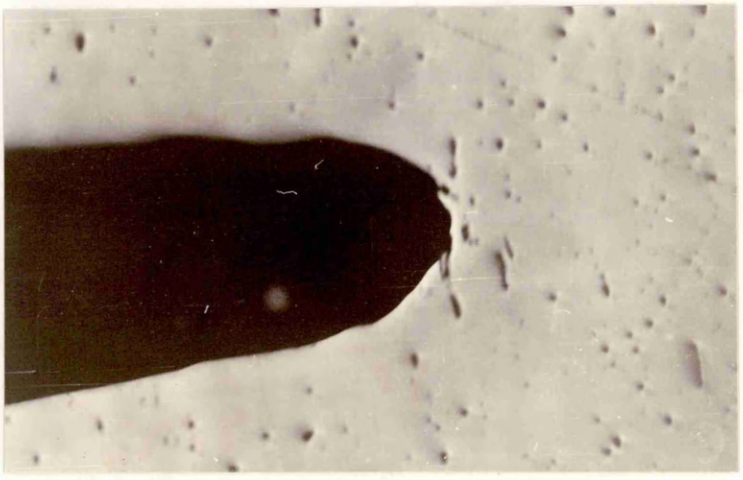

(c) 0.5 mm

Fig. 6.12 Crack tip damaged area at (a) θ=90 ,(b) θ=60 and (c) θ=15 in test 3.

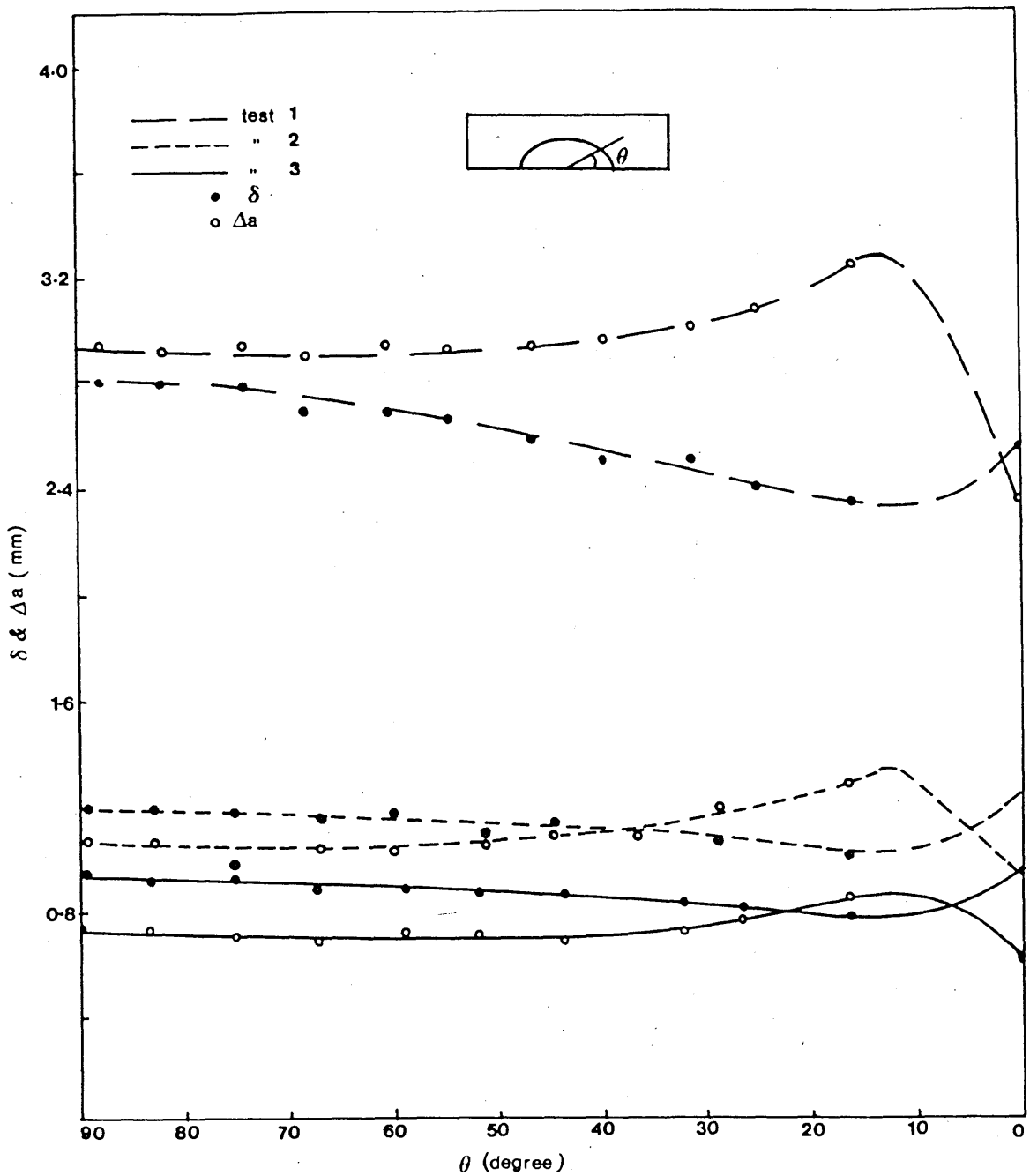

Fig. 6.13 Variation of crack opening displacement, COD , and crack extension, Δa , along the crack front as a function of angle θ .

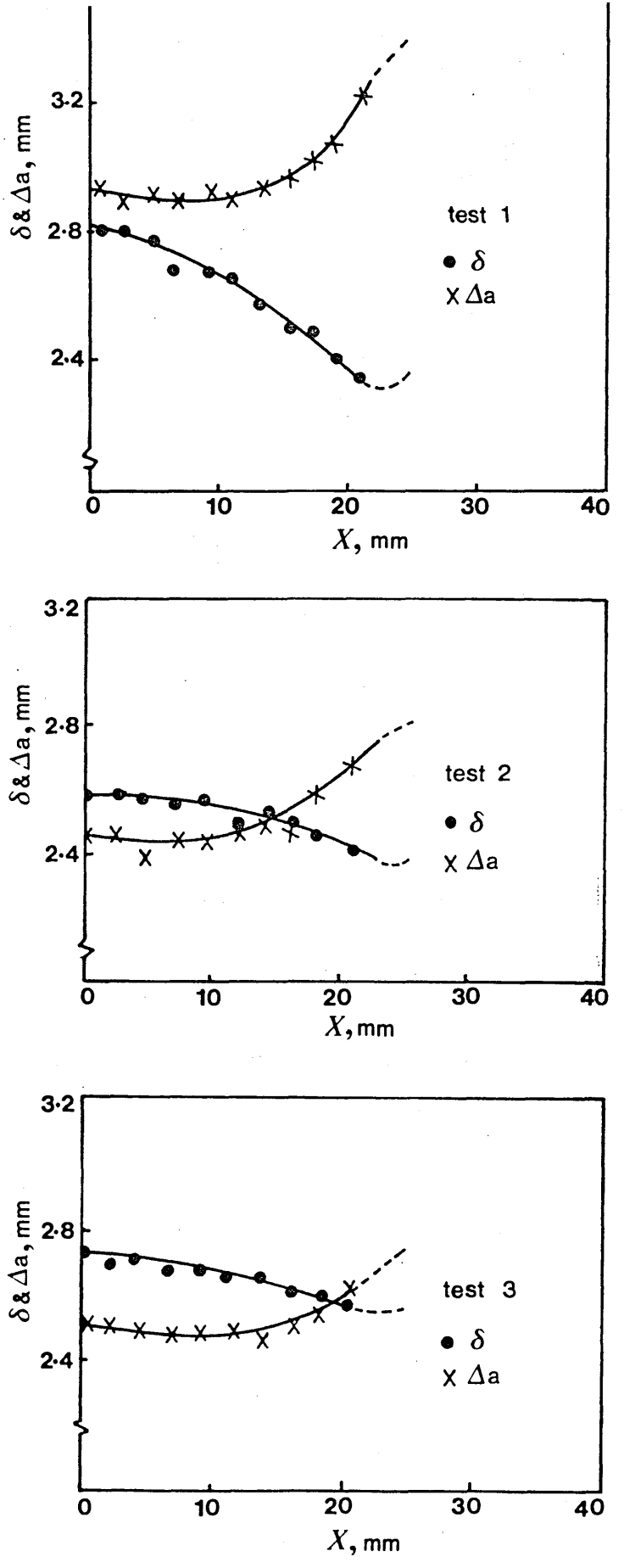

Fig. 6.14 Variation of COD and Δa along the crack front, as a function of distance x from the crack centre line.

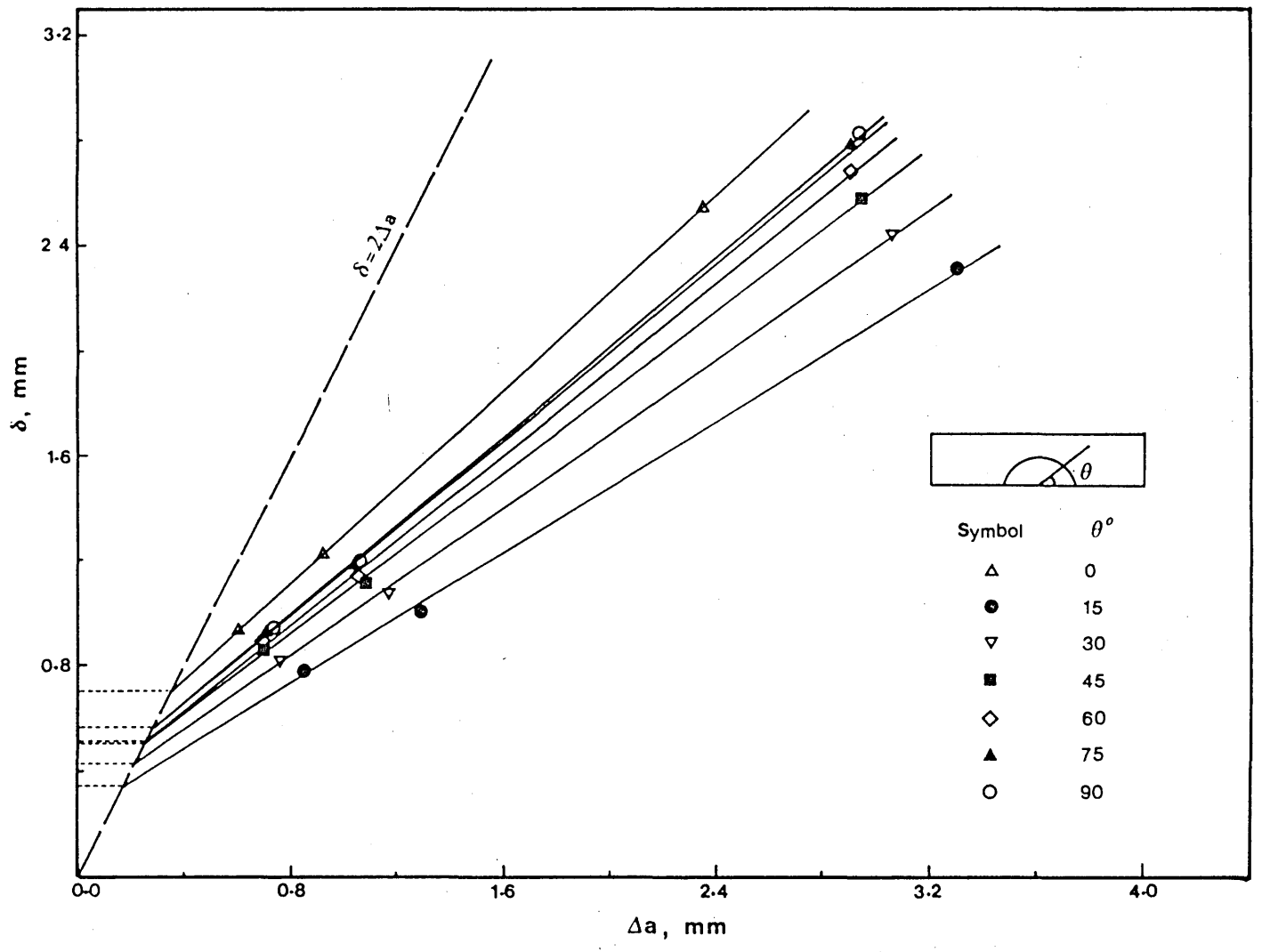

Fig. 6.15 COD R-curve for positions $\theta = 0$, 15, 30, 45, 60, 75 and 90 degrees along the crack front.

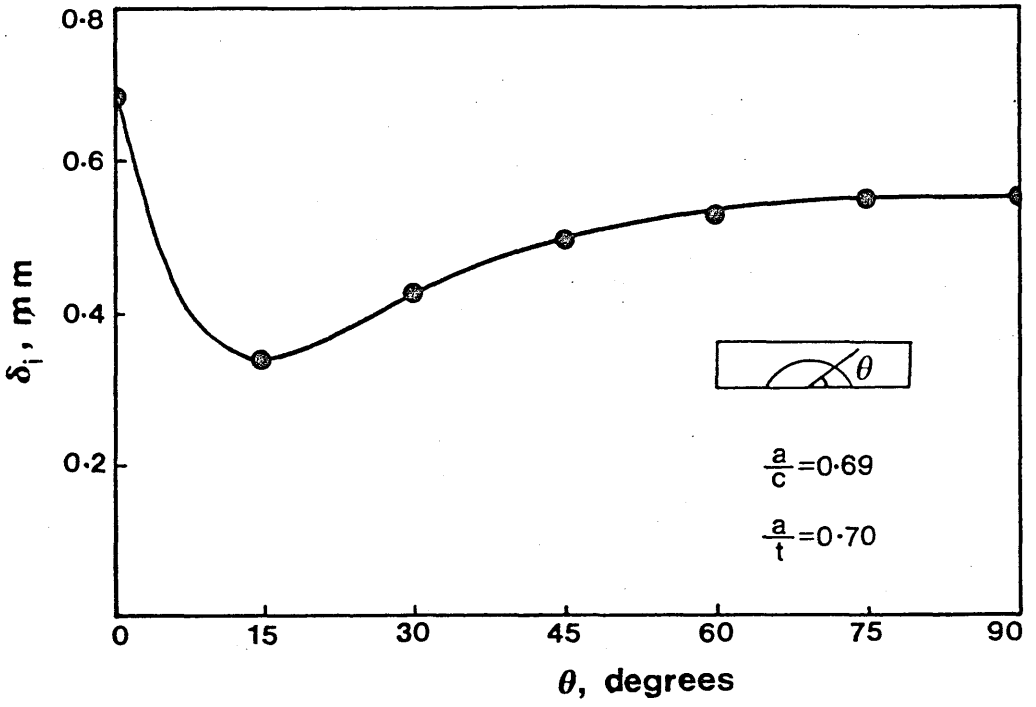

Fig. 6.16 Distribution of COD at the initiation of crack extension as a function of angle θ around the crack front.

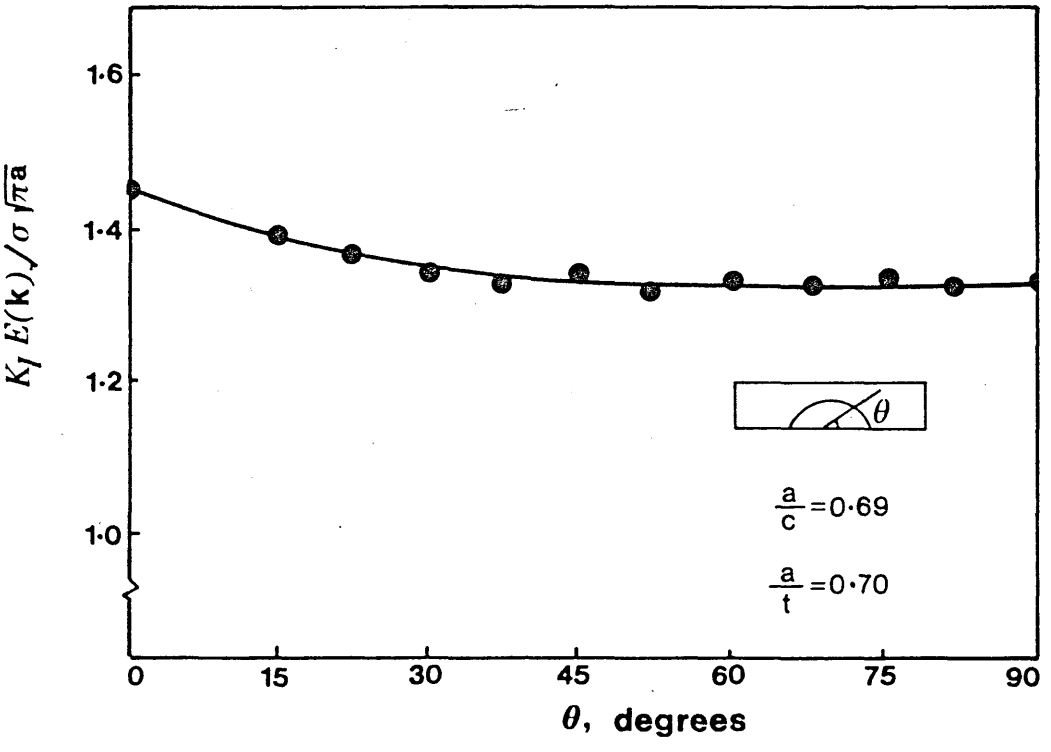

Fig. 6.17 Distribution of stress intensity factor around the periphery of a semi-elliptical crack of a/c=0.69 and a/t=0.7. (from data presented in section 5.7.2)

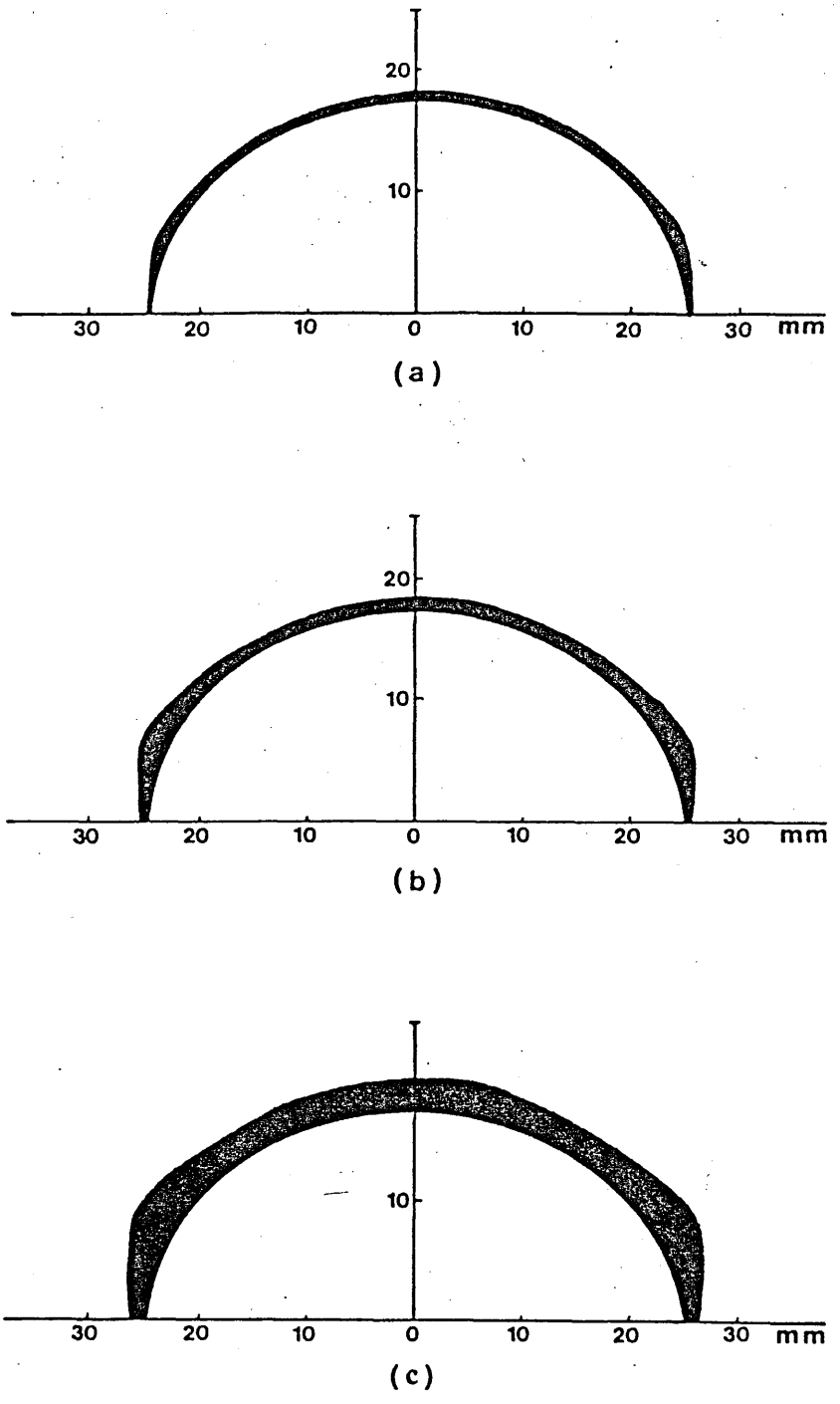

Fig. 6.18 The extent of the ductile tearing around the crack front measured in (a) test 3, (b) test2, and (c) test 1. This Fig. shows the development of crack profile under monotonic tensile loading for the limited amount of crack extention studied.

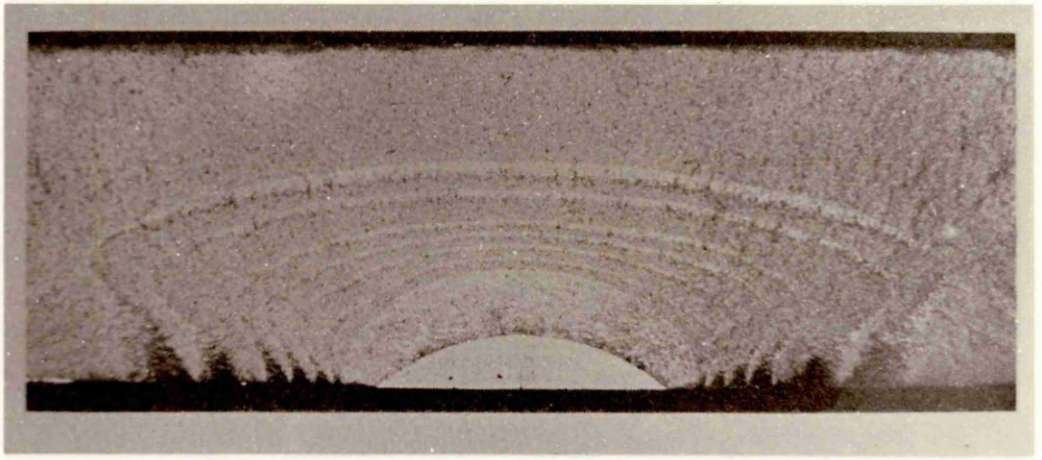

Fig. 6.19 Crack profile development under monotonic tensile loading in an Aluminium alloy test piece[8].

Section 7

CONCLUSIONS

7.1 The dependence of the ductile failure initiation strain on the stress state observed at ambient temperatures, is insensitive to temperature in the ductile-brittle transition region for the range of stress states studied.

7.2 At ambient temperatures, the post yield fracture initiation characterizing parameters are sensitive to the stress state in the crack tip region. This sensitivity decreases with decreasing temperature in the ductile-brittle transition region.

7.3 In the transition region when the brittle fracture criterion is satisfied, as a result of local stress level elevation at the crack tip, the cleavage mechanism interrupts the progress of the ductile failure mechanism. This results in a mixed mode failure initiation and propagation mechanism.

7.4 The morphology and mechanism of post yield failure on the upper shelf associated with the low constraint SECT geometry is different from that associated with more highly constrained flow fields at the same temperature.

7.5 The distribution of stress intensity factor around the boundary of a part-through crack, subjected to remote tensile loading is a function of the crack profile and is relatively well described by the Newman and Raju solution for fractional depths in the range $0.22 \leq {}^{a}/_{t} \leq 0.6$.

7.6 The distribution of initiation COD around the periphery of a part-through surface crack subjected to remote tensile loading is different from the distribution of stress intensity factor.

7.7 The initiation of post yield failure from pre-existing part-through defects, subjected to monotonic tensile loading, occurs first in regions of high constraint. The subsequent failure propagation modifies the crack profile considerably. Failure initiation may be correlated with fracture parameters measured in different types of standard laboratory through-crack test pieces.

7.8 The defect tolerance of part-through surface cracks in tensile fields may be characterized by the SECT crack geometry provided that the significant amount of tearing can be accommodated.

7.9 The limit loads predicted by defect assessment procedures commonly used in the U.K. have been found to be excessively conservative for the defect geometry studied.